HIGGSLESS SIMULATIONS OF RELATIVISTIC HYDRODYNAMICS AND GRAVITATIONAL WAVE PRODUCTION IN COSMOLOGICAL PHASE TRANSITIONS

Dissertation zur Erlangung des Doktorgrades
an der Fakultät für Mathematik, Informatik und Naturwissenschaften
der Universität Hamburg

vorgelegt von
Isak Stomberg

Hamburg, 2024

Gutachter der Dissertation:
Prof. Dr. Geraldine Servant
Dr. Thomas Konstandin
Gutachter der Disputation:
Prof. Dr. Geraldine Servant
Dr. Thomas Konstandin
Dr. Kai Schmidt-Hoberg
Prof. Dr. Oliver Gerberding
Prof. Dr. Jochen Liske
Vorsitzender der Prüfungsausschusses:
Prof. Dr. Jochen Liske
Datum der Disputation: 11.10.2024
Vorsitzender des Fach-Promotionsausschusses PHYSIK:
Prof. Dr. Markus Drescher
Leiter des Fachbereichs PHYSIK
Prof. Dr. Wolfgang J. Parak
Dekan der Fakultat MIN:
Prof. Dr.-Ing. Norbert Ritter

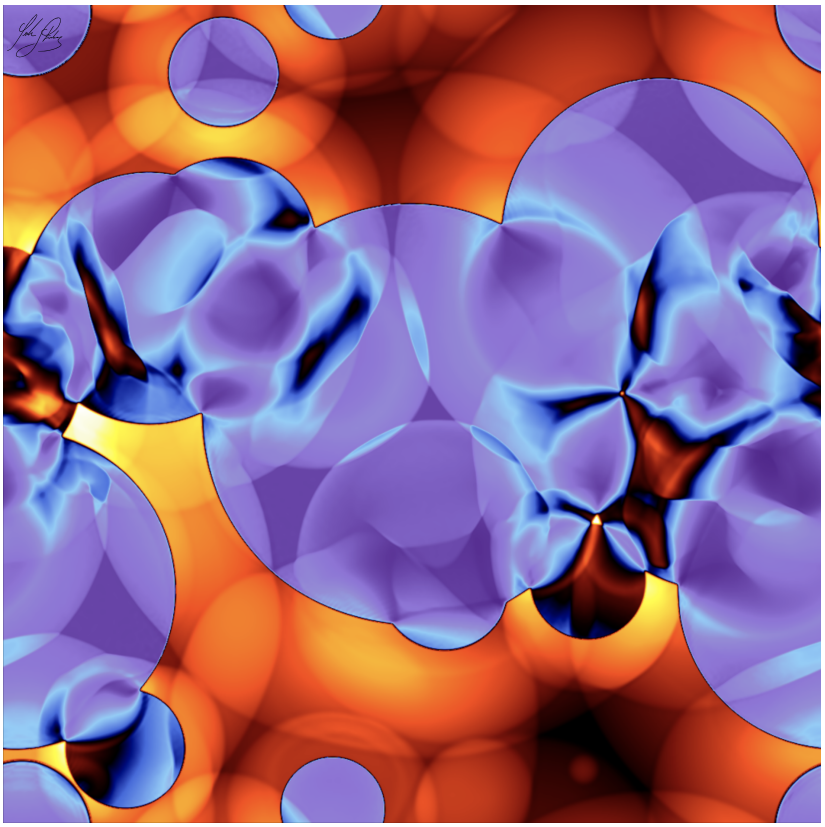

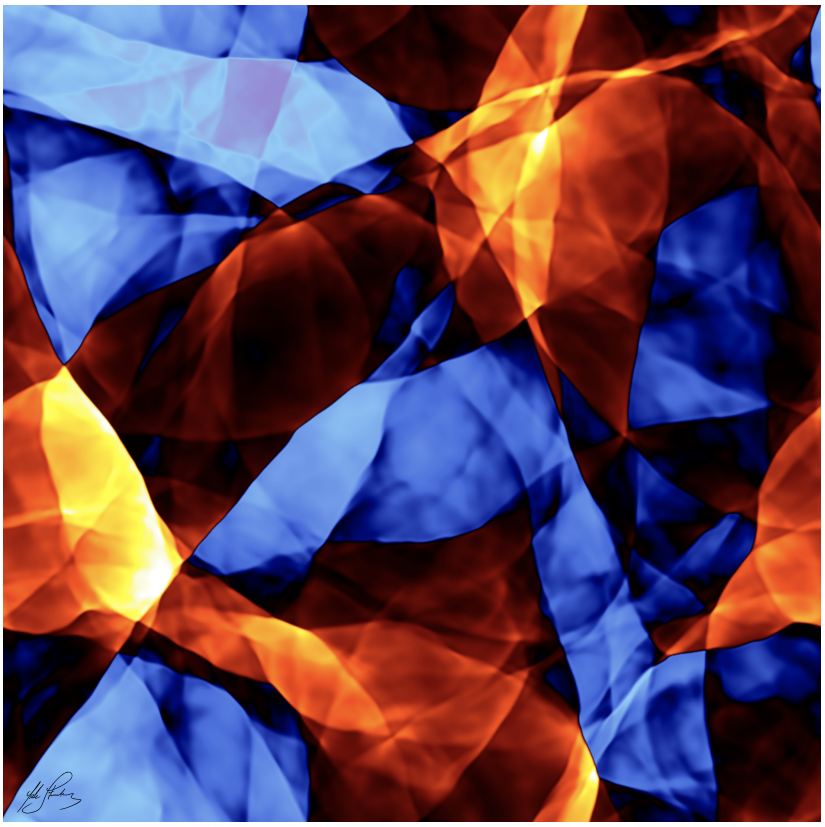

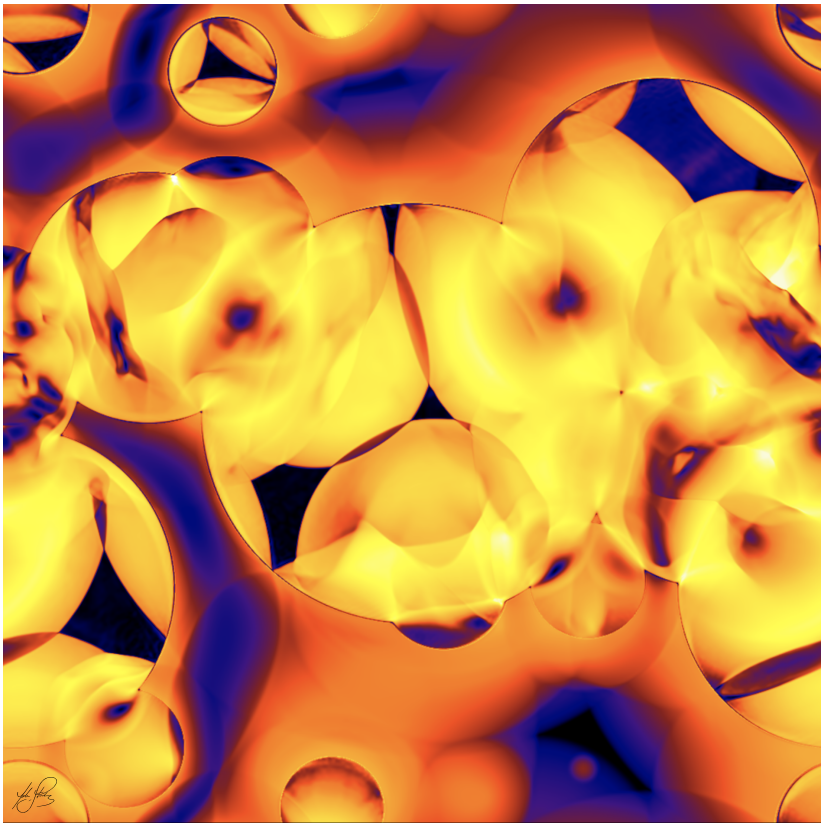

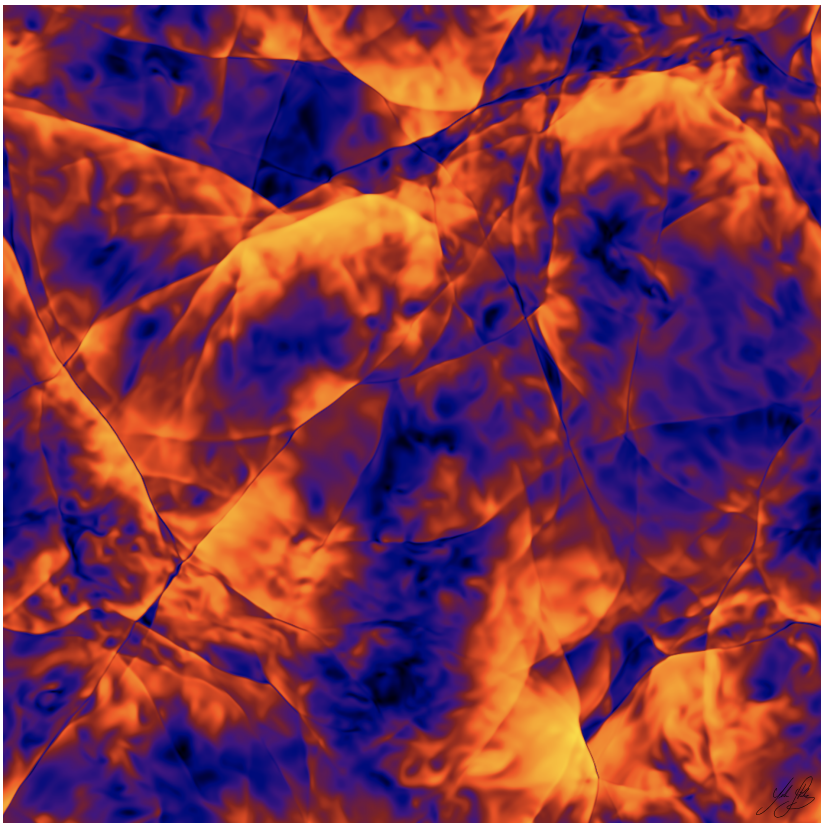

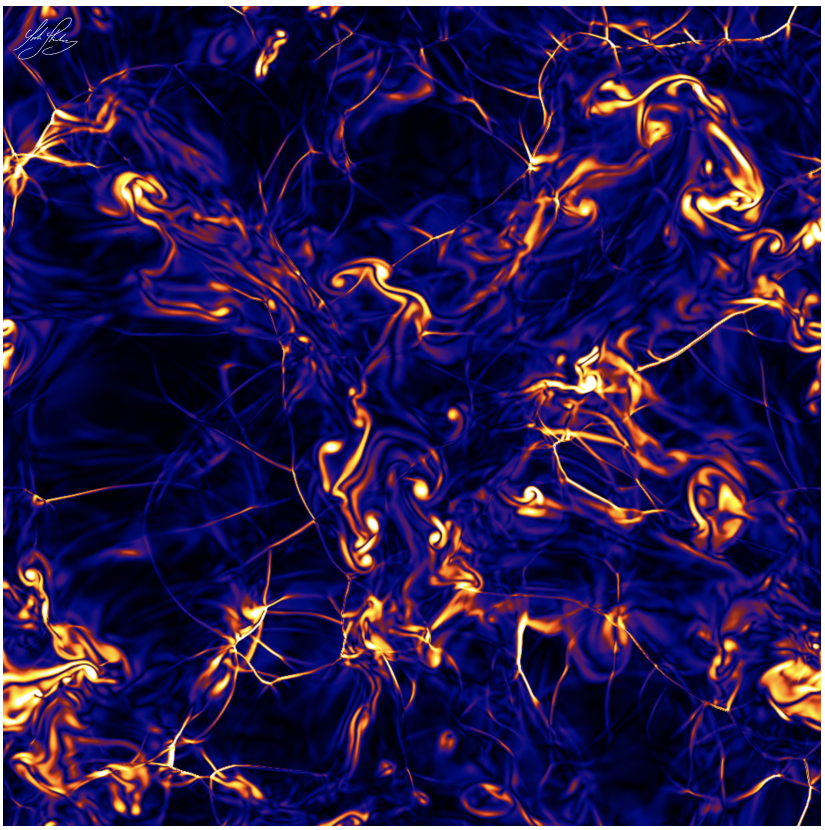

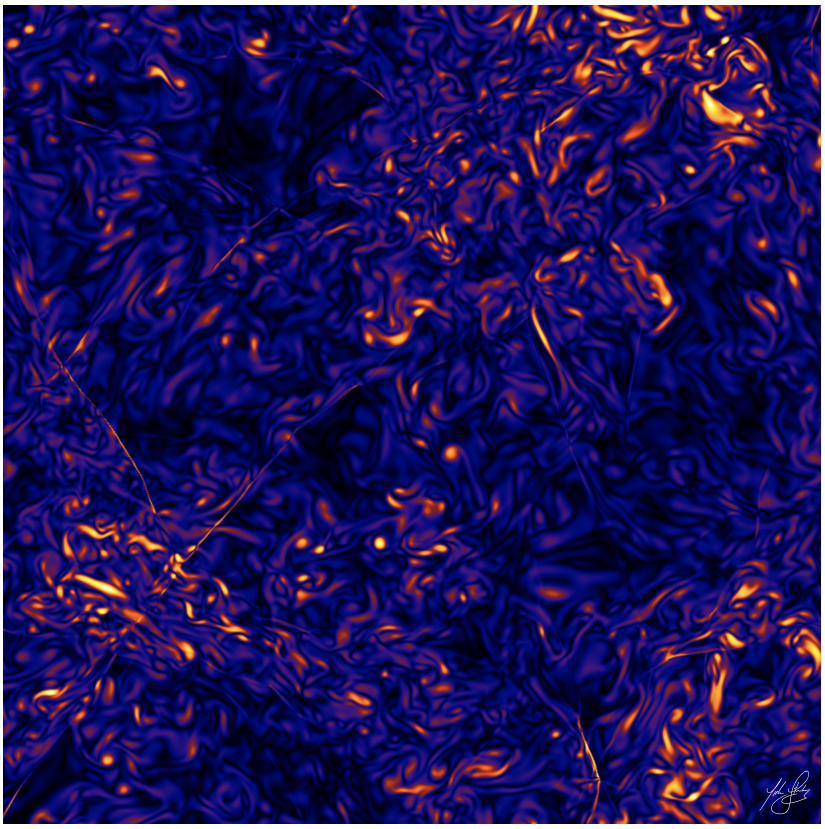

DECLARATION OF OATH

I hereby declare and affirm that this doctoral dissertation is my own work and that I have not used any aids and sources other than those indicated.

If electronic resources based on generative artificial intelligence (gAI) were used in the course of writing this dissertation, I confirm that my own work was the main and value-adding contribution and that complete documentation of all resources used is available in accordance with good scientific practice. I am responsible for any erroneous or distorted content, incorrect references, violations of data protection and copyright law or plagiarism that may have been generated by the gAI.

San Diego
September 6, 2024

Isak Stomberg

ABSTRACT

This thesis explores the production of gravitational waves (GWs) during first-order cosmological phase transitions (PTs) and presents the core findings from my doctoral research. Central to my work is the development of a novel simulation framework that leverages a Higgsless approach specifically designed to model the relativistic hydrodynamics and GW production associated with such transitions.

The Higgsless simulations introduce a highly efficient method designed to capture the nonlinear dynamics of the primordial fluid, offering precise extraction of GW spectra from first-order PTs. By excluding the Higgs field dynamics, the simulations achieve significant computational cost reduction without sacrificing accuracy, making it a valuable tool for further progress within the field and the broader community.

Our Higgsless approach has proven exceptionally effective at solving the relativistic hydrodynamic equations with great precision, resolving high-gradient phenomena such as shocks and nonlinear evolution - critical for accurate GW predictions - while maintaining computational efficiency. The Higgsless approach, therefore, effectively bridges the gap between the traditional semianalytic models and computationally expensive numerical simulations.

This thesis is divided into two main sections. Part I offers a concise theoretical foundation on GWs and PTs in cosmology, setting the stage for the subsequent scientific investigations. Part II delves into key theoretical concepts for numerical simulations, including central difference methods, before detailing the implementation, validation, and application of the Higgsless simulations. These simulations serve as the foundation for the thesis's primary results and scientific contributions.

Major achievements of my research include the development of a 3D, fully nonlinear hydrodynamical simulation code for modeling PT dynamics using the Higgsless approach. This innovation enabled novel predictions of GW production driven by fluid dynamics in PTs, marking the first-ever derivation of GW spectra from strong PTs. Additionally, it provided detailed insights into the parametric dependence of the GW spectrum on fundamental PT quantities across a broad range of the PT parameters space.

ZUSAMMENFASSUNG

Diese Dissertation untersucht die Erzeugung von Gravitationswellen (GWs) während kosmologischer Phasenübergänge (PTs) erster Ordnung und präsentiert die wesentlichen Ergebnisse meiner Doktorarbeit. Im Zentrum meiner Arbeit steht die Entwicklung eines neuartigen das Simulationskonzepts, der einen Higgs-losen Ansatz nutzt, der speziell zur Modellierung der relativistischen Hydrodynamik und der GW-Erzeugung in solchen Übergängen entwickelt wurde.

Die Higgs-losen Simulationen bieten eine hocheffiziente Methode zur Erfassung der nichtlinearen Dynamik des primordialen Fluids und ermöglichen die präzise Extraktion von GW-Spektren aus Phasenübergängen erster Ordnung. Durch den Verzicht auf die Dynamik des Higgs-Feldes wird eine erhebliche Reduzierung der Rechenkosten erreicht, ohne dass die Genauigkeit beeinträchtigt wird. Dies macht die Methode zu einem wertvollen Werkzeug für die weitere Entwicklung des Forschungsgebiets und für die wissenschaftliche Gemeinschaft insgesamt.

Unser Higgs-loser Ansatz hat sich als äußerst effektiv bei der Lösung der relativistischen hydrodynamischen Gleichungen mit hoher Präzision erwiesen und ermöglicht die Auflösung von Hochgradientenphänomenen wie Schocks und nichtlinearer Evolution – entscheidend für genaue GW-Vorhersagen – bei gleichzeitiger Erhaltung der Recheneffizienz. Der Higgs-lose Ansatz schließt somit effektiv die Lücke zwischen den traditionellen semianalytischen Modellen und rechenintensiven numerischen Simulationen.

Diese Dissertation ist in zwei Hauptteile gegliedert. Teil I bietet eine prägnante theoretische Einführung zu GWs und PTs in der Kosmologie und bildet die Grundlage für die nachfolgenden wissenschaftlichen Untersuchungen. Teil II behandelt die wichtigsten theoretischen Konzepte für numerische Simulationen, einschließlich zentraler Differenzmethoden, bevor die Implementierung, Validierung und Anwendung der Higgs-losen Simulationen im Detail erläutert werden. Diese Simulationen bilden die Grundlage für die wesentlichen Ergebnisse und wissenschaftlichen Beiträge dieser Dissertation.

Zu den wichtigsten Errungenschaften meiner Forschung gehört die Entwicklung eines 3D, vollständig nichtlinearen hydrodynamischen Simulationscodes zur Modellierung der PT-Dynamik mithilfe des Higgslosen Ansatzes. Diese Innovation ermöglichte neuartige Vorhersagen zur GW-Erzeugung durch die Fluiddynamik bei PTs und markiert die erste Ableitung von GW-Spektren aus starken PTs. Darüber hinaus lie-

ferte sie detaillierte Einblicke in die parametrische Abhängigkeit des GW-Spektrums von den fundamentalen Größen der PTs über einen weiten Bereich des PT-Parameterraums.

THESIS OUTLINE

This thesis, titled *Higgsless Simulations of Relativistic Hydrodynamics and Gravitational Wave Production in Cosmological Phase Transitions* is based on the published works [1], [2], [3]. It is divided into Part I, *Theory of gravitational waves and cosmological phase transitions*, Part II, *Higgsless Simulations*, and Part III, *Appendix*. Part I is outlined to establish the theoretical foundation and context necessary for understanding the scientific work presented in Part II.

Part I is divided into Chapter 2, beginning with Section 2.1, where I introduce GWs in flat, non-expanding space as small perturbations of the metric. I describe the GW equations of motion, express the energy and momentum of GWs, and derive Weinberg's formula for the GW production from a generic source of energy and momentum. Then, in Section 2.2, I review GWs in cosmology, justify the stochasticity of GW backgrounds, derive the redshifted GW amplitude and wavenumber, formally describe GWs in an expanding space-time, shed light on Weinberg's formula, and finally, review the production of GWs by sound waves.

This is followed by Chapter 3, which reviews cosmological phase transitions. In Section 3.1, I cover the basic concepts of phase transitions, including the effective potential, bubbles and their nucleation rate, statistics associated with bubble nucleation and expansion, the Bag model and equation of state, phase transition strength, and the hydrodynamics of singular bubbles. In Section 3.2, I review GWs from first-order phase transitions. I provide estimates of key features of the GW signal, discuss the scalar-field contribution to GW production in various models, explore the plasma contribution to GW production in different scenarios, and conclude with a few comments on the observational prospects for GW detection.

Part II, focusing on the design, implementation, evaluation, and application of our novel Higgsless simulations introduced in [1], is divided into four chapters. Chapter 4 serves as an overview of central difference methods, with particular emphasis on the method used in our simulations. In Section 4.1, I introduce hyperbolic conservation laws. In Section 4.2, I present the Lax-Friedrichs scheme as a prototypical example of a central difference method. Then, in Section 4.3, I introduce the Kurganov-Tadmore central difference method, the backbone of the Higgsless simulations, in both its semi-discrete and fully-discrete formulations, including generalizations to three dimensions, and offer some concluding remarks.

In Chapter 5, based mainly on the scientific work presented in my publication [1], I introduce our novel Higgsless simulations and present the first numerical findings. Section 5.1 provides background and context and outlines the scientific objectives. In Section 5.2, I review the physical setup governing the simulations. Section 5.3 explores the numerical methods and programmatic choices, detailing their impact on both the physics and measurements. In Section 5.4, I validate the simulation code, followed by the presentation of numerical results in Section 5.5. A discussion is provided in Section 5.6, with concluding remarks in Section 5.7. I close the chapter with a brief digression in Section 5.8, reviewing the results of my other publication [2], which constitutes a case applying the Higgsless simulations to PTs seeded by domain walls.

In Chapter 6, based on the work from my publication [3], I expand upon the previous Chapter 5, significantly advancing our understanding of the simulation's performance and, for the first time, deriving gravitational wave predictions from strong phase transitions. I further generalize the theoretical framework for gravitational waves generated by sound waves to incorporate a damped source. Section 6.1 introduces the study and the broader context and outlines its scientific objectives. In Section 6.2, I extend the model for gravitational wave production to account for damped sources and cosmic expansion. Section 6.3 discusses updates to the simulation code and the chosen parameters. The main numerical results, including findings from strong phase transitions and a template for gravitational wave production, are presented in Section 6.4. Finally, Section 6.5 summarizes the key findings and concludes the chapter.

I conclude the thesis in Chapter 7, where I reflect on the overarching scientific goals and achievements and propose avenues for future research.

Part III contains Appendix A, where I comment on the hydrodynamics and gravitational wave production in inverse phase transitions as a response to recent advances in the field.

PUBLICATIONS AND CONTRIBUTION

This thesis is based on the following publications:

- [1] **Ryusuke Jinno, Thomas Konstandin, Henrique Rubira, and Isak Stomberg.** "Higgsless simulations of cosmological phase transitions and gravitational waves." *JCAP*, vol. 02, 011, 2023. DOI: 10.1088/1475-7516/2023/02/011. arXiv: 2209.04369.

  ABSTRACT: *"First-order cosmological phase transitions in the early Universe source sound waves and, subsequently, a background of stochastic gravitational waves. Currently, predictions of these gravitational waves rely heavily on simulations of a Higgs field coupled to the plasma of the early Universe, the former providing the latent heat of the phase transition. Numerically, this is a rather demanding task since several length scales enter the dynamics. From smallest to largest, these are the thickness of the Higgs interface separating the different phases, the shell thickness of the sound waves, and the average bubble size. In this work, we present an approach to perform Higgsless simulations in three dimensions, producing fully nonlinear results, while at the same time removing the hierarchically smallest scale from the lattice. This significantly reduces the complexity of the problem and contributes to making our approach highly efficient. We provide spectra for the produced gravitational waves for various choices of wall velocity and strength of the phase transition, as well as introduce a fitting function for the spectral shape."*

  MY CONTRIBUTION: My contribution to this work lies primarily in the independent development and implementation of the Higgsless simulation code, which I used to run simulations for cross-checking data from the other authors' independent simulation implementations, ensuring full agreement among the numerical results. Specifically, I cross-checked the data used in the analysis, which was derived from Dr. Thomas Konstandin's implementation. Additionally, I assisted in the data analysis, produced several plots, and contributed to the writing of the publication.

- [2] **Simone Blasi, Ryusuke Jinno, Thomas Konstandin, Henrique Rubira, and Isak Stomberg**, "Gravitational waves from defect-driven phase transitions: domain walls," *JCAP*, vol. 10, 051, 2023. DOI: 10.1088/1475-7516/2023/10/051. arXiv: 2302.06952.

ABSTRACT: *"We discuss the gravitational wave spectrum produced by first-order phase transitions seeded by domain wall networks. This setup is important for many two-step phase transitions as seen for example in the singlet extension of the standard model. Whenever the correlation length of the domain wall network is larger than the typical bubble size, this setup leads to a gravitational wave signal that is shifted to lower frequencies and with an enhanced amplitude compared to homogeneous phase transitions without domain walls. We discuss our results in light of the recent PTA hints for gravitational waves."*

MY CONTRIBUTION: In this work, I contributed to the conception of the project, the theoretical work and implementation of the Metropolis algorithm, and the writing of the publication. The numerical data was derived from the Higgsless implementation by Dr. Thomas Konstandin.

- [3] **Chiara Caprini, Ryusuke Jinno, Alberto Roper Pol, Thomas Konstandin, Henrique Rubira, and Isak Stomberg**, "Gravitational waves from decaying sources in strong phase transitions," arXiv: 2409.03651.

ABSTRACT: *"We study the generation of gravitational waves (GWs) during a first-order cosmological phase transition (PT) using the recently introduced Higgsless approach to numerically evaluate the fluid motion induced by the PT. We present for the first time spectra from strong first-order PTs ($\alpha = 0.5$), alongside weak ($\alpha = 0.0046$) and intermediate ($\alpha = 0.05$) transitions previously considered in the literature. We test the regime of applicability of the stationary source assumption, characteristic of the sound-shell model, and show that it agrees with our numerical results when the kinetic energy, sourcing GWs, does not decay with time. However, we find in general that for intermediate and strong PTs, the kinetic energy in our simulations decays following a power law in time, and provide a theoretical framework that extends the stationary assumption to one that allows to include the time evolution of the source. This decay of the kinetic energy, potentially determined by non-linear dynamics and hence, related to the production of vorticity, modifies the usually assumed linear growth with the source duration to an integral over time of the kinetic energy fraction, effectively reducing the growth rate. We validate the novel theoretical model with the results of our simulations covering a broad range of wall velocities. We provide templates for the GW amplitude and spectral shape for a broad range of PT parameters."*

MY CONTRIBUTION: In this work, I was responsible for running the full set of simulations using my own independent Higgsless simulation implementation. I contributed to the conception of the project and the theoretical developments, performed the data analysis of the numerical simulation results, produced the vast majority of the plots, and contributed significantly to the writing of the manuscript.

This thesis will primarily focus on the first and third of these publications, which form the foundation of Chapters 5 and 6, respectively. The second publication, being more application-oriented and slightly diverging from the main theme of the thesis, will be discussed in Section 5.8 of Chapter 5, where a more concise overview is provided.

In addition to these publication, during my PhD studies, I was actively involved in a number of collaborations both within and outside of DESY and University of Hamburg. These gave rise to the following publications,

- **Hyungjin Kim, Alessandro Lenoci, Isak Stomberg, and Xiao Xue.** "Adiabatically compressed wave dark matter halo and intermediate-mass-ratio inspirals." *Phys. Rev. D*, vol. 107, no. 8, 2023, pp. 083005. arXiv:2212.07528. DOI: 10.1103/PhysRevD.107.083005,
- **Mesut Çalışkan, Yifan Chen, Liang Dai, Neha Anil Kumar, Isak Stomberg, and Xiao Xue.** "Dissecting the stochastic gravitational wave background with astrometry." *JCAP*, vol. 05, 2024, pp. 030. arXiv:2312.03069. DOI: 10.1088/1475-7516/2024/05/030,

of which I am a co-author. Since these works are topically distinct and have relatively little relevance to my primary research focus on simulations of cosmological phase transitions, I have chosen not to include them in this thesis.

To *all those students,*

who diligently toil in obscurity, to bring forth the noblest of treasures
- enlightenment.

ACKNOWLEDGMENTS

One person was always there to provide guidance, engage in discussions, share ideas, give me the freedom to explore, and share both personal endeavors and academic challenges. This person is my supervisor, Thomas Konstandin, to whom I owe immense gratitude. His support and mentorship made my PhD journey not only intellectually rewarding but also deeply enjoyable. I would like to extend my sincere thanks to Prof. Geraldine Servant for her invaluable support throughout my academic journey, from facilitating my initial arrival at DESY for my master's program to supporting my progression through the QU PhD program. Her leadership in assembling such a vibrant research group, where both scientific advancement and personal connections flourish, has been deeply appreciated. I am also grateful to Dr. Kai Schmidt-Hoberg for his mentorship and long-standing support through the years. I would like to thank Prof. Oliver Gerberding for being a source of inspiration and for agreeing to serve as a member of my thesis committee. I also extend my gratitude to Prof. Jochen Liske for accepting the role of committee chair. Additionally, for serving as a buffer between me and the bureaucracy and for helping me with various tasks throughout the years, I want to thank the administrative staff at DESY and the University of Hamburg.

Throughout my PhD candidacy, I have had the privilege of collaborating with many remarkable individuals, both at DESY and around the world. I would like to extend a sincere and special thank you to Prof. Axel Brandenburg at NORDITA, with whom I closely collaborated and who gave me the privilege of becoming a visiting PhD student. At NORDITA, I also began work with Dr. Ramkishor Sharma and Dr. Alberto Roper Pol as we implemented the Higgsless simulation approach in the Pencil Code. I am deeply grateful for the close collaboration with both, as our work together paves the way for a comprehensive program of future explorations.

Moreover, my collaboration with Dr. Alberto Roper Pol extended to Geneva in the form of a scientific visit, for which I am very appreciative. This experience also gave me the opportunity to meet and work with Prof. Chiara Caprini at the University of Geneva — a collaboration that has been very fruitful, resulting in significant scientific work that constitutes a cornerstone of this thesis. This partnership has been invaluable, providing me with fresh perspectives on my research and allowing me to see physics in a new light.

To Dr. Alberto Roper Pol, I want to express a particularly heartfelt thank you. From the late evenings we spent working in Geneva to our long and patient discussions, our incredible time skiing, the thoughtful conversations we shared over meals and drinks in Moriond, and for our plans to summit Mt. Blanc — your friendship has been a highlight of this journey, and I look forward to the exciting scientific program we have set out to explore together.

At DESY, I am grateful to the brilliant physicist Dr. Hyungjin Kim, with whom I had the pleasure of working. I am also very thankful to Dr. Xiao Xue, who introduced me to pulsar timing arrays and novel GW detection techniques using astrometry. Her exceptional skills, state-of-the-art knowledge, and patience during our many insightful discussions have genuinely enriched my understanding of the field. I eagerly look forward to our continued collaboration as we push the boundaries of unraveling anisotropies in the GW background.

While I had the pleasure of working with many brilliant people, my PhD experience would not have been the same without the close collaboration I shared with Dr. Henrique Rubira and Prof. Ryusuke Jinno. We spent countless hours together working on and discussing the three projects that form the foundation of this thesis. I am indebted to Henrique and Ryusuke for their dedication to making our research shine. Their mentorship, combined with their genuine, heartfelt consideration, extended beyond the scope of our research, and for that, I am deeply thankful.

I would like to express my gratitude to all the collaborators I had the privilege of working with during my PhD, including Dr. Ryusuke Jinno, Dr. Thomas Konstandin, Dr. Henrique Rubira, Dr. Simone Blasi, Prof. Chiara Caprini, Dr. Alberto Roper Pol, Dr. Hyungjin Kim, Dr. Alessandro Lenoci, Dr. Xiao Xue, Dr. Mesut Çalışkan, Dr. Yifan Chen, Prof. Liang Dai, Dr. Neha Anil Kumar, Prof. Axel Brandenburg, and Dr. Ramkishor Sharma. Their willingness to collaborate, their patience, and the insightful discussions we shared not only enriched my knowledge and scientific output but also significantly contributed to the advancement of this thesis.

I would like to thank the Quantum Universe Cluster of Excellence for their financial support under Germany's excellence strategy, Quantum Universe (EXC 2121 – 390833306), and for providing essential educational resources. My sincere thanks also go to the DESY for supporting my position as a doctoral research associate and the University of Hamburg for supporting my doctoral studies. I am grateful to NORDITA for the financial assistance that made several scientific visits possible through my visiting PhD fellowship. In addition, I acknowledge the financial support from COSMO'23 in Madrid, as well as from Rencontres de Moriond in 2023 and 2024, which allowed me

to participate in their fantastic conferences on cosmology and gravitational waves. Finally, I am deeply grateful for the opportunity to visit UCSD, University of San Diego, for three months, which was made possible through the ASYMMETRY initiative and the Horizon Europe Programme Staff Exchange project.

My scientific work has significantly benefited from the generous computational resources provided by the Maxwell cluster at DESY. I am deeply grateful for the freedom I was given to utilize these resources to my heart's content, which played a pivotal role in advancing my research.

Halfway through my PhD, the advent of generative artificial intelligence had a profound impact on the workflow of every researcher who chose to embrace it. I acknowledge the thoughtful use of AI, especially ChatGPT, for its support in proofreading and editing this manuscript. ChatGPT has also significantly enhanced my workflow by aiding in repetitive tasks such as plot generation and the creation of simple code segments. I wish to clarify, however, that AI was not involved in any part of the development and implementation of the Higgsless simulation code or in obtaining the core results of this thesis, as this development took place before the introduction of generative AI to the general public.

My PhD journey would not have been the same without the friendships and support of the Cosmology corridor, whose vibrant energy was always inviting, encouraging, and free from judgment. I would like to extend particular thank you to Dr. Alessandro Lenoci for many insightful discussions during our collaboration, to Dr. Philip Sørensen for his encouragement and for sharing dreams of the mountains amidst the flatness of Hamburg, to Margherita Putti for her energy and spirit, to Enrico Perboni for his valuable thoughts and insights into our mutual field of research, as well as his phenomenal character, to Dr. Aleksandr Chatrchyan for our scientific discussions and for being such a wonderful neighbor and friend, to Matthias "Koschi" Koschnitzke for his dedication in the Councils and friendship, to Dr. Julián Rey for his interest in music and acting as a sounding board for some of my crazy music technology ideas. At DESY, but outside of the Cosmology corridor, I would like to direct a particular thank you to Dr. Alexander Westphal, whose curiosity and excitement never end, and with whom I have spent many hours practicing rhythms only physicists can decipher, and who eagerly listened to so many of my rather peculiar musical ideas. Dr. Pablo Quílez, though you left the Cosmology corridor for San Diego, I had the pleasure of reconnecting with you during my visit to UCSD. Your boundless positivity and remarkable personality enriched my time in San Diego, leading to memorable adventures

and fostering a friendship I hope will endure, filled with further explorations and scientific endeavors.

How can I be more grateful to have had by my side such a wonderful and sparkling human as Dr. Gayatri Batra through my PhD? We shared a profound friendship, a near spiritual connection, and a home. Dr. Pragya Chopra, with a particular preference for strong black coffee and her exuberant, joyful spirit, has been one of my dearest and most cherished friends during my time in Hamburg. Without Pragya's and Gayatri's support during challenging periods, at times, I would have felt lonely and lost. I express my thanks to Dennis Maseizik for having taken me on great adventures in trekking and climbing the German Alps and for his friendship. Beyond Hamburg, I want to express gratitude to my many dear friends, among which I would like to especially mention Ylva Carlsson, Karl Holmberg, Klara Binder, Herman Wilén, Pererik Gallon, and Daniel Stagno, for enriching my life with countless happy memories and for having played a significant role in shaping the person I am today.

My time in Hamburg was greatly enriched by the Chamber Choir of the University of Hamburg. I thank Prof. Thomas Post for his amazing job of leading the choir and instilling such a resounding and loving community, as well as for the inaugural performance of my composition *Bortom det jag dunkelt anar* on my very 30th and extremely memorable birthday. I dearly thank all the members of the choir for our time rehearsing, concerts, magical rehearsal weekends, and the long-lasting after-concert parties.

I would like to extend my most sincere thanks to Kevin Hauber, for his blessings, for being my mentor, coach, therapist, listener, yoga instructor, and friend, who has helped me through many tough times; to Leslie Nelson, for giving so much love, support, and friendship, for sending countless survival packages, for making my stay in San Diego and California so wonderful, and for being such a radiant, colorful and amazing person, with whom I have shared many great moments and rock-hounding adventures, and who is also providing me with a family and a home; to Danny Hammarstedt, my math teacher at high school who always encouraged learning beyond his own comprehension and who always greatly supported his students and me; and to Prof. Vardha N. Bennert, for taking me as her student many years ago, her sincere and inspiring mentorship, and for encouraging me to pursue science.

I want to thank my family, my mother, Susanne Isaksen, and stepfather, Stefan Johansson, for their love and support, and for giving me a sense of stability and home amidst the nomadic life of a young physicist; to my Father, Dan Stomberg, for his love and for having planted the seeds of curiosity for nature and science since my very first foot-

steps, that continue to instill a strong sense of wonder to this day; to my maternal grandmother, Anneli Isaksen, for her love and for having introduced to me the wonders of growing plants and fruits, which ultimately gave me the tasty pleasure of harvesting my own grapes in Hamburg and plenty more in Sweden; and to my paternal grandmother, Siv Stomberg, for her dear love, her extremely time-consuming creation and gift of a *Delsbokofta* handcrafted both before and after she nearly died, for her strong words of instilling a commitment to work hard to complete this PhD, and for always letting me know she is proud of me. I also want to thank my large family in India for their very warm and generous welcome, their appreciation for science and arts, for letting me experience and be part of a new culture, and for feeding me some of the best food that the world has to offer. I would like to extend my heartfelt gratitude to Lisa Andersson, Erik Andersson, Inger Carlsson, Uno Eriksson, for their unconditional support, boundless generosity, and love. Their kindness has given me a sense of family and home that extends beyond my own. When in Sweden, I often recharged in the company of my great friend Klara Binder and her family, with whom I celebrated the arrivals of the New Year and Midsummer. I owe them a special thank you for their hospitality, love for music, and long, interesting discussions. I also owe a special thank you to my dear friend Monica Dare, who holds a special place in my heart. She inspired me with her cherished garden, always believed in me, and guided me with her wise words and captivating stories, shared over long Italian dinners, enjoyed during never-ending bright summer nights.

I paid two visits to the Himalayas over the course of my PhD, during which I met Passang Diki Sherpa in the small village of Syangbo, which is beautifully located inside the Singalila National Park. She inspired me with her exceptional strength, skills, love for nature, and far-reaching hospitality during my visits to her home in the mountains, to the extent that I am planning to head nearly straight to the base of Mt. Kangchenjunga in West Sikkim for a month-long mountaineering course following the successful completion of my PhD. I profoundly thank her for that and for having enriched my life.

I literally would not have been where I am if it were not for my brilliant and beloved partner, Dr. Oindrila Ghosh, with whom I shared a life in Hamburg. I thank her for her presence and loving care, both during the difficult times of recovery from surgery and through life, for her wise guiding words during times of confusion, for her excellent cooking that kept me healthy, for the magnificent birthday trips she gifted me, for our countless discussions about science and nature, for the strength and determination she demonstrates in pursuing her vi-

sions, and for sharing a glass of wine while relaxing after a sometimes challenging day at work.

Finally, there is one person I wish to thank. That is me, simply for daring to follow my dreams.

CONTENTS

1 PRELIMINARIES 1
1.1 Background 1
1.1.1 Cosmological phase transitions: the source 1
1.1.2 Gravitational waves: the signal 3
1.2 Motivation 5

I THEORY OF GRAVITATIONAL WAVES AND COSMOLOGICAL PHASE TRANSITIONS 6

2 GRAVITATIONAL WAVES 8
2.1 Gravitational waves in flat non-expanding space 8
2.1.1 GWs as metric perturbations 8
2.1.2 Equations of motion 9
2.1.3 Energy and momentum of GWs 13
2.1.4 Weinberg's formula 14
2.2 Gravitational waves in Cosmology 16
2.2.1 The stochasticity of GW backgrounds 16
2.2.2 Redshifting 18
2.2.3 GWs in an expanding space-time 19
2.2.4 Perspectives on Weinberg's formula 21
2.2.5 Sound wave production of gravitational waves 27
3 COSMOLOGICAL PHASE TRANSITIONS 30
3.1 Basic concepts 30
3.1.1 The effective potential 30
3.1.2 Bubbles and their nucleation rate 33
3.1.3 Bubble statistics 35
3.1.4 The Bag model and equation of state 37
3.1.5 Phase transition strength 41
3.1.6 Hydrodynamics of singular bubbles 41
3.2 GWs from a first-order phase transitions 46
3.2.1 Estimates of some GW signal features 48
3.2.2 GW spectrum contributions 51
3.2.3 The fluid contribution to GW production 55
3.2.4 Prospects for observational Detection 58

II HIGGSLESS SIMULATIONS 60

4 CENTRAL DIFFERENCE SCHEMES À LA KURGANOV AND TADMOR 62
4.1 Hyperbolic conservation laws 62
4.2 A prototypical example: the Lax & Friedrichs scheme 63
4.3 The Kurganov-Tadmor central difference method 65

4.3.1 Semi-discrete formulation 66
4.3.2 Fully-discrete formulation 68
4.3.3 Generalization to three dimensions 69
4.3.4 Concluding remarks 72
5 HIGGSLESS SIMULATIONS AND GRAVITATIONAL WAVES 74
5.1 Introduction 74
5.1.1 Background 74
5.1.2 Scientific objectives 77
5.2 Physical setup 77
5.2.1 Bubble nucleation and expansion 78
5.2.2 Fluid equations of motion 79
5.2.3 Bubbles and the equation-of-state 81
5.2.4 Inversion formulae 83
5.2.5 Spatial components $T^{ij}(K^{\mu})$ 84
5.2.6 Gravitational wave production 85
5.2.7 Summary of physical ingredients 86
5.3 Numerical methods and programmatic considerations 86
5.3.1 The lattice 86
5.3.2 The discrete Fourier transform 88
5.3.3 Power spectra on the lattice 90
5.3.4 Numerical scheme 92
5.3.5 Bubble nucleation histories 94
5.3.6 The encoding of bubbles 98
5.3.7 Computing GW spectra from the 3D Lattice 101
5.3.8 Parallelization 105
5.4 Evaluating the simulation 106
5.4.1 Single-bubble simulations 106
5.4.2 Energy-momentum conservation 112
5.4.3 Extrapolation of the kinetic energy 113
5.5 Numerical results 114
5.5.1 Multi-bubble simulations 114
5.5.2 GW production 119
5.6 Discussion 129
5.6.1 Reconnecting with the literature 129
5.6.2 Obtaining present day GW spectra 132
5.6.3 Future work 133
5.7 Summary and conclusion 135
5.7.1 Summary 135
5.7.2 Conclusion 137
5.8 Appendix: Gravitational waves from domain wall catalyzed phase transitions 138
5.8.1 Introduction 138
5.8.2 Modeling of the domain wall network and catalyzed bubble nucleation 139

5.8.3 Simulations and numerical results 141
5.8.4 Conclusion 144
6 GRAVITATIONAL WAVES FROM DECAYING SOURCES IN STRONG PHASE TRANSITIONS 145
6.1 Introduction 145
6.1.1 Background 145
6.1.2 Scientific objectives 146
6.2 GW production 147
6.2.1 Connecting with the notation in Chapter 5 147
6.2.2 GWs from stationary sound waves 148
6.2.3 GWs from a damped source 149
6.2.4 Recovering cosmic expansion 151
6.2.5 Summary of intended usage 154
6.3 Numerical setup 155
6.3.1 Updates to the simulation implementation 155
6.3.2 Simulations and parameter choices 158
6.4 Numerical results 160
6.4.1 Overview 160
6.4.2 Simulation slices 162
6.4.3 Convergence analysis of the kinetic energy and GW amplitude 163
6.4.4 Corrections to the kinetic energy for multiple bubbles 169
6.4.5 Kinetic energy evolution 175
6.4.6 Time evolution of the integrated GW spectrum and GW efficiency 179
6.4.7 The shape of gravitational wave spectrum 185
6.4.8 Sample variance of the GW spectrum 196
6.4.9 Initial findings and discussion on vorticity 196
6.5 Summary and conclusions 205
6.5.1 GW spectrum template 205
6.5.2 Summary 208
6.5.3 Conclusion 210
7 POSTLUDIUM 212

III APPENDIX 215
A HYDRODYNAMICS AND GRAVITATIONAL WAVES FROM INVERSE PHASE TRANSITIONS 217
A.1 Introduction 217
A.2 Self-similar profiles of inverse phase transitions 217
A.3 Gravitational wave production 218

BIBLIOGRAPHY 220

Figure 1 Effective potential for first- and second-order PTs. *Left plot: First-order PT* The effective potential $V(\phi, T)$ of (111) is shown for various temperatures T: $T > T_1$, $T = T_1$, $T = T_c$, and $T = T_0$. At $T > T_1$, the potential has a single minimum at $\phi = 0$. As T decreases, a second minimum appears at $T = T_1$, becomes degenerate at $T = T_c$, and the system transitions to a new global minimum for $T < T_c$. At $T = T_0$, the potential barrier vanishes, and any patch of the remaining symmetric phase will roll smoothly to the broken phase. *Right plot: Second-order PT* The effective potential $V(\phi, T)$ of (111) for $A = 0$ is plotted for $T = 1.4T_0$, $T = 1.0T_0$, $T = 0.6T_0$, and $T = 0.1T_0$. The transition is continuous, with the minimum shifting smoothly from $\phi = 0$ as T decreases. 32

Figure 2 Figure adopted from [86]. Fluid velocity profiles $v(\xi)$ in the bubble center frame (where $c_s^2 = \frac{1}{3}$). Detonation curves (dash-dotted line) start below $\mu(\xi, v) = c_s$ and end at $(\xi, v) = (c_s, 0)$. Deflagration curves (dashed line) start below $v = \xi$ and end at $\mu(\xi, v)\xi = c_s^2$, representing the shock front. Consistent solutions do not exist in the shaded regions. 43

Figure 3 Self-similar profiles of the fluid velocity (left panels) and enthalpy (right panels) perturbations for a single bubble nucleated at $t = 0$ as a function of the self-similar coordinate $\xi \equiv r/t$. The profiles are shown for weak (upper panels), intermediate (middle panels), and strong (lower panels) PTs, across the range of wall velocities used in the parameter scan of our simulations. 45

Figure 4 The vacuum energy transfer efficiency κ_ξ for single isolated bubbles with developed self-similar fluid profiles, for weak ($\alpha = 0.0046$), intermediate ($\alpha = 0.05$), and strong ($\alpha = 0.5$) PTs. 46

Figure 5 Bubble nucleation histories generated with different random seeds for $\tilde{L}/v_w = 20$ (upper panel) and $\tilde{L}/v_w = 40$ (lower panel). The nucleation times of each bubble nucleation history have been translated to nucleate the first bubble at the same time. Black lines indicate bubble nucleation histories used in the study, while colored lines show different realizations using the same procedure. 97

Figure 6 Minimal smoothing of ε to reduce oscillations. Blue curves indicate wall positions at adjacent time steps. Red lines indicate the step function representing bubble boundary conditions, while dotted-blue lines show the redefinition allowing to gradually deposit energy even at wall positions in-between lattice sites. 100

Figure 7 Convergence of self-similar profiles for weak PTs ($\alpha = 0.0046$) and wall velocities $v_w \in \{0.32, 0.48\}$ corresponding to two deflagrations. The box size is $\tilde{L} = 20 v_w$ and the resolution $N = 512$. The first and third panels show the radial velocity $|\mathbf{v}|$. The second and fourth panels show the enthalpy w normalized to the enthalpy in the far symmetric phase w_s. The profiles are obtained from the 2D slices of the simulations in the left column by binning quantities in 500 radial bins from the bubble center. The middle (right) column shows fluid profiles in the self-similar coordinate $\xi = r/t$ (radial coordinate r) at various times to indicate the convergence to self-similar profiles with time. Gray regions indicate the self-similar profiles reviewed in Section 3.1.6. 108

Figure 8 Same as figure 7, but for $v_w \in \{0.60, 0.80\}$ corresponding to a hybrid and detonation. 109

Figure 9 Same as figure 7, but for intermediate PTs ($\alpha = 0.05$). 110

Figure 10 Same as figure 7, but for intermediate PTs and $v_w \in \{0.60, 0.80\}$. 111

Figure 11 On the left side, the time evolution of the velocity profile as a function of $\xi \equiv r/t$ is depicted arising from a single bubble nucleated in a simulation box with dimensions $\tilde{L} = 20 v_w$ and resolution $N = 512$. The wall velocity is $v_w = 0.8$, and the PT strength $\alpha = 0.05$. On the right, the velocity profile is shown as a function of $\xi \equiv r/t$ for different values of N at $\tilde{t} = 3.2$, keeping $\tilde{L}/v_w$, v_w, and α constant. In both panels, 100,000 random points from the lattice are selected and re-scaled according to the respective simulation time to present the result in the self-similar coordinate ξ. The self-similar solution from [86] is highlighted in orange. 112

Figure 12 Time evolution of $\langle K^{\mu} \rangle$ for an intermediate PT $\alpha = 0.05$ and different grid sizes ($N = 64$, 128, 256 and 512). The wall velocity $v_w = 0.8$ corresponds to a detonation. The initial energy density is $K_0/w_s = \frac{3}{4}(1+\alpha)$, where w_s denotes the enthalpy density before the PT. 113

Figure 13 *Left figure:* The time evolution of the kinetic energy for different box sizes N for an intermediate PT with $v_w = 0.8$ is plotted. Dashed lines indicate $\langle w v^2 \gamma^2 \rangle$ and solid lines $\langle v^2 \rangle$. *Right figure:* The kinetic energy value at the first peak (around $\tilde{t} \simeq 7$) as a function of N for weak (lower lines) and intermediate (upper lines). Dashed lines indicate extrapolation to infinity simulation resolution. 114

Figure 14 Central 2D simulation slices of the fluid velocity amplitude $|\mathbf{v}(\tilde{\mathbf{x}})|$ and enthalpy $w(\tilde{\mathbf{x}})$. The resolution is $N = 512$ and the box size $\tilde{L} = 40 v_w$. The first three slices are chosen at equidistant times to show the bubble evolution before percolation while the fourth slice is at the end of the simulation to display the long-term behaviour. Upper (lower) panels show a weak (intermediate) PT with wall velocity $v_w = 0.32$ corresponding to deflagrations. 116

Figure 15 Same as in figure 14 but with $v_w = 0.6$ corresponding to hybrids. 117

Figure 16 Same as in figure 14 but with $v_w = 0.80$ corresponding to detonations. 118

Figure 17 A few example spectra for weak ($\alpha = 0.0046$, lower lines) and intermediate ($\alpha = 0.05$, upper lines) PTs with $N = 512$. The specific parameters for these PTs are detailed in the plot subtitles. The colored lines represent the shape function described in Equation (290), with distinct colors indicating the regions of different power-law indices 3 (red), 1 (green), and -3 (blue), as well as the regime of exponential damping (orange), separated by q_0, q_1, and q_e. 120

Figure 18 Example of the impact of the box size L and grid size N on the resulting GW spectrum. In this example we use $v_w = 0.8$ and intermediate strength ($\alpha = 0.05$). Note that in order to distinguish orange dots from green and blue, the orange dots have been manually shifted to lower values by a factor of 0.85 as dots would otherwise overlap. 120

Figure 19 The IR tail of GW spectra obtained from simulations of box size $\tilde{L} = 80 v_w$ and resolution $N = 512$ for a PT of intermediate strength, $v_w = 0.8$, and different simulation durations and integration time windows (in units of $1/\beta$) as specified in the plot legends. The lines are shifted by factors of 2 relative to each other to make them better visible. For reference, lines q^3 and q^5 are included. 122

Figure 20 *Upper panel:* The extracted fitting parameters q_0, q_1, and q_e as functions of the wall velocity. Blue (red) points correspond to weak (intermediate) PTs with $\alpha = 0.0046$ ($\alpha = 0.05$). In the upper left figure, we show the IR knee position q_0 for $\tilde{L} = 40 v_w$. In the upper right figure, we show the UV peak q_1 (dots), the shell thickness (crosses) defined in Equation (291), and the exponential damping q_e (solid lines) for $\tilde{L} = 20 v_w$. *Lower panel*: The integral of the GW spectrum growth rate $Q'_{\rm int}$ over momenta, defined in Equation (289), normalized by $\tilde{\epsilon}_{\rm shell}(\kappa\alpha)^2$ (left) and by the kinetic energy squared $\langle v^2\gamma^2 w\rangle^2$ measured in the lattice (right). 125

Figure 21 *Upper panel:* The extracted fitting parameters q_0, q_1, and q_e as functions of the wall velocity. Blue (red) data points correspond to weak (intermediate) PTs with $\alpha = 0.0046$ ($\alpha = 0.05$). Dots and solid lines are from simulations with small box size ($\tilde{L} = 20v_w$) while stars and dotted lines are from simulations with large box size ($\tilde{L} = 40v_w$). In the upper left figure, we show the IR knee position q_0 for $\tilde{L} = 40v_w$. In the upper right figure, we show the UV peak q_1 (dots), the shell thickness (crosses) defined in Equation (291), and the exponential damping q_e (solid lines) for $\tilde{L} = 20v_w$. *Lower panel:* The integral of the GW spectra Q'_{int} over momenta defined in Equation (289) normalized by $\xi_{shell}(\kappa\alpha)^2$ (left) and by the kinetic energy squared $\langle v^2\gamma^2 w\rangle^2$ measured in the lattice (right). 128

Figure 23 *Left column:* A realization of a DW network as per the method in the main text and footnote 2 is shown as dark lines. The bubble wall interface is shown as expanding red circles at various times in the simulation. *Right column:* The kinetic energy in the fluid is as obtained in the simulation at corresponding time steps. The PT parameters are $\alpha = 0.05$, $v_w = 0.8$, $L = 160v_w/\beta$, and $\xi_{DW} = 0.1L$. 142

Figure 24 Final spectra of the gravitational waves with (left) and without (right) a DW network. The strength of the PT is $\alpha = 0.05$, and the velocities of the bubble walls are $v_w = 0.4$, 0.55, and 0.8. The green points indicate the part of the spectrum used in the fit (shown in red). 143

Figure 25 Central 2D simulation slices of the fluid velocity amplitude $|\mathbf{v}(\tilde{\mathbf{x}})|$ and enthalpy $w(\tilde{\mathbf{x}})$ for a strong PT with $\alpha = 0.5$ The resolution is $N = 512$, and the box size $\tilde{L} = 40v_w$. The first three slices are chosen at equidistant times to show the bubble evolution before PT completion, while the fourth slice is at the end of the simulation to display the long-term behavior. The upper (lower) panels corresponds to a deflagration with $v_w = 0.5$ (hybrid with $v_w = 0.6$). 164

Figure 26 Same as the Figure 25, but for $v_w = 0.8$, corresponding to a hybrid. Note that for weak and intermediate PTs, this wall velocity gives rise to detonation solutions. 165

Figure 27 Plots showing the kinetic energy fraction K and the integrated GW spectrum $\mathcal{I}^{\text{int}}_{\text{sim}}$ as a function of grid spacing $\delta\tilde{x}/v_w = (\tilde{L}/v_w)/N$ for simulations with $\tilde{L}/v_w = 20$. *Upper panel:* Fit of Equation (328) to least-squares fitted values of the parameter K_0 in Equation (309) for simulations of resolutions $N \in \{64, 128, 256, 512\}$, normalized to K_ξ (defined from self-similar bubbles in Equation (168)). Solid lines indicate the fits, dots the data, and stars the extrapolated values. The left, middle, and right panels indicate weak, intermediate, and strong PTs, respectively. *Middle panel:* Same as upper panel, but for $K_{\text{rms}} \equiv K_{\text{int}}/\tilde{T}_{\text{GW}}^{1/2}$ normalized to K_ξ. Note that for strong PTs, the fit is inappropriate as per the definition in the main text for $v_w = 0.68$ and $v_w = 0.76$, in which case we instead connect the data points with dotted lines and indicate extrapolated values with the value at $N = 512$. *Lower panel:* Same as upper panel, but for $\mathcal{I}^{\text{int}}_{\text{sim}}$ normalized by a the product of $\tilde{\Omega}_{\text{GW}} \sim 10^{-2}$ [25, 69, 71] and $\tilde{T}_{\text{GW}} K_\xi^2 R_* \beta$, based on the expected scaling of Equation (308). Both K_{rms} and $\mathcal{I}^{\text{int}}_{\text{sim}}$ are computed for $\tilde{t}_{\text{init}} = 16$ and $\tilde{t}_{\text{end}} = 32$, with $\tilde{T}_{\text{GW}} = 16$. 168

Figure 28 Time evolution of the kinetic energy fraction in the broken-phase volume $K(\tilde{t})/\mathcal{V}(\tilde{t})$ for multiple-bubble simulations (solid lines), normalized by the single-bubble K_ξ, for different resolutions $N = \{64, 128, 256, 512\}$ in increased opacity and box size $\tilde{L}/v_w = 20$. Results are shown for weak (left panels), intermediate (middle panels), and strong (right panels) PTs, and for a range of wall velocities $v_w = \{0.36, 0.48, 0.6, 0.8\}$. Dashed lines correspond to the ratio $K_\Sigma(\tilde{t})/\mathcal{V}_\Sigma(\tilde{t})$ computed from the single-bubble simulations, such that the departures between the solid and dashed lines indicate the time when fluid-shell collisions take place in the multiple-bubble simulations. Black dots are the values of K_0 obtained from the fit $K(\tilde{t}) = K_0(\tilde{t}/\tilde{t}_0)^{-b}$ studied in Section 6.4.5 for different N. Red and green dots correspond to the estimated values $\mathcal{K}_0$ (see Equation (333)) and K_0^∞ (obtained from the convergence analysis of Section 6.4.3). Orange stars correspond to the factor $\mathcal{S}$ (see Equation (333)) at the collision $\tilde{t}_{coll}$, used to correct $\mathcal{K}_0$. 171

Figure 29 *Upper panel:* Values of the convergence-corrected continuum limit estimate $\mathcal{K}_0$ of K_0 as defined in (333) for resolution $N = 512$, normalized to K_ξ for self-similar profiles defined in Equation (168), for weak (left panel), intermediate (middle panel), and strong (right panel) PTs, as a function of v_w. Lines in increasing opacity correspond to increasing numerical resolution $N \in \{64, 128, 256, 512\}$. The vertical solid gray line indicates the sound speed, c_s, while the dashed lines indicate the Chapman-Jouguet velocity, v_{CJ}. Error bars show the standard deviation from 10 different bubble nucleation histories. *Lower panel:* Kinetic energy efficiency $\kappa_0 \equiv \mathcal{K}_0(1+\alpha)/\alpha$ defined from $\mathcal{K}_0$ as defined in (333) for resolution $N = 512$, for weak (blue), intermediate (red), and strong (orange) PTs. I also plot κ_ξ (black) for self-similar solutions as defined in Equation (166). The vertical line corresponds to c_s, and v_{CJ} is indicated by the dotted gray line. 174

Figure 30 Evolution of the measured kinetic energy fraction $K(\tilde{t})$ normalized to the single-bubble values K_ξ (see Equation (168)) for weak (left panels), intermediate (middle panels), and strong (right panels) PTs, for $N = 512$ (solid lines) and $\tilde{L}/v_w = 20$, and the same wall velocities as those in Figure 27. Dashed lines indicate the fits to the power-law decay of Equation (336) at times $\tilde{t} > \tilde{t}_0$. Values corresponding to K_0/K_ξ are marked with circles. In the lower panels, the kinetic energy fraction is shown for different numerical discretizations $N = \{64, 128, 256, 512\}$ (solid lines with increasing opacity), normalized to the corresponding values of the fit K_0 at each resolution N. The results for each v_w are shifted by a constant to distinguish between wall velocities. The presentation in the lower panels is chosen to emphasize the dependence of the time decay on resolution. 176

Figure 31 Decay index b (left panel) and half-life $\tilde{t}_{1/2}$ (right panel) as a function of v_w for $N = \{256, 512\}$ in increasing opacity for weak (blue lines), intermediate (red lines), and strong (orange lines) PTs. Dashed black lines with colored stars in the right panel correspond to the eddy turnover time $\tilde{t}_{\text{eddy}} = (\beta R_*)/\sqrt{K_\xi}$ that we compare with $\tilde{t}_{1/2}$ as we expect both time scales to be inversely proportional to K_ξ. Error bars in the left panel show the standard deviation from 10 different bubble nucleation histories for $N = 512$. 178

Figure 32 *Upper panel:* Dependence of the numerical integrated GW amplitude found in the simulations with $\tilde{L}/v_w = 40$ and $N = 512$ as a function of the source duration $\tilde{t} - \tilde{t}_{\text{init}}$ for weak (left column), intermediate (middle column), and strong (right column) PTs. The integrated GW amplitude is normalized as in the lower panels of Figure 27 for consistency. Dashed lines exemplify the linear growth expected under the stationary UETC assumption. *Lower panel:* Time evolution of $\tilde{\Omega}_{\text{GW}}$ computed as in Equation (338). 180

Figure 33 Gravitational wave production efficiency $\tilde{\Omega}_{GW}$ for weak (left), intermediate (middle), and strong (right) first-order PTs. Solid (dotted) lines correspond to $\tilde{L}/v_w = 20$ (40). Black lines with increasing opacity correspond to increasing resolutions $N \in \{64, 128, 256, 512\}$, while colored lines indicate $\tilde{\Omega}_{GW}^{\infty}$ as computed from the extrapolated values of $\mathcal{I}_{sim}^{int,\infty}$ and K_{int}^{∞} as per the description in Section 6.4.3. Dots and stars mark $\tilde{\Omega}_{GW}$ as presented in Tables 2 and 3 of [72] corresponding to predictions from the sound-shell model (SSM) for exponential nucleation of bubbles [72] and scalar field-hydrodynamical simulations for simultaneous nucleation [71], respectively. Gray dots correspond to SSM values found using the assumption described in 6.2.2 (following Appendix B of Ref. [73]), and computed using CosmoGW [166]. Error bars indicate the standard deviation from 10 different bubble nucleation histories for $\tilde{L}/v_w = 20$ (darker) and 40 (lighter). 181

Figure 34 Plots of the GW amplitude growth with the source duration $\tilde{\tau}_{sw} \equiv \tilde{t} - \tilde{t}_{init}$ as modeled in Equation (341) corresponding to $\beta/H_* = \infty$ (solid lines) and Equation (342) (dashed lines), for the two values of $\beta/H_* = 1000$ (normal opacity) and 100 (lower opacity). I furthermore indicate the numerical growth of the GW spectrum as found in the simulations but re-scaled by a factor K_0/K_0 and vertically translated by $\mathcal{I}_{\infty}^{int}(\tilde{t}_0, t_{init})$ (red line segments). Dots indicate the eddy turnover time $\tilde{t}_{eddy} = \beta R_*/\sqrt{K_\xi}$, which determines the expected scale for nonlinearities to develop (they do not appear in the plot for weak PTs with $v_w = 0.4$ and 0.8). 184

Figure 35 Fits of Equation (343) to the numerical results from weak, intermediate, and strong PTs (in each panel, amplitudes increase with larger α) with $N = 512$ for a range of v_w, and for $\tilde{L}/v_w = 20$ in brighter colors (white dots for the numerical data), and $\tilde{L}/v_w = 40$ in darker colors (black dots for the numerical data). Red lines indicate wave numbers below the knee k_1, green indicates intermediate wave numbers $k_1 < k < k_2$, and blue corresponds to wave numbers above the peak k_2. The dotted orange lines indicate wave numbers $k > k_e$, where exponential damping dominates. The light and dark gray lines indicate the resulting fitted double-broken power laws excluding the exponential damping. Vertical lines indicate the Nyquist wave numbers $k_{Nyq}R_* = \beta R_* N/\tilde{L}$. 187

Figure 36 Fitted UV index $n_3 \geqslant -3$. Note that for weak PTs, we fix $n_3 \equiv -3$ (shown for reference). The sample standard deviation, as determined from the *seed* simulations, is depicted as 1σ error bars at selected representative velocities. 190

Figure 37 Fitted characteristic wave numbers k_1 (left column), k_2 and k_e (middle column), and k_{peak} (right column) for weak (blue), intermediate (red), and strong (orange) PTs, using simulations with $N = 512$ and $\tilde{L}/v_w = 20$ (40) in solid (dotted) lines. Gray regions indicate the Nyquist frequency $\tilde{k}_{Nyq} = N/\tilde{L}$. In the upper panel, wave numbers are normalized as k/β, as presented in [67] and Chapter 5, while in the lower panel, they are normalized as $k R_*$. Thick colored lines of low opacity in middle panels indicate k_e for $\tilde{L}/v_w = 20$ (40) in solid (dotted) lines. In the upper panel (middle and right), thin black-and-color dashed lines indicate $1/\xi_{shell}$, while in the lower panel, they indicate the fitted value $2\pi * 0.49/\Delta_w$ (see Equation (349)). In the right column, the lower opacity regions indicate the peak as obtained using the double broken power law fit of Equation (343), neglecting the exponential numerical damping. 192

Figure 38 Comparison between the re-scalings associated with R_* and $R_{\rm eff}$. The pink dashed-doted line corresponds to a fit $1.36/(v_w + 0.24)$ to facilitate using $R_{\rm eff}$ without knowledge of the profiles. 193

Figure 39 Time evolution of the GW spectrum $\mathcal{I}(\tilde{t}_{\rm init}, \tilde{t}, \tilde{k})$, evaluated at times $\tilde{t} \in [17, 32]$ with $\tilde{t}_{\rm init} = 16$, for weak (left column), intermediate (middle column), and strong (right column) PTs. The wall velocities are $v_w = 0.32$ (0.36 for strong PTs) in the upper panels, 0.6 in the middle panels, and 0.8 in the lower panels. The numerical resolution is $N = 512$, and the box size is $\tilde{L}/v_w = 40$. The GW spectra are normalized by the reference value $\tilde{\Omega}_{\rm GW} \simeq 10^{-2}$ and the expected scaling $K_\xi^2 R_* \beta$. 197

Figure 40 Various GW spectral growth rates obtained as averages over 10 different bubble nucleation histories. Each spectrum shows the mean, the variance, and the min-max over the ten nucleation histories. The left (right) plots show spectra from simulations with box size $\tilde{L}/v_w = 20$ (box size $\tilde{L}/v_w = 40$). 198

Figure 41 2D simulation slices of the velocity amplitude $|\mathbf{v}(\tilde{\mathbf{x}})|$, enthalpy $w(\tilde{\mathbf{x}})$, and the vorticity $|\tilde{\nabla} \times \mathbf{v}(\tilde{\mathbf{x}})|$ field for a strong PT with $\alpha = 0.5$ and $v_w = 0.36$. The resolution is $N = 1024$, twice that of the simulations of the highest resolution in previous parts of this Chapter, and the box size $\tilde{L}/v_w = 20$. The wall velocity is chosen to be $v_w = 0.36$ since the production of vorticity is observed to be maximal at low wall velocity. Around the expanding bubble, spurious small-scale vorticity is seen, which is caused in part by small fluid transients around the shock and in part by the definition of the central numerical derivative, which picks up artifacts from the lattice symmetry. Sizeable macroscopic production is, however, observed in the interactions of overlapping fluid sound shells, indicating the physical presence and build-up of vorticity. 201

Figure 42 Longitudinal and transverse velocity power spectra of the fluid for two strong PTs with $\alpha = 0.5$ and wall velocities $v_w = 0.44$ (left column) and $v_w = 0.8$ (right column). The top panel illustrates the power in the longitudinal modes, the middle panel the power in the vortical modes, and the bottom panel the fraction of power in the vortical modes. Different lines correspond to different times in the simulation. For reference, bubble nucleation begins around $\tilde{t} \simeq 0$, first collisions occur around $\tilde{t} \simeq 5$, and PT completion takes place around $\tilde{t} \simeq 10$. 203

Figure 43 Examples of self-similar velocity profiles for inverse detonations (left), inverse hybrids (middle), and inverse deflagrations (right). This Figure is adopted from [168], to which I refer the reader for details. 218

Figure 44 Convergence towards the self-similar fluid profile for an inverse deflagration for $v_w = 0.75$ and $\alpha = -0.1202$. The pink dashed line for the self-similar velocity profiles is taken from [168] for the same parameters. 219

Figure 45 Off-central 2D simulation slices for an inverse-deflagration of the fluid velocity amplitude $|\mathbf{v}(\tilde{\mathbf{x}})|$ (upper panel), and enthalpy $w(\tilde{\mathbf{x}})$ (lower panel). The wall velocity is $v_w = 0.75$ and the strength $\alpha = -0.1202$ ($\tilde{x} \equiv x/\beta$). The resolution is $N = 512$, and the box size $\tilde{L}/v_w = 20$. The first three slices are chosen at equidistant times to show the bubble evolution before PT completion, while the fourth slice is at the end of the simulation to display the long-term behavior. 220

Figure 46 Fit of equation (345) to GW spectrum data for the inverse deflagration with $v_w = 0.75$ and strength $\alpha = -0.1202$. The color transition between red-blue marks the peak k_2, which in this example is equal to k_1, i.e., $k_1 = k_2$, as the sound shell thickness is rather thick and with, correspondingly, no separation of scales leading to an intermediate regime of linear scaling. The start location of dashed orange lines marks the scale k_e where exponential damping begins to dominate. Colored regions demarcate the range of wavenumber used for the fit, whereas transparent gray indicates the fitted function excluding exponential damping. 221

LIST OF TABLES

Table 1 Frequency scaling behaviour in the IR and UV for the GW spectrum emerging solely from the scalar field contribution as described in the envelope approximation, the bulk flow model, and in scalar field lattice simulations. 54

Table 2 GW spectrum slopes obtained from various approaches targeting fluid sound-wave-induced GW production. These models exhibit distinct features at wavenumbers k_0 and k_1, with three corresponding slopes: IR, intermediate, and UV. 58

Table 3 GW spectrum slopes obtained from various approaches targeting fluid sound-wave-induced GW production. These models exhibit distinct features at wavenumbers k_0 and k_1, with three corresponding slopes: IR, intermediate, and UV. 130

Table 4 Parameters extracted from the spectra shown in Fig. 24 are summarized. Values with a bar denote quantities obtained from simulations without DWs. q_0 is derived by fitting Equation (297) to the simulation data. The domain wall correlation length ξ_{DW} is determined from our model of the DW network using the Ising. 143

Table 5 Summary of simulation runs with physical and numerical parameter choices. *Reference* indicates simulations constructed from a single reference bubble nucleation history (one for each box size), thereby minimizing statistical differences among the sample of reference simulations. *Seeds* refers to simulations constructed from a set of 9 additional bubble nucleation histories, allowing to infer statistical sample variance for 3 selected wall velocities $v_w = 0.32$ (0.36), 0.6, and 0.8, which correspond to deflagrations, hybrids, and detonations for weak and intermediate PTs, while $v_w = 0.8$ is a hybrid for strong PTs. *Single-bubble* refers to simulations with a single isolated centrally nucleated bubble, allowing us to study the convergence of self-similar profiles. We take a range of $v_w \in [0.32, 0.8]$ in increments of 0.04 besides for strong PTs ($\alpha = 0.5$) for which we take $v_w \in [0.36, 0.8]$. A total of 1028 simulations have been performed. 158

Table 6 Numerical values of the fit parameters a, $K_\infty^{\rm rms}$, and $\mathcal{I}_\infty^{\rm int}$ of Equation (328) for the RMS kinetic energy fraction $K_{\rm rms}/K_\xi$ and the integrated GW amplitude $\mathcal{I}_{\rm sim}^{\rm int}$, as shown in the middle and lower panels of Figure 27. Relative errors ε are computed by comparing the extrapolated values to those obtained in the largest resolution simulations $N = 512$ when the fit is appropriate. When the fit is inappropriate (indicated with '–' in the values of a) we instead compare values among the two largest resolutions $N = 256$ and $N = 512$. 167

1 PRELIMINARIES

1.1 Background

1.1.1 Cosmological phase transitions: the source

On our sphere of life, the Earth, *phase transitions*, i.e. processes through which nature proceeds to change its local state as a result of changes in conditions, such as the temperature, pressure, or energy density, crossing a critical threshold, occur in abundance and diversity. They include the most well-acquainted melting of ice, vaporization of water, and the transition of a magnet from ferromagnetic to paramagnetic when heated. Perhaps less-known examples include the transition of a fluid from a superfluid to a normal fluid, the transition of a regular conductor into a superconductor, and the transition of a Bose-Einstein Condensate to an ordinary gas.

The list of examples of observed phase transitions can be made very long, yet none of them pertain to a cosmological context. In fact, while many cosmological phase transitions have been suggested, not one of them has been observed. However, the universal abundance of phase transitions in diverse physical systems warrants taking seriously the possibility that phase transitions have occurred, perhaps in abundance, also throughout cosmological history. Their hypothesized existences could, if confirmed true, imply a vast set of consequences for our universe as we know it and even explain conundrums that are difficult to explain in their absence.

Some such consequences of cosmological phase transition include primordial magnetic field generation [4, 5], generation of matter-antimatter asymmetry [6–10], production of topological defects, primordial black holes–[11–13], and GW production [14, 15]. Clearly, their phenomenology is vastly rich, and their cosmological consequences are far-reaching.

In the context of a first-order cosmological phase transition (PT), the order parameter initially remains in the symmetric phase while a broken true vacuum minimum develops. Vacuum or thermal fluctuations can then trigger a transition to the broken phase through the potential barrier, leading to the formation of small bubbles [16–18]. The vacuum energy released drives the expansion of these bubbles, which eventu-

ally collide with one another, causing anisotropic stresses in the energy distribution which source GWs [14, 15].

While bubble collisions themselves are a significant source of GWs [19–24], it has been demonstrated in [25] that the motion of the fluid driven by scalar field walls often dominates the GW spectrum in PTs where the bubble wall reach an asymptotic value rather than accelerate towards the speed of light c. In this case, most of the vacuum energy is deposited in the primordial fluid, inducing acoustic modes that continue to propagate through space even after PT completion, thus sourcing GWs for a possibly long period of time.

Throughout cosmological history, at least two possibly first-order PTs are likely to have occurred. At a temperature $T \sim 100GeV$, the Higgs field underwent spontaneous symmetry breaking in the electroweak PT (EWPT) responsible for giving particles mass through the Higgs mechanism. Studies of the electroweak model have found the EWPT is of second order in the standard model (SM) of particle physics [26–29]. This would imply that little to no GWs are produced, making it impossible to observe the EWPT through the channel of GWs. In extensions of the SM the EWPT may be first-order (see, e.g., [10, 30, 31]), thus producing a possibly observable amount of GWs if the PT is strong enough.

As the universe cooled further, at a temperature around $T \sim 100MeV$, free quarks were confined to form protons and neutrons in what is known as the QCD phase transition. Again, studies based on lattice QCD have demonstrated that also the QCD phase transition was of second order [32]. However, as is shown in, e.g., [33, 34], under certain conditions, e.g., in the presence of a sufficiently strong magnetic field, the QCD phase transition may be of first order.

The EWPT and the QCD phase transitions are prototypical examples, but a PT could have occurred in a hidden sector [35], and at any energy scale within a broad range spanning QCD scale $\sim \mathcal{O}\left(10^2\right)$ MeV up to the inflationary scale $\lesssim 10^{16}$GeV [36]. Probing scales far beyond the reach of all current and conceivable future experimental means that observational signatures of PTs may open a plausible and lucrative window to new physics.

In general, the message I want to deliver is that a first-order PT may come with rich phenomenological consequences, among which one is the production of a stochastic background of GWs, and that observation of such consequences carries the potential of unraveling physics far beyond the reach of any earthly experimental effort. This may thus bring us new information on the underlying high energy theory of the primordial universe, which should serve as a strong justification for their study.

1.1.2 Gravitational waves: the signal

The door to a new era with the promise of groundbreaking discovery was opened with the inaugural direct detections by the LIGO-Virgo collaboration of GWs emanating from mergers of black holes and neutron stars [37–39]. The forthcoming observing runs by the LIGO-Virgo-KAGRA (LVK) collaboration are expected to accumulate more events [40]. Collaborative efforts among Pulsar Timing Arrays (PTAs) have furthermore unveiled convincing evidence of a stochastic GW background (SGWB) at nano-Hertz frequencies [41–44]. While a compelling candidate for the source of this radiation from unresolved supermassive black hole mergers, i.e., of astrophysical origin, it is important to point out that primordial sources of cosmological origin can also explain the observed signal [45, 46]. These breakthroughs in GW detection gave us ears to astrophysical events and cosmological history inaccessible through all other means of observation, and we are poised to gather data that will revolutionize our understanding of astrophysics and cosmology. Looking ahead to the 2030s, the launch of the Laser Interferometer Space Antenna (LISA) mission [47–49], designed to probe GWs in the unexplored milli-Hertz frequency band, is poised to potentially revolutionize modern cosmology [49]. One particularly intriguing possibility is LISA's ability to observe GWs from first-order PTs [14] around the EW scale, as the expected peak of the GW spectrum would coincide with LISA's sensitivity band [50–52].

These groundbreaking GW observations have profoundly impacted astrophysics, offering new insights into the formation and evolution of black holes and neutron stars [37, 39], including intermediate-mass black holes, and proving the existence of binary systems with unexpectedly large massive black holes [53]. A notable example is GW190521, where the merging black holes had masses of approximately 85 and 66 solar masses, resulting in a final black hole of around 142 solar masses. This event challenges our understanding of stellar evolution, as black holes of such large masses are not expected to form from the collapse of a single star [54].

This surprising discovery underscores the exceptional discovery potential of *listening* for GWs. Beyond astrophysical insights, current GW detections serve as powerful probes of fundamental physics and cosmology. For instance, the first detection of the coalescence of two neutron stars, accompanied by the coincident detection of the same event across various electromagnetic bands [39], has placed strong constraints on the GW propagation speed, $-3 \times 10^{-15} \leqslant c_T - 1 \leqslant 7 \times 10^{-16}$, in units of $c = 1$ [55], and has also been used to estimate the present Hubble rate [56]. In cosmology, the detection of a stochastic

GW background by PTAs opens new avenues for studying the universe's large-scale structure and early cosmological events [41–43].

To shed some light on the importance of an SGWB in cosmology, let us first consider the Cosmic Microwave Background (CMB) and its discovery, which triggered a revolution and laid the foundation for modern precision cosmology. The CMB represents the era of photon decoupling, after which photons could propagate essentially undisturbed along geodesics until, eventually, some were detected by our telescopes. This unimpeded free propagation has led to the undeniable fact that much of what we know about the universe is due to our ability to *see* it. This remains true up to the time of the CMB, beyond which no inference of the universe may be attained through direct visual inspection.

The time of photon decoupling can be estimated by comparing the rate at which photons interact with the medium, $\Gamma = n_e \sigma_e c$, where n_e is the electron number density, σ_e is the electron cross-section, and c is the speed of light, to the Hubble expansion rate $H \propto a^{-3/2}$ in matter-domination, where a is the scale factor. As the universe cooled, electrons and protons combined to form neutral hydrogen, leading to a sharp decrease in the free electron density, n_e. Decoupling occurred rapidly when the photon scattering rate, $\Gamma \sim H$, so that the mean free path, λ, of the photons was comparable to the Hubble horizon H^{-1}, which can be shown to occur at a time of around 380,000 years after the Big Bang or at a redshift of around $z = 1100$ [57]. Following this decoupling, photons mostly followed geodesics without interactions along their path, which conveniently rendered the universe transparent to light or, more generally, electromagnetic radiation. This opened the venue for us to visually appreciate and learn about the universe through the observational channel of light up until the CMB, but no further.

For a SGWB, we may ask the same question: when did GWs decouple from the primordial medium of the universe? Knowing this answer, we would know the earliest time from which GWs can carry information to us. The question is answered by a similar comparison, namely, at what time did the GW interaction rate Γ equal the Hubble rate H? Thus, one computes [58]

$$\frac{\Gamma}{H} \sim \left(\frac{T}{M_{Pl}}\right)^3$$

where M_{Pl} denotes the Planck mass and T the temperature. From this estimate, it is clear that the universe is transparent to GWs up until the Planck scale at a temperature $T \sim M_{Pl} \sim 10^{19}$GeV, roughly corresponding to a time of just 10^{-43} seconds after the big bang. In other words, GWs propagate freely in the early universe immediately after they are

generated. This means that contrary to light, GWs carry information about the processes that produced them throughout most of conceivable cosmic history and can communicate the state of the universe at epochs and energy scales that are far unreachable by any other means.

We thus understand that the holy grail of early universe cosmology lay in the detection of a stochastic GW background of confirmed cosmological origin, with far-reaching consequences poised to revolutionize our understanding. Such a detection, nevertheless, is far from trivial and demands that the source of GWs is sufficiently strong. Phase transitions, however, potentially constitute such a source.

1.2 Motivation

This brief review highlights that GW astronomy is at the forefront of a new scientific frontier, poised to revolutionize our understanding of astrophysics, the universe's earliest epochs, and fundamental physics. I have particularly emphasized the generation of GWs from first-order PTs and the potential of future GW detectors, such as joint PTA efforts and LISA. The path from detecting new physics to interpreting SGWB is paved with the need for precise GW predictions. As experimental advancements bring the detection of new physics within reach, theoretical developments must keep pace to enable meaningful inference from the data.

In this thesis, significant strides are made to deepen our understanding of the violent hydrodynamics associated with vacuum energy release in first-order PTs and the resulting GW production. The goal is to provide the physics community with accurate predictions of GW spectra, parameterized by a few quantities that can be employed in data analysis and inference studies. This can be achieved through both analytical and numerical methods. In this work, I introduce a novel simulation setup, termed *Higgsless simulations*, to derive such predictions.

As we await the launch of LISA and the commissioning of future detection concepts, joint advancements in data analysis techniques and theoretical frameworks are essential to fully leverage the missions' potential. It is within this context that the present thesis finds its motivation.

Part I

THEORY OF GRAVITATIONAL WAVES AND COSMOLOGICAL PHASE TRANSITIONS

In this part, I establish the theoretical foundation. It is divided into Chapter 2, beginning with Section 2.1, where I introduce GWs in flat, non-expanding space as small perturbations of the metric. I describe the GW equations of motion, express the energy and momentum of GWs, and derive Weinberg's formula for the GW production from a generic source of energy and momentum. Then, in Section 2.2, I review GWs in cosmology, justify the stochasticity of GW backgrounds, derive the redshifted GW amplitude and wavenumber, formally describe GWs in an expanding space-time, shed light on Weinberg's formula, and finally, review the production of GWs by sound waves.

This is followed by Chapter 3, which reviews cosmological phase transitions. In Section 3.1, I cover the basic concepts of phase transitions, including the effective potential, bubbles and their nucleation rate, statistics associated with bubble nucleation and expansion, the Bag model and equation of state, phase transition strength, and the hydrodynamics of singular bubbles. In Section 3.2, I review GWs from first-order phase transitions. I provide estimates of key features of the GW signal, discuss the scalar-field contribution to GW production in various models, explore the plasma contribution to GW production in different scenarios, and conclude with a few comments on the observational prospects for GW detection.

2

GRAVITATIONAL WAVES

In this Chapter, I will introduce relevant concepts and theoretical results from general relativity and cosmology to ensure a somewhat self-contained treatment. There are countless resources that cover these subjects in great detail, and I refer the reader seeking a comprehensive treatment to those. The present Chapter is merely a brief overview, largely based on the references [58–62].

In Section 2.1, I introduce GWs in flat, non-expanding space as small perturbations of the metric. I describe the GW equations of motion, express the energy and momentum of GWs, and derive Weinberg's formula for the GW production from a generic source of energy and momentum. Then, in Section 2.2, I review GWs in cosmology, justify the stochasticity of GW backgrounds, derive the redshifted GW amplitude and wavenumber, formally describe GWs in an expanding space-time, shed light on Weinberg's formula, and finally, review the production of GWs by sound waves.

2.1 Gravitational waves in flat non-expanding space

In this Section, I will give a brief introduction to the notion of GWs as small perturbations to the metric of flat non-expanding space. I will review basic results and, in particular, derive a formula for the GW spectrum produced by a generic source of energy and momentum.

2.1.1 GWs as metric perturbations

Since at the fundament of the gravitational waves lay the general theory of relativity (GR), the formula from which we spring is the Einstein equation

$$\boxed{R_{\mu\nu} - \frac{1}{2} g_{\mu\nu} R = 8\pi G T_{\mu\nu}} \tag{1}$$

where the Riemann tensor is defined by

$$R^{\mu}{}_{\nu\rho\sigma} = \partial_\rho \Gamma^{\mu}_{\nu\sigma} - \partial_\sigma \Gamma^{\mu}_{\nu\rho} + \Gamma^{\mu}_{\alpha\rho}\Gamma^{\alpha}_{\nu\sigma} - \Gamma^{\mu}_{\alpha\sigma}\Gamma^{\alpha}_{\nu\rho}, \tag{2}$$

the Ricci tensor by

$$R_{\mu\nu} = R^{\alpha}{}_{\mu\alpha\nu}, \tag{3}$$

the Ricci scalar by

$$R = g^{\mu\nu} R_{\mu\nu}, \tag{4}$$

and the energy-momentum tensor $T_{\mu\nu}$, receiving contributions from whatever fields are present, is the source of curvature. The Christoffel symbols are computed from the metric as

$$\Gamma^{\rho}_{\mu\nu} = \frac{1}{2} g^{\rho\sigma} \left(\partial_\mu g_{\sigma\nu} + \partial_\nu g_{\sigma\mu} - \partial_\sigma g_{\mu\nu} \right). \tag{5}$$

In this thesis, we will exclusively regard GWs as small perturbations $h_{\mu\nu}$ around a flat expanding or non-expanding background. For the non-expanding case, the background metric is Minkowski, whereby the metric is perturbed as

$$\boxed{g_{\mu\nu} = \eta_{\mu\nu} + h_{\mu\nu}, \quad |h_{\mu\nu}| \ll 1,} \tag{6}$$

working with a negative-time metric signature such that $\eta_{\mu\nu} = \mathrm{diag}(-1, 1, 1, 1)$. Keeping terms at most of order $\mathcal{O}(h)$ in the equations of GR results in what is called *linearized theory*.

2.1.2 Equations of motion

For future convenience, define

$$h = \eta^{\mu\nu} h_{\mu\nu}, \tag{7}$$

$$\bar{h}_{\mu\nu} = h_{\mu\nu} - \frac{1}{2} \eta_{\mu\nu} h, \text{ and} \tag{8}$$

$$h_{\mu\nu} = \bar{h}_{\mu\nu} - \frac{1}{2} \eta_{\mu\nu} \bar{h}. \tag{9}$$

With these definitions, one can show that to linear order in $h_{\mu\nu}$, the Einstein equation (1) takes the form (see e.g. [60])

$$\Box \bar{h}_{\mu\nu} + \eta_{\mu\nu} \partial^\rho \partial^\sigma \bar{h}_{\rho\sigma} - \partial^\rho \partial_\nu \bar{h}_{\mu\rho} - \partial^\rho \partial_\mu \bar{h}_{\nu\rho} = -16\pi G T_{\mu\nu}. \tag{10}$$

One of our main reaming tasks in this Section is to exploit gauge symmetries of linearized GR to bring this equation into a form that, to the largest possible extent, reflects the physical degrees of freedom associated with GW propagation. We begin by simplifying the linearized Einstein equation itself.

It is apparent that if, in the last equation, one could choose $\bar{h}_{\mu\nu}$ such that

$$\partial^\nu \bar{h}_{\mu\nu} = 0 \tag{11}$$

the equation would greatly simplify. Under coordinate transformations of the form

$$x^\mu \to x'^\mu = x^\mu + \xi^\mu(x), \tag{12}$$

for as long as $|\partial_\mu \xi_\nu| \sim |h_{\mu\nu}|$ or smaller, the metric perturbation $h_{\mu\nu}$ transforms as

$$h_{\mu\nu}(x) \to h'_{\mu\nu}\left(x'\right) = h_{\mu\nu}(x) - \left(\partial_\mu \xi_\nu + \partial_\nu \xi_\mu\right), \tag{13}$$

which in turn, using that $\bar{h}' - \bar{h} = 2\partial^\alpha \xi_\alpha$, implies the transformation property of $\bar{h}_{\mu\nu}$

$$\bar{h}_{\mu\nu} \to \bar{h}'_{\mu\nu} = \bar{h}_{\mu\nu} - (\partial_\mu \xi_\nu + \partial_\nu \xi_\mu - \eta_{\mu\nu}\partial_\alpha \xi^\alpha) \equiv \bar{h}_{\mu\nu} - \xi_{\mu\nu}. \tag{14}$$

This means that subject to coordinate transformations of the form (12) and the condition that $|\partial_\mu \xi_\nu| \sim |h_{\mu\nu}|$ or smaller, the metric perturbation expressed in the new coordinates remain of the same order, thus ensuring the validity of the linearized Einstein equation (1).

Upon requirement of condition (11) on the transformed metric perturbation (14), it is immediately clear the functions $\xi_\mu(x)$ must satisfy

$$\partial^\nu \xi_{\mu\nu} = \Box \xi_\mu = 0\,. \tag{15}$$

Since this equation always admits solutions, this proves that condition (11) may always be satisfied under an appropriate choice of $\xi_\mu(x)$.

Condition (11) constitutes a choice of gauge often denoted *Lorentz* gauge, and reduces the number of degrees of freedom from 10 independent components of $h_{\mu\nu}$ to 6 through the imposition of 4 constraints. In Lorentz gauge, the linearized Einstein equation takes the simple form

$$\boxed{\Box \bar{h}_{\mu\nu} = -16\pi G T_{\mu\nu}\,.} \tag{16}$$

We should note here that applying the Lorenz gauge condition (11) to (16) means that, since partial derivatives commute, the energy-momentum tensor is conserved, i.e. $\partial^\mu T_{\mu\nu} = 0$, serving as a good sanity check.

We want to exploit the residual gauge freedom to isolate those degrees of freedom in $\bar{h}_{\mu\nu}$ that are physical and hence consider another transformation $\bar{h}_{\mu\nu} \to \bar{h}'_{\mu\nu}$ of the form (12). To this end, we therefore consider the possibility to require also that the trace $\eta^{\mu\nu}\bar{h}'_{\mu\nu} = \bar{h}' = 0$, for in this case $\bar{h}'_{\mu\nu} = h'_{\mu\nu}$, and the metric perturbations have the formidable property of conserving the volume element. The condition of tracelessness translates into the requirement on ξ_μ that

$$\partial_\alpha \xi^\alpha = -\frac{1}{2}\eta^{\mu\nu}\bar{h}_{\mu\nu}. \tag{17}$$

But $\Box\xi_\mu = 0$ must simultaneously be satisfied by the Lorentz gauge condition. Using that partial derivatives commute, the application of $\Box$ on (17) implies $\Box\bar{h}_{\mu\nu} = 0$, which are the GW equations of motion in vacuum, and thus guaranteed to be satisfied for as long as we as $T_{\mu\nu}(x) = 0$. The imposition of gracelessness, therefore, means we must be in a vacuum.

We will furthermore impose that $\bar{h}_{0i} = 0$, which requires of ξ_μ that

$$\bar{h}_{0i} = \partial_0\xi_i + \partial_i\xi_0, \tag{18}$$

while the Lorentz gauge condition implies

$$\partial^0\bar{h}'_{00} = 0 \Rightarrow \bar{h}'_{00} = \text{ const. } \equiv 0, \tag{19}$$

where in the last equality, we set the constant to 0 since, with GWs, we really mean the time-varying part evolving over a constant background. Now, since $h = T_{0\mu} = 0$, the Lorentz gauge condition simply reads $\partial^i h_{ij} = 0$, so that the polarization of h_{ij} is transverse the direction $\mathbf{k}$ or propagation.

Summarizing the current gauge constraints, we therefore have that

$$\boxed{h^{0\mu} = 0, \quad h^i{}_i = 0, \quad \partial^j h_{ij} = 0.} \tag{20}$$

The gauge defined by conditions (20) is called *transverse-traceless* (TT) gauge, and we will decorate quantities obeying (20) with sub- or superscript TT. Occasionally, and when exclusively Roman subscripts are used, TT gauge should be impliclty assumed. Thus, in this gauge, the GW EoMs reduce to

$$\boxed{\Box h^{TT}_{ij} = 0,} \tag{21}$$

which is a wave-equation admitting solutions of the form

$$h^{TT}_{ij} \propto e_{ij}(\hat{\mathbf{k}})e^{ik_\mu x^\mu} \tag{22}$$

for transverse-traceless polarization tensors e_{ij}, thus, satisfying $k^i e_{ij}(\hat{\mathbf{k}}) = 0$. The two residual degrees of freedom in TT gauge can be attributed to two polarization states, $+$ (plus) and $\times$ (cross), such that the most general solution takes the form

$$h_{ij}(\mathbf{x}, t) = \sum_{r=+,\times}\int \frac{d^3\mathbf{k}}{(2\pi)^3} h_r(\mathbf{k}, t)e^{-i\mathbf{k}\cdot\mathbf{x}}e^r_{ij}(\hat{\mathbf{k}}) \tag{23}$$

where the polarization tensors are defined by

$$e^+_{ij}(\hat{\mathbf{k}}) = \frac{1}{\sqrt{2}}(\hat{\mathbf{u}}_i\hat{\mathbf{u}}_j - \hat{\mathbf{v}}_i\hat{\mathbf{v}}_j), \quad e^\times_{ij}(\hat{\mathbf{k}}) = \frac{1}{\sqrt{2}}(\hat{\mathbf{u}}_i\hat{\mathbf{v}}_j + \hat{\mathbf{v}}_i\hat{\mathbf{u}}_j), \quad \hat{\mathbf{u}}, \hat{\mathbf{v}} \perp \hat{\mathbf{k}}, \quad \hat{\mathbf{u}} \perp \hat{\mathbf{v}}$$

(24)

with normalization

$$e^{r}_{ij}(\hat{\mathbf{k}})e^{r',ij}(\hat{\mathbf{n}}) = \delta^{rr'}, \quad r, r' \in \{+, \times\}. \tag{25}$$

Provided a generic symmetric tensor $H_{\mu\nu}$ which already satisfies the Lorentz condition (11), such as $h_{\mu\nu}$ or $T_{\mu\nu}$ (which satisfies (11) from energy-momentum conservation), one can project that tensor onto its transverse-traceless part following

$$H^{TT}_{ij} = \Lambda_{ij,kl}H_{kl}. \tag{26}$$

The projector, the *Lambda tensor*, $\Lambda_{ij,kl}$ is constructed as follows: Define the projector,

$$P_{ij}(\hat{\mathbf{k}}) = \delta_{ij} - \hat{\mathbf{k}}_i\hat{\mathbf{k}}_j, \tag{27}$$

then,

$$\Lambda_{ij,kl}(\hat{\mathbf{k}}) = P_{ik}P_{jl} - \frac{1}{2}P_{ij}P_{kl}. \tag{28}$$

The action of P_{ij} upon a vector $\mathbf{a}$ is thus to project $\mathbf{a}$ onto the planar subspace whose normal is $\hat{\mathbf{k}}$. $\Lambda_{ij,kl}(\hat{\mathbf{k}})$ is the tensor generalization of this projection. The following properties of the Lambda tensor are useful:

$$\Lambda_{ij,kl}\Lambda_{kl,mn} = \Lambda_{ij,mn}, \tag{29}$$

it is traceless w.r.t. the first and last two indices,

$$\Lambda_{ii,kl} = \Lambda_{ij,kk} = 0, \tag{30}$$

it is symmetric under $(ij) \leftrightarrow (kl)$, $(ij) \leftrightarrow (ji)$, and $(kl) \leftrightarrow (lk)$

$$\Lambda_{ij,kl} = \Lambda_{kl,ij} = \Lambda_{ji,kl} = \Lambda_{ij,lk}\,, \tag{31}$$

and it is transverse on all indices,

$$\hat{\mathbf{k}}^a\Lambda_{ij,kl} = 0, \quad a \in \{i, j, k, l\}. \tag{32}$$

The polarization tensors satisfy the completeness relations

$$\sum_r e^{r}_{ij}(\hat{\mathbf{k}})e^{r}_{lm}(\hat{\mathbf{k}}) = \frac{1}{2}\left(P_{il}P_{jm} + P_{im}P_{jl} - P_{ij}P_{lm}\right). \tag{33}$$

An alternative definition of P_{ij} in terms of $\hat{\mathbf{u}}$ and $\hat{\mathbf{v}}$ in the plane orthogonal to $\mathbf{k}$ reads

$$P_{ij} = \hat{\mathbf{u}}_i\hat{\mathbf{u}}_j + \hat{\mathbf{v}}_i\hat{\mathbf{v}}_j\,. \tag{34}$$

Therefore, the action of Λ onto a symmetric tensor H_{ij} may be expressed in terms of the $+$ and $\times$ polarization tensors as

$$H^{TT}_{kl} = \Lambda_{ij,kl}(\mathbf{k})H_{ij} = \left[e^{+}_{ij}(\hat{\mathbf{k}})e^{+}_{kl}(\hat{\mathbf{k}}) + e^{\times}_{ij}(\hat{\mathbf{k}})e^{\times}_{kl}(\hat{\mathbf{k}})\right] H_{ij}. \tag{35}$$

If we define the projection of H_{ij} onto the $+$ and $\times$ polarization basis

$$H_{+}(\mathbf{k}) \equiv e^{+}_{ij}(\mathbf{k})H_{ij}(\mathbf{k}), \quad H_{\times}(\mathbf{k}) \equiv e^{\times}_{ij}(\mathbf{k})H^{ij}(\mathbf{k}), \tag{36}$$

we can rewrite

$$\Lambda_{ij,kl}(\mathbf{k})H_{ij}(\mathbf{k})H_{kl}(\mathbf{k})^{*} = H_{+}(\mathbf{k})H^{*}_{+}(\mathbf{k}) + H_{\times}(\mathbf{k})H^{*}_{\times}(\mathbf{k}). \tag{37}$$

This result will be used in Chapter 5.

2.1.3 Energy and momentum of GWs

The notion of an energy-momentum tensor for GWs can be defined through (see e.g. [60])

$$T^{\mu\nu}_{GW} = \frac{1}{32\pi G}\left\langle \partial^{\mu}h_{\alpha\beta}\partial^{\nu}h^{\alpha\beta}\right\rangle, \tag{38}$$

where the average is typically taken either over many oscillations in time or over many wavelengths in space. The energy density associated with the GWs is given by the 00-component as

$$T^{00}_{GW} = \frac{1}{32\pi G}\left\langle \dot{h}^{TT}_{ij}\dot{h}^{TT}_{ij}\right\rangle. \tag{39}$$

To arrive at an expression for the energy flux, i.e., the energy carried GWs passing through a unit surface per unit time at a large distance r from the source an expression, consider the flux through a volume V enclosed by a sphere of radius r whose surface element is given by $dA = r^2 d\Omega$. On this sphere sufficiently far away from the source, the metric perturbations take the general form

$$h^{TT}_{ij}(t,r) = \frac{1}{r}f_{ij}(t-r). \tag{40}$$

Energy-momentum conservation,

$$\int_V d^3x\left(\partial_0 T^{00}_{GW} + \partial_i T^{i0}_{GW}\right) = 0, \tag{41}$$

then implies that

$$\frac{dE}{dt\,d\Omega} = \frac{r^2}{32\pi G}\left\langle \dot{h}^{TT}_{ij}(t,r)\dot{h}^{TT}_{ij}(t,r)\right\rangle \tag{42}$$

across the spherical surface.

2.1.4 Weinberg's formula

In this Section, I will derive a central expression, *Weinberg's formula* (54) for the GW production by a generic (non-stochastic) source of energy and momentum T_{ij}, an expression which I will use extensively to compute the GW spectrum in the Higgsless simulations. Due to its historical significance, and name conventions used in the literature, I will outline in this Section the original method through which this result was obtained. Later in Section 2.2.4 and in a cosmological setting, I will present an alternative, more rigorous derivation of the same expression from a stochastic source.

The spectrum of GWs produced by a generic source T_{ij} of energy-momentum was originally derived by Weinberg in his book [62]. A somewhat more detailed and digestable derivation was delivered by Maggiore in his text book [60]. For the completeness of this thesis, and to form a basis for discussion, I will review this derivation in some detail.

We will assume that GW production occurs in a flat non-expanding universe. In this case, the equations of motion for the metric perturbations $\bar{h}_{\mu\nu}$ subject to non-vanishing energy-momentum and in Lorentz gauge are given in equation (16). Since (16) is linear in $\bar{h}_{\mu\nu}$, the problem can be reduced to a simpler problem,

$$\Box_x G\left(x-x'\right) = \delta^4\left(x-x'\right), \tag{43}$$

which upon finding the solution $G\left(x-x'\right)$ allow for the construction of $\bar{h}_{\mu\nu}$ through convolution:

$$\bar{h}_{\mu\nu}(x) = -16\pi G \int_{V_S} d^4x' G\left(x-x'\right) T_{\mu\nu}\left(x'\right), \tag{44}$$

where the integral is taken over the source volume V_S. What this amounts to is studying the response of the system due to a minimal impulse $\delta^4\left(x-x'\right)$ at x'. Linearity then allows to construct the full response from the linear superposition of impulse responses as obtained from the convolution.

The solution $G\left(x-x'\right)$ that solves (43) is called the (retarded) Green's function and is given by [62]

$$G\left(x-x'\right) = -\frac{1}{4\pi\left|\mathbf{x}-\mathbf{x}'\right|}\delta\left(t-\left|\mathbf{x}-\mathbf{x}'\right|-t'\right). \tag{45}$$

Insertion of this expression into (44) and integrating over time, thus absorbing the delta function, leads to

$$\bar{h}_{\mu\nu}(t,\mathbf{x}) = 4G\int d^3\mathbf{x}'\frac{1}{\left|\mathbf{x}-\mathbf{x}'\right|}T_{\mu\nu}\left(t-\left|\mathbf{x}-\mathbf{x}'\right|,\mathbf{x}'\right). \tag{46}$$

Assuming that the source is sufficiently far away, we can make the approximation $1/(|\mathbf{x}-\mathbf{x}'|) = r$, where r is the distance to the (center of the) source. For the retarded time, we make the approximation that it is equal on planes intersecting the source orthogonal to the direction $\hat{\mathbf{n}} \equiv \hat{\mathbf{x}}$ pointing towards the observer, namely

$$t - \left|\mathbf{x}-\mathbf{x}'\right| \approx t - r + \mathbf{x}' \cdot \hat{\mathbf{n}}. \tag{47}$$

Since we are outside of the source, we can furthermore project on the transverse-traceless part, i.e. $h_{ij}^{TT} = \Lambda_{ij,kl}\bar{h}_{kl}$, and thus obtain

$$\boxed{h_{ij}^{TT}(t,r) = \frac{4G}{r}\int d^3\mathbf{x}'\Lambda_{ij,kl}(\hat{\mathbf{n}})T_{kl}\left(t-r+\mathbf{x}'\cdot\hat{\mathbf{n}},\,\mathbf{x}'\right).} \tag{48}$$

Using the Fourier convention,

$$\begin{aligned} T_{kl}(t,\mathbf{x}) &= \int \frac{d^4k}{(2\pi)^4} T_{kl}(q,\mathbf{k}) e^{-iqt+i\mathbf{k}\cdot\mathbf{x}}, \\ T_{ij}(q,\mathbf{k}) &= \int dt\, d^3\mathbf{x}\, T_{ij}(t,\mathbf{x}) e^{iqt-i\mathbf{k}\cdot\mathbf{x}} \end{aligned} \tag{49}$$

one finds that

$$h_{ij}^{TT}(t,r) = \frac{4G}{r}\Lambda_{ij,kl}(\hat{\mathbf{n}})\int_{-\infty}^{\infty}\frac{dq}{2\pi}T_{kl}(q,q\hat{\mathbf{n}})e^{-iq(t-r)}. \tag{50}$$

At a large distance from the source, the total radiated energy per unit solid angle $d\Omega$ through a spherical surface of radius r is described by Equation (42). Inserting the strain amplitudes (50) into this expression and integrating over time, one finds that

$$\begin{aligned} \frac{dE}{d\Omega} &= \frac{r^2}{32\pi G}\int_{-\infty}^{\infty} dt \dot{h}_{ij}^{TT}(t,r)\dot{h}_{ij}^{TT}(t,r) \\ &= \frac{G}{2\pi^2}\Lambda_{ij,kl}(\hat{\mathbf{n}})\int_0^{\infty} dq\, q^2 T_{ij}(q,q\hat{\mathbf{n}})T_{kl}^*(q,q\hat{\mathbf{n}}) \end{aligned} \tag{51}$$

where in the first line the ensemble average is removed since we are anyway integrating over time, while in the second line, the identity (29) for the Λ tensor as well as $T(-q,-\mathbf{k}) = T^*(q,\mathbf{k})$ were used. Thus, we can express the total amount of released energy per logarithmic frequency bin as

$$\frac{dE}{d\ln q} = \frac{2Gq^3}{\pi}\int\frac{d\Omega}{4\pi}\Lambda_{ij,kl}(\hat{\mathbf{n}})T_{ij}(q,q\hat{\mathbf{n}})T_{kl}^*(q,q\hat{\mathbf{n}}). \tag{52}$$

The interpretation of the expression concerns the total energy released from a generic source T_{ij}, which is sufficiently far away that we are in the wave zone where GWs appear as plane waves. Consider

instead the situation that an unlimited and statistically homogeneous distribution of similar sources is distributed in space to occupy an average volume V per source. Provided we are sufficiently far from the sources, we can apply Equation (52), and conclude that the energy density in GWs is Equation (52) divided by V, i.e.

$$\frac{d\rho_{GW}}{d\ln q} = \frac{2Gq^3}{\pi V}\int \frac{d\Omega}{4\pi}\Lambda_{ij,kl}(\hat{\mathbf{n}})T_{ij}(q, q\hat{\mathbf{n}})T^*_{kl}(q, q\hat{\mathbf{n}})\,. \tag{53}$$

It appears, therefore, that Weinberg's formula can be used to compute the energy density in GWs from an unlimited number of sources distributed uniformly in space. However, even with just one source in one spatial volume V, we can estimate the full spectrum. Given a generic source $T_{ij}(t, \mathbf{x})$, we can thus use Equation (53) to determine the resulting GW spectrum at production time (superscript p)

$$\Omega^p_{GW}(q) = \frac{1}{\bar{\rho}}\frac{d\rho_{GW}(q)}{d\ln q} = \frac{q^3}{4\pi^2 m_{Pl}^2 \bar{\rho} V}\int \frac{d\Omega}{4\pi}\left[\Lambda_{ij,kl}(\hat{\mathbf{k}})T_{ij}(q, \mathbf{k})T^*_{kl}(q, \mathbf{k})\right]_{|\mathbf{k}|=q}\,. \tag{54}$$

where I used $m_{Pl} = 1/\sqrt{8\pi G}$ and $\bar{\rho}$ is the average energy density. To honor the original derivation, to align with the literature, and owing to its central role in my work, I will call Equation 54 *Weinberg's formula*.

2.2 Gravitational waves in Cosmology

In this Section, I will generalize the treatment of GWs in Section 2.1 to a cosmological setting involving an expanding space-time and relaxing the assumption of being in a vacuum. I will review basic results and, in particular, re-derive Weinberg's formula (54) in this more realistic context, thus shedding light on its applicability in the context of this thesis and interpretation. Before considering more formal aspects, I will discuss some general results, giving order-of-magnitude estimations and justifying the description of cosmological sources of GWs as stochastic backgrounds.

2.2.1 The stochasticity of GW backgrounds

Any cosmological gravitational background that we earnestly want to measure is expected to be of a stochastic nature. In this Section, I will briefly review the arguments behind this statement.

In an expanding universe, the largest scale of correlation is set by the Hubble distance/time H^{-1}. Therefore, at the time of GW production, the largest spatial and temporal scale over which a GW signal can

be correlated is $(\Delta x_p, \Delta t_p)/H_p^{-1} \leqslant 1$. We wish to compare this to the current Hubble scale, and proceed to compute the redshifted value of the largest correlation scale Δx_p^0,

$$\frac{\Delta x_p^0}{H_0^{-1}} = \frac{\Delta x_p}{H_0^{-1}} \frac{a_0}{a_p} \leqslant \frac{H_p^{-1}}{H_0^{-1}} \frac{a_0}{a_p} = \frac{a_0/a_p}{\sqrt{\Omega_{rad}^p}} \tag{55}$$

where we assumed a radiation-dominated equation of state at production and defined $\Omega_{rad}^p \equiv \rho^p/\rho_c^0$ and $\rho_c^0 = 3H_0^2/(8\pi G)$ is the average density at production time.

As the universe expands adiabatically to a good approximation, the entropy per comoving volume is conserved [63], so that $g_S(T)T^3a^3(t) = \text{const.}$. This allows relating the amount of expansion that has taken place since production, a_0/a_p, to the current photon temperature $T_0 \simeq 2.35 \times 10^{-13}\text{GeV}$ [64] and the temperature T_p at production through

$$\frac{a_0}{a_p} = \left(\frac{g_S^p}{g_S^0}\right)^{1/3} \left(\frac{T_p}{T_0}\right) \simeq 1.25 \times 10^{13} \left(\frac{g_S^p}{100}\right)^{1/3} \left(\frac{T_p}{\text{GeV}}\right) \tag{56}$$

where we additionally assumed the value $g_S^0 = 3.91$ [65]. Using that $\rho_{rad} = \frac{\pi^2}{30} g_*(T)T^4$ during radiation domination, we can furthermore compute

$$\Omega_{rad}(T) = \Omega_{rad}^0 \left(\frac{g_S^0}{g_S(T)}\right)^{4/3} \left(\frac{g_*(T)}{g_*^0}\right) \left(\frac{a_0}{a}\right)^4 . \tag{57}$$

The redshifted correlation scale can therefore be estimated as

$$\begin{aligned} \frac{\Delta x_p^0}{H_0^{-1}} &\simeq \frac{a_0/a_p}{\sqrt{\Omega_{rad}^p}} = \frac{1}{\sqrt{\Omega_{rad}^0}} \left(\frac{g_S^p}{g_S^0}\right)^{1/3} \sqrt{\frac{g_*^0}{g_*^p}} \frac{T_0}{T_p} \\ &\approx 10^{-11} \left(\frac{100}{g_*^p}\right)^{1/6} \left(\frac{\text{GeV}}{T_p}\right) \end{aligned} \tag{58}$$

where in the last step, we used that $g_*^p \approx g_S^p$ and $g_*^0 = 2$ for the two polarization states of photons. It is immediately apparent that for the prototypical electroweak PT, $T_p \sim 100\,\text{GeV}$, and in fact, any other first-order PT occurring in the early universe, the maximal scale of the correlation will constitute only an extremely small fraction of the current Hubble scale $1/H_0^{-1}$. In fact, for the electroweak PT, the celestial sphere consists of the order of $\sim 10^{24}$ uncorrelated patches, rendering the resolution of individual causally connected regions unachievable.

Thus, we have seen how GW sources are correlated on scales much smaller than today's horizon. The cosmological principle nevertheless

demands that wherever we look at the celestial sphere, the observation is a realization of a specific process whose probability distribution is isotropic. The conclusion is that a cosmological GW background will be stochastic in nature, justifying call it a stochastic GW background (SGWB).

2.2.2 Redshifting

The energy in GWs can be characterized by the dimensionless quantity

$$\Omega_{GW}(f) = \frac{1}{\rho_c}\frac{d\rho_{GW}(f)}{d\log f}\,, \tag{59}$$

thus indicating how much energy is stored in GWs per logarithmic frequency interval normalized to the critical density

$$\rho_c = \frac{3H^2}{8\pi G}. \tag{60}$$

The frequency relates to the wavenumber k and angular frequency q through $k = q = 2\pi f$. We are interested in understanding the evolution of (59) with cosmic expansion and how wavenumbers at production time redshift.

Wavenumbers simply grow with the inverse scale factor a^{-1}, while the GW energy dilutes as radiation, i.e. $\Omega_{GW}(k) \propto a^{-4}$. Therefore, the present-day physical frequency is expressed in terms of the wavenumber k_p at production time as

$$f_0 = \left(\frac{a_p}{a_0}\right)\frac{k_p}{2\pi} \tag{61}$$

while the present-day GW spectrum

$$\Omega^0_{GW}(k) = \frac{\rho^p_c}{\rho^0_c}\left(\frac{a_p}{a_0}\right)^4\left(\frac{1}{\rho_c}\frac{d\rho_{GW}}{d\log k}\right)_p\,. \tag{62}$$

Equation (56) tells us that the ratio of scale factors obeys

$$\frac{a_0}{a_p} \simeq 1.25\times 10^{13}\left(\frac{g^p_{*S}}{100}\right)^{1/3}\left(\frac{T_p}{\text{GeV}}\right).$$

We can thus relate the present-day frequency to the wavenumber at production through

$$\begin{aligned} f_0 &= \frac{1}{2\pi\cdot 1.25\cdot 10^{13}}k_p\left(\frac{100}{g^p_*}\right)^{1/3}\left(\frac{\text{GeV}}{T_p}\right) \\ &= 1.27\cdot 10^{-14}\times H_p\left(\frac{k_p}{H_p}\right)\left(\frac{100}{g^p_*}\right)^{1/3}\left(\frac{\text{GeV}}{T_p}\right), \end{aligned} \tag{63}$$

now replacing $g_{*S} \to g_*$ since at relevant temperatures $g_* \approx g_{*S}$. Assuming radiation domination at GW production, and with the reduced Planck mass $m_{Pl} = 2.435 \times 10^{18}$GeV, the Hubble rate at production can be expressed as

$$H_p = \sqrt{\frac{\pi^2 g_* T_*^4}{90 m_{Pl}^2}} = 2.067 \cdot 10^7 \sqrt{\frac{g_*^p}{100}} \left(\frac{T_p}{\text{GeV}}\right) \text{ s}^{-1} \tag{64}$$

so that the present-day frequency is given by

$$f_0 = 2.63 \cdot 10^{-6}\,\text{Hz} \times \left(\frac{k_*}{H_p}\right) \left(\frac{g_*^p}{100}\right)^{1/6} \left(\frac{T_p}{100\text{GeV}}\right) . \tag{65}$$

To obtain the redshifted GW spectrum, one makes use of that the current critical density $\rho_c^0 = h^2 8.18 \times 10^{-47}$ GeV^4 [66] and again $g_*^p \simeq g_S^p$, so that

$$\Omega_{GW}^0(k) = \mathcal{T}_{GW} \left(\frac{1}{\rho_c} \frac{d\rho_{GW}(k)}{d \log k}\right)_p , \tag{66}$$

where I defined the redshift transfer coefficient

$$h^2 \mathcal{T}_{GW} = 1.65 \times 10^{-5} \left(\frac{100}{g_*^p}\right)^{1/3} \tag{67}$$

Thus, redshifted frequencies and the redshifted GW spectrum can be computed using Equations (63) and (66).

2.2.3 GWs in an expanding space-time

Section 2.1 served well as an introduction to GWs in general. While, as we shall later see, this description is largely adequate for the computational tasks in this thesis, the proper stage on which our physics takes place is Cosmology. This Section aims, therefore, to extend the results of the previous Section 2.1 to the more realistic setup of a spatially flat expanding space-time.

The Friedmann-Lemaître-Robertson-Walker metric (FLRW) metric which governs a spatially flat and expanding universe reads

$$\begin{aligned} ds^2 &= -dt^2 + a^2(t)\delta_{ij} dx^i\, dx^j \\ &= a^2(\tau)\left[-d\tau^2 + \delta_{ij} dx^i\, dx^j\right] , \end{aligned} \tag{68}$$

where a is the scale factor, x^i comoving coordinates, and t and τ the cosmological and conformal time respectively.

In cosmological perturbation theory, the only physical radiative degrees of freedom are the tensor perturbations h_{ij} obeying $h^i{}_i =$

$0, \quad \partial^j h_{ij} = 0$, i.e., they are transverse-traceless (TT). Including only tenor perturbations, these degrees of freedom perturb the FLRW metric (68) as $g_{\mu\nu} = \bar{g}^{FLRW}_{\mu\nu} + \delta g_{\mu\nu}$, where the only non-zero components of $\delta g_{\mu\nu}$ are $\delta g_{ij} = h_{ij}$, such that the line element in the perturbed metric reads

$$\begin{aligned} ds^2 &= a^2(\tau)\left[-d\tau^2 + \delta_{ij} dx^i\, dx^j\right] + h_{ij} dx^i\, dx^j \\ &\equiv a^2(\tau)\left[-d\tau^2 + \left(\delta_{ij} + \ell_{ij}\right) dx^i\, dx^j\right], \end{aligned} \tag{69}$$

where I defined the re-scaled tensor perturbation $\ell_{ij} \equiv h_{ij}/a^2$. The energy density in GWs is then given by

$$\begin{aligned} \Omega_{GW}(t_0) &\equiv \frac{1}{32\pi G \rho_c} \left\langle \dot{\ell}_{ij}(t_0, \mathbf{x})\, \dot{\ell}_{ij}(t_0, \mathbf{x}) \right\rangle \\ &= \frac{1}{32\pi G a^2 \rho_c} \left\langle \ell'_{ij}(t_0, \mathbf{x})\, \ell'_{ij}(t_0, \mathbf{x}) \right\rangle \\ &\approx \frac{1}{12\mathcal{H}_*^2} \left\langle H'_{ij}(\tau_0, \mathbf{x})\, H'_{ij}(\tau_0, \mathbf{x}) \right\rangle, \end{aligned} \tag{70}$$

where *dot* denotes derivative with respect to cosmological time t and *prime* to conformal time τ, and I additionally defined $H_{ij} = a\ell_{ij}$ for later convenience.

In conformal time, the transverse-traceless metric perturbations ℓ_{ij} obey the equations of motion

$$\ell''_{ij}(\mathbf{x}, \tau) + 2\mathcal{H}\ell'_{ij}(\mathbf{x}, \tau) - \nabla^2 \ell_{ij}(\mathbf{x}, \tau) = 16\pi G a^2 \bar{\rho} \Pi^{TT}_{ij}(\mathbf{x}, \tau) \tag{71}$$

where the Laplacian $\nabla^2 = \partial_i \partial_i$ is associated with the comoving coordinates x^i, $\mathcal{H} = a'/a = H/a$ is the conformal Hubble rate where $H = \dot{a}/a$ is the Hubble expansion rate, and Π^{TT}_{ij} is the transverse-traceless part of the anisotropic stress normalized to the average and critical density $\bar{\rho} \equiv 3\mathcal{H}^2/\left(8\pi G a^2\right)$, where I use an *over-bar* to distinguish it from the critical density at the present time. I will use this notation throughout the thesis.

In Fourier space with comoving momenta $\mathbf{k}$, and with $H_{ij}(\mathbf{k}, \tau) = a\ell_{ij}(\mathbf{k}, \tau)$, Equation (71) takes the form

$$H''_{ij}(\mathbf{k}, \tau) + \left(k^2 - \frac{a''}{a}\right) H_{ij}(\mathbf{k}, \tau) = 16\pi G a^3 \bar{\rho} \Pi^{TT}_{ij}(\mathbf{k}, \tau) = 6\mathcal{H}^2 a \Pi^{TT}_{ij}(\mathbf{k}, \tau), \tag{72}$$

using that $G = (3\mathcal{H}^2)(8\pi a^2 \bar{\rho})$. In Fourier space, the transverse-traceless part of anisotropic stress is obtained by projecting onto the plane orthogonal to the comoving momentum $\mathbf{k}$ by means of the lambda tensor (28),

$$\Pi^{TT}_{ij}(\mathbf{k}) = \frac{1}{\bar{\rho}} \Lambda_{ij,kl} T_{kl}(\mathbf{k}). \tag{73}$$

Note that $\Lambda_{ij,kl}$ obeys a number of identities (29), (30), (31), and (32), which will be useful shortly.

2.2.4 Perspectives on Weinberg's formula

Weinberg's formula (54), as derived in Section 2.1.4, is, to my knowledge, the simplest way the GW production from a generic source of energy and momentum can be derived. Presented in this way, it was originally introduced in Section 3.1 of Weinberg's textbook [62], and has been employed as the basis for computing the GW production in a number of publications (e.g. [23, 24, 67, 68]).

It is not completely transparent, however, that Weinberg's result is applicable to a realistic cosmological setting. In this section, I will therefore demonstrate a more rigorous and nuanced derivation of Weinberg's formula drawing inspiration from [36]. We will ultimately arrive at an identical result, but along the way, assumptions and approximations are made explicit so as to reveal the meaning of the final expression in cosmology.

We are interested in solving Equation (72) and eventually arriving at analytic expressions for the metric perturbations ℓ_{ij}. To this end, we make the assumption that GW production occurs during radiation domination. In this case, we can define the scale factor at the beginning of sourcing $a(\tau_*) = 1$, such that $a(\tau) = \mathcal{H}_*\tau$. Subject to this assumption, we can replace in the RHS of Equation (72) $a \to \mathcal{H}_*\tau$ and $\mathcal{H}^2 \to 1/\tau^2$, which then becomes $6\mathcal{H}_*\Pi_{ij}^{TT}(\mathbf{k},\tau)/\tau$, while the LHS simplifies from $a'' = 0$. The equation that should hereby be solved is reduced to

$$H_{ij}''(\mathbf{k},\tau) + k^2 H_{ij}(\mathbf{k},\tau) = \frac{6\mathcal{H}_*}{\tau}\Pi_{ij}^{TT}(\mathbf{k},\tau)\,, \tag{74}$$

Introducing the variable $x \equiv k\tau$, this equation further simplifies to

$$\frac{d^2 H_{ij}}{dx^2}(\mathbf{k},x) + H_{ij}(\mathbf{k},x) = \frac{6\mathcal{H}_*}{k}\frac{\Pi_{ij}^{TT}(\mathbf{k},x)}{x}\,, \tag{75}$$

The inhomogeneous solution is obtained using the Greens function

$$\mathcal{G}(x,x_1) = \sin(x-x_1) \tag{76}$$

such that

$$H_{ij}\,(\mathbf{k}, x_* < x < x_{fin}) = \frac{6\mathcal{H}_*}{k}\int_{x_*}^{x}\frac{dx_1}{x_1}\sin(x-x_1)\Pi_{ij}^{TT}(\mathbf{k},x_1) \tag{77}$$

while the homogeneous solution is given by

$$H_{ij}\,(\mathbf{k}, x \geqslant x_{fin}) = A_{ij}(\mathbf{k})\cos x + B_{ij}(\mathbf{k})\sin x\,. \tag{78}$$

The coefficients are obtained by matching at the end of sourcing, and one finds

$$\begin{aligned} A_{ij}(\mathbf{k}) &= \frac{6\mathcal{H}_*}{k}\int_{x_*}^{x_{fin}}\frac{dx_1}{x_1}\sin(-x_1)\Pi_{ij}^{TT}(\mathbf{k},x_1), \\ B_{ij}(\mathbf{k}) &= \frac{6\mathcal{H}_*}{k}\int_{x_*}^{x_{fin}}\frac{dx_1}{x_1}\cos(x_1)\Pi_{ij}^{TT}(\mathbf{k},x_1). \end{aligned} \tag{79}$$

Note that a simpler way of writing the solution post-sourcing emerges as

$$H_{ij}^{TT}(\mathbf{k}, x \geqslant x_{fin}) = \frac{6\mathcal{H}_*}{k}\int_{x_*}^{x_{fin}} \frac{dx_1}{x_1}\sin(x-x_1)\Pi_{ij}^{TT}(\mathbf{k}, x_1)\,. \tag{80}$$

Migrating back to conformal time, we have found the solutions to Equation (72) in radiation domination during and after GW production

$$\boxed{\begin{aligned} H_{ij}(\mathbf{k}, \tau_* \leqslant \tau < \tau_{fin}) &= \frac{6\mathcal{H}_*}{k}\int_{\tau_*}^{\tau} \frac{d\tau_1}{\tau_1}\sin k(\tau-\tau_1)\Pi_{ij}^{TT}(\mathbf{k}, \tau_1)\,, \\ H_{ij}(\mathbf{k}, \tau \geqslant \tau_{fin}) &= \frac{6\mathcal{H}_*}{k}\int_{\tau_*}^{\tau_{fin}} \frac{d\tau_1}{\tau_1}\sin k(\tau-\tau_1)\Pi_{ij}^{TT}(\mathbf{k}, \tau_1)\,. \end{aligned}} \tag{81}$$

Evaluated at the present time, the total energy fraction in GWs Ω_{GW} and the GW spectrum $\Omega_{GW}(\tau_0, k)$ are defined by

$$\begin{aligned} \Omega_{GW} &\equiv \int_{-\infty}^{\infty} \Omega_{GW}(k)\, d\ln k \\ &= \frac{1}{32\pi G a_0^2 \rho_c}\left\langle \ell'_{ij}(\tau_0, \mathbf{x})\, \ell'_{ij}(\tau_0, \mathbf{x})\right\rangle \\ &\approx \frac{1}{12\mathcal{H}_0^2 a_0^2}\left\langle H'_{ij}(\tau_0, \mathbf{x})\, H'_{ij}(\tau_0, \mathbf{x})\right\rangle\,, \end{aligned} \tag{82}$$

where in the last expression I neglected terms proportional to $\mathcal{H}_0$ and $\mathcal{H}_0^2$. This approximation is valid for the following reason: the strain $h_{ij} \propto 1/k$ while $\mathcal{H} = 1/\tau$ .Therefore, the second to last expression contains terms $\propto 1/(k\tau_0)$, which are negligible since we are only interested in modes that are deep in the Horizon by now.

Following the Fourier convention (49),

$$H_{ij}(\tau_0, \mathbf{x}) = \int \frac{d^3\mathbf{k}}{(2\pi)^3} H_{ij}(\tau_0, \mathbf{k})\, e^{i\mathbf{k}\cdot\mathbf{x}} \tag{83}$$

the RHS of Equation (82) becomes

$$\begin{aligned} &\frac{1}{12\mathcal{H}_0^2 a_0^2}\left\langle H'_{ij}(\tau_0, \mathbf{x})\, H'_{ij}(\tau_0, \mathbf{x})\right\rangle \\ &= \frac{1}{12\mathcal{H}_0^2 a_0^2}\int \frac{d^3\mathbf{k}_1\, d^2\mathbf{k}_2}{(2\pi)^6}\left\langle H'_{ij}(\tau_0, \mathbf{k}_1)\, H'^{*}_{ij}(\tau_0, \mathbf{k}_2)\right\rangle e^{i(\mathbf{k}_1-\mathbf{k}_2)\cdot\mathbf{x}} \end{aligned} \tag{84}$$

The strain derivatives H'_{ij} are given by

$$H'_{ij}(\mathbf{k}, \tau \geqslant \tau_{fin}) = 6\mathcal{H}_*\int_{\tau_*}^{\tau_{fin}} \frac{d\tau_1}{\tau_1}\cos k(\tau-\tau_1)\Pi_{ij}^{TT}(\mathbf{k}, \tau_1)\,, \tag{85}$$

such that

$$\left\langle H'_{ij}(\tau_0, \mathbf{k}_1) H'^{*}_{ij}(\tau_0, \mathbf{k}_2)\right\rangle = 36\mathcal{H}_*^2 \int_{\tau_*}^{\tau_{\text{fin}}} \frac{d\tau_1}{\tau_1} \int_{\tau_*}^{\tau_{\text{fin}}} \frac{d\tau_2}{\tau_2} \cos k_1(\tau_0 - \tau_1) \times \cos k_2(\tau_0 - \tau_2) \left\langle \Pi_{ij}^{TT}(\tau_1, \mathbf{k}_1) \Pi_{ij}^{TT*}(\tau_2, \mathbf{k}_2)\right\rangle \tag{86}$$

To this end, we treat the anisotropic stress as a stochastic field and impose assumptions of homogeneity and isotropy. Accordingly, we define the unequal-time correlator (UETC) E_Π to characterize the spectrum of the anisotropic stresses through

$$\left\langle \Pi_{ij}(\tau_1, \mathbf{k}) \Pi^{*}_{ij}(\tau_2, \mathbf{k}_2)\right\rangle \equiv (2\pi)^6 \delta^3(\mathbf{k} - \mathbf{k}_2) \frac{E_\Pi(\tau_1, \tau_2, k)}{4\pi k^2}. \tag{87}$$

Inserting (87) into (86) and (86) into (84), one arrives at the comparatively mundane expression for the present-day GW spectrum $\Omega_{GW}(\tau_0, k)$, namely

$$\Omega_{GW}(\tau_0, k) = 3k \left(\frac{\mathcal{H}_*}{\mathcal{H}_0}\right)^2 \left(\frac{a_*}{a_0}\right)^2 \int_{\tau_*}^{\tau_{\text{fin}}} \frac{d\tau_1}{\tau_1} \int_{\tau_*}^{\tau_{\text{fin}}} \frac{d\tau_2}{\tau_2} \times E_\Pi(\tau_1, \tau_2, k) \cos k(\tau_0 - \tau_1) \cos k(\tau_0 - \tau_2)\,, \tag{88}$$

where I reintroduced a_*. Note that we have already encountered the prefactor

$$\left(\frac{\mathcal{H}_*}{\mathcal{H}_0}\right)^2 \left(\frac{a_*}{a_0}\right)^2 = \left(\frac{H_*}{H_0}\right)^2 \left(\frac{a_*}{a_0}\right)^4 = \left(\frac{\bar{\rho}_*}{\bar{\rho}_0}\right)^2 \left(\frac{a_*}{a_0}\right)^4 \equiv \mathcal{T}_{GW} \tag{89}$$

in Section 2.2.2 where we concluded in Equation (67) that

$$h^2 \mathcal{T}_{GW} = 1.65 \times 10^{-5} \left(\frac{100}{g_*^p}\right)^{1/3}, \tag{90}$$

which accounts for the redshifting of the GW energy with cosmic expansion. Equation (88) constitutes an expression for the GW spectrum as obtained from UETC of the anisotropic stresses. We have left to recast this expression into a form consistent with Weinberg's formula.

To this end, consider that

$$2\cos k(\tau_0 - \tau_1)\cos k(\tau_0 - \tau_2) = \cos k(\tau_1 - \tau_2) + \cos 2k\tau_0 \cos k(\tau_1 + \tau_2) + \sin 2k\tau_0 \sin k(\tau_1 + \tau_2)\,. \tag{91}$$

Then, for as long as the GWs are measured over many oscillations in $\tau_0 \to \tau_0 + \Delta\tau$, i.e. if $k\Delta\tau_0 >> 1$, the τ-average becomes

$$\langle \cos k(\tau - \tau_1)\cos k(\tau - \tau_2)\rangle_\tau = \frac{1}{2}\cos k(\tau_1 - \tau_2) \tag{92}$$

so that an effective GW energy density can be obtained as

$$\Omega_{\mathrm{GW}}(k) \approx \frac{3}{2} k \mathcal{T}_{\mathrm{GW}} \int_{\tau_*}^{\tau_{\mathrm{fin}}} \frac{d\tau_1}{\tau_1} \int_{\tau_*}^{\tau_{\mathrm{fin}}} \frac{d\tau_2}{\tau_2} E_\Pi(\tau_1, \tau_2, k) \cos k(\tau_1 - \tau_2) \,, \quad (93)$$

which now only depends on τ_0 through the redshift transfer coefficient. At this point, let us take the opportunity to define

$$\mathcal{I}(\tau_*, \tau_{\mathrm{fin}}, k) = \frac{k}{2} \int_{\tau_*}^{\tau_{\mathrm{fin}}} \frac{d\tau_1}{\tau_1} \int_{\tau_*}^{\tau_{\mathrm{fin}}} \frac{d\tau_2}{\tau_2} E_\Pi(\tau_1, \tau_2, k) \cos k(\tau_1 - \tau_2) \,. \quad (94)$$

The GW spectrum as a present-day observable can then be compactly expressed as

$$\Omega_{\mathrm{GW}}(k) = 3 \mathcal{T}_{\mathrm{GW}} \mathcal{I}(k) \,. \quad (95)$$

We must now seek an estimate of the UETC $E_\Pi(\tau_1, \tau_2, k)$. Formally,

$$\delta^{(3)}(\mathbf{k} - \mathbf{k}) = \int \frac{d^3\mathbf{x}}{(2\pi)^3} e^{i(\mathbf{k}-\mathbf{k})\cdot\mathbf{x}} \equiv \frac{V}{(2\pi)^3} \,, \quad (96)$$

where V denotes the divergent volume of comoving $\mathbf{x}$-space. Setting $\mathbf{k} = \mathbf{k}'$ in Equation (87) and using relation (96), the UETC can be estimated as an average over wavenumbers $\mathbf{k}$ of equal magnitude k on the sphere

$$\begin{aligned} E_\Pi(\tau_1, \tau_2, k) &= \frac{k^2}{2\pi^2 V} \int_{\Omega_k} \frac{d\Omega_k}{4\pi} \Pi_{ij}^{TT}(\tau_1, \mathbf{k}) \Pi_{ij}^{TT*}(\tau_2, \mathbf{k}) \\ &= \frac{k^2}{2\pi^2 V} \int_{\Omega_k} \frac{d\Omega_k}{4\pi} \frac{\Lambda_{ij,kl} T_{kl}(\tau_1, \mathbf{k})}{\bar{\rho}(\tau_1)} \frac{\Lambda_{ij,ab} T_{ab}^*(\tau_2, \mathbf{k})}{\bar{\rho}(\tau_2)} \\ &= \frac{k^2}{2\pi^2 V} \int_{\Omega_k} \frac{d\Omega_k}{4\pi} \frac{\Lambda_{ij,kl} T_{ij}(\tau_1, \mathbf{k}) T_{kl}^*(\tau_2, \mathbf{k})}{\bar{\rho}(\tau_1) \bar{\rho}(\tau_2)} \,. \end{aligned} \quad (97)$$

With this expression for the UETC, we can rewrite Equation (94) as

$$\begin{aligned} \mathcal{I}(k) = \frac{k^3}{4\pi^2 V} &\int_{\Omega_k} \frac{d\Omega_k}{4\pi} \Lambda_{ij,kl} \\ &\times \int_{\tau_*}^{\tau_{\mathrm{fin}}} \frac{d\tau_1}{\tau_1} \frac{T_{ij}(\tau_1, \mathbf{k})}{\bar{\rho}(\tau_2)} \int_{\tau_*}^{\tau_{\mathrm{fin}}} \frac{d\tau_2}{\tau_2} \frac{T_{kl}^*(\tau_2, \mathbf{k})}{\bar{\rho}(\tau_2)} \\ &\times \cos k(\tau_1 - \tau_2) \,, \end{aligned} \quad (98)$$

where I have separated the factors depending on τ_1 and τ_2 in the integrals as far as possible. To make further progress, we must decompose $\cos k(\tau_2 - \tau_1)$ into factors that depend on τ_1 and τ_2 separately. To this end, note that

$$e^{ik\tau_1} e^{-ik\tau_2} = \cos k(\tau_1 - \tau_2) + i \sin k(\tau_1 - \tau_2) \quad (99)$$

It appears, therefore, that if we simply make the replacement $\cos k(\tau_1 - \tau_2) \to e^{ik\tau_1} e^{-ik\tau_2}$ in Equation (98), the real part of the resulting expression for the GW spectrum remain unchanged, while we may introduce a spurious imaginary contribution. Clearly, the GW spectrum is real, so we can simply ignore any such part, but, as we soon shall see explicitly, the imaginary part will indeed be zero. Therefore, making this replacement, Equation (98) becomes

$$\begin{aligned}\mathcal{I}(k) &= \frac{k^3}{4\pi^2 V}\int_{\Omega_k}\frac{d\Omega_k}{4\pi}\Lambda_{ij,kl} \\ &\times \int_{\tau_*}^{\tau_{fin}}\frac{d\tau_1}{\tau_1}\frac{T_{ij}(\tau_1,\mathbf{k})\,e^{ik\tau_1}}{\bar{\rho}(\tau_1)}\int_{\tau_*}^{\tau_{fin}}\frac{d\tau_2}{\tau_2}\frac{T^*_{kl}(\tau_2,\mathbf{k})\,e^{-ik\tau_2}}{\bar{\rho}(\tau_2)} \\ &= \frac{k^3}{4\pi^2 V}\int_{\Omega_k}\frac{d\Omega_k}{4\pi}\Lambda_{ij,kl} \\ &\times \left(\int_{\tau_*}^{\tau_{fin}}\frac{d\tau_1}{\tau_1}\frac{T_{ij}(\tau_1,\mathbf{k})\,e^{ik\tau_1}}{\bar{\rho}(\tau_1)}\right)\left(\int_{\tau_*}^{\tau_{fin}}\frac{d\tau_2}{\tau_2}\frac{T_{kl}(\tau_2,\mathbf{k})\,e^{ik\tau_2}}{\bar{\rho}(\tau_2)}\right)^*.\end{aligned} \tag{100}$$

The last two integrals are each other's conjugates, and since T_{ij} is real, the product of the conjugates is real. Therefore, we have shown that the sin contribution in (99) indeed vanishes, and we need not worry about taking the real part of the GW spectrum as defined from (100).

That we were able to separate the τ integrals completely is a rather remarkable result and was made possible from the bold move of assuming full knowledge of the energy-momentum tensor T_{ij} rather than statistical information about T_{ij} as a stochastic variable. Generally, this is not possible and one must be satisfied with a statistical description. In our case, however, we will indeed gain the required full knowledge of T_{ij} from the Higgsless simulations.

Now, the integrals with respect to τ_1 and τ_2 are fully separated, and the respective integrals constitute what looks like Fourier transforms (taking the τ integration limits to $\pm\infty$ and assuming that the source abruptly starts and ends at τ_* and τ_{fin}) but which are modified by the multiplication of factors of the form $1/(\tau\bar{\rho}(\tau))$. These factors can be remedied by further making the approximation that Hubble expansion is negligible during GW sourcing, i.e. during the time in the interval $[\tau_*, \tau_{fin}]$. In this case, and since we are in radiation domination with $a_* \equiv 1$, $\frac{1}{\tau} = \frac{\mathcal{H}}{a} \sim \frac{\mathcal{H}_*}{a_*}$ and $\bar{\rho}(\tau) \sim \bar{\rho}_*$, we can approximate

$$\frac{d\tau}{\tau}\frac{1}{\bar{\rho}(\tau)} \approx \frac{dt\mathcal{H}_*}{\bar{\rho}_*}, \tag{101}$$

where we also took the opportunity to migrate back to cosmological time t. Following this approximation, Equation (100) becomes

$$\begin{aligned}\mathcal{I}(k) &= \frac{k^3}{4\pi^2 V}\frac{\mathcal{H}_*^2}{\bar{\rho}_*^2}\int_{\Omega_k}\frac{d\Omega_k}{4\pi}\Lambda_{ij,kl} \\ &\times\left(\int_{t_*}^{t_{fin}} dt_1\, T_{ij}\,(t_1,\mathbf{k})\, e^{ikt_1}\right)\left(\int_{t_*}^{t_{fin}} dt_2\, T_{kl}\,(t_2,\mathbf{k})\, e^{ikt_2}\right)^* \\ &= \frac{k^3}{12\pi^2 V m_{Pl}^2\bar{\rho}_*}\int_{\Omega_k}\frac{d\Omega_k}{4\pi}\Lambda_{ij,kl}T_{ij}\,(k,\mathbf{k}\,|\,t_{fin})\,T^*_{kl}\,(k,\mathbf{k}\,|\,t_{fin})\end{aligned} \tag{102}$$

where I defined

$$T_{ij}\,(q,\mathbf{k}\,|\,t) \equiv \int_{t_*}^{t} dt\, T_{ij}\,(t,\mathbf{k})\, e^{iqt}\,, \tag{103}$$

which becomes the actual Fourier transform of the source if the source abruptly starts and ends at t_* and t. Therefore, we have arrived at an expression for the present-day GW spectrum

$$\boxed{\begin{aligned}\Omega_{GW}\,(q) &= 3\mathcal{T}_{GW}\mathcal{I}(q) \\ &= \mathcal{T}_{GW}\frac{q^3}{4\pi^2 m_{Pl}^2\bar{\rho}_* V} \\ &\times\int_{\Omega_k}\frac{d\Omega_k}{4\pi}\left[\Lambda_{ij,kl}(\hat{\mathbf{k}})T_{ij}\,(q,\mathbf{k}\,|\,t_{fin})\,T^*_{kl}\,(q,\mathbf{k}\,|\,t_{fin})\right]_{q=|\mathbf{k}|}\,.\end{aligned}} \tag{104}$$

Redshifting back, i.e. dividing this expression by $\mathcal{T}_{GW}$, and taking (103) to indeed correspond to the full Fourier transform so that the full source duration is considered, Equation (104) reduces to an expression identical to Weinberg's formula (54) , for which we now understand the detailed assumptions that underlay its applicability in a cosmological setting. Indeed, Weinberg's formula in cosmology is now to be understood as giving the present-day GW spectrum redshifted back to the time of production applicable for modes that are well within the present horizon. It should be understood as representing an effective GW energy density obtained after averaging over many oscillations. It is furthermore applicable only in the case that GW production is sufficiently short that expansion can be neglected during its course and when the full source duration has been taken into account in the Fourier transform.

Now we have gained perspective on Weinberg's formula, and with these insights, for historical reasons, I will proceed to also call the present expression (104) (including the factor $\mathcal{T}_{GW}$) Weinberg's formula despite its derivation being fundamentally quite different.

2.2.5 Sound wave production of gravitational waves

In the previous Section 2.2.4, we arrived at an expression for the present GW spectrum in terms of the UETC in Equation (93), namely that

$$\Omega_{GW}(k) = 3\mathcal{T}_{GW}\mathcal{I}(k)$$

where $\mathcal{I}(k)$, defined in Equation (94), was expressed in terms of the source T_{ij} in Equation (102). To arrive at this expression, we departed from a stochastic description and derived Weinberg's formula by making explicit use of that the UETC, in the rare occasion that complete knowledge of the energy-tensor T_{ij} is given, can be exactly separated into two similar multiplicative components depending individually on t_1 and t_2. This meant that $\mathcal{I}$ in (102) could be exactly computed. In the present section, we will instead consider general stochastic sources fully characterized by their UETC and quote characteristic behaviors of the resulting spectra.

For the particular case that the energy-momentum tensor T_{ij} is exactly known, we found in Equation (97) an explicit expression for the UETC, repeated here for ease of reference:

$$E_{\Pi}(t_1, t_2, k) = \frac{k^2}{2\pi^2 V}\int_{\Omega_k}\frac{d\Omega_k}{4\pi}\frac{\Lambda_{ij,kl}T_{ij}(t_1, \mathbf{k})\,T^*_{kl}(t_2, \mathbf{k})}{\bar{\rho}(t_1)\,\bar{\rho}(t_2)}\,.$$

Since $K(t) \equiv \langle\rho_{kin}\rangle(t)/\bar{\rho}(t) = \langle w(t)\gamma^2(t)v^2(t)\rangle/\bar{\rho}(t)$, where average is taken over space, and the part of $T_{ij}(t, \mathbf{x})$ which contributes to anisotropic stress is simply $w\gamma^2 v_i v_j$, it is natural to extract a factor of $K(t)$ and express

$$\frac{T_{ij}(t, \mathbf{x})}{\bar{\rho}(t)} = K(t)\frac{w(t, \mathbf{x})\gamma^2(t, \mathbf{x})v_i(t, \mathbf{x})v_j(t, \mathbf{x})}{\langle w\gamma^2 v^2\rangle(t)} \equiv K(t)\mathcal{T}_{ij}(t, \mathbf{x}) \quad (105)$$

in order to express it as a product of a factor that scales with the overall kinetic energy density, which determines the overall amplitude, and one that does not.

Sound waves as a source of GWs have been extensively studied in the literature (see e.g. [25, 69–74]) since the realization that they last for long durations and consequentially act as a long-lasting source of GWs that may come to dominate the GW production. That their duration is long follows immediately by the assumption of fully linear evolution, predicting that no damping occurs and that the average kinetic energy of the system is constant in time. In fact, the entire statistical description is stationary, implying, in particular, that the UETC is time translation invariant and thus depends only on the time difference $t_- \equiv t - t'$. In a system composed of sound waves, therefore, the kinetic energy is constant, and $K(t) = K = \text{const.}$. With this insight, we make the ansatz

that the UETC is *stationary* so that it can be factorized as [25, 69–73, 75–79]

$$E_\Pi(t_1, t_2, k) = 2k^2 K^2 f(t_-, k) \tag{106}$$

where $t_- = t_2 - t_1$. In this ansatz, K^2 captures overall amplitude, while $f(t_-, k)$ parameterizes the strength of the correlations at different times separated by t_-, i.e. the support, which is assumed stationary.

Then, and again neglecting expansion,

$$\mathcal{I}(t_*, t_{\rm fin}, k) = k^3 K^2 H_*^2 \int_{t_*}^{t_{\rm fin}} dt \int_{t_*-t}^{t_{\rm fin}-t} dt_- \, f(t_-, k) \cos k t_- \,. \tag{107}$$

To make progress from here, the authors of [70, 72] in the context of the sound-shell model assumed that the limits of the second integral in t_- can be extended to $\pm\infty$. This is justified if one assumes that $f(t_-, k)$ has limited support so that it quickly approaches zero for growing $|t_-|$. If this is not the case, they show in [73] that one must impose that the period of the oscillations is much shorter than $t_{\rm sw}$, i.e., $k t_{\rm sw} \gg 1$, or equivalently, $k R_* \gg \sqrt{\langle v_f^2 \rangle}$. They furthermore show that the condition $t_{\rm sw}/R_* \sim 1/\sqrt{\langle v_f^2 \rangle} \gg 1$, which implies that the duration of the sound waves must be long compared to the characteristic scale. Following extending the integral limits to $\pm$ comes the privilege of being able to separate the two integrals since now the second no longer depends on t:

$$\begin{aligned} \mathcal{I}(t_*, t_{\rm fin}, k) &\approx k^3 K^2 H_*^2 \int_{t_*}^{t_{\rm fin}} dt \int_{-\infty}^{\infty} dt_- \, f(t_-, k) \cos k t_- \\ &= k^3 K^2 H_*^2 \, t_{\rm SW} \int_{-\infty}^{\infty} dt_- \, f(t_-, k) \cos k t_- \,, \end{aligned} \tag{108}$$

where I defined the sound wave duration $t_{\rm SW} \equiv \int_{t_*}^{t_{\rm fin}} dt = t_{\rm fin} - t_*$. Evidently, under these assumptions, the GW spectrum grows linearly with the sound wave duration $t_{\rm SW}$. In Chapter 5, this linear growth will be our assumption. Later, in Chapter 6, we depart from this assumption and derive the growth rate associated with a damped source.

Now, assuming a stationary UETC, we need to impose a cutoff on the sourcing time $t_{\rm SW}$. In the fluid, nonlinearities are expected to develop on timescales $t_{\rm nl} \sim R_c/v_c$ [80], where R_c and v_c are characteristic scales and velocities in the system. The characteristic velocity is often taken to be the RMS velocity of the system, $v_c = \sqrt{\langle v_f^2 \rangle}$. In the present case of interest, namely fluid perturbations on the scale of bubbles in first-order PTs, the characteristic scale $R_c = R_* = (8\pi)^{1/3} \max(v_w, c_s)/\beta$ being the typical bubble separation (which we

determine in section 3.1.3) and $\beta/H_* \sim \mathcal{O}(100)$, and v_w and c_s being the bubble wall velocity and fluid speed of sound, respectively. Therefore, it is often assumed that $t_{sw} = t_{nl} \sim R_*/\sqrt{\langle v_f^2 \rangle}$.

As for the remaining t_--integral, they demonstrate in e.g. [73] that it is proportional to R_*/c_s, so that Equation (93) can be parameterized as [25, 52, 69–73, 81, 82]

$$\Omega_{GW}(k) = 3\,\mathcal{T}_{GW}\,\tilde{\Omega}_{GW}\,K^2\,(H_*R_*)(H_*t_{sw})\,S(kR_*)\,, \tag{109}$$

where $\tilde{\Omega}_{GW}$ corresponds to the GW production efficiency which must be determined through some numerical method, and S is a spectral shape normalized such that $\int d\ln k\, S(k) = 1$.

The above results have been obtained under the assumption that cosmic expansion can be neglected. However, if the sound-wave duration is long compared to the Hubble time $1/H_*$, the kinetic energy in the fluid would redshift, leading to a suppression of the GW amplitude. Then, to account for cosmic expansion, one can substitute the linear growth factor $H_*\tau_{sw}$ in Equation (109) by the factor $\Upsilon = H_*\tau_{sw}/(1 + H_*\tau_{sw})$ [73, 78], so as to instead parameterize the present-day GW spectrum as

$$\Omega_{GW}(k) = 3\,\mathcal{T}_{GW}\,\tilde{\Omega}_{GW}\,K^2\,(H_*R_*)\Upsilon(H_*, t_{sw})\,S(kR_*)\,. \tag{110}$$

This result, which will be discussed in slightly more detail in Section 6.2.4 in Chapter 6, allows recovering the effect of expansion on the final GW amplitude.

3

COSMOLOGICAL PHASE TRANSITIONS

In this Chapter, I review cosmological PTs. In Section 3.1, I cover the basic concepts of PTs, including the effective potential, bubbles and their nucleation rate, statistics associated with bubble nucleation and expansion, the Bag model and equation of state, PT strength, and the hydrodynamics of singular bubbles. In Section 3.2, I review GWs from first-order PTs. I provide estimates of key features of the GW signal, discuss the scalar-field contribution to GW production in various models, explore the fluid contribution to GW production in different scenarios, and conclude with a few comments on the observational prospects for GW detection. I am mostly concerned with those aspects of PTs that will eventually be relevant in the context of Higgsless simulations. For a brief review of the general importance cosmological PTs hold in cosmology, I refer the reader to the introductory Section 1.1.1.

3.1 Basic concepts

As the universe undergoes cooling or changes in energy density, regions with lower energy configurations begin to form bubbles of the new phase. These bubbles then grow and expand, eventually dominating the universe's composition as the PT progresses. The dynamics of bubble nucleation and growth play a crucial role in determining the properties of the resulting PT, including its duration, energy release, and impact on the cosmological evolution. Much of the text that follows in this Section will examine these concepts in some detail.

3.1.1 The effective potential

The dynamics of a PT is dictated by some effective potential $V(\phi, T)$, which depends on temperature T and the value of the order parameter ϕ. In our case, ϕ will carry the interpretation of a scalar field, and by virtue of the Electroweak PT being an important candidate, we will often, and interchangeably, call this the Higgs field. While the effective potential is model dependent, and generally derived by computing finite-temperature and higher-loop corrections to the tree-level potential [83, 84], to study the dynamics of a PT in a general sense, it suffices to consider an effective potential which demonstrates the required be-

havior of developing a broken phase true minimum as we decrease T below some threshold.

A prototypical effective potential is of the form [61, 70]

$$V(\phi, T) = \frac{1}{2}\gamma\left(T^2 - T_0^2\right)\phi^2 - \frac{1}{3}AT\phi^3 + \frac{1}{4}\lambda\phi^4\,, \tag{111}$$

where γ, A and λ are positive constants.

As we decrease the temperature, at the temperature $T = T_0$, the second derivative of the potential turns negative at the origin, which becomes an unstable local maxima. If the field configuration is such that part of the field occupies this value, it would smoothly roll to the true minimum of the potential. We therefore assume $T > T_0$ and analyze the potential in this regime where $\phi = 0$ corresponds to either a local or global minimum depending on the temperature.

The behavior of the potential is such that at a temperature

$$T_1 = \frac{T_0}{\sqrt{1 - A^2/(4\lambda\gamma)}} \tag{112}$$

a second minimum emerges at

$$\phi = \phi_1 \equiv AT_1/(2\lambda) \tag{113}$$

(evidently we must also assume $A^2/(4\lambda\gamma) < 1$). Lowering the temperature further, at a critical temperature

$$T_c = \frac{T_0}{\sqrt{1 - 2A^2/(9\lambda\gamma)}}\,, \tag{114}$$

this minimum becomes degenerate with that at $\phi = 0$. Therefore, at temperatures $T < T_c$, it is energetically favorable for the field to attain a configuration around the broken phase minimum $\langle\phi\rangle \equiv \phi_b > 0$ rather than high-temperature symmetric phase $\langle\phi\rangle = 0$. However, since $T > T_0$, a potential wall separates the true minima and so that the field cannot simply roll smoothly to the broken phase. Thus, to acquire the vacuum expectation value (VEV) of the broken phase, the field must locally tunnel through the potential barrier either quantum-mechanically or thermally. An example effective potential of the form (111) illustrating the qualitative behavior as we lower the temperature is shown in figure 1.

With this qualitative picture established, the cosmological PT can proceed through, in a very general sense, the following steps: (1) The high-temperature universe has only one vacuum as per the effective potential and is fully stable. (2) At a temperature T_1, a second non-global minimum emerges. (3) At a critical temperature T_c, a degenerate vacuum emerges. (4) At temperatures below T_c, it is energetically

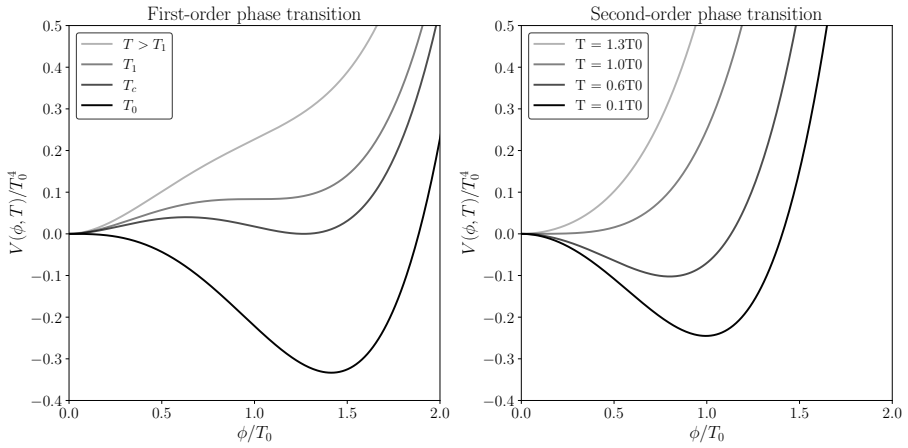

Figure 1: Effective potential for first- and second-order PTs. *Left plot: First-order PT* The effective potential $V(\phi, T)$ of (111) is shown for various temperatures T: $T > T_1$, $T = T_1$, $T = T_c$, and $T = T_0$. At $T > T_1$, the potential has a single minimum at $\phi = 0$. As T decreases, a second minimum appears at $T = T_1$, becomes degenerate at $T = T_c$, and the system transitions to a new global minimum for $T < T_c$. At $T = T_0$, the potential barrier vanishes, and any patch of the remaining symmetric phase will roll smoothly to the broken phase. *Right plot: Second-order PT* The effective potential $V(\phi, T)$ of (111) for $A = 0$ is plotted for $T = 1.4T_0$, $T = 1.0T_0$, $T = 0.6T_0$, and $T = 0.1T_0$. The transition is continuous, with the minimum shifting smoothly from $\phi = 0$ as T decreases.

favorable to attain field VEV $\langle\phi\rangle = \phi_b > 0$. If the barrier is sufficiently weak, the field can tunnel through the potential barrier locally. This leads to the nucleation of *bubbles* that quickly, as they grow from their initial seeds, approach radially symmetric and expanding solutions to the field equations of motion, interpolating between broken phase VEV ϕ_b and symmetric phase VEV $\phi = 0$. The nucleation of bubbles is probabilistic and will be discussed in Section 3.1.2. (5) As these bubbles expand, they collide and eventually fill the entire universe with the symmetric phase, whereby the PT completes. (6) If, however, the PT has failed to complete before $T = T_0$, the remaining patches of the unbroken phase will smoothly roll to the broken phase, thus completing the PT. This general description is true in a non-expanding universe. When cosmic expansion is prevalent, however, for the PT to complete, it is mandated that the bubble nucleation rate $\Gamma(T)$ be larger than the Hubble rate at some point during the critical temperature window $T_0 < T < T_c$.

Above, we have identified two distinct behaviors: (1) when $T > T_0$ and the PT proceeds through tunneling through the potential barrier,

and (2) when $T < T_0$ and the PT proceeds through smooth rolling of the field towards the broken phase.

In case (1), the PT is said to be of *first-order*, and in case (2), it is said to be of *second-order*. For us, only case (1) is of interest as it locally perturbs the universe rather than globally, resulting in, as we shall see, violent dynamics that may produce GWs. Henceforth, in this thesis, even when referred to as just *PT*, it should be understood as being of first order. A visual comparison between a first- and second-order PT is shown in figure 1.

3.1.2 Bubbles and their nucleation rate

The bubble nucleation rate $\Gamma \equiv \mathrm{d}\,\#\,\text{nucleated bubbles}/\,\mathrm{d}V/\,\mathrm{d}t$ in a first-order PT can be shown to be determined by (see e.g. [61])

$$\Gamma \simeq T^4 e^{-S_{3,B}(T)/T} \tag{115}$$

to within an $\mathcal{O}(1)$ factor. In this expression, $S_{3,B}$ is the Euclidean action

$$S_{3,B} = 4\pi \int_0^\infty dr r^2 \left[\frac{1}{2} \left(\frac{d\phi}{dr} \right)^2 + V(\phi, T) \right]_{\phi=\phi_B}, \tag{116}$$

where $V(\phi, T)$ is the finite temperature effective potential introduced in Section 3.1, evaluated at the bounce-solution ϕ_b, which solves the equation of motion

$$\frac{d^2\phi}{dr^2} + \frac{2}{r}\frac{d\phi}{dr} = V'(\phi, T)$$

subject to the boundary conditions

$$\lim_{r\to\infty} \phi(r) = 0,$$

to ensure a finite action, and

$$\left.\frac{d\phi}{dr}\right|_{r=0} = 0,$$

to ensure non-divergence at the origin.

Provided such a solution, the time t_*, or equivalently the temperature T_*, at which the PTs can be said to occur can be determined from the requirement that the probability that one bubble has nucleated in a Hubble volume $V_H = 1/H^3$ up until that moment is unity, i.e.,

$$\int_0^{t_*} dt\, \Gamma\, V_H(t) = \int_{T_*}^\infty \frac{dT}{T} \left(\frac{45}{4\pi^3 g_*(T)} \right)^2 \left(\frac{M_{Pl}}{T} \right)^4 e^{-S_3(T)/T} = O(1)$$

(117)

where in the second equality, radiation domination is assumed. Appreciating that this integral is dominated by its value at production, it can be approximated by,

$$\left(\frac{45}{4\pi^3 g_*(T_*)}\right)^2 \left(\frac{M_{Pl}}{T_*}\right)^4 e^{-S_3(T_*)/T_*} = O(1) \tag{118}$$

which implies for the Euclidean action evaluated at T_* that

$$\frac{S_3(T_*)}{T_*} \simeq 4 \ln \frac{M_{Pl}}{T_*} - 11.4 \tag{119}$$

using that $g_* \simeq 106.75$ in the standard model in the high-temperature limit.

Equipped with the notion of a time and temperature at which the PT takes place, we can Taylor expand the Euclidean action

$$\frac{S_{3,B}(T)}{T} \simeq \left(\frac{S_{3,B}(T)}{T}\right)_{t=t_*} + (t - t_*) \frac{d}{dt}\left(\frac{S_{3,B}(T)}{T}\right)_{t=t_*} \tag{120}$$

and thus define

$$\begin{aligned} \beta &= -\frac{d}{dt}\left(\frac{S_{3,B}(T)}{T}\right)_{t=t_*} = H_* T_* \frac{d}{dT}\left(\frac{S_{3,B}(T)}{T}\right)_{T=T_*} \\ &\approx H_* \left(4 \ln \frac{M_{Pl}}{T_*} - 11.4\right), \end{aligned} \tag{121}$$

where in the second equality, I used that $T \propto 1/a$ such that $dT/T = -H dt$ and in the last approximation that one can very crudely expect that [61]

$$\frac{S_3(T_*)}{T_*} \sim T_* \frac{d}{dT}\left(\frac{S_{3,B}(T)}{T}\right)_{T=T_*}, \tag{122}$$

in order to have some analytical estimate of what value β may take at hand. For then, we can parameterize the bubble nucleation rate

$$\Gamma(t) \simeq \Gamma_* e^{\beta(t-t_*)} \tag{123}$$

and conclude that for $T_* = 100\,\text{MeV}$ ($\sim$ QCD scale), $T_* = 100\,\text{GeV}$ ($\sim$ EW scale), $T_* = 100\,\text{TeV}$, β/H_* take on value 173, 145, and 118, respectively, based on the crude but informative approximation in Equation (121). We will often take $\beta/H_* = 100$ as a benchmark. While this is just an estimate, it gives us the hint that, since β^{-1} sets the timescale associated with the PT's duration, it implies that we can expect the duration to be short compared to the Hubble time $t_{H_*} = 1/H_*$, and consequently that one can ignore Hubble expansion during the course of the PT. This fact

simplifies the numerical implementation of our Higgsless simulations, as we shall see in later Chapters.

The parameterization (123) implies that the bubble nucleation rate increases exponentially with time. Thus, we expect the PT within a given Hubble volume to commence with the nucleation of a single isolated bubble whose nucleation time $t_{n,1}$ is statistically distributed relative to t_*. Since the nucleation probability is still small, some time will pass until the next bubble nucleates, leading to the system being dominated by the first bubble to nucleate. However, bubbles will begin to nucleate at an exponentially increasing rate, quickly bringing the PT to completion, thus converting the entire universe to the new broken phase vacuum.

3.1.3 Bubble statistics

As a result of an exponentially increasing bubble nucleation probability Γ, bubbles of various sizes will be present at each stage of the PT after the second bubble has nucleated. Therefore, it makes sense to derive statistical expectation values for quantities such as the number of nucleated bubbles, their separation, typical size at collision, etc.

In the previous Section, I introduced the notion of a bubble nucleation rate Γ with a simple parameterization in Equation 123. This is, in fact, not a rate per se, but a measure of the probability of nucleation, such that the expected number of bubbles to nucleate in an infinitesimal time-volume element $dt\, d^3\mathbf{x}$ is

$$dP = \Gamma(t)\, dt\, d^3\mathbf{x}. \tag{124}$$

There is a subtlety hidden in this expression, for it assumes that $d^3\mathbf{x}$, indeed, corresponds to a small patch of universe that is not already in the broken phase. As the PT proceeds and bubbles of the broken phase fill the universe, clearly, the amount of remaining volume in the symmetric phase decreases at an exponential rate. Therefore, to adequately determine what is the probability dP, one must include a factor $\mathcal{V}_s(t) \equiv V_s(t)/V$ where $V_s(t)/V$ is the fraction of the volume in the symmetric phase to the total volume, so that when adequately accounting for the decreasing fraction of false vacuum,

$$dP = \mathcal{V}_s(t)\Gamma(t)\, dt\, d^3\mathbf{x}\,. \tag{125}$$

In [85], they show that $\mathcal{V}_s(t)$ is obtained as

$$\mathcal{V}_s(t) = \exp\left[-\frac{4\pi}{3}v_w^3\int_{-\infty}^{t} dt'(t-t')^3\Gamma(t')\right] = \exp\left[-8\pi v_w^3\frac{\Gamma_*}{\beta^4}e^{\beta(t-t_*)}\right], \tag{126}$$

where in the second equality I made use of the parameterization of Γ in Equation (123), $\Gamma(t) = \Gamma_* e^{\beta(t-t_*)}$, to compute the integral.

The total number of nucleated bubbles N_b can now be obtained as

$$N_b = \int dP = \int \mathcal{V}_s(t)\Gamma(t)dt^3\mathbf{x} \tag{127}$$

$$= V\int_{-\infty}^{\infty} dt\, \exp\left[-12\pi v_w^3 \frac{\Gamma_*}{\beta^4} e^{\beta(t-t_*)}\right] \times \Gamma_* e^{\beta(t-t_*)} \tag{128}$$

$$= \frac{\beta^3 V}{8\pi v_w^3}\,. \tag{129}$$

The average bubble separation is therefore given by

$$R_\Delta = \left(\frac{V}{N_b}\right)^{\frac{1}{3}} = (8\pi)^{\frac{1}{3}}\frac{v_w}{\beta} \simeq \frac{3v_w}{\beta}. \tag{130}$$

We are also interested in obtaining an expression for the average bubble radius at collision $\langle r\rangle$. To this end, consider the situation that a point $\mathbf{x}$ is traversed by a bubble wall for the first time at time t. Bubbles responsible for such a traversal could have emerged from nucleation sites a distance of $v_w(t-t_n)$ away, corresponding to a sphere of radius $r = v_w(t-t_n)$ centered on $\mathbf{x}$, which we can think of as the analog of a past light-cone, and just call it *cone*. When promoted to an infinitesimally thin shell, the volume is $dV_\Omega(r) = 4\pi r^2 dr$, so that the probability for nucleation within this shell during the time interval $[t,\, t+dt]$ is $dP = 4\pi r^2\Gamma(t-r/v_w)\,dr\,dt$. We must consider, however, the possibility that another bubble nucleates inside of this past cone. Each such bubble would contribute to that $\mathbf{x}$ is crossed by a bubble wall at an earlier instance, i.e., that $\mathbf{x}$ transitions to the true vacuum earlier than at t, which violates that $\mathbf{x}$ was first crossed at t. We must thus exclude these events, and the probability for this to not have happened is exactly the probability that $\mathbf{x}$ is still in the false vacuum $\mathcal{V}_s(t)$. Therefore, the probability that a point $\mathbf{x}$ is traversed by a bubble wall for the first time by a bubble of radius r is

$$dP = \mathcal{V}_s(t)\Gamma(t-r/v_w)\,dV_\Omega(r)\,dt \tag{131}$$

$$= \exp\left[-8\pi v_w^3\frac{\Gamma_*}{\beta^4}e^{\beta(t-t_*)}\right] \times 4\pi r^2 \times \Gamma_* e^{\beta(t-r/v_w-t_*)}\,dr\,dt\,. \tag{132}$$

Integrating over all times, one finds that

$$\frac{dP(r)}{dr} = \frac{\beta^3}{2v_w^3}r^2 e^{-\beta r/v_w}. \tag{133}$$

Since $\int_0^\infty \frac{dP(r)}{dr}\,dr = 1$, $\frac{dP(r)}{dr}$ can be interpreted as a probability distribution associated with the radius of bubbles traversing the point $\mathbf{x}$.

We can thus compute the expected bubble size R_* as

$$R_* \equiv \langle r \rangle = \int dr\, rP(r) = \frac{3v_w}{\beta}. \tag{134}$$

We see that the expected bubble size R_* and the average bubble R_Δ are similar.

These expressions are true for bubbles. As we shall see in the upcoming Sections, these bubbles induce perturbations in the fluid, which, before colliding with other perturbations, take the shape of self-similar profiles (see Section 3.1.6). If the wall velocity v_w is larger than the speed of sound in the fluid, which we will always assume to be constant $c_s = \sqrt{1/3}$, then the self-similar fluid sound shells have radii $r_{ss} \sim r_b$, for r_b the bubble radius. However, when the wall velocity is below the speed of sound, the self-similar profile front is not determined by v_w but c_s, since this is the speed at which perturbations propagate. Therefore, if we want to characterize the average radius at collision, and if we by collision instead mean when the sound-shells collide, we must make the replacement $v_w \to \max(v_w, c_s)$, so that

$$R_* = \frac{3\max(v_w, c_s)}{\beta}. \tag{135}$$

Furthermore, when $v_w < c_s$, the fluid is heating in front of the bubble wall where bubbles can, in principle, still nucleate. The increase in temperature nevertheless causes a suppression in the bubble nucleation rate, which can be substantial for large α [52]. Then, also the average bubble separation R_Δ receives a similar correction so that in the limit that no bubbles form within the fluid sound shell, [52],

$$R_\Delta = \frac{(8\pi)^{\frac{1}{3}}}{\beta} \max(v_w, c_s). \tag{136}$$

We see that, again, $R_\Delta \approx R_*$, and we will henceforth simply define

$$R_* = R_\Delta = (8\pi)^{\frac{1}{3}} \max(v_w, c_s)/\beta \tag{137}$$

and use the concepts of average bubble separation and average size at collision synonymously.

3.1.4 The Bag model and equation of state

So far, we have been concerned with general aspects of first-order PTs and the dynamics of the scalar field ϕ. Of greatest interest to us, however, is not the scalar field in isolation, but rather the effect it has on its surroundings and, in particular, that it induces perturbations in the primordial radiation fluid.

The energy-momentum tensor of the Higgs field ϕ is given by

$$T^{\phi}_{\mu\nu} = \partial_\mu\phi\partial_\nu\phi - g_{\mu\nu}\left[\frac{1}{2}\partial_\rho\phi\partial^\rho\phi - V_0(\phi)\right], \tag{138}$$

where V_0 is the renormalized vacuum potential. I am aligning the discussion in this Section to arrive at the *Bag equation of state*. In this model, the scalar field is modeled to take on a constant value $\phi = 0$ outside bubbles and $\phi = \phi_b$ inside bubble, corresponding to the false and the true vacuum phases. At the boundary, the field is modeled to discontinuously jump between the phases. Therefore, the time derivative and gradient terms of the pressure contribute only at the bubble wall interface, and we neglect them. We thus arrive at the conclusion that the Higgs field contributes to the total pressure

$$p_\phi(\phi) = -V_0(\phi)\,. \tag{139}$$

The energy-momentum tensor for the fluid, which we assume to be perfect, is given by

$$T^{f}_{\mu\nu} = w_f u_\mu u_\nu - g_{\mu\nu}p_f\,, \tag{140}$$

where w_f and p_f are the fluid enthalpy and pressure, respectively, and u_μ is the four-velocity field of the fluid, related to the three-velocity $\mathbf{v}$ though

$$u_\mu = \frac{(1,\mathbf{v})}{\sqrt{1-\mathbf{v}^2}} = (\gamma,\gamma\mathbf{v}). \tag{141}$$

The total pressure p is determined by the free energy of the system $\mathcal{F} = V$ [86]

$$\begin{aligned} -p &= V(\phi,T) \\ &= V_0(\phi) + V_T(T,\phi) \\ &= V_0(\phi) + T\int\frac{d^3p}{(2\pi)^3}\sum_i N_i \log\left[1 \mp e^{-E_i/T}\right] \\ &= V_0(\phi) + \frac{T^4}{2\pi^2}\sum N_i Y_{b/f}\left(m_i(\phi)/T\right)\,, \end{aligned} \tag{142}$$

where $E_i^2 = p^2 + m_i^2(\phi)$, and

$$Y_{b/f}(x) = \int_0^\infty dy y^2 \log\left[1 \mp \exp\left(-\sqrt{x^2+y^2}\right)\right]\,. \tag{143}$$

The $-/+$ signs correspond to bosons/fermions, and i denotes a specific particle species with N_i the internal degrees of freedom, defined to be negative for fermions in this notation. For small masses $m(\phi) < T$, the function $Y_{b/f}(m_i(\phi)/T)$ is nearly constant and asymptotically

approaches the value $-\pi^4/45$ for bosons and $7\pi^4/360$ for fermions, while for heavier particles $m_i(\phi) >> T$, $Y_{b/f}(m_i/T) \sim \pm \exp(-m_i/T)$ so that their contribution is exponentially suppressed [86]. In the following, therefore, we will neglect particle species that are very heavy compared to T.

It makes sense, therefore, to decompose

$$V_T(T,\phi) = V_{m<T}(T,\phi) + V_{m\sim T}(T,\phi)\,. \tag{144}$$

Define

$$a(T,\phi) = \frac{\pi^2}{30} g_*(T,\phi) \tag{145}$$

where

$$g_*(T,\phi) \equiv \sum_{m_i(\phi)<T} \left[N_i^b + \frac{7}{8} \left| N_i^f \right| \right] \tag{146}$$

is the number of effective relativistic degrees of freedom at temperature T and ϕ, where b/f correspond to bosons/fermions and i denotes a specific particle species with N_i the internal degrees of freedom, and the masses $m_i(\phi)$ depend on ϕ. Then, we can explicitly write

$$V_{m<T}(T,\phi) \equiv \frac{T^4}{2\pi^2} \sum_{m_i(\phi)<T} N_i Y_{b/f}(0) = -\frac{1}{3} a(T,\phi) T^4 \equiv -p_{rad}(T,\phi) \tag{147}$$

while

$$V_{m\sim T}(T,\phi) \equiv \frac{T^4}{2\pi^2} \sum_{m_i(\phi)\sim T} N_i Y_{b/f}(m_i(\phi)) \equiv -\mathcal{P}(T,\phi) \tag{148}$$

carrying contributions only from those degrees of freedom that have masses similar to the temperature T.

We thus decompose the pressure in the fluid as $p_f(T,\phi) = p_{rad}(T,\phi) + \mathcal{P}(T,\phi)$, so that the total pressure

$$p(T,\phi) = p_{rad}(T,\phi) - V_0(\phi) + \mathcal{P}(T,\phi)\,. \tag{149}$$

The enthalpy and energy densities are generally defined as

$$w \equiv T\frac{\partial p}{\partial T}, \quad \rho \equiv T\frac{\partial p}{\partial T} - p\,. \tag{150}$$

The total energy and enthalpy densities are thus given by

$$\begin{aligned}\rho(T,\phi) &= T\frac{\partial p_{rad}(T,\phi)}{\partial T} - p_{rad}(T,\phi) + T\frac{\partial \mathcal{P}(T,\phi)}{\partial T} - \mathcal{P}(T,\phi) + V_0(\phi) \\ &= \rho_{rad}(T,\phi) + V_0(\phi) + T\frac{\partial \mathcal{P}(T,\phi)}{\partial T} - \mathcal{P}(T,\phi)\,,\end{aligned}$$

(151)

where I defined $\rho_{\rm rad} \equiv a(T,\phi)T^4$, and

$$w = \rho(T,\phi) + p(T,\phi) = \rho_{\rm rad}(T,\phi) + p_{\rm rad}(T,\phi) + T\frac{\partial \mathcal{P}(T,\phi)}{\partial T}\,. \quad (152)$$

To summarize, we have found for the total pressure, energy, and enthalpy densities that

$$\boxed{\begin{aligned} p(T,\phi) &= p_{\rm rad}(T,\phi) - V_0(\phi) + \mathcal{P}(T,\phi) \\ \rho(T,\phi) &= \rho_{\rm rad} + V_0(\phi) + T\frac{\partial \mathcal{P}(T,\phi)}{\partial T} - \mathcal{P}(T,\phi) \\ w(T,\phi) &= \rho_{\rm rad}(T,\phi) + p_{\rm rad}(T,\phi) + T\frac{\partial \mathcal{P}(T,\phi)}{\partial T}\,. \end{aligned}} \quad (153)$$

Now, if there are no particles with masses $m_i(\phi) \sim T$, then $\mathcal{P}(T,\phi)$ vanishes. If there are particles with $\mathcal{P}(T,\phi) \sim T$, under the assumption that those degrees of freedom are outnumbered by the light degrees of freedom, $\mathcal{P}(T,\phi)$ can be neglected. Therefore, if we define $V_0(0) = \epsilon$ and $V_b(\phi) = 0$, and following standard notation, denote the symmetric phase ($\phi = 0$) by subscript $+$, and the broken phase ($\phi = \phi_b$) by subscript $-$, the pressure, energy, and enthalpy densities outside bubbles become

$$\boxed{p_+ = \frac{1}{3}a_+T_+^4 - \epsilon, \quad \rho_+ = a_+T_+^4 + \epsilon, \quad w = \frac{4}{3}a_+T_+^4\,,} \quad (154)$$

where $a_+ = a(T_+,\phi_b)$, while inside bubbles,

$$\boxed{p_- = \frac{1}{3}a_-T_-^4, \quad \rho_- = a_-T_-^4+, \quad w = \frac{4}{3}a_-T_-^4\,,} \quad (155)$$

where $a_- = a(T_-,\phi = 0)$. Equations (154) and (155) constitute the *Bag equation of state* [86] in the *Bag model* originally introduced in [87].

Henceforth in this thesis, I will abide by the Bag model, entailing that ϕ is either 0 outside of bubbles and ϕ_b inside, with a discontinuity at the bubble wall, whereby the the pressure, energy, and enthalpy densities are given by the equation of state (154) and (155) whose validity I will always assume.

The total energy-momentum tensor is the sum of the two components

$$T_{\mu\nu} = T^{\phi}_{\mu\nu} + T^{f}_{\mu\nu}\,. \quad (156)$$

The equations of motion are given by the total energy-momentum conservation

$$\partial^\mu T_{\mu\nu} = \partial^\mu T^{\phi}_{\mu\nu} + \partial^\mu T^{f}_{\mu\nu} = 0\,. \quad (157)$$

In the Bag model, however, ϕ experiences a discontinuity on the bubble wall but is otherwise static. Thus, akin to the pressure p_ϕ, we neglect the kinetic and gradient terms so that the total energy-momentum tensor becomes that of a radiation-dominated fluid but with a pressure contribution $-V_0 = -\epsilon$ in the symmetric phase. Thus, with $w = w_{\text{rad}}$ and $p = p_{\text{rad}} - \epsilon$ denoting the total enthalpy end pressure, the energy-momentum tensor for the system becomes

$$T_{\mu\nu} = w u_\mu u_\nu - g_{\mu\nu} p \,. \tag{158}$$

and the equations of motion reduce to

$$\partial^\mu T_{\mu\nu} = \partial^\mu (w u_\mu u_\nu - g_{\mu\nu} p) \,, \tag{159}$$

which constitute the equations that we will eventually implement on the lattice in Chapter 5 to numerically solve for the fluid dynamics subject to expanding bubbles. To go beyond the bag model, see, e.g., [88].

3.1.5 Phase transition strength

The strength of a PT α parameterizes the ratio of available latent heat, i.e. vacuum energy, to the energy density of radiation.

For the Bag equation of state, the PT strength can thus be characterized as the ratio of vacuum energy density ϵ to that of radiation in the symmetric phase immediately before the PT (sub/sup-script s), namely

$$\alpha_\epsilon \equiv \frac{V_0(0) - V_0(\phi_b)}{\rho_{\text{rad}}} = \frac{\epsilon}{\rho^s_{\text{rad}}} = \frac{4\epsilon}{3w_s}. \tag{160}$$

This definition has been brought forward in, e.g., [52, 86].

Alternatively, a more general approach states that the relevant quantity for the determination of the PT strength α, is the difference $D\theta$ in trace of the energy-momentum tensor $\theta = g_{\mu\nu} T^{\mu\nu} = \rho - 3p$ between the two phases evaluated at the temperature of the symmetric phase (see e.g. [89])

$$\alpha_\theta = \frac{D\theta}{3w_s} \tag{161}$$

We have that $D\theta = 4\epsilon$, whereby $\alpha_\theta = \frac{4\epsilon}{3w_s} = \alpha_\epsilon$. Similarity between the two is granted by the Bag equation of state. Henceforth, whenever the strength of the PT is referred to, we will simply denote it α.

3.1.6 Hydrodynamics of singular bubbles

In this thesis, we are mostly concerned not with the dynamics of ϕ but with the primordial fluid, which is assumed to fill the universe

as the PT occurs. In this Section, I will review basic results from the literature concerning the perturbations in the fluid associated with the conversion of vacuum energy into thermal and kinetic energy. These results will be important later in Chapter 5 as they serve as a testing ground for the accuracy of the simulations.

In Section 3.1.4, we saw that the energy-momentum tensor is given by that of a perfect fluid with a pressure contribution from the vacuum, Equation (158),

$$T_{\mu\nu} = w u_\mu u_\nu - g_{\mu\nu} p \,,$$

with pressure p, density ρ, and enthalpy w given by the Bag equation of state Equations (155) and (154).

Since bubbles are radially expanding spherically symmetric solutions to the field equations of motion, the perturbed fluid solution must obey the same symmetry. Furthermore, since there is no intrinsic length scale in the problem at a macroscopic level beyond the bubble size itself, the solutions are self-similar in the radial coordinate $\xi \equiv r/t$. Note that with this definition, at the bubble interface, $\xi_w = v_w$, so that we may interchangeably denote the wall velocity either v_w or ξ_w, depending on the context.

The relativistic hydrodynamical equations for the fluid are derived from the conservation law $\partial^\mu T_{\mu\nu} = 0$. In [86], the radial equation of motion for the radial velocity field $v(\xi)$ is found to be

$$2\frac{v}{\xi} = \gamma^2 (1 - v\xi) \left[\frac{\mu^2}{c_s^2} - 1 \right] \partial_\xi v, \tag{162}$$

where μ is the Lorentz-transformed fluid velocity

$$\mu(\xi, v) = \frac{\xi - v}{1 - \xi v} \,, \tag{163}$$

and $c_s = \sqrt{1/3}$ the speed of sound which is assumed constant. Equation (162) can be solved in full generality to obtain solutions $v(\xi)$. In fact, since $v(\xi)$ is double-valued, the authors of [86] instead solve for $\xi(v)$, to obtain the solutions in Figure 2 which I adopt here without modification.

Thus far, Equation (162) with corresponding solutions in Figure 2 are derived in all generality. In the physical situation of interest, it is clear that both at some distance in front of and behind the bubble wall $v(\xi)$ must go to zero. To accommodate this requirement, self-similar velocity profiles developing around expanding bubbles must evidently be constructed by patching together part of the solutions in Figure 2 with the trivial solution $v(\xi) = 0$ or with a different part of itself. This patching will lead to discontinuities in hydrodynamical quantities, which usually occur at the bubble wall interface modeled as a step function

in the Bag model. To match the solution across the the bubble wall and developed shocks, one employs matching conditions. A detailed account on these and how the self-similar velocity profiles are constructed is found in [86]. In the present context, it suffices to conclude that analytically derived profiles are well defined and obtainable once the strength of the PT and the wall velocity v_w have been specified. Once the velocity profile $v(\xi)$ has been obtained, the corresponding self-similar enthalpy profile can subsequently be computed as [86]

$$w(\xi) = w_0 \exp\left[\int_{v_0}^{v(\xi)} \left(1 + \frac{1}{c_s^2}\right) \gamma^2 \mu dv\right] . \tag{164}$$

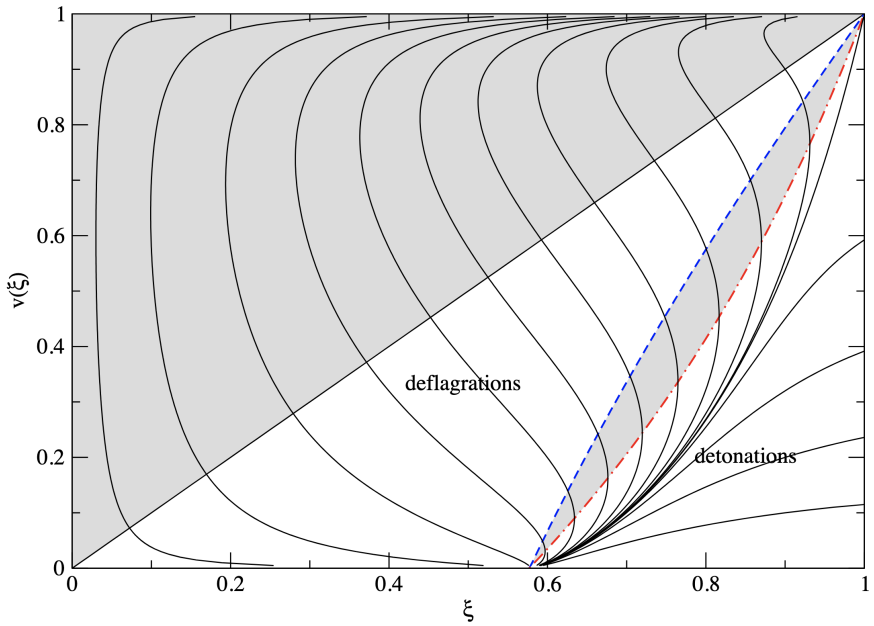

Figure 2: Figure adopted from [86]. Fluid velocity profiles $v(\xi)$ in the bubble center frame (where $c_s^2 = \frac{1}{3}$). Detonation curves (dash-dotted line) start below $\mu(\xi, v) = c_s$ and end at $(\xi, v) = (c_s, 0)$. Deflagration curves (dashed line) start below $v = \xi$ and end at $\mu(\xi, v)\xi = c_s^2$, representing the shock front. Consistent solutions do not exist in the shaded regions.

These self-similar profiles can qualitatively be divided into three distinct types. When the wall velocity is below the speed of sound, the self-similar solution is a *deflagration*, with fluid velocities vanishing behind the wall but with a shock wave in front of it. When the wall velocity is larger than the speed of sound but smaller than the Jouguet velocity ξ_J [86],

$$\xi_J \equiv \frac{\sqrt{\alpha\,(2 + 3\alpha)} + 1}{\sqrt{3}\,(1 + \alpha)} \tag{165}$$

the solution is a hybrid, which consists of a shock wave in front of the bubble and a rarefaction wave behind it. These solutions are called *hybrids* due to their hybrid nature. Finally, when the wall velocity is greater than both ξ_J and c_s, the solution is a *detonation*, for which the fluid in front of the bubble has no time to react to the incoming bubble wall and remains at rest while a rarefaction wave develops behind the wall.

In Figure 3, I plot self-similar velocity and enthalpy profiles for strengths $\alpha = 0.0046$, $\alpha = 0.05$, and $\alpha = 0.5$ corresponding to weak, intermediate, and strong PTs respectively, for selected wall velocities in the range $[0.32, 0.8]$. For these strengths, the Jouguet velocities are $\xi_J = \{0.63, 0.73, 0.89\}$ respectively. Note, therefore, that only for $\alpha = 0.0046$ and $\alpha = 0.05$ do all three types of solutions develop, while for $\alpha = 0.5$, only deflagrations and hybrids develop. These choices of parameters correspond to those for which I will run simulations, as presented in Chapter 5 (weak and intermediate) and Chapter 6 (weak, intermediate, and strong). Having at hand self-similar profiles obtained semi-analytically thus provides an invaluable means of evaluating the performance of our simulations as it allows us to directly compare simulations of isolated bubbles with the expected self-similar behavior and thus study to what degree these analytical profiles are reproduced.

We are ultimately interested in the fluid dynamics in first-order PTs because of the GW production potential, which may serve us well as a window to new physics at uncharted energy scales. GW production is first and foremost not determined by the vacuum energy density ϵ, but by what fraction of this energy is transferred to the fluid in the form of kinetic energy since only this energy component contributes to the anisotropic stress, and consequently GW production. This energy fraction is often denoted $\kappa = \rho_{\rm kin}/\rho_{\rm vac}$, where $\rho_{\rm kin} \equiv \langle w\gamma^2 v^2 \rangle$ is the average kinetic energy density in the system and, in our case, $\rho_{\rm vac} = \epsilon$. The quantity κ is often called the *vacuum energy transfer efficiency*, as it quantifies what fraction of the vacuum energy is converted into kinetic energy of the fluid.

For isolated self-similar bubbles, integrating the kinetic energy in the self-similar profile and dividing by the bubble volume, the corresponding vacuum energy transfer efficiency is computed as [86]

$$\kappa_\xi \equiv \frac{3}{\epsilon \xi_w^3} \int w(\xi) v^2(\xi) \gamma^2(v) \xi^2 \, d\xi \,, \tag{166}$$

which I illustrate in figure 4. I use subscript $_\xi$ to indicate its definition from self-similar profiles.

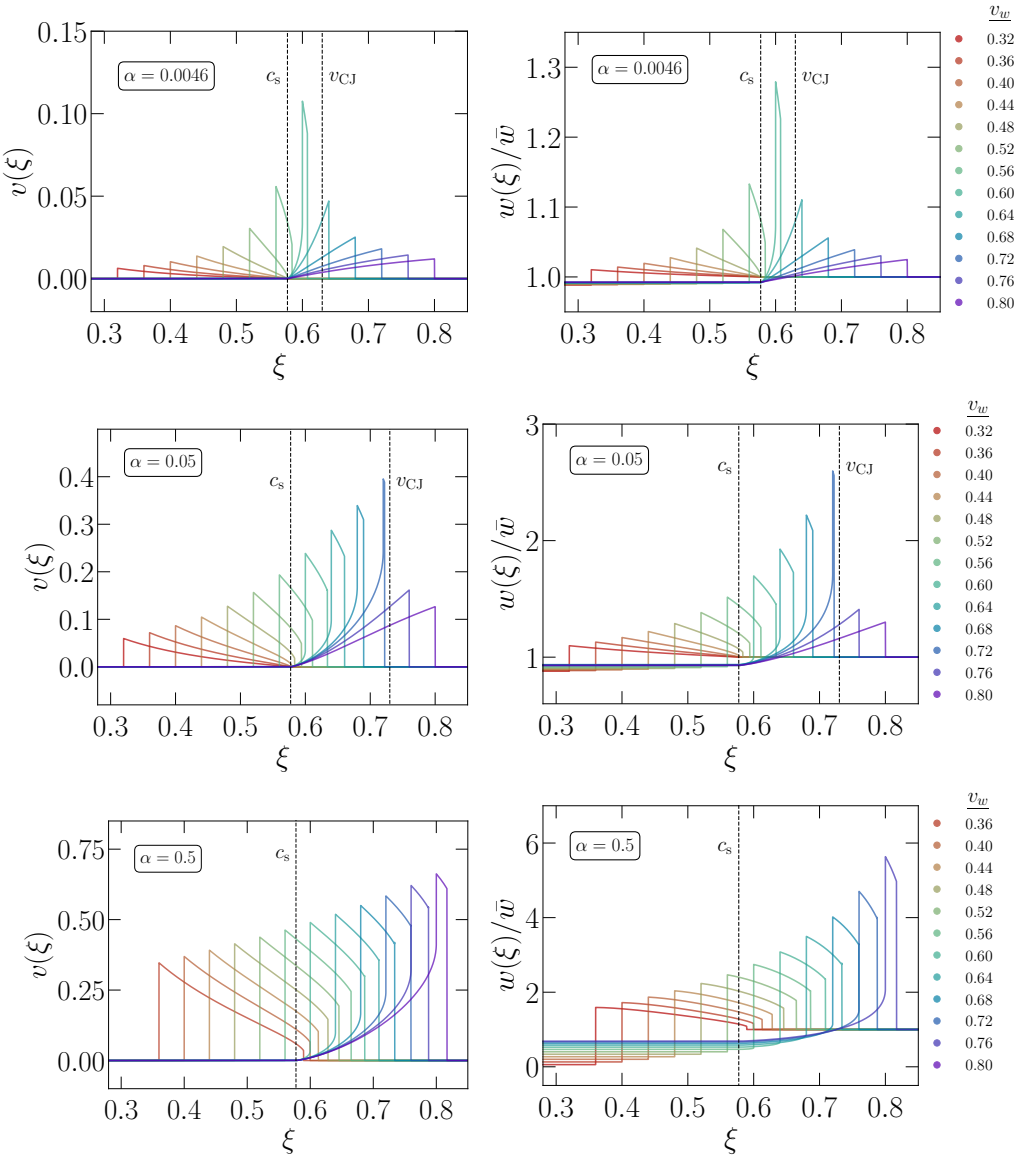

Figure 3: Self-similar profiles of the fluid velocity (left panels) and enthalpy (right panels) perturbations for a single bubble nucleated at $t = 0$ as a function of the self-similar coordinate $\xi \equiv r/t$. The profiles are shown for weak (upper panels), intermediate (middle panels), and strong (lower panels) PTs, across the range of wall velocities used in the parameter scan of our simulations.

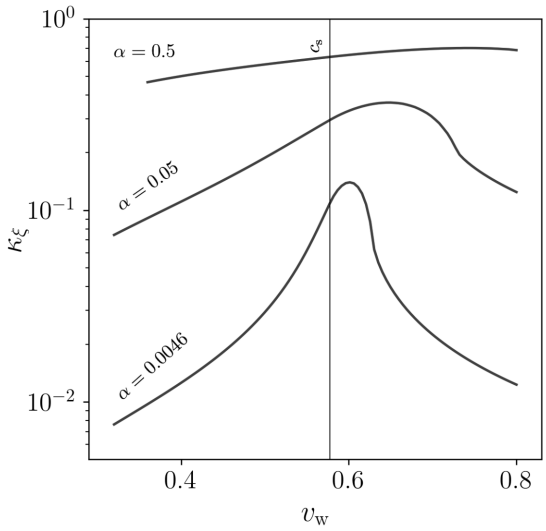

Figure 4: The vacuum energy transfer efficiency κ_ξ for single isolated bubbles with developed self-similar fluid profiles, for weak ($\alpha = 0.0046$), intermediate ($\alpha = 0.05$), and strong ($\alpha = 0.5$) PTs.

Another useful quantity is the fraction of kinetic energy to the total energy density ρ_{tot}, which relates to κ and the strength α as

$$K_\xi \equiv \frac{\rho_{kin}}{\rho_{tot}}, \tag{167}$$

which for the self-similar profiles is defined as

$$K_\xi = \frac{\kappa_\xi \alpha}{1+\alpha} \tag{168}$$

where the densities are computed over the volume of the true vacuum.

We have now covered the essential concepts concerning first-order PTs to understand the contents of forthcoming Sections and Chapters in context. Before proceeding to deliver an account of my original research, however, I will review some of the efforts that have already been made to understand the GW production associated with such PTs in the remaining Sections of this Chapter.

3.2 GWs from a first-order phase transitions

We begun this Chapter by discussing the dynamics of a scalar field tunneling through the potential barrier in an effective potential leading to a first-order PT. We saw how the PT proceeds through the nucleation and expansion of bubbles that expand and subsequently collide. In the simplest case, the PT occurs in vacuum, in which case the bubbles experience no interactions with the surroundings and, consequently,

no friction. With no resistance to the bubble growth, the bubble wall accelerates towards the speed of light, whereby the energy released by the PT is fully carried by the wall. Upon bubble collision, spherical symmetry is broken, a significant quadrupole moment in the energy distribution is generated, and GW production occurs.

In a more realistic scenario, and indeed the scenario with which this thesis is concerned, the PT does not occur in vacuum but in a fluid during the epoch of radiation domination. The expanding bubbles thus experience friction with the fluid and reach a terminal expansion velocity. In this case, since the energy of the bubbles scales with their squared radius, while the released vacuum energy scales with their radius cubed, the vacuum energy is almost exclusively transferred to the fluid, whereby the fluid dominates subsequent GW production.

The GW spectrum produced by the dynamics of a first-order PT is largely determined by a few key parameters with which we have already acquainted ourselves. These are T_*, β, α, and v_w. Let me briefly describe their respective roles:

1. **The temperature at which the first-order PT occurs,** T_*: This is defined as the temperature at which the integrated probability that a bubble has nucleated inside a Hubble patch is 1. It sets the scale of the PT. At this temperature, the Hubble expansion $H_*(T_*)$, which determines the maximum spatial correlation scale and is thus related to the expected frequency peak of the GW spectrum, is directly determined from $\rho_{\text{rad}}(T_*)$ using the Freedman equation. We will assume that T_* is sufficiently close to the temperature at which GW production commences at collision time so that T_* characterizes the energy scale at initial GW production.

2. **The inverse duration of the PT,** β: Defined and estimated in Equation (121), β determines the duration of the PT and allows determining the typical bubble size or average bubble separation R_* as in Equation (135). This parameter is important for characterizing the GW spectrum as it corresponds to the largest characteristic length of features that are expected to carry a substantial. This scale thus relates closely to the GW spectrum peak location. R_* furthermore parameterized the overall amplitude of the GW spectrum, e.g., as in the case of sound waves in equation (110).

3. **The strength parameter,** $\alpha = \rho_{\text{vac}}/\rho^*_{\text{rad}}$: This ratio describes the strength of the PT, where ρ_{vac} is the vacuum energy density and ρ^*_{rad} is the radiation energy density at T_*. Generally, the larger α, the larger the GW spectrum amplitude since there is more energy available. Furthermore, α, together with v_w, determines

the vacuum energy transfer efficiency κ, and, as can be seen in Figure 4, the larger α the larger the transfer efficiency. Thus, the overall GW amplitude is enhanced significantly as the strength does.

4. **The wall velocity,** v_w: This parameter describes the speed at which the bubble walls expand and critically determines the nature of the hydrodynamic solutions. The wall velocity is thus important in that it determines, together with the strength α, the energy budget of the PT characterized by κ. Determining the wall velocity in PTs requires complex out-of-equilibrium calculations involving solving Boltzmann and scalar field equations (see, e.g., [90, 91]). These calculations depend on the specifics of the scalar sector and how particles obtain masses through their coupling to the scalar field responsible for the PT, rendering results highly model-dependent and warranting a case-by-case approach. In this thesis, we will always treat v_w as an input parameter and leave its determination from fundamental theory as a task for other scientific explorations.

While the specific values of these parameters must be determined from first principles and the particle physics model in question, the main features of the GW signal can be described in terms of these parameters in a phenomenological, largely model-independent way. In the Higgsless simulations, we will solve the equations of motion in a way that both H_*, which is determined from T_*, and β, are scaled out. We are thus left with only parameters α and v_w, spanning a two-dimensional parameter space. The gravity of the above statement is thus evident, for if the main features and overall expected GW signal are captured by the remaining parameters α and v_w, then, since the parameter space over which to scan to characterizes all (non-vacuum) first-order PT GW signals is only two-dimensional, it appears conceivable that soon, we have reasonably accurate GW spectrum estimates at hand for a large region of this parameter space. This, in fact, is a major scientific objective of the present thesis.

3.2.1 Estimates of some GW signal features

In this Section, I wish to demonstrate how the GW spectrum peak frequency and amplitude can be estimated from simple arguments.

3.2.1.1 GW spectrum peak frequency

In Section 2.2.2, we obtained expressions relating the wavenumbers and GW spectrum at production time to their redshifted present-time

counterparts. Normalizing k_* to β, a fundamental scale in the problem, and β to H_*, the Hubble constant at the PT, the present-day frequency can be obtained by rewriting Equation (169) as

$$f_0 = 2.63 \cdot 10^{-6}\,\mathrm{Hz} \times \left(\frac{k_*}{\beta}\right)\left(\frac{\beta}{H_*}\right)\left(\frac{g_*}{100}\right)^{1/6}\left(\frac{T_*}{100\mathrm{GeV}}\right). \quad (169)$$

A typical wavenumber at production is $k_* = \beta$, so that the GW spectrum peak generally occurs at $k_{peak} = \text{few} \times \beta$. Furthermore, using that, generally, we expect $\beta/H_* \sim 100$, and $g_* \approx 100$ near $T_* = 100\,\mathrm{GeV}$ or otherwise that we can neglect the weak dependence, the redshifted GW spectrum peak occurs at

$$f_0^{\mathrm{peak}} \sim \mathcal{C}\, 10^{-3}\,\mathrm{Hz} \times \left(\frac{T_*}{100\mathrm{GeV}}\right). \quad (170)$$

where $\mathcal{C}$ is expected to take values in the range $[0.1, 10]$. Thus, for a PT occurring at the EW scale $T_* \sim 100\,\mathrm{GeV}$, the peak should occur at frequencies between 0.1 mHz to 10 mHz, which excitingly overlaps substantially with the sensitivity band of LISA [48]. If the PT instead occurs around the QCD scale $T_* \sim 100\,\mathrm{MeV}$, the peak frequency should occur at frequencies between 0.1 μHz to 10 μHz. Generally, the peak position scales linearly with the PT temperature T_*, so that the further back in the past the PT occurred, the higher the peak frequency.

3.2.1.2 GW spectrum amplitude

We found in Section 2.2.2 that the present day GW spectrum is given by Equation (66)

$$h^2\Omega_{GW}^0(k) = 1.65 \times 10^{-5}\left(\frac{100}{g_*(T_*)}\right)^{1/3}\left(\frac{1}{\bar{\rho}}\frac{d\rho_{GW}(k)}{d\log k}\right)_*,$$

so that using $h \sim 0.7$,

$$\Omega_{GW}^0 \sim 3 \cdot 10^{-5}\Omega_{GW}^*. \quad (171)$$

Now, assuming that a GW source lasts over some time Δt and that a fraction $\mathcal{K} = \rho_{source}/\rho_c^*$ of total energy density contributes to GW production, then the energy fraction in GWs at production time parametrically becomes

$$\Omega_{GW} \sim 10^{-5}\,(\mathcal{K}\Delta t H_*)^2. \quad (172)$$

In Equation (72), it is evident that the sourcing term on the RHS carries contributions only from the anisotropic part of the energy and momentum. To be more precise, we saw in Section 3.1.6 and Equation (168)

that a fraction $K_\xi = \kappa_\xi \alpha/(1+\alpha)$ of the total energy eventually takes the form of fluid kinetic energy. For $\alpha = 0.001$, a typical value $\kappa \sim 0.01$ [86], so that $\mathcal{K}^2 \sim 10^{-8}$. Only a fraction of this contributes to anisotropic stress. Therefore, plausible values of $\mathcal{K}$ are substantially lower than 1.

If GW production is dominated by the collision phase of a PT and hence $\Delta t \sim 1/\beta$, we see that

$$\Omega_{GW} \sim 10^{-5} \left(\mathcal{K} H_*/\beta\right)^2 \sim 10^{-9} \mathcal{K}\,, \tag{173}$$

taking $\beta/H_* \sim 100$. For vacuum PTs, assuming that the scalar field is quickly dampened after collision, this would give an adequate estimate provided $\mathcal{K}$ is known.

In recent studies (e.g., [1, 3, 25, 69, 71]), including the works which I am to present in this thesis, it has been highlighted that sound waves propagating through the fluid can persist much longer than β^{-1}. In particular, in these works, and as we shall see in this thesis, it is demonstrated that sound waves can endure for timescales on the order of H_*^{-1} before being dissipated by nonlinear dynamics such as shocks and turbulence, resulting in an enhancement of Ω_{GW} by a factor of β/H_*, leading to an enhancement of the GW spectrum by two to three orders of magnitude.

When the sourcing time scale is longer, as is expected for sound waves in the fluid following a PT, say $\Delta t \sim 1/H_*$, then the narrow support of the UETC means that the source is expected to grow linearly rather than quadratically with time. Thus, as compared to the short-lasting source, an estimate for the sound-wave production of GWs instead reads

$$\Omega_{GW} \sim 10^{-5} \mathcal{K}^2 H_*/\beta\,, \tag{174}$$

which qualitatively explains the factor of (β/H_*) enhacement.

3.2.1.3 GW spectrum slopes

The UETC of anisotropic stresses in Equation (87) is uncorrelated at scales beyond causality, i.e., on super-Hubble scales at the time of GW production. Therefore, we expect that $E_\Pi \propto k^2$ on super-Hubble scales, resulting in the GW spectrum scaling as k^3 in the IR. As long as the UETC remains uncorrelated, this k^3 scaling may persist. However, as we approach the system's correlation scale β^{-1}, correlations will inevitably cause deviations.

On general grounds, the only statement that can be made about the UV slope of the GW spectrum is that the total integrated GW energy must be finite, which imposes a limit on the UV slope. The exact dependence on the UV slope is determined by the detailed dynamics responsible for the UETC, which must be established through analytical or numerical methods.

3.2.2 GW spectrum contributions

So far, we have discussed short-lasting sources from the initial collision phase and long-lasting sources from sound waves or, more generally, compressional or acoustic modes. We mentioned the dissipation of the sound waves due to nonlinear dynamics such as shocks and turbulence. In fact, turbulence can itself be a significant source of GWs [75, 77, 92–96].

Therefore, in a first-order cosmological PT, the GW sources constitute bubble collisions, sound waves or compressional modes, and turbulence so that the GW spectrum can be decomposed as [97]

$$\Omega_{\mathrm{GW}} = \Omega_{\mathrm{coll}} + \Omega_{\mathrm{sw}} + \Omega_{\mathrm{turb}} \,. \tag{175}$$

In the case of long-lasting sound waves, we saw that Ω_{coll} is subdominant. If PTs are not too strong, the dynamics are largely linear [1], allowing to measure Ω_{sw} relatively well modulo the uncertainty associated with the sound-wave source duration. This is one of the main accomplishments in [1] on which Chapter 5 is based.

In weak-to-intermediate PTs (see Chapter 5 for a definition), fully capturing the PT into the nonlinear and turbulent regime requires running simulations for a long time, which may be practically impossible. Therefore, capturing Ω_{turb} is not straightforward in most cases. For strong PTs, however, the shock formation time and the time it takes for turbulence to develop are well within simulation reach [3], making it plausible to model the PT from a system dominated by compressional modes to a system possibly dominated by compressional and vortical turbulence. In Chapter 6, which is based on [3], we observe clear signs of nonlinear dynamics and turbulence. However, we attempt not to separate the contributions to the GW production into Ω_{sw}, Ω_{turb}, but instead introduce a way to model the total GW production from a source experiencing nonlinear energy dissipation in a general sense without the need to disentangle the respective contributions.

3.2.2.1 The scalar-field contribution to GW production

The production of GWs from the bubbles themselves, while not the primary focus of this thesis, has played a historically important role in the field. Therefore, this thesis would not be complete without at least a brief review of this topic. Accordingly, in this Section, I will review a few approaches through which the GW spectrum arising from scalar field bubble collisions can estimated.

ENVELOPE APPROXIMATION Historically, directly attempting to numerically solve for the scalar-field evolution in a many-bubble sys-

tem was infeasible due to the excessive computational resources it required. In 1992, however, Kosowsky, Turner, and Watkins successfully obtained through numerical means [19] the GW production from two colliding bubbles. This feat was made possible by exploiting the $O(2,1)$ symmetry possessed by the two-bubble system, which even then proved exceedingly difficult with the computational resources of that day. The most general case of many bubbles in three dimensions has no symmetries and was far beyond computing capabilities at the time. Just like we argued in the motivation for the Higgsless approach, the problem was difficult numerically because of the presence of two separate scales: the bubble wall thickness at nucleation is small compared to the size of bubbles at collision. Additionally, highly relativistic walls are made thinner due to Lorentz contraction, which further separates the scales.

A critical observation concerns the insensitivity of the GW production to the fine-grained details of the bubble dynamics. In particular, they found that the GW spectrum and its production efficiency depend only on the overall features of the PT and bubble collisions, such as the strength of the PT and the size of bubbles at the end of their simulations. Despite the scalar-field dynamics after bubble collisions being quite intricate, the overall production of GW radiation from the small-scale motions adds incoherently and is subdominant, they concluded.

The insensitivity to the small-scale dynamics prompted the authors to develop the *envelope approximation* [21]: bubbles are approximated as infinitely thin shells, and in the regions where bubbles overlap, the bubble wall is completely ignored as a contribution to the anisotropic stress. Only the envelope, i.e., the uncollided part of the bubble wall network, is considered. This approximation successfully reproduced previous numerical results for two-bubble systems and was thus put to test in systems with hundreds of bubbles.

The envelope approximation provides a simplified yet efficient approach to estimate the GW signal generated from the scalar field dynamics during first-order PTs. The approximations that enter the envelope approximation are, to summarize:

1. The energy is concentrated in the thin walls of the expanding bubbles (thin-wall approximation).

2. Upon collision, the walls of the bubbles disappear instantaneously, and only the uncollided parts (i.e., the envelope) continue to source gravitational waves, while the contribution from the collided regions ceases

The envelope approximation was additionally exploited in the numerical simulations of [23], and it was realized in [98] that under the

stipulated assumptions, the envelope contribution to GWs can be obtained analytically.

Above works resulted in the prediction that (in the envelope approximation), the spectrum of GWs is characterized by a peak frequency depending on the bubble expansion velocity. The spectral shape is characterized by a q^3 growth at small frequencies and a q^{-1} decrease at high frequencies. For analytical fits to the data, I refer the reader to [98].

BULK FLOW MODEL The development of the envelope approximation was a significant milestone in understanding GW production during first-order PTs. A natural extension of the envelope approximation is to assume that upon colliding, the infinitely thin bubble wall interface does not instantaneously vanish but dampens over time. This refined model was proposed in [99] in which the authors obtained GW production results analytically, which were subsequently confirmed in numerical simulations [24]. Note that while in this Section we take the bulk-flow model to model the bubbles, it can similarly be interpreted as a model of the fluid and sound wave provided in the limit of very thin sound shell profiles [24, 99]. In fact, this was the main motivation for the bulk flow model in [24]. For if the thin shells are freely propagating after the collision, they decay as $\propto 1/r^2$ where r is the expanding radius of the shells, a behavior which can be captured in the bulk-flow model. Note, however, that in the bulk flow model, $r \propto v_w$, whereas after the collision, the sound shell wave propagates with the sound speed c_s. For $v_W \sim c_s$, the bulk flow model should nevertheless give reasonable estimates and capture the qualitative features.

Unlike the envelope approximation, the bulk flow model reveals that the GW spectrum experiences an IR flattening. Specifically, the spectrum shifts from the $\propto q^3$ behavior seen in the envelope approximation to q^a, where $a \in [1, 3]$, depending on the decay time of the collided bubble regions. It is also found that in the UV, the GW spectrum scales as q^{-3}. Additionally, the peak position shifts from smaller to larger scales as the decay time of the collided regions increases, with a change by a factor of approximately two in the long-lasting limit.

SCALAR FIELD LATTICE SIMULATIONS While the envelope approximation and bulk flow model provide accessible estimates for GW production within certain physical scenarios, advancements in computational resources have paved the way for more precise predictions. Rather than relying on these approximations and assumptions, solving the scalar field evolution directly on the lattice with high precision allows for capturing subtle, fine-grained dynamical features and accu-

rately modeling the full nonlinear dynamics, leading to more reliable and detailed GW predictions.

Such attempts were made in [100], where results from large-scale numerical simulations of scalar-field dynamics and GW production are presented. It was found that the gravitational wave power spectrum in the IR is consistent with a q^3 scaling as predicted by causality and found in the envelope approximation. However, the dynamic range in their simulations is insufficient to produce an independent estimate. At large frequencies in the UV, the GW spectrum decreases as $q^{-1.5}$, as compared to q^{-1} in the envelope approximation and q^{-3} in the bulk flow model. They also find that the peak of the power spectrum is shifted to slightly larger scales, consistent with the bulk flow model. Accounting for the full scalar field dynamics, they additionally observe a linearly growing UV feature. This feature is observed to peak at wave numbers corresponding to the bubble wall thickness, but it has a negligible contribution to the total energy in gravitational waves in most scenarios of interest.

In Table 1, I summarize the various scaling behaviors observed in different models for the scalar field contribution to the GW production. It is worth noting that a single scale, associated with the typical bubble bubble size, or equivalently the PT duration, divides the IR and UV regions, with the Higgs scale residing deeply in the UV and far beyond the reach of any simulation. Both the envelope and the scalar lattice models concur on the IR q^3 scaling, which is supported by causality [76]. The bulk flow model captures a longer-lasting source of GWs in the IR, resulting in a q^1 scaling. In the UV, the bulk flow model differs as it exhibits fewer kinks and cusps in the bubble configurations compared to the envelope approximation, leading to a faster decay of the spectrum in the UV. Scalar field lattice simulations also observe a stronger decay. Furthermore, the position of the peak varies slightly between the envelope approximation and the lattice simulations and bulk-flow model, whereas the latter two are in better agreement.

	IR	UV	References
Envelope approximation	3	-1	[23, 98]
Bulk flow model	[1, 3]	-3	[24, 99]
Scalar field lattice simulations	3	-1.5	[100]

Table 1: Frequency scaling behaviour in the IR and UV for the GW spectrum emerging solely from the scalar field contribution as described in the envelope approximation, the bulk flow model, and in scalar field lattice simulations.

3.2.3 The fluid contribution to GW production

We have seen how some of the first simulations of gravitational waves from scalar field dynamics were made possible through the simplifications offered in the envelope approximation. This approach was refined in the bulk flow model applied to a scalar field-only setup, which brought new insights and observations of different GW spectrum scaling behaviors. Additional insights were gained in full 3D scalar field lattice simulations at the cost of significant computational demands. All of these approaches, however, neglected or failed to adequately model the relativistic fluid dynamics with extended sound shells and complex interactions. We have nevertheless seen how GW production from long-lasting sound waves may lead to the dominant contribution.

In this regard, and since we are mostly concerned with fluid hydrodynamics and consequent GW production in this thesis, I wish to highlight a few state-of-the-art approaches to modeling GW production by the fluid and, in particular, sound waves. These approaches include the Sound-shell model, coupled scalar field + fluid lattice simulations, and a recent hybrid approach, which I will briefly review below.

THE SOUND SHELL MODEL The sound shell model offers a semi-analytical method for calculating the sound-wave production of gravitational waves during a first-order PT. As first outlined in the original publications of the sound-shell model introduced [70, 72], the GW spectrum is obtained similarly to Equation (93), but instead of assuming full knowledge of the anisotropic stress as we did to arrive at Weinberg's formula (104), they proceed to derive the UETC from a stochastic source analytically. Note that they and furthermore assume that the second integral in (93) can be extended to $\pm\infty$, thus obtaining the linear growth rate of Equation (108) as we did in Section 2.2.5. The UETC is then obtained by first computing the self-similar velocity and enthalpy profiles [86]. Then, the velocity power-spectrum is computed from the velocity profiles of the associated bubbles statistically distributed assuming either a simultaneous or exponential bubble nucleation history. With knowledge of the velocity spectrum, the UETC can be computed, which in turn allows computing the associated GW spectra.

The predicted GW spectra are found to exhibit two distinct length scales: the average bubble separation and the sound shell width upon collision. The peak of the power spectrum occurs at wavenumbers determined by the sound shell width. In the UV, the power spectrum is found to decrease as k^{-3}. In the IR, recent sound-shell model results with refined assumptions [73, 74] have found a k^3 scaling (to be contrasted with the earlier prediction of k^9 scaling). An intermediate

regime between the two scales corresponding to the typical bubble size and sound shell thickness with a linear k^1 scaling is furthermore observed. With the refined assumptions, an intricate spectrum structure emerges where, e.g. the previously found k^9 UV scaling is observed in a narrow band just to the left of the peak. The detailed form of the spectrum depends sensitively on the wall velocity and PT strength.

The sound shell model has proven immensely important and leverages the power of analytical computation, thus allowing for efficient probing of large parameter spaces. However, its limitations lay in the assumption of linearity among the sound waves. Indeed, the scenarios of greatest interest are those of stronger PTs due to their boosted, and thus more easily observable, GW signals. These PTs can be expected to involve strong nonlinear dynamics, which is precisely what is not captured in the sound-shell model. Therefore, while the sound-shell model offers an excellent framework within which the parametric dependence of the GW signal can be studied for the class of weak PTs and possibly intermediate PTs, to move beyond this limitation, one must resort to other methods that can solve adequately for the fully nonlinear evolution of the fluid dynamics.

SCALAR FIELD + FLUID LATTICE SIMULATIONS Diametrically opposite to the sound-shell model, coupled scalar field + fluid lattice simulations [25, 69, 71, 101] enter the stage as a robust attempt at capturing the GW spectrum from the PT dynamics employing a fully numerical approach without many compromising assumptions. Here, quite straightforwardly, the authors solve on the lattice for the dynamical evolution of a scalar field and the fluid coupled through a phenomenological friction term.

Utilizing these simulations, it is found that the GW spectrum is consistent with the UV k^{-3} scaling as predicted in the sound-shell model. This observation is particularly clear for detonations, while for deflagrations, it is moderately steeper. I will quote the k^{-3} scaling as their main finding in this regard. Furthermore, it was found that sound shell thickness sets the location of the peak of the GW spectrum peak. Due to insufficient IR statistics, the IR behavior of the GW spectrum could not be inferred.

HYBRID SIMULATIONS Bridging the gap between the sound-shell model and the scalar field + fluid lattice simulations, one finds the hybrid scheme [67]. In this approach, bubbles are modeled as spherically symmetric and expand at a constant wall velocity. Rather than solving for the full 3D evolution, the fluid equations of motion are solved radially in simulations of only one dimension. The fluid profiles before collision are the already known self-similar profiles discussed in 3.1.6

as obtained in [86]. In the hybrid approach, the authors implement an efficient and high-resolution solver capable of solving for the free propagation of the initial conditions defined by the self-similar profiles and thus solve for the radial evolution in the free propagation regime post-collision. This way, the radial and time-dependent relaxation of the initial profiles involving shocks is obtained nonlinearly.

The main point of the hybrid approach, however, is not the radial 1D evolution after collision but the 3D embedding of those 1D solutions into a 3D grid. The starting point is a bubble nucleation history, constructed assuming an exponentially increasing bubble nucleation history similar to the prescription in 3.1.3. The hybrid simulations use this nucleation history to embed the 1D fluid profiles into the 3D grid as a superposition on non-interacting velocity and enthalpy fields. Considering the contribution from each bubble individually, radially from the nucleation center, either the self-similar profile or the freely propagating time-evolving profile is embedded depending on whether that particular direction of the bubble has collided or not.

The superposition of such radial profiles on the 3D grid allows tracking the energy-momentum tensor over space and time, and thus the computation of the GW spectrum in complete analogy with the Higgsless simulations. The superposition of such shells implies that the hybrid approach is explicitly linear in the sense that once the radial 1D profiles are embedded, those profiles do not interact; only the single bubble evolution is solved nonlinearly.

In the hybrid approach, it is found that the IR part of the GW spectrum scales as k^a where $a \in [2, 4]$, the UV part scales as k^b where $b \in [-4, -3]$, and that an intermediate linear plateau is present between the inverse scales of the average bubble size and shell thickness at collision.

In Table 2, I summarize the scaling behaviors of the GW spectrum observed across the above-mentioned approaches, including results from the Higgsless simulations, for reference. Most approaches consistently exhibit a k^3 scaling in the IR, although the hybrid simulations reveal some variability in the IR slope around 3. Additionally, all approaches agree on a k^{-3} scaling in the UV, with the hybrid simulations indicating a slightly steeper scaling, approaching k^{-4}. An intermediate regime linking the scales of the inverse average bubble size and shell thickness at collision is also identified across all approaches. In most cases, the scaling in this regime is linear, k^1, except in the hybrid simulations, where a negative scaling is observed, with an exponent between $[-1, 0]$.

	IR	Intermediate	UV	References
Sound-shell model	3	1	-3	[70, 72]
Scalar + fluid lattice simulations	-	1	-3	[25, 69, 71, 101]
Hybrid simulations	[2,4]	[-1,0]	[-4,-3]	[67]
Higgsless simulations	[3]	1	[-3,-2.5]	This thesis

Table 2: GW spectrum slopes obtained from various approaches targeting fluid sound-wave-induced GW production. These models exhibit distinct features at wavenumbers k_0 and k_1, with three corresponding slopes: IR, intermediate, and UV.

3.2.4 Prospects for observational Detection

Before concluding this first part of the thesis, I would like to highlight recent advancements in GW detectors and discuss the observational prospects for detecting GWs originating from a first-order PT.

Global Pulsar Timing Arrays (PTAs) efforts, which probe nano-Hertz frequencies, have recently provided compelling evidence for a stochastic GW signal [41–44]. While unresolved supermassive black hole mergers are a strong candidate for this radiation, suggesting an astrophysical origin, it is crucial to consider that primordial cosmological sources could also account for the observed signal [45]. Indeed, the signal is consistent with predictions from a cosmological PT [46, 102, 103]. It is notable that as the sensitivity of PTAs improves with increased observation time and data joint data analysis among the collaborations, expectations are that the observed signal if indeed stemming from a stochastic GW signal, will be clearly seen. Furthermore, the upcoming Square Kilometre Array (SKA) [104] is expected to push the observational limits further.

For cosmologists, the Laser Interferometer Space Antenna (LISA) [47–49], scheduled for launch in 2035, designed to probe GWs in the milli-Hertz frequency band, presents potentially an even more exciting prospect. Several studies have explored whether LISA can detect GWs from cosmological PTs [50–52] and how well it can observe features of GW spectra from first-order PTs [105, 106]. Although a detailed discussion of these studies is beyond the scope here, the consensus is that LISA should be able to detect GW signals from cosmological PTs if they occur around the electroweak scale ($\sim 100\,\mathrm{GeV}$), last for a sufficiently long duration ($H_*/\beta > 10^{-3}$), and are sufficiently strong ($\alpha > 0.1$) [97].

Looking beyond LISA, upcoming gravitational wave observatories such as the Einstein Telescope (ET) [107], Big Bang Observer (BBO) [108], and Deci-hertz Interferometer Gravitational-wave Observatory (DECIGO) [109] are set to play important roles in detecting GWs

from phase transitions, as they, together with SKA and LISA, cover a vast frequency band. These observatories will significantly enhance our ability to probe the early Universe with GWs.

The ultimate goal of this section is to underscore the importance of advancing accurate gravitational GW predictions in light of the substantial investments in GW experiments, which will be justified only if the data can be effectively utilized and compared against various theoretical predictions. Furthermore, since cosmological PTs are indeed expected to be observable in certain parts of parameter space, they constitute a valid target for these GW experiments to probe. This fact is the primary motivation and justification for the research that I am hereby to present.

Part II

HIGGSLESS SIMULATIONS

In this part, I focus on the design, implementation, evaluation, and application of our Higgsless simulations introduced in [1]. It is divided into four chapters. Chapter 4 provides an overview of central difference methods. Section 4.1 introduces hyperbolic conservation laws, followed by the Lax-Friedrichs scheme as a prototypical example of a central difference method in Section 4.2. Section 4.3 presents the Kurganov-Tadmore method, a vital component of the Higgsless simulations.

In Chapter 5, based mainly on my publication [1], I introduce our novel Higgsless simulations and present the first numerical findings. Section 5.1 provides background and context and outlines the scientific objectives. In Section 5.2, I review the physical. Section 5.3 explores the numerical methods and programmatic choices. In Section 5.4, I validate the simulation code, followed by the presentation of numerical results in Section 5.5. A discussion is provided in Section 5.6, with concluding remarks in Section 5.7. I close the chapter with a brief digression in Section 5.8, reviewing the results of my other publication [2] on phase transitions seeded by domain walls.

In Chapter 6, based on the work from my publication [3], I expand upon the previous Chapter 5, significantly advancing our understanding of the simulation's performance and, for the first time, deriving gravitational wave predictions from strong phase transitions. Section 6.1 introduces the study and the broader context and outlines its scientific objectives. In Section 6.2, I extend the model for gravitational wave production to account for damped sources and cosmic expansion. Section 6.3 discusses updates to the simulation code and the chosen parameters. The main numerical results, including findings from strong phase transitions and a template for gravitational wave production, are presented in Section 6.4. Finally, Section 6.5 summarizes the key findings and concludes the chapter.

I conclude in Chapter 7, reflecting on the thesis' achievements and suggesting future research directions.

4

CENTRAL DIFFERENCE SCHEMES À LA KURGANOV AND TADMOR

This Chapter serves as an overview of central difference methods, with particular emphasis on the method used in our simulations. In Section 4.1, I introduce hyperbolic conservation laws. In Section 4.2, I present the Lax-Friedrichs scheme as a prototypical example of a central difference method. Then, in Section 4.3, I introduce the Kurganov-Tadmor central difference method, the backbone of the Higgsless simulations, in both its semi-discrete and fully-discrete formulations, including generalizations to three dimensions, and offer some concluding remarks.

4.1 Hyperbolic conservation laws

Hyperbolic Conservation Laws describe the flow of conserved quantities such as mass, momentum, or energy in a system. Mathematically, they can be written as

$$\frac{\partial}{\partial t}u(x,t) + \frac{\partial}{\partial x}f(u(x,t)) = 0 \tag{176}$$

for a conserved scalar quantity u in one spatial dimension, or more generally, for a system of equations in d spatial dimensions

$$\frac{\partial \mathbf{u}}{\partial t} + \sum_{j=1}^{d} \frac{\partial}{\partial x_j}\mathbf{f}^j(\mathbf{u}) = 0 \tag{177}$$

where $\mathbf{u}$ is the vector of conserved quantities and $\mathbf{f}(\mathbf{u})$ is the flux vector. The form of (177) is called conservative, which stems from the fact that it explicitly ensures the conservation of $\mathbf{u}$ over time. Conversely, all $\mathbf{u}^i$'s are termed conserved quantities. The term $\mathbf{f}(\mathbf{u})$ represents the rates at which the quantities $\mathbf{u}$ flow through space. Hyperbolic conservation laws describe numerous physical phenomena found in, e.g., fluid mechanics, astrophysics, and meteorology. An intriguing feature of hyperbolic conservation laws is that discontinuities, such as shock waves, can develop even from smooth initial conditions [80].

A common example is the system of Euler equations (in one spatial dimension) for the dynamics of a gas,

$$\frac{\partial}{\partial t}\begin{bmatrix}\rho\\ m\\ E\end{bmatrix}+\frac{\partial}{\partial x}\begin{bmatrix}m\\ \rho v^2+p\\ v(E+p)\end{bmatrix}=0, \tag{178}$$

where the quantities $\rho, v, m = \rho v, p$, and E are the density, velocity, momentum, pressure, and total energy, respectively. In this case, $\mathbf{u} = (\rho,\, m,\, E)^T$ with flux function $\mathbf{f}(\mathbf{u}) = \left(m,\, \rho v^2 + p,\, v(E+p)\right)^T$.

4.2 A prototypical example: the Lax & Friedrichs scheme

Central schemes are universal finite-difference methods for solving hyperbolic conservation laws. This universality means that once numerically implemented, they are in principle applicable to all physical systems governed by equations of the form (177), with degrees of success depending on the detailed structure of the central scheme and the complexity of the problem.

One of the most naive central schemes to solve (177) is obtained by simple Taylor-expansion and rearrangement of the terms, whereby

$$u_j^{n+1} = u_j^n - \frac{\lambda}{2}\left[f\left(u_{j+1}^n\right) - f\left(u_{j-1}^n\right)\right], \tag{179}$$

where, $\lambda := \Delta t/\Delta x$ is the constant mesh ratio, and u_j^n is an approximate value of $u\left(x_j, t^n\right)$ at the grid point $\left(x_j := j\Delta x, t^n := n\Delta t\right)$. Replacing $u_j^n \to \frac{u_{j+1}^n + u_{j-1}^n}{2}$, i.e. by letting

$$u_j^{n+1} = \frac{u_{j+1}^n + u_{j-1}^n}{2} - \frac{\lambda}{2}\left[f\left(u_{j+1}^n\right) - f\left(u_{j-1}^n\right)\right], \tag{180}$$

Lax and Friedrichs (LxF) improved upon the stability of this scheme [110, 111], resulting in a widely celebrated first-order stable central difference method.

It is enlightening to study what implications are associated with the replacement $u_j^n \to \frac{u_{j+1}^n + u_{j-1}^n}{2}$ acting to stabilize the LxF scheme. Equation (180) can be recast in a viscous form

$$\frac{u_j^{n+1} - u_j^n}{\Delta t} + \frac{f\left(u_{j+1}^n\right) - f\left(u_{j-1}^n\right)}{2\Delta x} = \frac{1}{2\Delta t}\left[\left(u_{j+1}^n - u_j^n\right) - \left(u_j^n - u_{j-1}^n\right)\right]. \tag{181}$$

This expression represents a discretized version of an equation of the form

$$\frac{\partial u}{\partial t} + \frac{\partial f(u)}{\partial x} = \frac{(\Delta x)^2}{\Delta t}\frac{\partial^2 u}{\partial x^2}. \tag{182}$$

The LxF scheme, thus apparently, introduces to the R.H.S. a dissipative term proportional to $(\Delta x)^2/\Delta t$ as a direct consequence of the scheme stabilization. This dissipation is the price one must pay for the scheme stabilization and results in large numerical viscosity acting to artificially smoothen solutions.

Even worse, taking the limit of $\Delta t \to 0$, the viscous form of the LxF scheme implies the divergence of the R.H.S. while the L.H.S. is well-behaved. Keeping the numerical viscosity constant thus implies that increased temporal resolution must be balanced with increased spatial resolution,

$$(\Delta t)_0 \to \Delta t \Rightarrow \Delta x \to (\Delta x)_0\sqrt{\frac{\Delta t}{(\Delta t)_0}}, \tag{183}$$

or, otherwise, the dissipative term grows and fatally approaches ∞. Increasing the spatial resolution to reduce numerical viscosity is clearly only possible within the bounds of computational resources, so one must choose the smallest permissible Δt for the specified problem.

Schemes that suffer divergences in the limit $\Delta t \to 0$ only admit a *fully-discrete* formulation in which Δt is always finite, while schemes for which the limit $\Delta t \to 0$ is well-behaved can be expressed in a *semi-discrete* formulation where the spatial part is discretized but the temporal part is not.

The choice of Δt, however, is governed by the Courant-Friedrichs-Lewy (CFL) condition. To ensure stability, this condition states that information must never propagate faster than between two neighboring grid points in one time step, and typically much slower, to ensure stability. This then signifies that

$$\frac{\Delta t}{\Delta x} \leqslant \frac{C}{\max|f'(u)|}, \tag{184}$$

where the constant $C \ll 1$ (typically) and whose exact value depends on the central scheme in question and the details of the physics to be modeled, and $\max|f'(u)|$ is the maximum local speed of propagation. This implies a trade-off between spatial resolution and time-stepping. In practice, C must generally be determined by inspection of the solutions. Clearly, Δt is limited from above by the CFL condition, and one can never do better with regard to the numerical viscosity than what is allowed by this upper bound.

It is interesting, nevertheless, to note that the LxF scheme still conserves u globally. Compute the Riemann sum of u_j^{n+1} over all J grid points,

$$\begin{aligned}\sum_{j=0}^{J-1} u_j^{n+1}\Delta x &= \sum_{j=0}^{J-1}\left[\frac{1}{2}\left(u_{j+1}^n + u_{j-1}^n\right) - \frac{\lambda}{2}\left(f\left(u_{j+1}^n\right) - f\left(u_{j-1}^n\right)\right)\right]\Delta x \\ &= \frac{1}{2}\left(u_{-1}^n + u_0^n + 2u_1^n + \ldots + 2u_{J-2}^n + u_{J-1}^n + u_j^n\right)\Delta x \\ &+ \frac{\lambda}{2}\left(f\left(u_{-1}^n\right) + f\left(u_0^n\right) - f\left(u_{J-1}^n\right) - f\left(u_J^n\right)\right)\Delta x\,.\end{aligned} \tag{185}$$

Quite often, however, numerical schemes are implemented assuming periodic boundary conditions, such that the points $(-1, J-1)$ and $(0, J)$ are mapped to one another. Therefore, the flux terms collapse, while all u_j^n's add up in pairs, and the sum reduces to

$$\sum_{j=0}^{J-1} u_j^{n+1}\Delta x = \sum_{j=0}^{J-1} u_j^n \Delta x\,. \tag{186}$$

The total amount of u is thus conserved between time steps, and the LxF scheme globally conserves u despite demonstrating significant numerical viscosity.

For problems where smooth solutions are expected and relatively large time steps are permissible, the LxF scheme may perform well. In our case of interest, namely strong relativistic hydrodynamics driven by bubble walls, which we will model as discontinuous time-varying boundary conditions, one must employ significantly higher performing central difference methods to resolve shocks and nonlinear dynamics [67]. The next Sections of this Chapter will discuss a capable high-resolution scheme that constitutes the backbone of the Higgsless simulations.

4.3 The Kurganov-Tadmor central difference method

We have seen how excessive numerical viscosity appears as an artifact of numerical schemes that do not admit a semi-discrete formulation. To this end, Kurganov and Tadmor (KT) [112] devised a scheme that does, which I am hereby to review in some detail. A compact description of this scheme is also given in [113].

4.3.1 Semi-discrete formulation

In the semi-discrete formulation and in one spatial dimension, their central scheme takes the form:

$$\frac{d}{dt}u_j(t) = -\frac{\left(f\left(u^+_{j+1/2}(t)\right)+f\left(u^-_{j+1/2}(t)\right)\right)-\left(f\left(u^+_{j-1/2}(t)\right)+\left(f\left(u^-_{j-1/2}(t)\right)\right)\right)}{2\Delta x} + \frac{1}{2\Delta x}\left\{a_{j+1/2}(t)\left[u^+_{j+1/2}(t)-u^-_{j+1/2}(t)\right]-a_{j-1/2}(t)\left[u^+_{j-1/2}(t)-u^-_{j-1/2}(t)\right]\right\}. \tag{187}$$

Here, u and f should be interpreted as a list of one or many conserved quantities and flux functions. Definitions of the terms used in this equation are discussed next.

The first items on the R.H.S. reads

$$-\frac{\left(f\left(u^+_{j+1/2}(t)\right)+f\left(u^-_{j+1/2}(t)\right)\right)-\left(f\left(u^+_{j-1/2}(t)\right)+\left(f\left(u^-_{j-1/2}(t)\right)\right)\right)}{2\Delta x}. \tag{188}$$

One immediate difference from the LxF scheme is that quantities are evaluated at *staggered* grid points $j \pm 1/2$. These are defined from Taylor expansions around points j (superscript -) and $j+1$ (superscript +),

$$u^+_{j+1/2} := u_{j+1}(t) - \frac{\Delta x}{2}(u_x)_{j+1}(t), \quad u^-_{j+1/2} := u_j(t) + \frac{\Delta x}{2}(u_x)_j(t) \tag{189}$$

with approximate derivatives $(u_x)_j$. A suitable definition of these derivatives is subtle and warrants a discussion of its own. The terms of the form

$$\frac{f\left(u^+_{j\pm1/2}(t)\right)+f\left(u^-_{j\pm1/2}(t)\right)}{2}$$

thus approximate the flux at the point $x_{j\pm1/2}$ through the mean value of its two Taylor expansion estimates approaching from different sides. The difference between such terms divided by Δx thus approximates the flux derivative.

The second term on the R.H.S.

$$\frac{1}{2\Delta x}\left\{a_{j+1/2}(t)\left[u^+_{j+1/2}(t)-u^-_{j+1/2}(t)\right]-a_{j-1/2}(t)\left[u^+_{j-1/2}(t)-u^-_{j-1/2}(t)\right]\right\} \tag{190}$$

is more interesting and contains the key piece of information that makes the KT scheme powerful. We have already seen from the CFL

(184) condition the importance of the maximal fluid velocity in determining the minimal time step Δt. It seems plausible, therefore, that if information about the maximal local fluid velocity could be embedded into the central scheme itself, one could improve upon its stability. In the second term on the R.H.S., $a_{j+1/2}$ is defined as

$$a_{j+1/2} := \max\left\{\rho\left(\frac{\partial f}{\partial u}\left(u^-_{j+1/2}\right)\right), \rho\left(\frac{\partial f}{\partial u}\left(u^+_{j+1/2}\right)\right)\right\} \tag{191}$$

where $\partial f/\partial u$ is the Jacobian matrix of f with respect to the conserved quantities u and $\rho(\partial f/\partial u)$ is the spectral radius, i.e. the magnitude of the largest eigenvalue of the Jacobian $\partial f/\partial u$. The quantity $a_{j+1/2}$, therefore, carries the interpretation of the largest characteristic speed in the system at which any disturbance or wave can propagate, estimated from the left and right approximations $u^+_{j+1/2}$ and $u^-_{j+1/2}$ at the staggered grid point $j+1/2$. When solutions are sufficiently smooth, the second term on the R.H.S. of (187) contributes numerical viscosity [112]

$$\sim (\Delta x)^3 \left(a(u)u_{xxx}\right)_x/8 \propto \mathcal{O}(\Delta x)^3\,, \tag{192}$$

which should be contrasted with the much larger $\mathcal{O}\left((\Delta x)^2/\Delta t\right)$ for the LxF scheme. Note that the numerical viscosity of the KT scheme (192) is well-behaved in the limit of $\Delta t \to 0$ by virtue of the semi-discrete formulation.

If we define the numerical flux term

$$\begin{aligned} H_{j+1/2}(t) := &\frac{f\left(u^+_{j+1/2}(t)\right) + f\left(u^-_{j+1/2}(t)\right)}{2} \\ &- \frac{a_{j+1/2}(t)}{2}\left[u^+_{j+1/2}(t) - u^-_{j+1/2}(t)\right], \end{aligned} \tag{193}$$

the KT scheme (187) can be written in a simple conservative form

$$\frac{d}{dt}u_j(t) = -\frac{H_{j+1/2}(t) - H_{j-1/2}(t)}{\Delta x}\,. \tag{194}$$

In the KT scheme, spatial derivatives are computed as

$$(u_x)_j := \operatorname{minmod}\left(\theta\frac{u_j - u_{j-1}}{\Delta x}, \frac{u_{j+1} - u_{j-1}}{2\Delta x}, \theta\frac{u_{j+1} - u_j}{\Delta x}\right), \quad 1 \leqslant \theta \leqslant 2\,, \tag{195}$$

where $\operatorname{minmod}(a, b, c)$ selects the smallest element by modulus if all arguments have the same sign or else-wise return zero. This definition helps prevent the formation of spurious oscillations around discontinuities and local maxima that are characteristic of the Gibbs phenomenon [114], as flux cannot both enter or leave the cell from both

directions at the same time. It acts as a nonlinear flux limiter and allows the regulate the steepness of gradients by means of the parameter θ. Choosing $\theta = 1$ is the most conservative choice, overall reducing the gradient, while $\theta = 2$ is the least conservative, overall admitting larger gradients at the cost of reduced stability. One must determine adequate values of θ through the evaluation of particular solutions so as to maintain stability while achieving the desired resolution.

The derivative and minimum-modulus flux-limiter (195) is quoted on discrete lattice sites; on staggered grid cells, one simply makes the replacement $j \to j \pm 1/2$.

The semi-discrete formulation of the KT scheme is now be summarized as the collection definitions, the conservative form (194) with the definition of the numerical flux (193), local fluid velocities (191), and flux-limiting choice of spatial derivative (195).

As a final note, and as did for the LxF scheme, let us explicitly verify that the KT scheme conserves u globally. To this end, compute the time derivative of the Riemann sum of u^j's,

$$\begin{aligned} \frac{d}{dt}\sum_j u_j(t)\Delta x &= -\sum_j \left(\frac{H_{j+1/2}(t) - H_{j-1/2}(t)}{\Delta x}\right)\Delta x \\ &= H_{-1/2}(t) - H_{J-1/2}(t)\,. \end{aligned} \tag{196}$$

Again, assuming an implementation with periodic boundary conditions, the points $(-1/2, J-1/2)$ are mapped to the same which causes the whole sum to collapse. Therefore,

$$\frac{d}{dt}\sum_j u_j(t)\Delta x = 0\,, \tag{197}$$

showing explicitly that the quantity u is globally conserved.

4.3.2 Fully-discrete formulation

The conservative form (194) is an ordinary differential equation (ODE) of the form

$$\frac{du}{dt} = C[u]\,. \tag{198}$$

A second benefit of the semi-discrete formulation is now evident; one can choose any ODE solver, of any order of accuracy, to solve (198),

and for this, a particularly useful choice is the third-order Runge-Kutta (RK) method

$$\begin{aligned} u^{(1)} &= u^n + \Delta t^n C\left[u^n\right] \\ u^{(1+1)} &= \eta_1 u^n + (1-\eta_1)\left(u^{(1)} + \Delta t^n C\left[u^{(1)}\right]\right) \\ u^{(2+1)} &= \eta_2 u^n + (1-\eta_2)\left(u^{(2)} + \Delta t^n C\left[u^{(2)}\right]\right) \\ u^{n+1} &:= u^{(3)}, \end{aligned} \tag{199}$$

where $\eta_1 = 3/4$ and $\eta_2 = 1/3$. If we define

$$C[u] := -\left[\frac{H_{j+1/2}(u) - H_{j-1/2}(u)}{\Delta x}\right], \tag{200}$$

then the third order RK scheme (199) brings the semi-discrete KT scheme (194) into a fully-discrete form, which is second-order in space and third-order in time.

4.3.3 Generalization to three dimensions

All expressions introduced thus far generalize rather trivially from one to three spatial dimensions x, y, and z, indicated by indices j, k, l. The equations are quite lengthy, but for the sake of at least once being explicit, I will quote the resulting expressions that are implemented on the lattice in the forthcoming Chapters.

The semi-discrete and conservative formulation of the KT scheme generalizes to

$$\boxed{\begin{aligned} \frac{d}{dt}u_{j,k,l}(t) = &- \frac{H^x_{j+1/2,k,l} - H^x_{j-1/2,k,l}}{\Delta x} \\ &- \frac{H^y_{j,k+1/2,l} - H^y_{j,k-1/2,l}}{\Delta y} \\ &- \frac{H^z_{j,k,l+1/2} - H^z_{j,k,l-1/2}}{\Delta z}, \end{aligned}} \tag{201}$$

where $H^x_{j+1/2,k,l}$, $H^y_{j,k+1/2,l}$, and $H^z_{j,k,l+1/2}$ are numerical fluxes in the x, y, and z directions and depend on time. They are defined through

$$\begin{aligned}
H^x_{j+1/2,k,l}(t) &:= \frac{f^x\left(u^+_{j+1/2,k,l}(t)\right) + f^x\left(u^-_{j+1/2,k,l}(t)\right)}{2} \\
&\quad - \frac{a^x_{j+1/2,k,l}(t)}{2}\left[u^+_{j+1/2,k,l}(t) - u^-_{j+1/2,k,l}(t)\right], \\
H^y_{j,k+1/2,l}(t) &:= \frac{f^y\left(u^+_{j,k+1/2,l}(t)\right) + f^y\left(u^-_{j,k+1/2,l}(t)\right)}{2} \\
&\quad - \frac{a^y_{j,k+1/2,l}(t)}{2}\left[u^+_{j,k+1/2,l}(t) - u^-_{j,k+1/2,l}(t)\right], \\
&\text{and} \\
H^z_{j,k,l+1/2}(t) &:= \frac{f^z\left(u^+_{j,k,l+1/2}(t)\right) + f^z\left(u^-_{j,k,l+1/2}(t)\right)}{2} \\
&\quad - \frac{a^z_{j,k,l+1/2}(t)}{2}\left[u^+_{j,k,l+1/2}(t) - u^-_{j,k,l+1/2}(t)\right].
\end{aligned} \tag{202}$$

where f^x, f^y, and f^z, are the x, y, and z components of the flux. The conserved quantities are evaluated on staggered grid points

$$\begin{aligned}
u^+_{j+1/2,k,l} &:= u_{j+1,k,l}(t) - \frac{\Delta x}{2}(u_x)_{j+1,k,l}(t), \\
u^-_{j+1/2,k,l} &:= u_{j,k,l}(t) + \frac{\Delta x}{2}(u_x)_{j,k,l}(t), \\
u^+_{j,k+1/2,l} &:= u_{j,k+1,l}(t) - \frac{\Delta y}{2}(u_y)_{j,k+1,l}(t), \\
u^-_{j,k+1/2,l} &:= u_{j,k,l}(t) + \frac{\Delta y}{2}(u_y)_{j,k,l}(t), \\
u^+_{j,k,l+1/2} &:= u_{j,k,l+1}(t) - \frac{\Delta z}{2}(u_z)_{j,k,l+1}(t), \\
u^-_{j,k,l+1/2} &:= u_{j,k,l}(t) + \frac{\Delta z}{2}(u_z)_{j,k,l}(t),
\end{aligned} \tag{203}$$

and the spatial derivatives computed utilizing the minimum-modulus flux-limiter

$$\begin{aligned}
(u_x)_{j,k,l} &:= \operatorname{minmod}\left(\theta\frac{u_{j,k,l}-u_{j-1,k,l}}{\Delta x}, \frac{u_{j+1,k,l}-u_{j-1,k,l}}{2\Delta x}, \theta\frac{u_{j+1,k,l}-u_{j,k,l}}{\Delta x}\right), \\
(u_y)_{j,k,l} &:= \operatorname{minmod}\left(\theta\frac{u_{j,k,l}-u_{j,k-1,l}}{\Delta y}, \frac{u_{j,k+1,l}-u_{j,k-1,l}}{2\Delta y}, \theta\frac{u_{j,k+1,l}-u_{j,k,l}}{\Delta y}\right), \\
(u_z)_{j,k,l} &:= \operatorname{minmod}\left(\theta\frac{u_{j,k,l}-u_{j,k,l-1}}{\Delta z}, \frac{u_{j,k,l+1}-u_{j,k,l-1}}{2\Delta z}, \theta\frac{u_{j,k,l+1}-u_{j,k,l}}{\Delta z}\right),
\end{aligned} \tag{204}$$

where $1 < \theta < 2$, selecting the smallest argument by modulus if they share the same sign or else returns zero. The local maximum speeds a^x, a^y, and a^z, in directions x, y, and z are computed as

$$\begin{aligned}
a^x_{j+1/2,k,l}(t) &:= \max_{\pm} \rho\left(\frac{\partial f^x}{\partial u}\left(u^{\pm}_{j+1/2,k,l}(t)\right)\right), \\
a^y_{j,k+1/2,l}(t) &:= \max_{\pm} \rho\left(\frac{\partial f^y}{\partial u}\left(u^{\pm}_{j,k+1/2,l}(t)\right)\right), \\
a^z_{j,k,+1/2l}(t) &:= \max_{\pm} \rho\left(\frac{\partial f^z}{\partial u}\left(u^{\pm}_{j,k,l+1/2}(t)\right)\right),
\end{aligned} \tag{205}$$

A fully-discrete scheme in three spatial dimensions and time can thus be constructed through time evolution using the third-order RK method

$$\begin{aligned}
u^{(1)} &= u^n + \Delta t^n C\left[u^n\right] \\
u^{(1+1)} &= \eta_1 u^n + (1-\eta_1)\left(u^{(1)} + \Delta t^n C\left[u^{(1)}\right]\right) \\
u^{(2+1)} &= \eta_2 u^n + (1-\eta_2)\left(u^{(2)} + \Delta t^n C\left[u^{(2)}\right]\right) \\
u^{n+1} &:= u^{(3)},
\end{aligned}$$

$$\text{where } \eta_1 = 3/4,\ \eta_2 = 1/3, \text{ and} \tag{206}$$

$$\begin{aligned}
C[u] := &-\frac{H^x_{j+1/2,k,l} - H^x_{j-1/2,k,l}(u)}{\Delta x} \\
&- \frac{H^y_{j,k+1/2,l} - H^y_{j,k-1/2,l}(u)}{\Delta y} \\
&- \frac{H^z_{j,k,l+1/2} - H^z_{j,k,l-1/2}(u)}{\Delta z}.
\end{aligned}$$

I thus define the *KT+RK3* scheme in (207):

Definition: ***the KT+RK3 scheme***
The collection of equations (201), (202), (203), (204), (205), and (206) define a numerical scheme which we denote *KT+RK3*.

(207)

This scheme constitutes a 3+1 dimensional fully-discrete second-order in space and third-order in time central difference method.

4.3.4 Concluding remarks

This Chapter has aimed to give a brief overview of central difference methods, starting with the simple LxF scheme as the prototypical example, followed by the introduction and examination of the KT scheme of low numerical viscosity. We thus arrived at the 3+1 dimensional representation of the fully-discrete KT+RK3 scheme, which combines the strengths of both the second-order KT and third-order (in time) RK scheme. This resulted in a high-performance, high-resolution central scheme with very small numerical viscosity that conserves u globally.

In the numerical examples given in [112], the KT scheme with its fully discrete extensions utilizing, e.g., third- and fourth-order RK methods, demonstrate extraordinary abilities at resolving shocks, rarefactions and structures with large gradients. This furthermore allows the schemes to resolve the formation and evolution of large-gradient phenomena, e.g., shocks, which are expected to develop spontaneously through nonlinear dynamics. We thus expect that the KT+RK3 scheme is particularly suitable for the demanding conditions of the highly relativistic and nonlinear dynamics of the early universe, which is a topic that will be covered in detail in the forthcoming Chapters.

Now we understand at some technical level why the above statements are true. Once the 3+1 dimensional KT+RK3 scheme (207) is established, it can be implemented as a black-box PDE solver for any hyperbolic conservation law. The robustness of the KT+RK3 scheme is what is ultimately responsible for the success of the Higgsless approach. The KT scheme has been widely used in physics and engineering (see e.g. [113, 115–118]) with at least one reference exploring its prospects in modeling relativistic hydrodynamics and propagation of relativistic jets [119]. In these references, the KT scheme has been shown to constitute a good replacement for significantly more computer-intensive Exact Riemann solvers and demonstrated an exceptional ability to resolve and propagate high-gradient phenomena. The KT scheme is thus widely celebrated, but its application to relativistic hydrodynamics in cosmology is, as to my knowledge at the

time of writing, novel, with the only exception being its inaugural implementation in the Hybrid simulations [67] of first-order cosmological PTs developed by some of my collaborators, on which the work in this thesis draws inspiration.

5

HIGGSLESS SIMULATIONS AND GRAVITATIONAL WAVES

This Chapter extensively draws upon the scientific work outlined in the publication *Higgsless simulations of cosmological phase transitions and gravitational waves* [1], co-authored by myself, Ryusuke Jinno, Thomas Konstandin, and Henrique Rubira. While firmly rooted in our published findings, I incorporate supplementary material not present in the original manuscript. This additional content aims to enrich the narrative by providing a broader perspective, reinforcing key conclusions, and elucidating concepts beyond the confines of the initial publication.

In Section 5.1, I provide background and context and outline the scientific objectives. In Section 5.2, I review the physical setup governing the simulations. Section 5.3 explores the numerical methods and programmatic choices, detailing their impact on both the physics and measurements. In Section 5.4, I validate the simulation code, followed by the presentation of numerical results in Section 5.5. A discussion is provided in Section 5.6, with concluding remarks in Section 5.7. I close the Chapter with a brief digression in Section 5.8, reviewing the results of the publication [2], co-authored by myself, Ryusuke Jinno, Thomas Konstandin, Henrique Rubira, and Simone Blasi, which constitutes a case applying the Higgsless simulations to PTs seeded by domain walls.

5.1 Introduction

5.1.1 Background

In Chapter 3, I delivered an introduction to cosmological first-order PTs and their associated GW production. In particular, we concluded that long-lasting sound waves constitute a potentially dominant source of anisotropic stress so that the resulting GW signal may be dominated by sound wave production.

Owing to this fact, analytical models to understand GW production from, in particular, sound waves have been developed (see e.g. [70, 72, 73, 76, 99]). The sound waves are initially generated during the bubble expansion phase, where detonation and rarefaction waves develop around the bubble wall. As bubbles collide, so do these waves, which may lead to complex nonlinear interactions if fluid velocities are

sufficiently large. These interactions may generate additional hydrodynamic disturbances, which in turn contribute to the gravitational wave signal.

While analytical models such as the sound-shell model (see, e.g., [70] and Section 3.2.3) allow to readily predict GW spectra from fully linear sound-waves, which may indeed be an accurate description for weak PTs, above points should convince the reader that to present GW signal predictions with confidence requires to take seriously the possibility that nonlinear dynamics alter the physics to the degree that one simply cannot neglect it. To this end, numerical simulations help in understanding these interactions and their effects on the resultant GW signals since they allow us to accurately model the fully nonlinear dynamics of the hydrodynamical evolution as well as account for the non-trivial geometries associated with bubble nucleation. Thus, numerical simulations are crucial for advancing the scientific understanding of gravitational wave signals from cosmological sources and, in particular, GWs from sound waves in first-order PTs.

As of this writing, excluding the Higgsless simulation which I am about to introduce, the state-of-the-art methods for simulating gravitational wave production from cosmological first-order PTs involving a fluid component are characterized by two distinct approaches.

COUPLED SCALAR FIELD AND FLUID SIMULATIONS The first approach, developed by the Helsinki-Sussex group, involves solving a system of hydrodynamical and scalar field equations on a lattice, using a phenomenological friction term to link the two sectors. This approach is described in more detail in Section 3.2.3 and originally presented in [25, 69, 71, 101]. Accounting for the co-dependent evolution of both the fluid and scalar fields, results from these simulations, while model-dependent, may present us with the most robust results of GW spectra to date. However, and despite their crucial role in advancing our understanding of gravitational wave production from cosmological PTs, these simulations have notable limitations.

These simulations are computationally very costly. This follows from the requirement of resolving two separated scales on the same lattice: the bubble wall interface, which is of the order of the inverse mass of the scalar field, and the size of bubbles, which is of cosmological scale. For the case of the EW PT, this amounts to a separation of the scale of the order $\mathcal{O}(10^{17})$, which is clearly inconceivable. Thus, arguments to bridge this gap must be made so as to reduce this separation to within reason. Nevertheless, the shape of the wall interface must be sufficiently steep for the adequate development of fluid profiles to develop, as these would otherwise smoothen. Thus, resolutions of the order $N \approx 4000$ (so that the total number of grid points is 4000^3) are used,

which makes these simulations extremely costly to run. Then, to ensure sufficient resolution of individual bubbles, the simulated volume is small so as to effectively limit the number of bubble nucleations to typically fewer than 100. This leads to poor IR statistics, which makes it difficult to extract the IR behavior of the GW spectrum.

To mitigate the issue of a single bubble dominating the simulation or extending beyond the computational domain, bubbles are often nucleated simultaneously, which is not what is expected with realistic exponentially increasing bubble nucleation rates. This approach, while practical, limits the sample statistics, leads to IR artifacts, and thwarts a measurement of IR slope of the GW spectrum. Additionally, the high computational cost constrains systematic studies of the dependence on key parameters such as wall velocity and PT strength. This implies that GW spectra and their features are only attainable for isolated parameter points, which renders impossible meaningful interpolation between the points. Finally, the results of these simulations are model-dependent in the sense of relying on a phenomenological friction term and effective potential.

HYBRID SIMULATIONS The second approach, which I also discuss in Section 3.2.3, was introduced in [67] and presents a hybrid approach. In this approach, a one-dimensional spherically symmetric hydrodynamic simulation is embedded within a three-dimensional lattice. The Higgs field is incorporated as a space- and time-dependent boundary condition in the 1D simulation, utilizing the bag equation of state (see [86, 88, 89] and Section 3.1.4), thus eliminating the challenge of disparate scales as the dynamical evolution of the Higgs field need not be solved for. While the isolated simulations in the radial direction are performed fully nonlinearly, their embedding in 3D space takes into account no nonlinear interactions as the free-propagation of sound shells is modeled by simple superposition. This renders results unreliable whenever nonlinear dynamics is expected, e.g., in stronger PTs.

We thus note a space of opportunity: there appears to exist a need for a method to obtain accurate GW predictions that are relatively cost-efficient while still accurately solving for the full nonlinear evolution. This would allow for performing extensive parameter scans and capturing the relevant nonlinear dynamics, which may eventually dictate the final shape and amplitude of the GW spectrum. The Higgsless simulations aspire to claim precisely this space of opportunity.

5.1.2 Scientific objectives

The scientific objectives of this study are broadly categorized into two main areas. The first objective pertains to the numerical implementation of the Higgsless simulations. Specifically, we aimed to:

- develop, from scratch, a fully nonlinear 3D relativistic hydrodynamics simulation code utilizing the KT+RK3 scheme (207),
- employ this code to model the dynamics of first-order PTs using a Higgsless approach based on the bag equation of state,
- and evaluate the performance of the simulations and the numerical scheme.

The second objective focuses on utilizing these simulations to study GW production. In particular, we aimed to:

- investigate and quantify sound wave-induced GW production within the simulations,
- conduct a parameter scan over wall velocities in the range $[0.32, 0.8]$ for weak ($\alpha = 0.0046$) and intermediate ($\alpha = 0.05$) PTs,
- derive GW spectrum amplitudes based on the simulation outcomes,
- characterize the general shape of the GW spectrum,
- explore how spectral features depend on the input parameters v_w and α,
- and provide a fitted spectrum for use in phenomenological studies.

It is important to emphasize that the authors of this work, including myself, my supervisor Thomas Konstandin, and my collaborators Ryusuke Jinno and Henrique Rubira, each developed independent simulation implementations. Only when all simulations agreed with exceptional precision did we trust the simulation results. The results presented in this Chapter are based on the Higgsless simulation implementation by Thomas Konstandin.

Let us now proceed to discuss the physical setup of this work.

5.2 Physical setup

In this Section, I introduce the basic physical setup in the Higgsless simulations simulations. In particular, I will review

1. how bubble nucleation and expansion is described under the assumption of an exponentially increasing nucleation probability,
2. what are the equations of motions governing the fluid dynamics,
3. how the bag equation of state can be used to track the PT evolution and encode the expansion of bubbles,
4. how to relate the conserved quantities $T^{0\mu}$ of the conservative form of the equations of motion to the primitive hydrodynamical variables pressure p, energy density ρ, enthalpy w, and velocity v,
5. how do derive an expression for the spatial components of the energy-momentum tensor T^{ij} in terms of $T^{0\mu}$,
6. and how these components may be used to compute the GW spectrum and its growth rate in our simulations.

I conclude with a summary of the physical ingredients of the Higgsless approach.

5.2.1 Bubble nucleation and expansion

In the Higgsless approach, a fundamental assumption is made regarding the bubble expansion velocity v_w of the Higgs bubbles: it is assumed to approach a constant value on microscopic timescales, whereby, given a space-time nucleation site, the wall interface expands symmetrically so that the bubble radius and locations of the wall interface are known for all times. This, importantly, means that no dynamical equations for the Higgs field must be solved to obtain this information, thus greatly simplifying the problem. We will take the wall velocity v_w as an external parameter which we give as an input to the simulations.

The assumption of a constant wall velocity allows for the construction of *bubble nucleation histories*, i.e., space-time sites at which bubbles nucleate, as described in Section 5.3.5. These histories are constructed in accordance with an exponentially increasing probability of bubble nucleation, $\Gamma(t) \simeq \Gamma_* e^{\beta(t-t_*)}$ as in Equation (123). This exponentially increasing nucleation probability is expected from realistic scenarios as outlined in Section 3.1.2 and enables accurate modeling of the fluid dynamics and the resulting GW spectrum across an extensive range of scales.

Since β appears as the fundamental time scale in PTs, we adopt it as the fundamental unit in the numerical implementation of the simulation and always measure length and time scales in units of β^{-1}. We

will demarcate time and space coordinates normalized to β with a $\tilde{}$, i.e., $\tilde{x} = x\beta$ and $\tilde{t} = t\beta$.

5.2.2 Fluid equations of motion

In the concordance model of cosmology, the state of the early universe was that of a relativistic fluid after inflation. We are interested in modeling the hydrodynamical behavior of such a fluid and begin by considering some general aspects of the setup we have in mind. In Section 3.1.4 and 5.4.1, we modeled the fluid as a perfect fluid. In the Higgsless simulations, we will do the same.

A perfect fluid is described by an energy-momentum tensor that in a locally co-moving reference frame of the fluid takes the simple form

$$T = \begin{bmatrix} \rho & 0 & 0 & 0 \\ 0 & p & 0 & 0 \\ 0 & 0 & p & 0 \\ 0 & 0 & 0 & p \end{bmatrix}. \tag{208}$$

where ρ is the local energy density and p the local pressure.

In a general frame of reference, the energy-momentum tensor takes the form

$$T^{\mu\nu} = wu^{\mu}u^{\nu} - \eta^{\mu\nu}p\,, \tag{209}$$

in the time-positive metric signature where $\eta = \mathrm{diag}(1, -1, -1, -1)$, and where the *enthalpy* $w = p + \rho$ and $u^{\mu} = \gamma(v)(1, \mathbf{v})$ is the four-velocity. Note that for $\mathbf{v} = 0$, equation (209) reduces to (208). An implication of (209) is that only the first term $wu^{\mu}u^{\nu}$ contributes to the anisotropic stress and, thus, GW production.

The equations of motion governing the dynamical behavior of the fluid can, as we already saw in Sections 3.1.4 and 3.1.6, be stated as a conservation law

$$\partial_{\mu}T^{\mu\nu} = 0\,. \tag{210}$$

To make a connection with conventional fluid mechanics, I will lead us on a short detour to explore the non-relativistic limit of (210). To proceed, we project (210) onto u^{μ} as well as the orthogonal subspace, and thus define the projector

$$P^{\sigma\nu} = g^{\sigma\nu} - u^{\sigma}u^{\nu}, \tag{211}$$

which upon application projects on the subspace orthogonal to u^{μ}. Notice, furthermore, that since $u_{\mu}u^{\mu} = 1$, $u_{\nu}\partial_{\mu}u^{\nu} = \frac{1}{2}\partial_{\mu}(u_{\nu}u^{\nu}) =$

0. We will furthermore make use of that in the non-relativistic limit $|v^i| \ll 1$, and assume that $p \ll \rho$.

Projecting onto u^μ, we find

$$\begin{aligned} u_\nu \partial_\mu T^{i\nu} =& \partial_t(w\gamma) + \nabla\cdot(wr\mathbf{v}) - \gamma\partial_t p - \gamma\mathbf{v}\cdot\nabla p \\ \overset{\text{non-rel.}}{=}& \partial_t\rho + \nabla\cdot(\rho\mathbf{v}) = 0 \end{aligned} \tag{212}$$

while projecting onto the orthogonal directions,

$$\begin{aligned} P^\sigma_\nu \partial_\mu T^{\mu\nu} =& w\gamma\left(\partial_t\left(\gamma v^i\right)\right) + w\gamma^2(\mathbf{v}\cdot\nabla)v^i + \partial_i p + \gamma^2 v^i \partial_t \rho + \gamma^2 v^i(\mathbf{v}\cdot\nu p) \\ \overset{\text{non-rel.}}{=}& \rho\left(\partial_t v^i + (\mathbf{v}\cdot\nabla)v^i\right) + \partial_i p = 0 \end{aligned} \tag{213}$$

where in the last step terms of the order $v\partial p$ have been neglected.

Thus, in the non-relativistic limit, the relativistic equations of motion (210) for the fluid reduce to

$$\begin{aligned} \partial_t\rho + \nabla\cdot(\rho\mathbf{v}) &= 0 \\ \rho\left[\partial_t\mathbf{v} + (\mathbf{v}\cdot\nabla)\mathbf{v}\right] &= -\nabla p, \end{aligned} \tag{214}$$

which are just the continuity and Euler equations in conventional fluid mechanics for an inviscid fluid. This small detour demonstrates that the perfect relativistic fluid description is just the relativistic equivalent of a conventional inviscid flow.

In the Higgsless simulations, we thus adopt the relativistic perfect fluid description and aspire to solve, on the lattice, equations of the form (210), i.e., $\partial_\mu T^{\mu\nu} = 0$ with the energy-momentum tensor (209), $T^{\mu\nu} = wu^\mu u^\nu - g^{\mu\nu}p$. Here, I say *of the form*, as actually, and as we shall see in the next Section, in the equations that we solve on the lattice, the pressure p receives a contribution from the vacuum.

These are four equations, so we can track the evolution of four independent variables. For the numerical implementation, we choose as dynamical variables (those which we time-evolve) the conserved quantities

$$K^\mu := T^{\mu 0} = wu^0 u^\mu - p\,\delta^{0\mu}, \tag{215}$$

whereby the conservation law in question, eq. (210), reads

$$\partial_t K^0 + \partial_i K^i = 0, \tag{216}$$

$$\partial_t K^i + \partial_i T^{ij}[K^\mu] = 0, \tag{217}$$

At first sight, $T^{\mu\nu}$ is a symmetric 4 by 4 tensor, and thus appear to have 10 independent components. With only four equations, we must, therefore, to be successful in our strides, express the remaining 6 spatial elements T^{ij} in terms of the dynamical variables K^μ, i.e. $T^{ij} = T^{ij}[K^\mu]$. To do this, however, requires the introduction of an equation of state. This is the topic of the next Section.

5.2.3 Bubbles and the equation-of-state

The length scale of the Higgs wall interface is microscopically determined by the inverse mass m_ϕ^{-1}, which at the electro-weak scale $\sim$ 100GeV implies a separation between the largest (Hubble) and the smallest scale of 10^{17}. As far as our simulations are concerned, therefore, the wall interface is simply a step function. If we furthermore assume that all oscillations are immediately dampened by friction with the fluid, then the Higgs field dynamics is simply described by $\phi = 0$ outside the bubble and $\phi = \phi_b$ outside. With these assumptions, and additionally assuming that the wall velocity v_w is constant, we can make great use of nucleation histories, i.e., bubble space-time nucleation sites, introduced in 5.3.5. For now, these bubble nucleation histories tell us exactly how the evolution of the scalar field proceeds. In fact, it completely removes the need to dynamically solve for its evolution, which is instead prescribed based on the simple information of a bubble-nucleation history and the expansion velocity v_w.

In the bag model introduced in Section 3.1.4, based on identical assumptions of the Higgs field, we arrived at the bag equation of state (Equations 155 and 154), which reads

$$p_+ = \frac{1}{3}a_+T_+^4 - \epsilon, \quad \rho_+ = a_+T_+^4 + \epsilon, \quad w = \frac{4}{3}a_+T_+^4, \quad \text{outside bubbles},$$

$$p_- = \frac{1}{3}a_-T_-^4, \quad \rho_- = a_-T_-^4+, \quad w = \frac{4}{3}a_-T_-^4, \quad \text{inside bubbles},$$

where $a(T,\phi) = \frac{\pi^2}{30}g_*$ and g_* the number of effective relativistic degrees of freedom. Then, determined from a given bubble nucleation history, we can define

$$\epsilon(t,\mathbf{x}) = \begin{cases} 0 & \text{inside bubbles}, \\ \epsilon & \text{outside bubbles}, \end{cases}, \tag{218}$$

so that in terms of the radiation energy density and pressures

$$\begin{aligned} p &= p_{rad} - \epsilon(t,\mathbf{x}) \\ \rho &= \rho_{rad} + \epsilon(t,\mathbf{x}) \\ w &= p + \rho = p_{rad} + \rho_{rad} \end{aligned} \tag{219}$$

where $p_{rad} = \frac{1}{3}aT^4$ and $\rho_{rad} = aT^4$. Henceforth, ϵ should be understood as a time- and space-dependent quantity.

When solving for the dynamics of the fluid in the Higgsless simulations, the pressure of fluid equations of motion (210) should thus be understood as that of Equation (219), so that the conservation law, in fact, corresponds to total energy-momentum conservation as in (157).

These assumptions lead to a simplified system description where the dynamical Higgs field is effectively removed and replaced by a time-evolving, non-dynamical equation of state. This equation of state evolves according to a predetermined bubble nucleation history. The advantages of this approach are substantial: the simulations only need to resolve the length scale associated with fluid dynamics, which, as we will demonstrate, reduces computational costs by a factor of approximately 1000 compared to the coupled-scalar field hydrodynamics simulations discussed in Section 3.2.3 [25, 69, 71, 101]. The bag equation of state is therefore central to the Higgsless approach, allowing for the effective removal of the Higgs field and thus justifying the term *Higgsless*. This choice is crucial for the method's success, as it enables efficient encoding of bubble evolution without the need for a dynamical Higgs field.

The strength of the PT can now be characterized through the bag constant ϵ as in Equation (160), namely

$$\alpha \equiv \frac{\epsilon}{\rho^{s}_{\text{rad}}} = \frac{4\epsilon}{3w_{s}} \tag{220}$$

where subscript $_{s}$ indicates quantities in the symmetric phase immediately before the PT.

A final note is warranted: While we benefit from the substantial reduction in numerical costs due to the removal of the Higgs field, this removal, by virtue of the assumptions in the bag equation of state, introduces discontinuities through the time-evolving boundary conditions of the bubbles. This comes with two consequences. The first is related to the fact that discontinuities are numerically challenging to handle, often incurring spurious oscillations in the hydrodynamical solutions [120]. We must, therefore, employ a carefully selected scheme that remains stable against such discontinuities. Secondly, since the bag equation of state was assumed in Section 3.1.6 in which self-similar profiles were introduced, we expect that the Higgsless simulations produce exactly these solutions in the limit of infinite resolution. Consequently, we are presented with the opportunity to evaluate the simulation against these self-similar profiles, which is an opportunity we will take.

5.2.4 Inversion formulae

To begin, we note that

$$K^0 := T^{00} = w\gamma^2 - p = \gamma^2 w - \frac{1}{4}w + \epsilon, \tag{221}$$

$$K^i := T^{0i} = w\gamma^2 v^i, \tag{222}$$

$$K := \sqrt{\sum_i (K^i)^2} = w\gamma^2 v\,. \tag{223}$$

Define $\bar{K}^0 := K^0 - \epsilon$. Expressions (221) and (223) form a system of two equations that can be solved for w and v,

$$w = \frac{4}{3}\left(-\bar{K}^0 + \sqrt{4\bar{K}^{0^2} - 3K^2}\right) \tag{224}$$

$$v = \frac{2\bar{K}^0 - \sqrt{4\bar{K}^{0^2} - 3K^2}}{K} \tag{225}$$

or

$$v^2 = \frac{4\bar{K}^0\left(2\bar{K}^0 - \sqrt{4\bar{K}^{0^2} - 3K^2}\right)}{K^2} - 3 \tag{226}$$

It is convenient to define

$$\lambda = \frac{3}{4}\left(\frac{\bar{K}^0}{K}\right)^2 = \frac{12v^2}{(3+v^2)^2} < \frac{3}{4} \quad \forall\, v < 1, \tag{227}$$

which, importantly, is finite in the limit $v \to 0$ and is always smaller than 1. In terms of λ and $\bar{K}^0$,

$$w = \frac{4}{3}\bar{K}^0(2\sqrt{1-\lambda} - 1) \tag{228}$$

$$v = -\frac{\sqrt{3}(-1+\sqrt{1-\lambda})}{\sqrt{\lambda}} \tag{229}$$

$$v^2 = \frac{3(2-2\sqrt{1-\lambda}-\lambda)}{\lambda} = \frac{3\lambda}{(1+\sqrt{1-\lambda})^2}, \tag{230}$$

where in the last expression, v^2 is recast in a well-defined and numerically stable form in the limit $\lambda \to 0$. The numerical stability is important, for even though the limit is mathematically well-behaved, numerically, floating point errors may lead to spurious behavior had we not taken care to explicitly ensure that very small numbers are never divided by very small numbers.

Equations (228), (229), and (230) are the inversion formulae we need, for, through $w(K^\mu)$, we can express the density and pressure as functions of K^μ, as

$$\rho = \frac{3}{4} w\,(K^\mu) + \varepsilon \tag{231}$$

$$p = \frac{1}{4} w\,(K^\mu) - \varepsilon\,. \tag{232}$$

To conclude, the relevant inversion formulae are

$$\begin{aligned}
w &= \frac{4}{3}\bar{K}^0(2\sqrt{1-\lambda}-1)\\
v^2 &= \frac{3\lambda}{(1+\sqrt{1-\lambda})^2}\\
&\text{from which the remaining quantities}\\
\rho &= \frac{3}{4}w + \varepsilon\\
p &= \frac{1}{4}w - \varepsilon\\
v^i &= \frac{1-v^2}{w}K^i\\
&\text{can be obtained, where}\\
\lambda &= \frac{3}{4}\left(\frac{\bar{K}^0}{K}\right)^2\\
\bar{K}^0 &= K^0 - \epsilon\\
K &= \sqrt{\sum_i (K^i)^2}.
\end{aligned} \tag{233}$$

5.2.5 Spatial components $T^{ij}(K^\mu)$

We are now ready to derive an expression for the spatial components T^{ij} as functions of the conserved quantities K^μ, and proceed to write

$$T^{ij} = \frac{1-v^2}{w\gamma^2}K^iK^j + p\delta^{ij} \equiv F\,K^iK^j + p\delta^{ij}. \tag{234}$$

The form of F can thus be obtained from the inversion formulae (233), and one finds

$$F = \frac{3}{2\bar{K}^0}\frac{1}{1+\sqrt{1-\lambda}}. \tag{235}$$

Since $0 < \lambda < 3/4$, F is always well-defined and numerically stable and thus allows solving the conservation law (210) written in the form (216) and (217) on the lattice.

5.2.6 Gravitational wave production

Results for the GW production and corresponding GW spectra from a generic stochastic source of stress-energy were derived in Section 2.2.4. Using these results, the GW spectrum as a present-time observable is computed using Weinberg's formula (104), which is recited here for ease of reference

$$\begin{aligned}\Omega_{\mathrm{GW}}(q) &= 3\mathcal{T}_{\mathrm{GW}}\mathcal{J}(q)\\ &= \mathcal{T}_{\mathrm{GW}}\frac{q^3}{4\pi^2 m_{\mathrm{Pl}}^2\bar{\rho}_* V}\\ &\times\int_{\Omega_k}\frac{d\Omega_k}{4\pi}\left[\Lambda_{ij,kl}(\hat{\mathbf{k}})T_{ij}(q,\mathbf{k}\,|\,t_{\mathrm{fin}})\,T^*_{kl}(q,\mathbf{k}\,|\,t_{\mathrm{fin}})\right]_{q=|\mathbf{k}}\,,\end{aligned}$$

where $\bar{\rho}_*$ is the average total energy density of the Universe at production time t_*, q and $\mathbf{k}$ are the GW angular frequency and wavenumber, respectively, with $k \equiv |\mathbf{k}|$, V is, formally, the volume of space, and

$$T_{ij}(q,\mathbf{k}\,|\,t_{\mathrm{fin}}) = \int_{t_*}^{t_{\mathrm{fin}}} dt\, e^{iqt}\int d^3\mathbf{x}\, e^{-i\mathbf{k}\cdot\mathbf{x}}\,T_{ij}(t,\mathbf{x})\,, \tag{236}$$

as defined in Equation (103), now explicitly writing both the temporal and spatial transforms, where t_{fin} is the final time of GW sourcing. The projector Λ, defined as

$$\Lambda_{ij,kl} = P_{il}P_{jk} - \frac{1}{2}P_{ij}P_{kl} \tag{237}$$

with

$$P_{ij} = \delta_{ij} - k_i k_j/k^2\,, \tag{238}$$

projects on the transverse-traceless part of the energy-momentum tensor,

$$\Lambda_{ij,kl}T_{kl} = \Lambda_{ij,kl}\; w\gamma^2 v_k v_l\,, \tag{239}$$

where the pure trace proportional to the pressure p is omitted since it does not contribute to anisotropic stress by its definition and, by consequence, GW production. Since we have complete knowledge of the source $T_{ij}(q,\mathbf{k})$ from our simulations, Weinberg's formula allows us to efficiently compute the GW spectrum. Note that in our case, T^{ij} exclusively derives contributions from the fluid. Also, note that Weinberg's formula neglects the expansion of the Universe so that one must assume that the source duration is short, $t_{\mathrm{fin}} - t_* \ll H_*^{-1}$. For a detailed derivation and a discussion of all assumptions that enter the usage of Weinberg's formula, see Section 2.2.4.

5.2.7 Summary of physical ingredients

We have seen how realistic exponential-in-time bubble nucleation histories can be constructed, whereby the predetermined evolution of spherically expanding bubble shells is obtained under the assumption of constant wall velocity; a fundamental assumption of the Higgsless approach. The wall interface of these Higgs bubbles is approximated as a step function, allowing encoding the PT evolution using the bag equation of state where the space-time dependence of the bag constant is determined directly from the bubble nucleation history. Solving for the spatial components of T^{ij} in terms of the conserved quantities $K^{\mu} \equiv T^{0\mu}$ reveals that the fluid is coupled to the state of the vacuum through the time-varying bag constant $\epsilon(t, \mathbf{x})$, whose evolution, therefore, triggers the fluid to respond to the vacuum energy injection. This, therefore, eliminates the need to solve for the evolution of the Higgs field itself; the equation of state is all that is required. The perturbed fluid leads to the development of bulk motion in the form of sound waves and possibly turbulence, thus resulting in anisotropic stress, which sources a spectrum of GWs that we will simulate and measure in the Higgsless simulations utilizing Weinberg's formula.

5.3 Numerical methods and programmatic considerations

In this section, I review the key programmatic and numerical components of the Higgsless simulation implementation, with a focus on areas where non-trivial decisions were made or aspects that require further clarification—whether due to theoretical considerations, efficiency concerns, or simply for thoroughness. The simulation code is written in C++, chosen for its superior computational efficiency.

The main purpose of this Section is to explain the connection between physics and numerical and programmatic implementation. The emphasis will be on detailing how theoretical concepts are translated into computational algorithms and the rationale behind the specific choices made in the implementation. This Section aims to provide a clear understanding of how the physics is embedded in the code and how these decisions impact the overall performance and accuracy of the Higgsless simulation.

5.3.1 The lattice

In our simulations, we mean by the *lattice* a set of points $\{\mathbf{n}\}$ arranged on a cubical grid in one, two, or three spatial dimensions; we will al-

ways work in three. Denoting with N the number of points in any one direction, which in the Higgsless simulation will be the same number in all three spatial directions. The lattice, then, has a total of N^3 sites. We label these sites

$$\mathbf{n} = (n_0, n_1, n_2), \quad \text{with} \quad n_0, n_1, n_2 \in \{0, 1, \ldots, N-1\}. \tag{240}$$

Note that we will often use the alternative and slightly shorter notation for the indices $j = n_0$, $k = n_1$, $l = n_2$. We furthermore define unit vectors $\hat{1} \equiv (1,0,0)$, $\hat{2} \equiv (0,1,0)$ and $\hat{3} \equiv (0,0,1)$. Any point $\mathbf{n}$ in the lattice can thus be reached through a linear combination of the unit vectors

$$\mathbf{n} = n_x\hat{1} + n_1\hat{2} + n_2\hat{3}. \tag{241}$$

The lattice spacing is defined by

$$\delta x \equiv \frac{L}{N}, \tag{242}$$

where L is the physical scale of the lattice side. Any physical coordinate is thus obtained as

$$\mathbf{x} = \mathbf{n}\delta x. \tag{243}$$

whereby a continuum function $f(\mathbf{x})$ in space has values

$$f_{\mathbf{n}} = f\left((n_0\hat{1} + n_1\hat{2} + n_2\hat{3})\delta x\right) \tag{244}$$

on the lattice.

We likewise discretize time by a time index n_0 (which we will often call just n), such that the temporal spacing

$$\delta t = \frac{T}{N_0}, \tag{245}$$

where T is the total simulation time and N_0 the total number of time-steps. Any physical time coordinate is thus given by

$$t = n_0\delta t. \tag{246}$$

In the Higgsless simulations, for practical purposes, values of quantities on the 3D lattice are stored as 1D arrays. Using row-major ordering, an element $\mathbf{n} = (j,k,l)$ is located at the index $i_{rm} = l + N(k + Nj)$, constituting a mapping from a 3D to a 1D representation. The Higgsless simulations furthermore employ periodic boundary conditions, such that any point n_i is equivalent to n_{i+N} where $i \in 1, 2, 3$. In particular, this means that $n_N = n_{-1}$. This avoids modeling of boundary effects and guarantees the conservation of conserved quantities as discussed in Section 4.3.1.

5.3.2 The discrete Fourier transform

We are interested in computing on the lattice the Fourier transform (5.2.6), involving a transformation both in space and time. We begin by considering the former.

The discretized equivalent of the spatial Fourier transform $\mathcal{F}$ is the discrete Fourier transform (DFT), defined on the dual lattice $\{\tilde{\mathbf{n}}\}$ through

$$\begin{aligned}\mathcal{F}[f]_{\tilde{\mathbf{n}}} \equiv f_{\tilde{\mathbf{n}}} &\equiv \sum_{\mathbf{n}} e^{-i\frac{2\pi}{N}\tilde{\mathbf{n}}\cdot\mathbf{n}} f_{\mathbf{n}} \\ &= \sum_{n_0=0}^{N-1}\sum_{n_1=0}^{N-1}\sum_{n_2=0}^{N-1} e^{-i\frac{2\pi}{N}(\tilde{n}_1 n_0+\tilde{n}_2 n_1+\tilde{n}_3 n_2)} f_{n_0 n_1 n_2}\,,\end{aligned} \tag{247}$$

with $\tilde{\mathbf{n}} = (\tilde{n}_1, \tilde{n}_2, \tilde{n}_3)$, and $\tilde{n}_1, \tilde{n}_2, \tilde{n}_3 \in \{0, 1, \ldots, N-1\}$. The inverse DFT is given by

$$f_{\mathbf{n}} \equiv \frac{1}{N^3}\sum_{\tilde{\mathbf{n}}} e^{+i\frac{2\pi}{N}\tilde{\mathbf{n}}\cdot\mathbf{n}} f_{\tilde{\mathbf{n}}}\,. \tag{248}$$

Note that the DFT, just like functions on the original lattice $\{\mathbf{n}\}$, is N-periodic in the dual lattice $\{\tilde{\mathbf{n}}\}$. Care must therefore be taken when interpreting $\tilde{\mathbf{n}}$ as a physical wavenumber. Since

$$e^{ik_j(\delta x n_j)} = e^{i\frac{2\pi}{N}\tilde{n}_j n_j}\,, \tag{249}$$

we have that

$$k_j \delta x = \frac{2\pi}{N}\tilde{n}_j. \tag{250}$$

The softest mode, i.e. smallest wavenumber, on the lattice is therefore $k_{IR} = \frac{2\pi}{N\delta x} = \frac{2\pi}{L}$, corresponding to the size of the simulation box. k_{IR} therefore, by construction, defines the cutoff scale below which no data points can be obtained.

The hardest mode, i.e. the largest physical wavenumber, requires accounting for the periodicity. In particular, we need to introduce a mapping such that lattice points $\tilde{n}_j$ and $\tilde{n}_j + N$, etc., are mapped to the same physical wavenumber. One natural way to do this suggests itself by making the observation that the wavenumber, for a derivative operator ∇_i and in the continuum, obeys the relation

$$\mathcal{F}[\nabla_i f](\mathbf{k}) = -ik_i f(\mathbf{k}). \tag{251}$$

The equivalent construction on the lattice reads

$$\mathcal{F}[\nabla_i f](\tilde{\mathbf{n}}) = -ik_{\text{Lat},i}(\tilde{\mathbf{n}}) f(\tilde{\mathbf{n}})\,, \tag{252}$$

where $k_{\mathrm{Lat},i}(\tilde{\mathbf{n}})$ is the lattice momentum corresponding to the lattice site $\tilde{\mathbf{n}}$. On the lattice, two common choices for the derivative operator are the backward and forward prescriptions

$$\left[\nabla_i^{\pm} f\right] = \frac{\pm f(\mathbf{n} \pm \hat{\imath}) \mp f(\mathbf{n})}{\delta x} \tag{253}$$

and the central difference

$$\left[\nabla_i^{(0)} f\right] = \frac{f(\mathbf{n}+\hat{\imath}) - f(\mathbf{n}-\hat{\imath})}{2\delta x}\,. \tag{254}$$

For these two prescriptions, one can identify related lattice momenta,

$$k^{+}_{\mathrm{Lat},i} = k^{-}_{\mathrm{Lat},i} = 2\frac{\sin\left(\pi\tilde{n}_i/N\right)}{\delta x} \tag{255}$$

and

$$k^{0}_{\mathrm{Lat},i} = \frac{\sin\left(2\pi\tilde{n}_i/N\right)}{\delta x}\,, \tag{256}$$

which therefore constitute two natural choices of mappings of dual lattice sites $\tilde{\mathbf{n}}$ to physical momenta $\mathbf{k} = \mathbf{k}^{\dagger}_{\mathrm{Lat}}$, where $\dagger \in 0, +, -$ or something else depending on the lattice derivative operator.

In the first version of the Higgsless simulations, which is used for the results of the current Chapter, we will employ these mappings (255) and (256) for the physical wavenumber. Which one is used will depend on the circumstances, and, in particular, on whether the sign of the wavenumber is important. Note that the hardest mode corresponds to the physical wavenumber $k_{\mathrm{UV}} = \sqrt{3}/\delta x$, which is the UV cutoff beyond which no results are obtained. Note also that large $\tilde{n}_i \sim N$ corresponds, in fact, to small physical wavenumbers and thus constitutes soft modes.

There is a subtlety regarding the mappings (255) and (256), as it appears evident that a large subset of modes around $\tilde{n}_i \sim N/2$ are mapped to either very hard or very soft modes depending on which prescription is used, which is clearly unphysical. The mappings are thus reliable only in the linear regime of the sin-function near $\tilde{n}_i \sim 0$ and $\tilde{n}_i \sim N$. Elsewhere, there is contamination from modes $\tilde{n}_i \sim N/2$. In practice, however, this contamination is small, since contributions from $\tilde{n}_i \sim N/2$ are in the far UV where no physical features can be resolved in the simulation, leaving only numerical artefacts contributing. In practice, therefore, one must compare results using both prescriptions, only to conclude that differences are insignificant in the resolved wavenumber regimes. Refraining from trusting data beyond the linear regime of the sin-function, say above $2\pi|\tilde{n}_i|/N = \pi/4$ (noting that $|\tilde{n}_i|$ also includes negative $\tilde{n}_i < 0 \Leftrightarrow \tilde{n}_i - N$ from periodicity), should be

sufficient, and one should only consider as reliable results for physical wavenumbers $k = |\mathbf{k}| < \pi/(4\delta x) \sim 0.45 k_{UV}$.

We shall see that well within this limit, there are other artefacts stemming from numerics that render the data unreliable above some scale $k_{lim} < 0.45 k_{UV}$. In practice, therefore, the limit $k < 0.45 k_{UV}$ is essentially theoretical in nature with few implications for the actual data analysis, as one must always obey stricter limits. For as long as the linear range of the mapping from dual lattice sites $\tilde{n}_i$ to physical momenta is sufficiently large, the exact choice of mapping is less important.

For the practical implementation of the DFT computation in the Higgsless simulation code, utilizing a rigorously tested and highly optimized library is essential. In this context, the FFTW library [121] stands out as a premier C subroutine library designed for computing the discrete Fourier transform (DFT) in one or more dimensions. In the Higgsless simulations, the FFTW library is employed to compute the three-dimensional spatial DFT.

We have extensively discussed the 3D spatial DFT. As for the DFT in the time-direction, we take a markedly different approach. Naively, one could simply propose to compute the temporal DFT as

$$\mathcal{F}[f]_{\tilde{n}_0} \equiv f_{\tilde{n}_0} \equiv \sum_{n_0} e^{-i\frac{2\pi}{N}\tilde{n}_0 \cdot n_0} f_{n_0} \,. \tag{257}$$

utilizing the FFTW library. In our case, however, f_{n_0} is a function on the lattice, such that for each time step n_0, a total of $\sim N^3$ data points must be stored. To give an example, we will often use $N = 512$ and the total number of time steps $N_0 \sim 3000$. Storing data using double precision occupying 8 bytes of data per variable, the full simulation data needed to execute the temporal DFT using the FFTW library would require $\sim$ 3TB of internal memory, even for a modest 512^3 simulation. Clearly, we must resort to another method and instead approximate the temporal Fourier transform in (5.2.6) through its Riemann sum

$$T_{ij}\,(q, \mathbf{k}\,|\,t) = \sum_{t'=t_{init}}^{t} e^{iqt'} T_{ij}\left(t', \mathbf{k}\right) \,, \tag{258}$$

by stacking past time slices weighed by a complex factor from t_{init} until $t \leqslant t_{end}$ for each time step over which the GWs are sourced. Note that I intentionally leave out the factor δt from the Riemann sum to make it dimensionally consistent with the definition of the DFT.

5.3.3 Power spectra on the lattice

In the Higgsless simulations, we will need to compute power spectra on the lattice. In the continuum, the power spectrum $P(k)$ of some func-

tion $f(\mathbf{x})$ of three spatial dimensions is defined through the ensemble average of $f(\mathbf{x})$'s Fourier transform,

$$\left\langle f(\mathbf{k}) f^*(\mathbf{k}') \right\rangle = (2\pi)^3 P(k) \delta^3 \left(\mathbf{k} - \mathbf{k}'\right) . \tag{259}$$

We wish to derive an equivalent discretized form on the lattice. To accomplish this, first note that the Dirac and Kronecker delta functions can be computed as

$$\delta^{(3)}\left(\mathbf{k} - \mathbf{k}'\right) = \int \frac{d^3\mathbf{x}}{(2\pi)^3} e^{i(\mathbf{k}-\mathbf{k}')\cdot\mathbf{x}} \quad \text{and} \quad \delta^{(3)}_{\tilde{\mathbf{n}}\tilde{\mathbf{n}}'} = \frac{1}{N^3} \sum_{\mathbf{n}} e^{i\frac{2\pi}{N}(\tilde{\mathbf{n}}-\tilde{\mathbf{n}})\cdot\mathbf{n}} \tag{260}$$

respectively. Discretizing the Dirac delta thus leads to the conclusion that

$$\delta^{(3)}\left(\mathbf{k} - \mathbf{k}'\right) \sim \frac{V}{(2\pi)^3} \delta^{(3)}_{\tilde{\mathbf{n}}\tilde{\mathbf{n}}'} , \tag{261}$$

and consequently, that the power spectrum on the lattice, i.e. the discretized equivalent of (259), is suitably defined by

$$\left\langle f(\tilde{\mathbf{n}}) f^*(\tilde{\mathbf{n}}') \right\rangle = V \delta^{(3)}_{\tilde{\mathbf{n}}\tilde{\mathbf{n}}'} P(|\tilde{\mathbf{n}}|) . \tag{262}$$

Taking $\tilde{\mathbf{n}} = \tilde{\mathbf{n}}'$, this implies

$$P(k) = \frac{1}{V} \langle |f(\mathbf{k})| \rangle \tag{263}$$

where we have replaced $\tilde{\mathbf{n}} \to \mathbf{k}$ since we are ultimately interested in the power spectrum expressed over physical wavenumber. In the literature, the practical implementation of the ensemble average varies (see e.g. [122] for a review of various averaging strategies). Typically, however, one distributes $f(\mathbf{k})$ over J bins of width Δk based on the wave vector magnitude $k = |\mathbf{k}|$. For each bin i, the power spectrum is defined as the average over all $f(\mathbf{k})$'s in that bin, i.e.

$$P(k_i) = \frac{1}{\#\,\text{of}\,\mathbf{k}'\text{s in bin}\,i} \times \sum_{k_i - \frac{\Delta k}{2} \leqslant |\mathbf{k}| < k_i + \frac{\Delta k}{2}} f(\mathbf{k}) \tag{264}$$

Alternatively, one can avoid binning altogether and average only over those combinations of dual lattice sites $\tilde{\mathbf{n}}$ yielding physical momenta of equal magnitude. For example, $\tilde{\mathbf{n}} \in \{(1,0,0), (0,1,0), (0,0,1), (N-2, N-1, N-1), (N-1, N-2, N-1), (N-1, N-1, N-2)\}$ all give rise to the same physical momenta and has multiplicity 6. Averaging $f(\mathbf{k})$ for these six combinations gives the power spectrum at that wavenumber. This method sacrifices no data in the sense of binning the few data

points in the IR into one or a few bins, potentially making it impossible to see any scaling behavior. However, it has the disadvantage that the power spectrum samples an enormous amount of points in the UV. The former averaging method involving binning, on the other hand, sacrifices the scarce data in the IR but results in a smoother and more compact spectrum.

For the Higgsless simulations, I have chosen to implement a hybrid ensemble averaging approach in the following sense: for wavenumbers below some selected value k_{lim}, I avoid binning by averaging over combinations of physical momenta akin to the second approach above, and for wavenumbers above k_{lim}, I bin in narrow bins akin to the first approach. This results in a power spectrum where all information in the IR is preserved while avoiding storing unnecessary data in the UV. Definition (263) thus allows to efficiently compute the power spectrum of any quantity on the lattice provided its DFT has been obtained.

5.3.4 Numerical scheme

We discussed in Chapter 4 the KT scheme as a numerical method designed to solve hyperbolic partial differential equations, with high resolution stemming from its ability to handle sharp gradients and discontinuities without introducing significant numerical diffusion. For us, general and important key features of the KT scheme include:

1. *Non-Oscillatory Nature*: The KT scheme avoids spurious oscillations near discontinuities, which is critical for accurately capturing shock waves and other sharp features in the fluid flow.

2. *Conservative Formulation*: The scheme maintains the conservation properties of the underlying physical system, ensuring that energy and momentum are correctly conserved throughout the simulation.

3. *Versatility*: The KT scheme is versatile and can be applied to a wide range of problems in fluid dynamics beyond cosmological applications, including astrophysical phenomena and high-energy physics.

4. *Efficiency and Stability*: Despite its high resolution, the KT scheme remains computationally efficient and stable due to its semi-discrete formulation allowing to use, e.g., a third-order Runge-Kutta solver for the time-stepping. This allows us to run simulations over more extended periods, which are necessary to capture the evolution of cosmological PTs.

In the context of first-order PTs and regarding the modeling of the primordial fluid and GW production, this means that the KT scheme is particularly suitable for the following reasons:

1. *Capturing Shock Waves*: Shock waves are a prominent feature in PT dynamics. The KT scheme's ability to handle shocks without excessive numerical diffusion allows for precise modeling of these features, which are crucial for understanding the resulting GW signals.

2. *Resolving Fine Structures*: The high-resolution nature of the KT scheme enables the resolution of fine structures in the fluid flow and may, e.g., allow the resolve of small-scale vorticity, which may come to play a significant role in the dynamics of the PT and the subsequent GW production.

Owing to these facts, we adopt the KT+RK3 scheme defined in (207), i.e., the KT scheme utilizing a third-order Runge-Kutta method, for the purpose of solving the conservation law (210) on the lattice.

More explicitly, (210) can be expanded as in (216) and (217), and reads

$$\begin{aligned} \partial_t K^0 + \partial_i K^i &= 0 \\ \partial_t K^j + \partial_i T^{ij}\left[K^\mu\right] &= 0 \end{aligned}$$

where the anisotropic stress in terms of the conserved quantities K^0 and K^i is given by equation (234),

$$T^{ij} = F K^i K^j + p\delta^{ij}$$

where

$$F = \frac{3}{2\overline{K}^0}\frac{1}{1+\sqrt{1-\lambda}}$$

and λ is defined in the inversion formulae (233). We thus conclude that the conservation law (216) and (217) constitute a system of four hyperbolic equations which can be solved by the KT+RK3 scheme. Using standard notation, the conserved quantities are

$$\mathbf{u} := \left(K^0,\, K^1, K^2, K^3\right)^T \tag{265}$$

and the flux function

$$\mathbf{f} := \begin{pmatrix} \left(K^1, K^2, K^3\right)^\top \\ \left(T^{11}\left[K^\mu\right], T^{12}\left[K^\mu\right], T^{13}\left[K^\mu\right]\right)^T \\ \left(T^{21}\left[K^\mu\right], T^{22}\left[K^\mu\right], T^{23}\left[K^\mu\right]\right)^T \\ \left(T^{31}\left[K^\mu\right], T^{32}\left[K^\mu\right], T^{33}\left[K^\mu\right]\right)^T \end{pmatrix}. \tag{266}$$

In our setup using the bag equation of state, the local maximal speeds $a^x_{j+1/2,k,l}$, etc., in (191) can be computed analytically. The eigenvalues of the Jacobian $\partial \mathbf{f}_\mu / \partial \mathbf{u}$ for the flux in direction $\mu \in \{t, x, y, z\}$ can be obtained utilizing the inversion relations (233), whereby one finds, e.g., in the x-direction two eigenvalues that are given by $3v_x/2/(1+\kappa)$ while the other two have long closed expressions. In the limit of small fluid velocities, however, the two largest eigenvalues become $\pm c_s = \pm\frac{1}{\sqrt{3}}$ since the sound speed is the fastest speed at which information can propagate. Then, since in this initial study, we aspire to study weak and intermediate PTs, and we expect from self-similar profiles in Figure 3 derived velocity profiles [86] that maximal fluid velocities are well below the speed of sound c_s, we may approximate the maximal local speeds as $a^x_{j+1/2,k,l} \approx c_s$, etc. This furthermore means that a fixed step size δt in accordance with the CFL stability condition will always be near optimal, and there is no need to change it dynamically. We verified that computing the maximal local speeds using the full analytical expressions does not change our results in any noticeable way. One does, however, incur a computational burden when choosing to do so. Therefore, we always approximate the maximum local speeds with c_s rather than relying on the full analytical expressions. We nevertheless point out that stronger PTs may produce fluid velocities approaching the speed of light. These cases, therefore, may require special attention since when the fluid velocities become large, the maximal velocities in (191) may increase beyond c_s and negatively impact the stability of the KT+RK3 scheme. Care must then be taken to increase the maximal local speeds are correspondingly increased.

5.3.5 Bubble nucleation histories

With the assumption of constant wall velocity v_w and an exponentially increasing probability of bubble nucleation, $\Gamma(t) \simeq \Gamma_* e^{\beta(t-t_*)}$ as in Equation (123), *bubble nucleation histories*, i.e. lists of space-time nucleation sites are readily constructed.

In practice, to generate bubble nucleation histories, we proceed as follows. First, consider bubbles expanding at the speed of light $v_w = 1$ and suppose that we request the nucleation of N_τ bubbles. Now, a simple way to produce an exponential-in-time nucleation history is to nucleate bubbles uniformly in a four-volume consisting of the three spatial dimensions and the *exponential-time* $\tau = \exp[\beta(t - t_0)]$ (rather than in linear-time), of volume $(L\beta)^3 \Delta\tau$, where L is the physical size of the simulation box, τ is chosen to be within $\tau \in [0, 1]$ such that $\Delta\tau = 1$, and t_0 can be chosen to nucleate the first bubble as desired.

The exponential nature of the nucleation probability is apparent, as the physical nucleation times are obtained by simply taking the logarithm.

This procedure nucleates bubbles uniformly in all of space. What is yet to be accounted for, however, is that bubble nucleation can only occur in the meta-stable phase, which constitute an exponentially decreasing fraction of volume that goes to zero at percolation. Thus, after completing the randomized nucleation procedure, bubbles nucleated within the forward light-cone (since $v_w = 1$) of any previously nucleated bubble are removed. Out of the initially requested N_τ bubbles, only a smaller number $N_b < N_\tau$ remain.

It's noteworthy that the outcome of this algorithm is independent of the volume of τ or the number N_τ of bubbles, provided N_τ is sufficiently large. Suppose we double N_τ so as to request $2N_\tau$ bubbles. Then, the first bubble typically nucleates around $\tau \sim 1/(2N_\tau)$. Consequently, due to the doubling, the PT on average commences earlier by $\delta t \simeq \ln(2)/\beta$ as compared to before the doubling. Having doubled the number of bubbles, half will nucleate before $\tau < 1/2$ and half after, but if $N_\tau/2$ was already adequately large, the PT already concludes by $\tau = 1/2$ when percolation was already complete. Consequently, all bubbles with $\tau > 1/2$ lie within the forward light cone of other bubbles and are discarded. For as long as N_τ is chosen sufficiently large, saturation of the number of bubbles takes place and the nucleation procedure will always be independent of the actual choice of N_τ. In essence, as long as $N_\tau \gg N_b$, increasing N_τ merely results in a slight shift of nucleations to earlier times. Similarly, adjustments to the τ volume is inconsequential. The number of bubbles expected to pass the light-cone test was derived in Equation (127) and reads:

$$N_b \simeq \frac{1}{8\pi}\left(\frac{L\,\beta}{v_w}\right)^3 . \tag{267}$$

Now that a general procedure for the nucleation of bubbles is established, let us admit that $v_w \neq 1$. A very simple generalization of the procedure, however, is obtained if we define the physical simulation size to scale with the wall velocity v_w so that $\tilde{L} \propto v_w$. In the simulations that we run, the v_w normalized box-size $\tilde{L}/v_w$ takes on typical values 20, 40, and 80. It is then evident from Equation (127) that, for a given random seed, the number of bubbles N_b depends only on the choice of $\tilde{L}/v_w$ and not on the wall velocity v_w. Thus, once a bubble nucleation history is constructed for $v_w = 1$, it can be used for every choice of v_w provided the spatial coordinates in the bubble nucleation history are rescaled by v_w. This has the benefit that a single nucleation history is used for every choice of v_w, thus minimizing the variance associated with the bubble sample statistics.

This procedure assumes homogeneity in the spatial probability distribution of bubbles. While this is generally a good approximation, it is nevertheless true that β varies locally. For instance, temperature fluctuations during the nucleation phase can significantly impact the number of bubbles, their spatial distribution, and the resulting GW spectra. This effect is explored in [68], where it is demonstrated that such fluctuations can enhance the GW spectra by up to two orders of magnitude. While it is, in principle, straightforward to generalize our nucleation procedure to accommodate other statistical distributions, we impose spatial homogeneity in this initial study to maintain generality. We will see in Appendix 5.8 how a bubble nucleation history for nucleation sites exclusively on a domain wall network may be constructed.

In our simulations, $\tilde{L}/v_w$ takes on values of 20, 40, and 80, resulting in the nucleation of approximately 300, 2500, and 20400 bubbles, respectively. In figure 5, I plot bubble nucleation histories generated with different random seeds for box sizes $\tilde{L}/v_w = 20$ and $\tilde{L}/v_w = 40$. Note the initial exponential rise in the nucleation rate, which is followed by a peak and a rapid decline in the rate as percolation is approached and saturation is reached. The nucleation times of each bubble nucleation history have been translated to nucleate the first bubble of each history at the same time. For the smaller $\tilde{L}/v_w = 20$, the scatter in the location of the peak is more prominent due to the time translation and limited statistics, while for $\tilde{L}/v_w = 40$, the histories appear more uniform due to much better sample statistics.

For equal numerical resolution N, simulations with $\tilde{L}/v_w = 40$ reduce statistical variance by increasing the number of bubbles, thereby enhancing the resolution of measured quantities in the IR regime. Conversely, simulations with $\tilde{L}/v_w = 20$ offer a broader dynamical range in the UV regime since a smaller box size means that individual bubbles occupy more space, effectively increasing the resolution. A potential issue with small box sizes is that for small wall velocities, the shock in front of the wall of the first nucleated bubble might collide with its mirror images (from periodic boundary conditions) before percolation takes place.

For comparison, the number of bubbles for $\tilde{L}/v_w = 40$ ($N_b \simeq 2500$) in our work and in previous Higgsless simulations [123] generally exceeds that of most coupled scalar field - hydrodynamical simulations [69, 71, 101], allowing for a reduction in statistical variance. For example, in [69] the authors use $N_b = 32558$ for a weak PT with $v_w = 0.44$, while other simulations in the same study employ $N_b = 988$, 125, or 37, depending on the PT parameters. In [71], simulations of weak PTs involve 5376 bubbles in certain cases, while other weak PTs, as well as

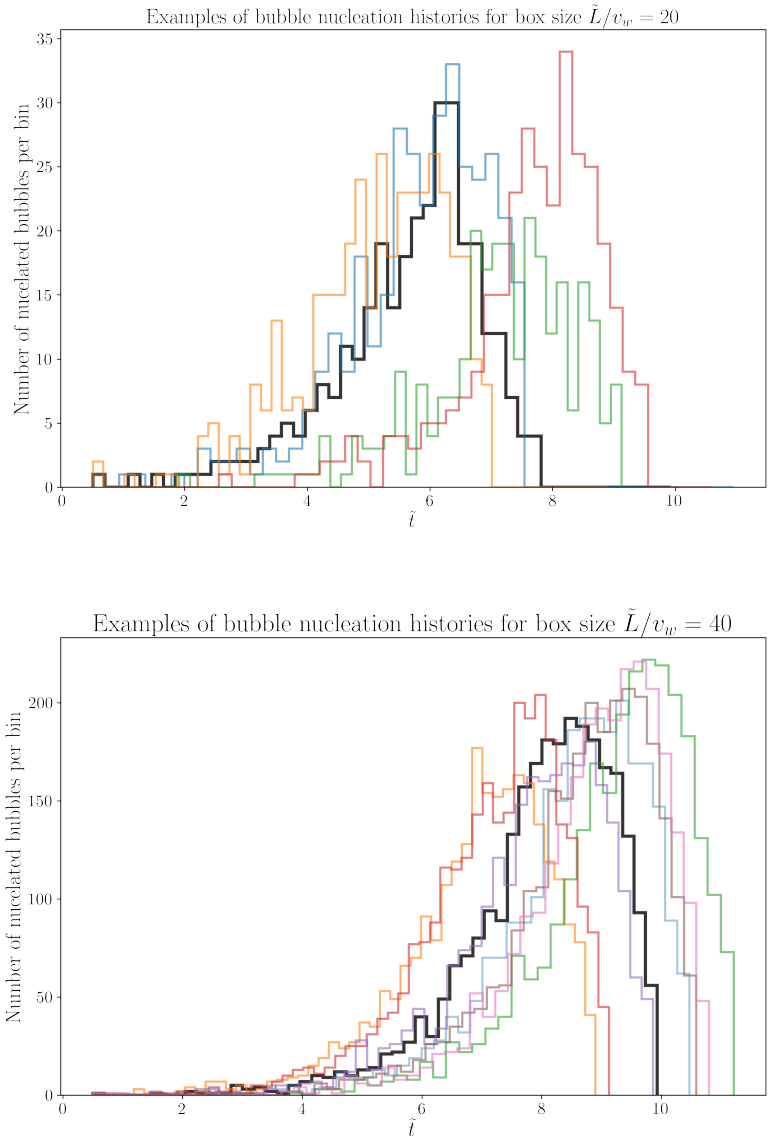

Figure 5: Bubble nucleation histories generated with different random seeds for $\tilde{L}/v_w = 20$ (upper panel) and $\tilde{L}/v_w = 40$ (lower panel). The nucleation times of each bubble nucleation history have been translated to nucleate the first bubble at the same time. Black lines indicate bubble nucleation histories used in the study, while colored lines show different realizations using the same procedure.

intermediate ones, use either 11 or 84 bubbles. Meanwhile, in [101], the authors consistently employ 8 bubbles across all simulations.

In this work, we neglect cosmic expansion during the PT and thus also in the construction of bubble-nucleation histories. In comoving space, one can, in principle, account for expansion by letting the comoving-wall velocity decrease with time. However, since we saw in Section Section 3.1.2 that $\beta/H_* \sim 140$ for the EW PT and that generally, cosmological completes quickly as compared to the Hubble time with $\beta/H_* \sim \mathcal{O}\left(10^{1-5}\right) \gg 1$ [22], neglecting expansion during the course of the PT is expected to be a good approximation.

5.3.6 The encoding of bubbles

In Section 5.2.1 and 5.3.5, I reviewed how space-time nucleation sites can be constructed from the assumption of a uniform-in-space and exponential-in-time nucleation probability. We call the collection of such sites a bubble nucleation history. In Section 5.2.3, I furthermore explain how these sites together with an assumed constant wall velocity v_w, PT strength α, and the bag equation of state enables capturing the macroscopic evolution of the PT without solving for detailed Higgs field dynamics. In this Section, I will review some details regarding how the connection between bubbles and the vacuum state is incorporated into the simulation.

Define the bubble nucleation history as the collection of bubble nucleation sites $\mathcal{B} = \{t_i, \mathbf{x}_i\}$ in accordance with the construction scheme in 5.3.5. A given site $\mathbf{x}$ in the simulation is thus traversed by the wall of bubble i at time

$$t_{\mathbf{x},i} = \frac{|\mathbf{x} - \mathbf{x}_i|}{v_w} + t_i \,. \tag{268}$$

In particular, we know that the vacuum energy at that site changes from ϵ to 0 whenever it is traversed by a bubble wall for the first time, namely, at the time of local symmetry breaking

$$t_{\mathbf{x},SB} = \min\{t_{\mathbf{x},i},\ i \in \mathcal{B}\} \,. \tag{269}$$

The time- and space-varying bag constant $\epsilon(t, \mathbf{x})$ is thus given by

$$\varepsilon(t, \mathbf{x}) = \begin{cases} \varepsilon & \text{if } t < t_{\mathbf{x},SB} \\ 0 & \text{otherwise} \end{cases} \,. \tag{270}$$

At each time step n_0 and lattice site $\mathbf{n}$ of the simulation, expression (270) can be evaluated. While this may seem like a natural approach, it is highly inefficient. For if at each time step and lattice

site (270) is evaluated, one must loop over every bubble in the bubble nucleation history $N_0 N^3$ times, which is computationally very costly given that a typical number of bubbles extends to the thousands in our simulations.

One may, however, trade this inefficiency for some memory: Knowing how to compute $t_{\mathbf{x},SB}$ for one site, we can do it once for all. In particular, I introduce a 3D field t_{SB} of the same size N^3 as the simulation lattice, and compute for each lattice site $\mathbf{n} = \{n_1, n_2, n_3\}$ the time $t_{\mathbf{n},SB}$ of symmetry breaking. This time is then stored in the corresponding site location of t_{SB}, i.e.

$$t_{SB}(\mathbf{n}) \equiv t_{\mathbf{n},SB}\,, \tag{271}$$

where $t_{\mathbf{n},SB}$ should be understood as $t_{\delta x\mathbf{n},SB}$. The population of t_{SB} with the symmetry breaking times needs to be performed only once for all lattice sites $\mathbf{n}$, which makes this approach a factor N_0 more efficient. It comes, however, at the cost of needing to store a large field t_{SB} of size N^3; a price which is more than justified in our case. Once t_{SB} has been computed, I define

$$\varepsilon(t, \mathbf{n}) = \begin{cases} \varepsilon & \text{if } t < t_{SB}(\mathbf{n}) \\ 0 & \text{if } t \geqslant t_{SB}(\mathbf{n}) \end{cases}. \tag{272}$$

which is evaluated at each simulation time step and lattice site to determine the state of the vacuum.

Having established the means by which we track bubbles on the lattice, I would like to discuss a few subtleties regarding what implications inevitably come with this choice. The first point I want to address concerns the discreteness of $t_{SB}(\mathbf{n})$. While the simulations track hydrodynamical variables on discrete lattice sites at discrete time steps, bubbles do not live on the lattice. Therefore, bubble space-time nucleation times are non-discrete, and the positions of bubble walls vary continuously over continuous time. Expression (272) evidently, however, entails no such continuum tracking of the bubble walls as bubble wall crossing times are only stored on the lattice. This comes with some consequences.

Consider, for the sake of concreteness, the case that $N_0 = 2N$. Suppose that at time step n_0, the bubble wall has just reached grid point $(n_x, 0, 0)$ and is moving horizontally along the x-axis. Over the course of the next time step, the bubble wall physically moves half a space step (since the physical size of the lattice $L \propto v_w$). This means that, physically, energy deposition has taken place, which should drive the development of self-similar fluid profiles. However, the choice of (272) makes this energy deposition occur only when the bubble wall traverses the next grid point along the x-axis, or in this case, after 2

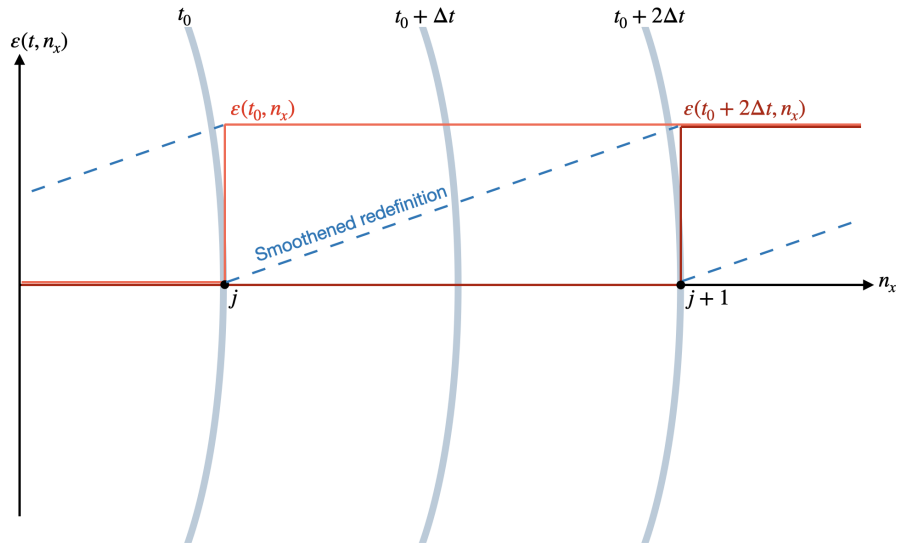

Figure 6: Minimal smoothing of ε to reduce oscillations. Blue curves indicate wall positions at adjacent time steps. Red lines indicate the step function representing bubble boundary conditions, while dotted-blue lines show the redefinition allowing to gradually deposit energy even at wall positions in-between lattice sites.

consecutive time steps. In a more realistic setup, one often has that $N_0 \sim 6N$, such that only in roughly one out of six time steps does energy injection occur along a certain axis. This departure from continuum modeling of the bubble wall position leads to small transients and oscillatory features in the fluid at the bubble wall interface. Attempts to remedy the situation include the smoothing of the wall front over a number of grid points. To this end, the least invasive proposition would be a redefinition of (272) according to

$$\varepsilon(t, \mathbf{n}) = \begin{cases} \varepsilon & \text{if } t < t_{SB}(\mathbf{n}) - \delta x / v_w(\mathbf{n}) \\ \varepsilon \frac{t_{SB}(\mathbf{n}) - t}{\delta x / v_w} & \text{if } t_{SB}(\mathbf{n}) - \delta x / v_w \leqslant t < t_{SB}(\mathbf{n}) \\ 0 & \text{if } t \geqslant t_{SB}(\mathbf{n}) \end{cases} , \tag{273}$$

akin to a linearly connecting $\varepsilon(t, \mathbf{n})$ between the grid points as illustrated in Figure 6.

This allows for a gradual energy transfer, thus helping reduce oscillations while keeping the wall interface as sharp as possible. While this method has been implemented and tested, we find that oscilations are never large enough to cause any issues and are immediately dampened upon bubble collision.

The second point which I want to address concerns the definition of the flux functions $H_{j+1/2,k,l}$, etc, in the KT+RK3 scheme; it is de-

fined on staggered lattice points. $t_{SB}(\mathbf{n})$, however, is not. On staggered lattice points, we therefore choose to approximate

$$\varepsilon(t, j + 1/2, k, l) \approx \frac{\varepsilon(t, j, k, l) + \varepsilon(t, j + 1, k, l)}{2}, \tag{274}$$

etc, which adequately solves the problem.

5.3.7 Computing GW spectra from the 3D Lattice

Ultimately, our primary interest lies in the GW spectra generated by the hydrodynamics of first-order PTs, which the Higgsless simulations are designed to model. With all the necessary components at hand, we are now equipped to compute this spectrum. Due to its critical importance, I will provide a thorough and explicit explanation of the process by which we obtain these spectra.

While simulations constitute invaluable means of probing physics beyond analytical reach, they are ultimately bounded by their intrinsic limitations. An example of such a limitation influential to the GW production is the finite simulation time and box size: Ideally, one would desire to run simulations for long enough that fluid motion is completely dampened upon simulation completion, for in this case, the complete GW spectra are captured. For linear sound waves and neglecting nonlinear dynamics, however, one does not expect the fluid kinetic energy to decay for other reasons than Hubble expansion. Since we neglect expansion, this, therefore, would mean that a very long simulation time is typically necessary, which is often impractical, if not impossible, due to limited computational resources. Furthermore, long simulation times mean that to avoid systematic effects due to limited box size and periodic boundary conditions, resulting in, e.g., sound waves propagating across the simulation volume multiple times, one would need to extend the box size proportionally to the simulation duration. This comes with the consequence of needing to resolve an enormous amount of bubbles, leading to unfeasible requirements on the resolution, or otherwise, non-convergence of self-similar profiles and the consequent under-resolution of the detailed hydrodynamical evolution. This thwarts the reliability of the results. Under-resolving the physics may also lead to excessive numerical viscosity, thus artificially dissipating kinetic energy and, again, thwarting meaningful results.

Optimizing choices of simulation parameters, thus, constitutes a complex procedure where compromises must always be made. As for the simulation duration, it should not be too long compared to the box size. Rather than computing final GW spectra, it is thus more realistic to measure the GW production power, which may be measured during

the limited simulation time. To this end, we introduce the dimensionless GW spectrum growth rate $Q'(q)$, defined by

$$Q'(q) \equiv \frac{q^3\beta}{w_s^2 V T_{GW}} \int \frac{d\Omega_k}{4\pi} \left[\Lambda_{ij,kl} T_{ij}(q,\mathbf{k}\,|\,t_{fin}) T^*_{kl}(q,\mathbf{k}\,|\,t_{fin})\right]_{q=k} . \quad (275)$$

where q is the frequency, w_s is the enthalpy before the PT, V the simulation volume, T_{GW} the GW sourcing time, and $T^{(}_{kl} q,\mathbf{k}\,|\,t_{fin})$ defined in Equation (236). Knowledge of the growth rate Q' then allows computing the GW spectrum as

$$\Omega_{GW}(q) = \mathcal{T}_{GW} \frac{w_s^2 t_{sw}}{4\pi^2 \bar{\rho}_* m_{Pl}^2 \beta} \times Q'(q) = \mathcal{T}_{GW} \frac{4(H_*/\beta)(H_*\, t_{sw})}{3\pi^2} \times Q'(q) , \quad (276)$$

where t_{sw} is the GW sourcing duration, which can, e.g., be assumed to be the time it takes nonlinearities to develop, $t_{sw} \sim R_*/\sqrt{\langle v_f^2\rangle}$, as we discussed in Section 2.2.5, with $R_* \equiv (8\pi)^{1/3} \max(v_w, c_s)/\beta$ and $\sqrt{\langle v_f^2\rangle} \sim \sqrt{K}$. The definition of $Q'(q)$ implies that the Hubble rate H_* at production time need only be specified in post when knowledge of GW spectra for a given ratio H_*/β is desired.

The dimensionless form of Q' is particularly suited to our simulation setup where energies are normalized to w_s, the enthalpy just before the PT in the symmetric phase, and lengths and times to β^{-1}, roughly the inverse duration of the PT. For with this normalization, dimensionful factors in (275) combine to form dimensionless simulation variables. This normalization represents how quantities are stored numerically in the simulation, and I will indicate such variables with a $\tilde{}$. In terms of system variables, Q' can be directly computed as

$$Q' \equiv \frac{\tilde{q}^3}{\tilde{V}\tilde{T}} \int \frac{d\Omega_k}{4\pi} \left[\Lambda_{ij,kl} \tilde{T}_{ij}(\tilde{q},\tilde{\mathbf{k}}\,|\,\tilde{t}_{fin}) \tilde{T}^*_{kl}(\tilde{q},\tilde{\mathbf{k}}\,|\,\tilde{t}_{fin})\right]_{\tilde{q}=|\tilde{\mathbf{k}}|} . \quad (277)$$

To compute the GW spectrum from the lattice, the starting point is a dimensionless form of GW spectrum $Q \equiv \tilde{T} Q'$:

$$Q(\tilde{q}) \equiv \frac{\tilde{q}^3}{\tilde{V}} \int \frac{d\Omega_k}{4\pi} \left[\Lambda_{ij,kl} \tilde{T}_{ij}(\tilde{q},\tilde{\mathbf{k}}) \tilde{T}^*_{kl}(\tilde{q},\tilde{\mathbf{k}})\right]_{\tilde{q}=\tilde{k}} . \quad (278)$$

The first step consists of populating the energy-momentum tensor at each time step. From the simulations, we obtain $\tilde{w}(\mathbf{n})$ and $v^i(\mathbf{n})$ at each time step. Associated with each lattice point, we thus construct the energy-momentum tensor

$$\tilde{T}^{ij}(\mathbf{n}) = \tilde{w}(\mathbf{n}) \gamma^2(\mathbf{n}) v^i(\mathbf{n}) v^j(\mathbf{n}) \quad (279)$$

which constitute six independent three-dimensional fields. Since the second pressure term of the RHS of (209) does not contribute anisotropic stress, it does not source GWs and we shall neglect it.

The second step consists of computing the spatial DFT of (279). For this job, I use the FFTW library [121] as outlined in Section 5.3.2 above. This yields $\tilde{T}_{ij}(\tilde{t}, \tilde{\mathbf{k}})$.

The third step concerns the projection onto the transverse-traceless part of T_{ij}. As for the mapping of dual lattice sites $\tilde{\mathbf{n}}$ to physical momenta $\mathbf{k}$, I use the prescription (255)

$$k_i \equiv k^0_{\mathrm{Lat},i} = \frac{\sin(2\pi\tilde{n}_i/N)}{\delta x},$$

since the sign of the momentum is critical to obtain the correct projection for modes at sites with any $j, k, l \sim N$.

We saw in Section 2.1 that the projection onto the transverse-traceless part can be computed as

$$\Lambda_{ij,kl}(\mathbf{k})T_{ij}(\mathbf{k})T_{kl}(\mathbf{k})^* = T_+(\mathbf{k})T^*_+(\mathbf{k}) + T_\times(\mathbf{k})T^*_\times(\mathbf{k}) \tag{280}$$

where the projection of T_{ij} onto the $+$ and $\times$ polarization basis is defined through

$$T_+(\mathbf{k}) \equiv e^+_{ij}(\mathbf{k})T_{ij}(\mathbf{k}), \quad T_\times(\mathbf{k}) \equiv e^\times_{ij}(\mathbf{k})T^{ij}(\mathbf{k}). \tag{281}$$

The $+$ and $\times$ polarization tensors are defined in Equation 24,

$$e^+_{ij}(\hat{\mathbf{k}}) = \frac{1}{\sqrt{2}}(\hat{\mathbf{u}}_i\hat{\mathbf{u}}_j - \hat{\mathbf{v}}_i\hat{\mathbf{v}}_j) \quad \text{and} \quad e^\times_{ij}(\hat{\mathbf{k}}) = \frac{1}{\sqrt{2}}(\hat{\mathbf{u}}_i\hat{\mathbf{v}}_j + \hat{\mathbf{v}}_i\hat{\mathbf{u}}_j),$$

with mutually orthogonal unit vectors $\hat{\mathbf{u}}$ and $\hat{\mathbf{v}}$ in the plane orthogonal to $\mathbf{k}$. It is in this form that the projection in (275) is numerically implemented. We therefore proceed to compute $T_+(\mathbf{k})$ and $T_\times(\mathbf{k})$.

The $\mathbf{k} = 0$ mode corresponds to a stationary constant background and does not contribute to GW production. Furthermore, with $\mathbf{k} = 0$, the orthonormal basis vectors $\hat{\mathbf{u}}$ and $\hat{\mathbf{v}}$ are ill-defined. In this case, we simply enforce $T_+(0) = T_\times(0) = 0$. For the non-zero modes, define the angles ϕ and θ as the azimuthal and polar angles, respectively, in a spherical coordinate system:

$$\tan\phi = \frac{k_2}{k_1} \quad \cos\theta = \frac{k_3}{k}. \tag{282}$$

Then, we can define the orthonormal basis $\hat{\mathbf{u}}$, $\hat{\mathbf{v}}$, and $\hat{\mathbf{k}}$, as

$$\hat{\mathbf{u}} = \begin{pmatrix} \cos\phi\cos\theta \\ \sin\phi\cos\theta \\ -\sin\theta \end{pmatrix}, \quad \hat{\mathbf{v}} = \begin{pmatrix} -\sin\phi \\ \cos\phi \\ 0 \end{pmatrix}, \quad \hat{\mathbf{k}} = \begin{pmatrix} \cos\phi\sin\theta \\ \sin\phi\sin\theta \\ \cos\theta \end{pmatrix}.$$

(283)

With these vectors at hand, one readily computes the projection of T_{ij} onto the $+$ and $\times$ polarization basis (281).

The fourth step consists of performing the temporal Fourier transform. As explained in Section 5.3.2, in the time direction, we resort to approximating the Fourier transform through its Rieman sum (258) to save memory, i.e. we compute and update for every time step

$$T_{ij}(q, \mathbf{k} \,|\, t) = \sum_{t_n = t_{\text{init}}}^{t} e^{iqt_n} T_{ij}(t_n, \mathbf{k}) \,, \tag{284}$$

where t_{init} is the time at which we start sourcing GWs, which will be $\tilde{t}_{\text{init}} = 16$ for all simulations in the current Chapter, and $\tilde{t} \leqslant \tilde{t}_{\text{fin}}$, with $\tilde{t}_{\text{fin}}$ being the final time of the simulation which will typically be $\tilde{t}_{\text{fin}} = \tilde{t}_{\text{end}} = 32$. Here, we enforce $q = |\mathbf{k}|$, but since the sign of the momentum is unimportant, we instead use the mapping (255)

$$k_i \equiv k^{+/-}_{\text{Lat},i} = 2 \frac{\sin(\pi \tilde{n}_i / N)}{\delta x} \,,$$

from the dual lattice to physical momentum.

The fifth and final step consists of computing the average over shells of equal wave-number $|\mathbf{k}|$. Migrating to the lattice means that the integral over solid angles should be interpreted as an average over wave vectors of equal magnitude $k = q$. Furthermore, to make the definition of the spatial DFT and time integration in Equation 284 consistent with the definition of (275) demands the introduction of factors $\Delta\tilde{x}^6$ and $\Delta\tilde{t}^2$. Thus, the resulting and final form of the dimensionless GW spectrum $Q(\tilde{q})$ which is numerically encoded is

$$Q(\tilde{q}, \tilde{t}) = \frac{\tilde{q}^3 \tilde{V} \Delta\tilde{t}^2}{N^6} \left\langle \left| \tilde{T}_+(\tilde{q}, \tilde{\mathbf{k}} \,|\, \tilde{t}) \right|^2 + \left| \tilde{T}_\times(\tilde{q}, \tilde{\mathbf{k}} \,|\, \tilde{t}) \right|^2 \right\rangle \Bigg|_{\tilde{q} = |\tilde{\mathbf{k}}|} \,. \tag{285}$$

As for the averaging over shells, I employ the hybrid strategy described in Section 5.3.3 involving averaging only over the lattice site of equal physical momenta in the IR while binning in the UV to avoid storing excessive data and smoothen the spectrum.

From the discussion in Section 2.2.4, we understand that the expression (285) is proportional to the present-day GW spectrum had the source immediately vanished at time t. Equation (285) is, therefore, better interpreted not as the resulting GW spectrum but as an intermediate step in the computation of the growth rate $Q'(\tilde{q}, \tilde{t}) = Q(\tilde{q}, \tilde{t})/T_{\text{GW}}$, where $T_{\text{GW}} = \tilde{t} - \tilde{t}_{\text{init}}$, i.e.,

$$Q(\tilde{q}, \tilde{t}) = \frac{\tilde{q}^3 \tilde{V} \Delta\tilde{t}^2}{N^6 T_{\text{GW}}} \left\langle \left| \tilde{T}_+(\tilde{q}, \tilde{\mathbf{k}} \,|\, t) \right|^2 + \left| \tilde{T}_\times(\tilde{q}, \tilde{\mathbf{k}} \,|\, t) \right|^2 \right\rangle \Bigg|_{\tilde{q} = |\tilde{\mathbf{k}}|} \,, \tag{286}$$

which carries the interpretation of the GW growth rate and which is something that we can meaningfully measure in the Higgsless simulations of limited duration.

Since, in the current work, we are interested in weak and intermediate PTs, we expect interactions to be largely linear. Then, from Equation (109, we expect to observe a linear GW spectrum growth rate so that $Q'(\tilde{q})$ is approximately constant in time. In Section 2.2.5, we mentioned that for the linear growth rate to be valid, one must impose that the period of the oscillations be much shorter than t_{sw}, i.e. $kt_{sw} \gg 1$, or equivalently, $kR_* \gg \sqrt{\langle v_f^2 \rangle}$, and that the duration of the sound waves be long compared to the characteristic scale condition $t_{sw}/R_* \sim 1/\sqrt{\langle v_f^2 \rangle} \gg 1$. In our simulations, both of the conditions are satisfied for most wavenumbers away from the IR tail and, in particular, for wavenumbers around the peak, which is of most significant interest.

To render the measurement of the GW growth rate as robust as possible, we switch on GW production at some time $\tilde{t}_{init} = 16$. By this time, the PT has completed (which occurs around $\tilde{t} = 10$), the system is no longer dominated by the largest bubble, and the fluid motion is rather uncorrelated from time to time (thus ensuring the limited support of the UETC) so that effects of the transient initial fluid sound shell collisions do not affect the resulting long term linear growth rate measurement significantly. This ensures the robustness.

5.3.8 Parallelization

Finally, I would like to discuss the parallelization of the Higgsless implementation. To reduce the simulation runtime to manageable scales — ideally on the order of a day — it is essential to employ parallelization techniques. For this purpose, I have utilized OpenMP [124]. OpenMP provides a flexible and efficient framework for parallelizing code over multiple cores within a single node, making it suitable for the computational demands of our simulations.

In our setup, the majority of simulation runs have been executed on the DESY Maxwell cluster, which supports parallelization across up to 256 cores. By leveraging this capability, we significantly decrease the time required for each simulation. This level of parallelization is not just beneficial but necessary to handle the extensive computations involved.

5.4 Evaluating the simulation

Every simulation must be evaluated and tested against some benchmark problem and other evaluating metrics to be trusted. The topic of this Section is to review the results of some of these tests for the Higgsless simulations.

5.4.1 Single-bubble simulations

In the present case, the prototypical benchmark problem to be evaluated against is the recovery of self-similar fluid profiles [86], reviewed in Section 3.1.6. Therefore, before proceeding to run realistic simulations with multiple bubbles, I first run simulations containing only one centrally nucleated bubble and study the resulting hydrodynamical solutions.

For the simulation to be deemed successful, the resulting radial fluid profiles must converge towards the self-similar profiles on reasonable timescales. It is important to note that achieving such performance is not trivial and cannot be assumed a priori, given that the numerical solutions must remain well-behaved even under the discontinuities associated with the bubble wall. This test, therefore, is critical and extremely important not only from the point of view of doing science with the simulations but also for the potential observation that the KT+RK3 scheme indeed presents an adequate means to resolve the violent dynamics, including shocks, with only modest computational resources.

In the panels of figures 7, 8, 9, 10, I show 2D simulation slices and the time evolution of the radial velocity and enthalpy profiles for weak ($\alpha = 00046$) and intermediate ($\alpha = 0.05$) PTs and wall velocities $v_w \in \{0.32, 0.48, 0.60, 0.8\}$. For these simulations, the box size is $\tilde{L} = 20 v_w$ and the resolution $N = 512$. The profiles are obtained from the 2D slices of the simulations in the left column by binning quantities in 500 radial bins from the bubble center.

In these figures, the convergence to the self-similar profiles is striking. Initially, no shock front is observed; rather, there is a transient phase where the fluid reacts to the evolving boundary conditions of the expanding bubble $\epsilon(\mathbf{x}, t)$. As time advances, shocks are generated and sustained, thanks to the robustness of the KT+RK3 scheme (207). For the parameters, $N = 512$, and $\tilde{L} = 20$ and $\tilde{L} = 40$ shocks are evident by $\tilde{t} \gtrsim 1.6$. The first nucleated bubbles, which play a crucial role in the GW spectrum since they carry most of the energy, generally evolve for periods longer than this before colliding. This implies that shocks have already formed by the typical collision time, and the profiles of the

colliding walls have become largely self-similar. In the next Chapter 6, I will perform a more detailed and systematic analysis of what effect insufficient convergence has on the resulting GW spectrum.

For weak PTs ($\alpha = 0.0046$) both deflagrations (e.g. $v_w = 0.4$) and detonations (e.g. $v_w = 0.8$), the structures are well-reproduced. However, for hybrid solutions, the profiles are significantly thinner. This renders the grid resolution insufficient for the thinnest walls to accurately capture the fluid's self-similar shape at the typical collision time. Consequently, it is anticipated that for thin shells, the GW power is somewhat underestimated and that there may be an underestimated separation of scales between the bubble size and sound shell thickness.

For intermediate PTs ($\alpha = 0.05$), deflagrations and detonations are resolved well, as large bubbles exhibit self-similarity at the point of collision. In these scenarios, the hybrid case shows improved performance compared to weak PTs due to the increased shell thickness, and we expect that the GW power is well captured due to the milder separation of scales between the bubble size and sound shell thickness.

I have discussed the convergence of the solutions with increased simulation time. It turns out we can make an illuminating connection with resolution N. To explore the impact of resolution, we run simulations with $N = 64$, $N = 128$, $N = 256$, and $N = 512$, for a few benchmark parameter points. The right panel of figure 11 illustrates the velocity profile at $\tilde{t} = 3.2$ for these values of N. It is evident that the transient stage preceding shock formation is longer for smaller values of N. In fact, there is a resemblance between the left and right panels of figure 11: doubling the time has the same effect as doubling the resolution. This conclusion is somewhat expected, as doubling the time virtually doubles the number of grid points available for the resolution of the self-similar profile. Therefore, doubling the simulation time should have a similar effect as doubling the resolution. I have furthermore confirmed that reducing or increasing δt has no significant impact on the time to self-similar convergence for as long as the choice of δt ensures the stability of the solution. These observations imply that the transient phase of self-similar convergence is a numerical artifact.

Overall, the 3D Higgsless simulation implementation swiftly produces accurate single-bubble wall profiles and sustains precise shock dynamics over time. Notably, the accurate self-similar profile reproduction seems dependent on the parameter α only due to its influence on the shell thickness. This implies that the framework can be extended to model stronger PTs with minimal adjustments, primarily involving the simulation's time step and possibly refining the definition of the local velocity a to preserve stability as outlined in Sec. 4.3. While the examination of stronger PTs is reserved for the next Chapter, our cur-

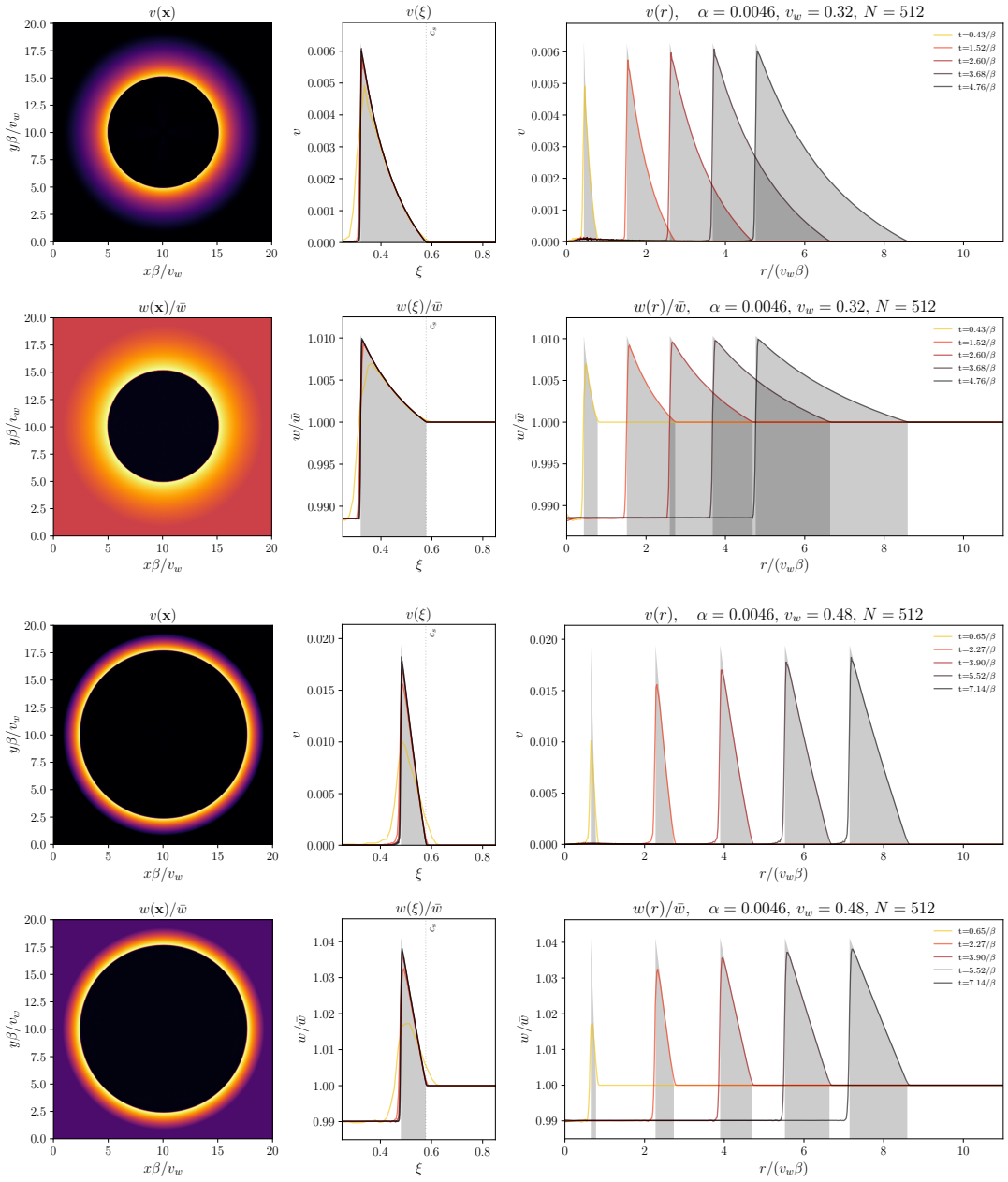

Figure 7: Convergence of self-similar profiles for weak PTs ($\alpha = 0.0046$) and wall velocities $v_w \in \{0.32, 0.48\}$ corresponding to two deflagrations. The box size is $\tilde{L} = 20v_w$ and the resolution $N = 512$. The first and third panels show the radial velocity $|\mathbf{v}|$. The second and fourth panels show the enthalpy w normalized to the enthalpy in the far symmetric phase w_s. The profiles are obtained from the 2D slices of the simulations in the left column by binning quantities in 500 radial bins from the bubble center. The middle (right) column shows fluid profiles in the self-similar coordinate $\xi = r/t$ (radial coordinate r) at various times to indicate the convergence to self-similar profiles with time. Gray regions indicate the self-similar profiles reviewed in Section 3.1.6.

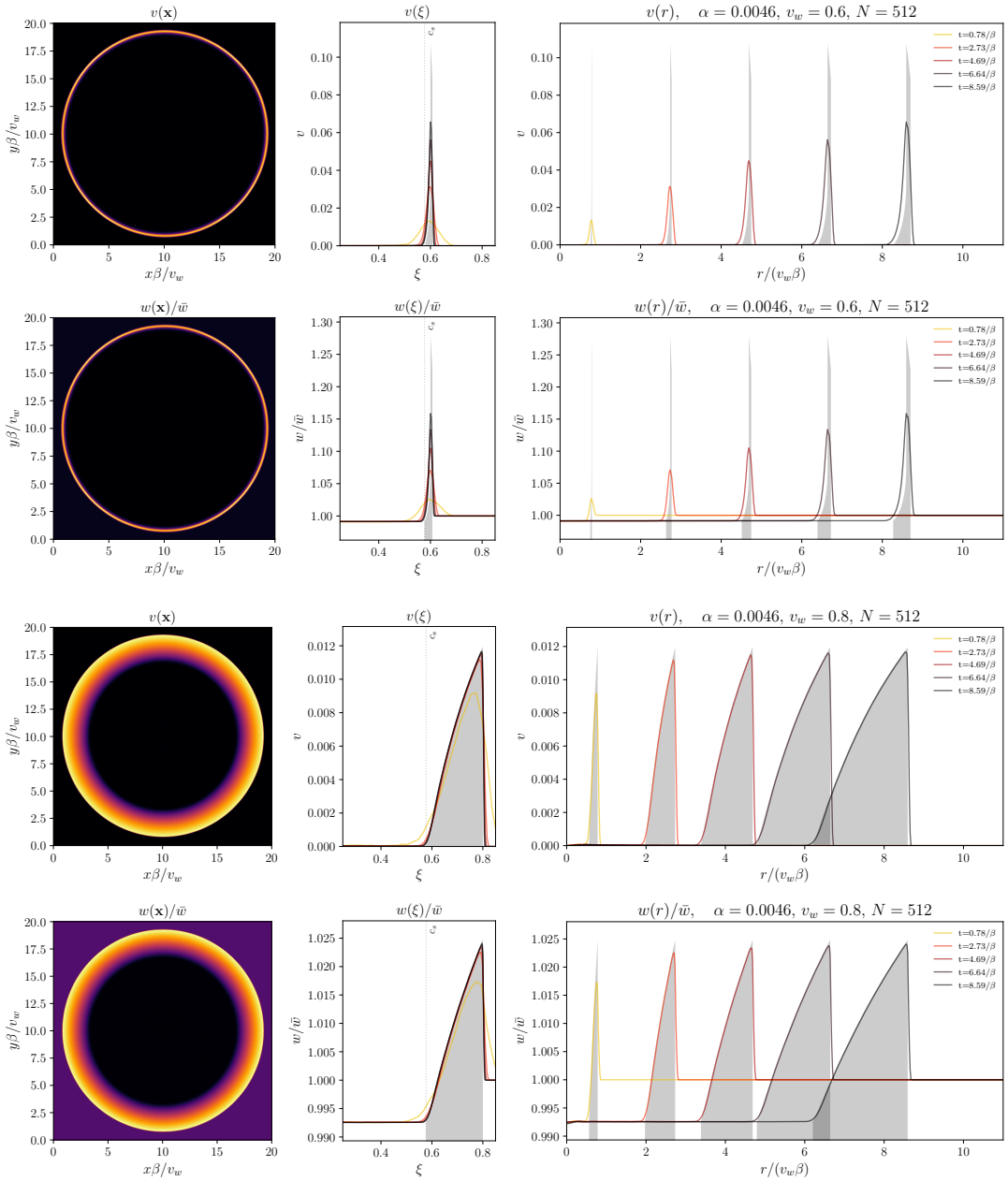

Figure 8: Same as figure 7, but for $v_w \in \{0.60, 0.80\}$ corresponding to a hybrid and detonation.

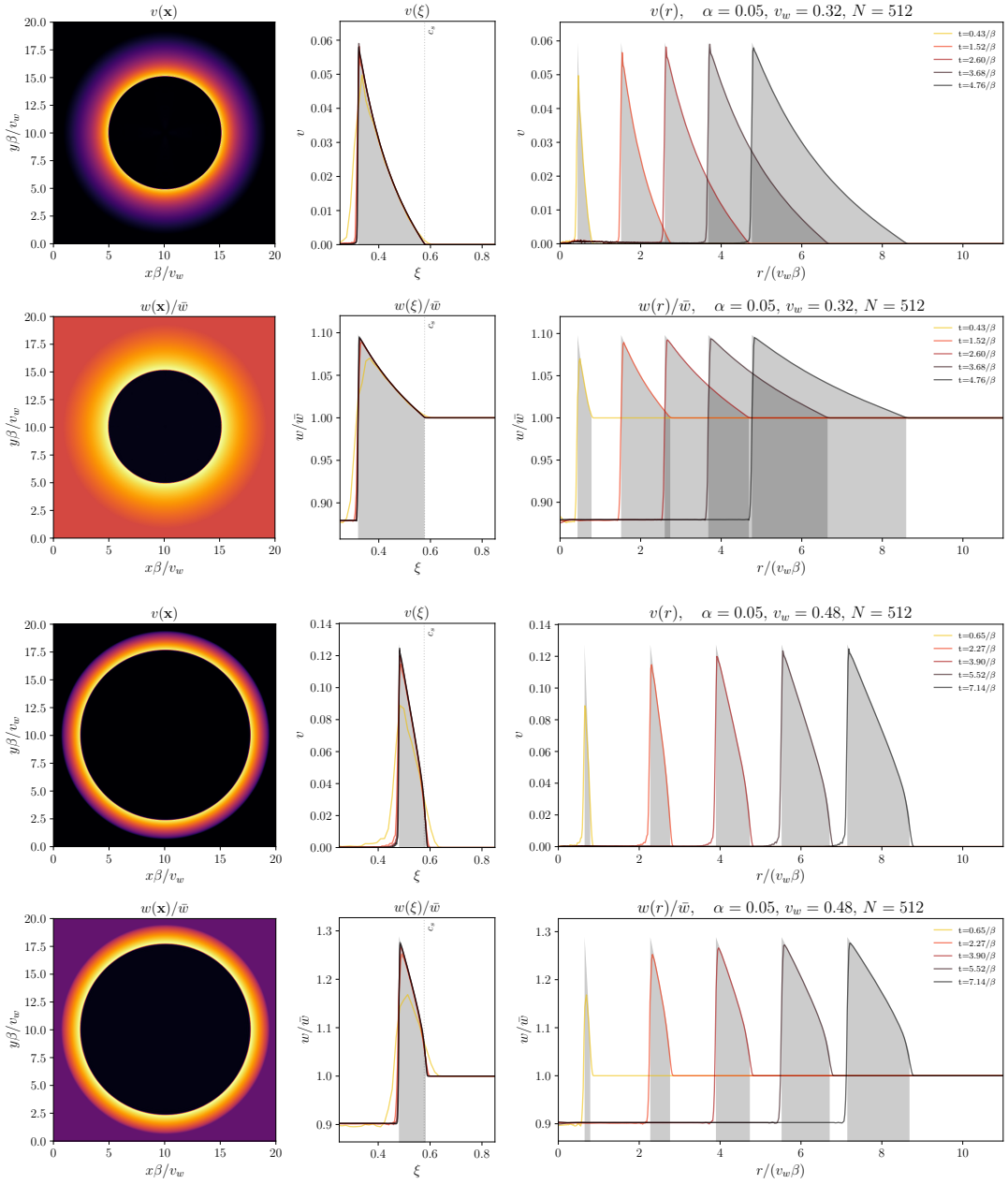

Figure 9: Same as figure 7, but for intermediate PTs ($\alpha = 0.05$).

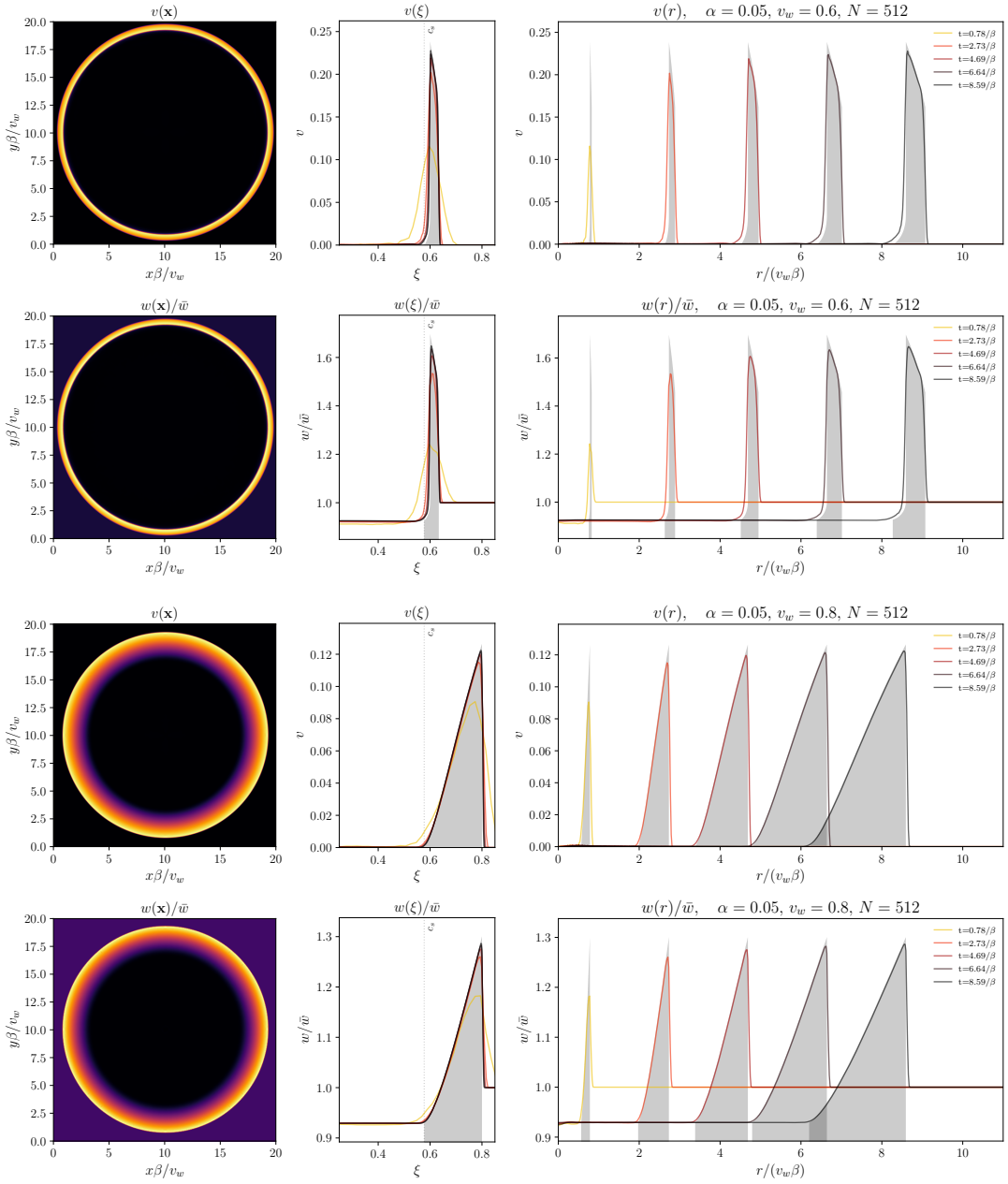

Figure 10: Same as figure 7, but for intermediate PTs and $v_w \in \{0.60, 0.80\}$.

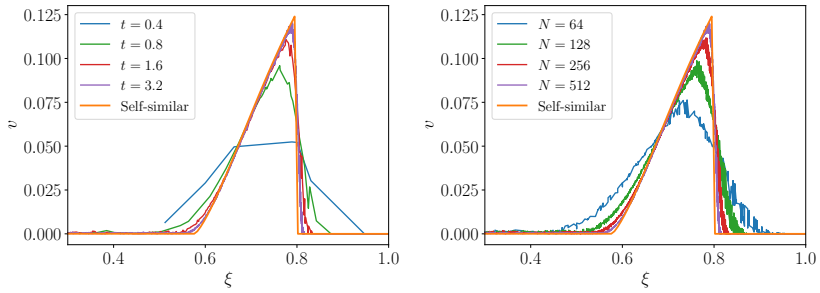

Figure 11: On the left side, the time evolution of the velocity profile as a function of $\xi \equiv r/t$ is depicted arising from a single bubble nucleated in a simulation box with dimensions $\tilde{L} = 20 v_w$ and resolution $N = 512$. The wall velocity is $v_w = 0.8$, and the PT strength $\alpha = 0.05$. On the right, the velocity profile is shown as a function of $\xi \equiv r/t$ for different values of N at $\tilde{t} = 3.2$, keeping $\tilde{L}/v_w$, v_w, and α constant. In both panels, 100,000 random points from the lattice are selected and re-scaled according to the respective simulation time to present the result in the self-similar coordinate ξ. The self-similar solution from [86] is highlighted in orange.

rent study aligns with established literature [67, 71] by focusing on weak ($\alpha = 0.0046$) and intermediate ($\alpha = 0.05$) PTs.

In conclusion, the robustness and precision of the 3D Higgsless simulation framework, as demonstrated in resolving self-similar profiles, positions it as a powerful tool for studying PTs with multiple bubbles. Moreover, the exceptionally high resolution and efficiency of the KT+RK3 scheme (207) is evident in its capability to evolve and sustain shocks.

5.4.2 Energy-momentum conservation

Another critically important point to examine is energy-momentum conservation in the simulations as demanding this ensures the fidelity of the fluid solutions. The failure of simulations to conserve energy and momentum implies that the solutions deviate from the actual physical behavior. At the same time, adequate energy-momentum conservation may indicate that simulation results are robust.

To demonstrate energy-momentum conservation, I illustrate the time-evolution of the lattice averaged values of each component of $K^\mu := T^{\mu 0}$ in Figure 12 for multi-bubble simulations (see Section 5.5.1). Given that before the PT $\langle K^0 \rangle / w_s = \frac{3}{4}(1+\alpha)$, we subtract this contribution and instead plot $\langle K^0 \rangle / w_s - \frac{3}{4}(1+\alpha)$. It is evident from the plot that all conserved quantities are conserved to within machine precision, with deviations from zero at worst as large $\sim 10^{-12}$. This means that energy and momentum are optimally conserved.

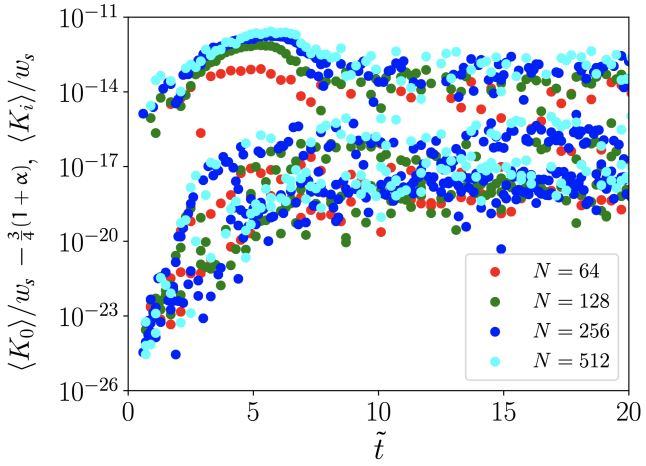

Figure 12: Time evolution of $\langle K^\mu \rangle$ for an intermediate PT $\alpha = 0.05$ and different grid sizes ($N = 64, 128, 256$ and 512). The wall velocity $v_w = 0.8$ corresponds to a detonation. The initial energy density is $K_0/w_s = \frac{3}{4}(1+\alpha)$, where w_s denotes the enthalpy density before the PT.

It is noteworthy that this result was anticipated beforehand since, as we saw in Section 4.3.1, the KT scheme implemented as a solver for a hyperbolic conservation law exactly conserves $\mathbf{u}$ (the conserved quantities) when periodic boundary conditions are used.

5.4.3 Extrapolation of the kinetic energy

In this Section, we comment on the time evolution of the kinetic energy of the fluid as well as the convergence with increasing resolution. Even though the kinetic energy is not conserved per se, it should be conserved on average as long as fluctuations are small enough that the fluid can be treated as a superposition of freely propagating plane waves and numerical viscosity is small.

In the left panel of Figure 13, two probes of the fluid kinetic energy as a function of time for intermediate PTs with $v_w = 0.8$: v^2 (solid line) and $wv^2\gamma^2$ (dashed line) are plotted. Different colors represent various grid resolutions N. It is observed that the kinetic energy saturates around $\tilde{t} = 7$, marking the completion of the PT. Increasing the resolution results in a substantial rise in kinetic energy, although the difference between $N = 256$ and $N = 512$ is relatively small. Since the GW spectrum is roughly proportional to v^4, the kinetic energy can be extrapolated to infinite simulation resolution to estimate the potential underestimation of the GW spectrum.

In the right panel of Figure 13, I show the kinetic energy as a function of grid resolution for weak (lower lines) and intermediate PTs (up-

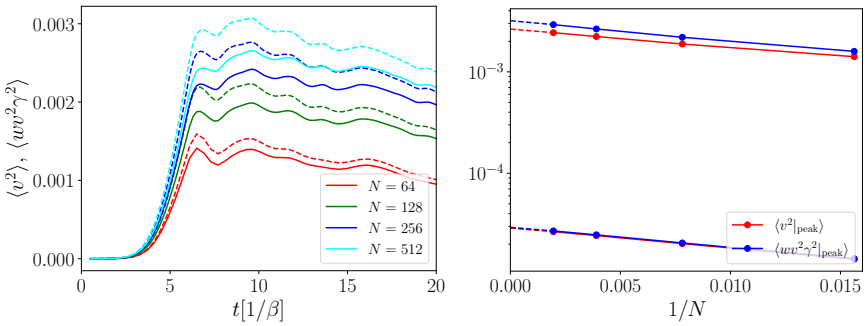

Figure 13: *Left figure:* The time evolution of the kinetic energy for different box sizes N for an intermediate PT with $v_w = 0.8$ is plotted. Dashed lines indicate $\langle wv^2\gamma^2 \rangle$ and solid lines $\langle v^2 \rangle$. *Right figure:* The kinetic energy value at the first peak (around $\tilde{t} \simeq 7$) as a function of N for weak (lower lines) and intermediate (upper lines). Dashed lines indicate extrapolation to infinity simulation resolution.

per lines). The dashed lines indicate the extrapolated values for infinite resolution. This extrapolation suggests a 10% loss in kinetic energy for both weak and intermediate PTs, which implies an approximate 20% underestimation of the GW spectrum. A more detailed analysis of kinetic energy underestimation and a refined extrapolation scheme to improve measurements will be discussed in Chapter 6.

5.5 Numerical results

In this Section, I will present numerical results for simulation runs based on realistic exponential-in-time bubble nucleation histories and the resulting GW production.

5.5.1 Multi-bubble simulations

Having successfully passed the evaluations of the previous Section, the Higgsless simulation code is ready to be used in realistic multiple-bubble scenarios to extract information about the GW spectrum. To this end, we run simulations of box size $\tilde{L} = 20v_w$ and $\tilde{L} = 40v_w$ for which exponential-in-time bubble nucleation histories have been constructed according to the prescription in Section 5.3.5. The resolution is always $N = 512$ while the number of time steps is chosen to ensure $\delta t/\delta x < 1/4$, which we empirically find to yield excellent stability. We run the simulations from $\tilde{t} = 0$ until $\tilde{t} = 32$ and source GWs from $\tilde{t}_{\text{init}} = 16$ to respect the discussion in Section 5.3.7. With this setup, we scan over the parameter space $v_w \in \{0.32, 0.36, \ldots 0.8\}$ and $\alpha \in \{0.0046, 0.05\}$, resulting in 52 simulations.

To begin with, I wish to present a few 2D time slices of the simulation to illustrate the rich dynamics and geometry of the colliding fluid sound shells. I show in figures 14, 15, and 16 central 2D simulation slices of the fluid velocity $|\mathbf{v}(\tilde{\mathbf{x}})|$ and $w(\tilde{\mathbf{x}})$ at four different simulation times for weak and intermediate PTs and box size $\tilde{L} = 40v_w$. The first three slices are chosen at equidistant times to show the bubble evolution before percolation, while the fourth slice is at the end of the simulation at $\tilde{t} = 32$ to highlight the long-term evolution. These parameter choices correspond to deflagrations, hybrids, and detonations, and should constitute a representative subset of simulations exhibiting qualitatively different features.

In these figures, we note that, initially, the bubble size is the predominant physical scale. At later stages, the typical sound-shell thickness associated with the average bubble size at collision appears to be the dominant scale. Generally, the typical bubble size or, equivalently, the average bubble separation at collision R_* defined in Equation 135 and shell thickness for that R_* are the two predominant scales, which we expect to determine the shape of the GW spectrum.

The panels of Figures 14, 15, and 16 are outlined to facilitate comparison between weak and intermediate PTs. In the first three time steps, despite the larger fluid velocities and enthalpy of the intermediate PT, the evolution for the two choices of α appears morphologically very similar. However, when comparing the slices at the final time step, $\tilde{t} = 32$, more pronounced differences emerge.

For weak PTs, the dynamics initially support sharp features associated with the fluid profiles, but these features become smoothed after percolation due to free propagation. In contrast, intermediate PTs exhibit sharper features even toward the end of the simulations. These sharp features correspond to large gradient phenomena, or shocks, which may develop spontaneously due to nonlinear dynamics.

Typical fluid velocities are 0.005 and 0.05 for weak and intermediate PTs, respectively, and typical shell widths at collision are approximately $1/\beta$. Generally, shocks are expected to develop on timescales of $\sim l/v$, where l is a characteristic length scale and v is a characteristic velocity. Thus, we estimate the shock formation times to be around $200/\beta$ for weak PTs and $20/\beta$ for intermediate PTs. According to these crude estimates, shocks should begin to appear towards the end of simulations of intermediate PTs, while in simulations of weak PTs, we do not expect to see such features. This aligns with our visual observations.

Overall, we observe the stability of the solutions which appear well-behaved throughout the entire simulation duration. Having in our possession detailed knowledge about the energy and momentum of the system at each time step, and having concluded that the simulation

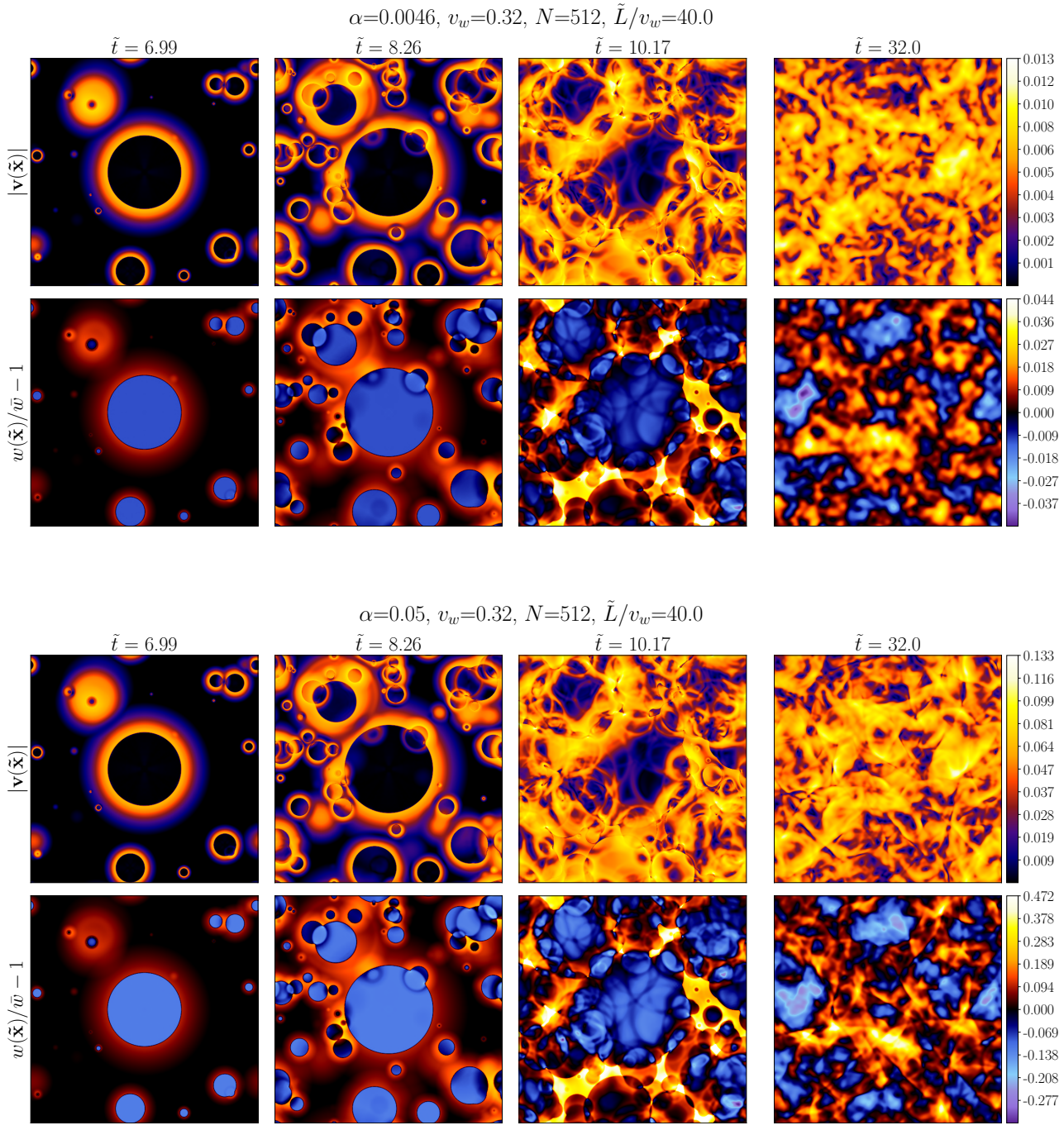

Figure 14: Central 2D simulation slices of the fluid velocity amplitude $|\mathbf{v}(\tilde{\mathbf{x}})|$ and enthalpy $w(\tilde{\mathbf{x}})$. The resolution is $N = 512$ and the box size $\tilde{L} = 40v_w$. The first three slices are chosen at equidistant times to show the bubble evolution before percolation while the fourth slice is at the end of the simulation to display the long-term behaviour. Upper (lower) panels show a weak (intermediate) PT with wall velocity $v_w = 0.32$ corresponding to deflagrations.

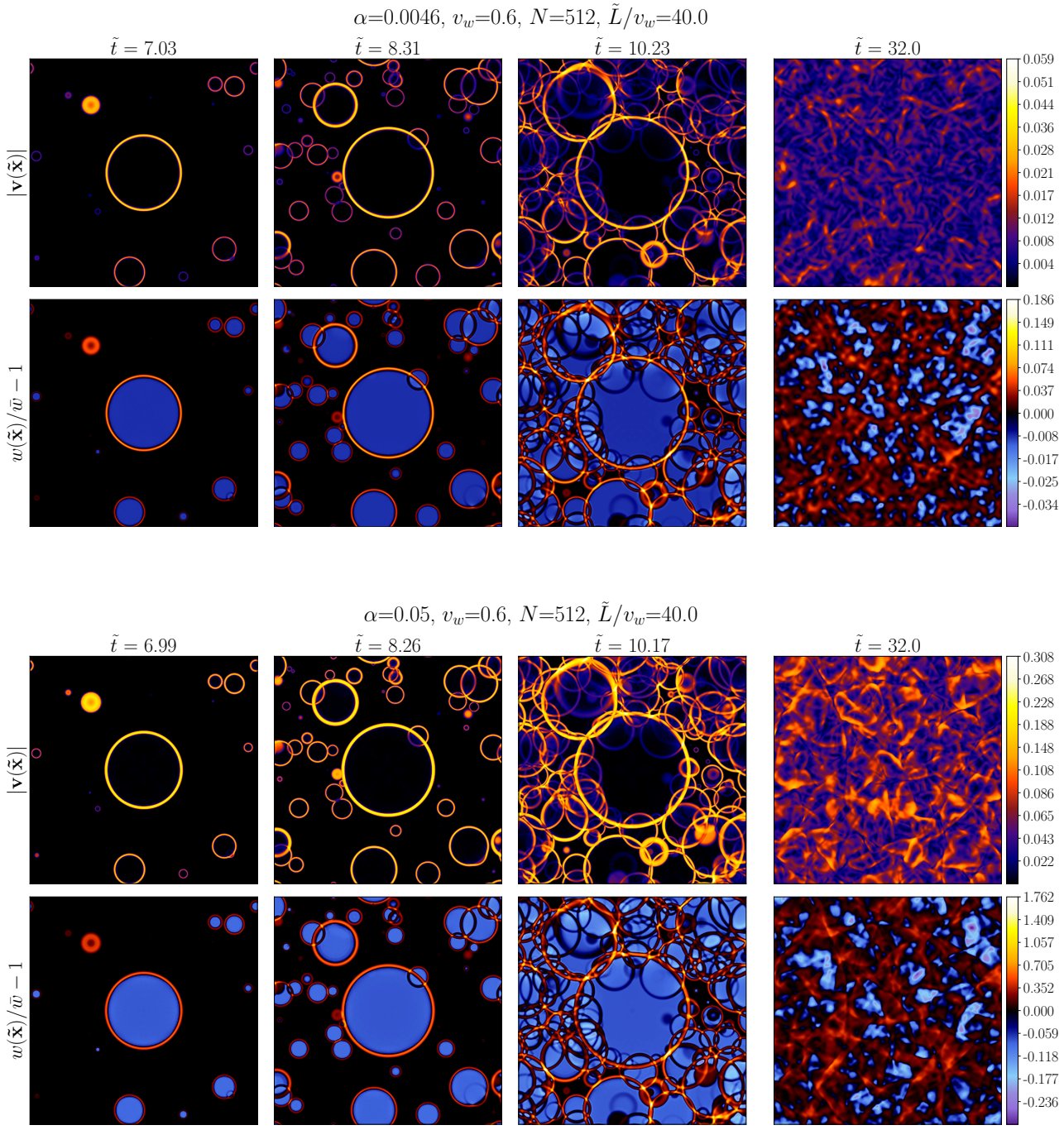

Figure 15: Same as in figure 14 but with $v_w = 0.6$ corresponding to hybrids.

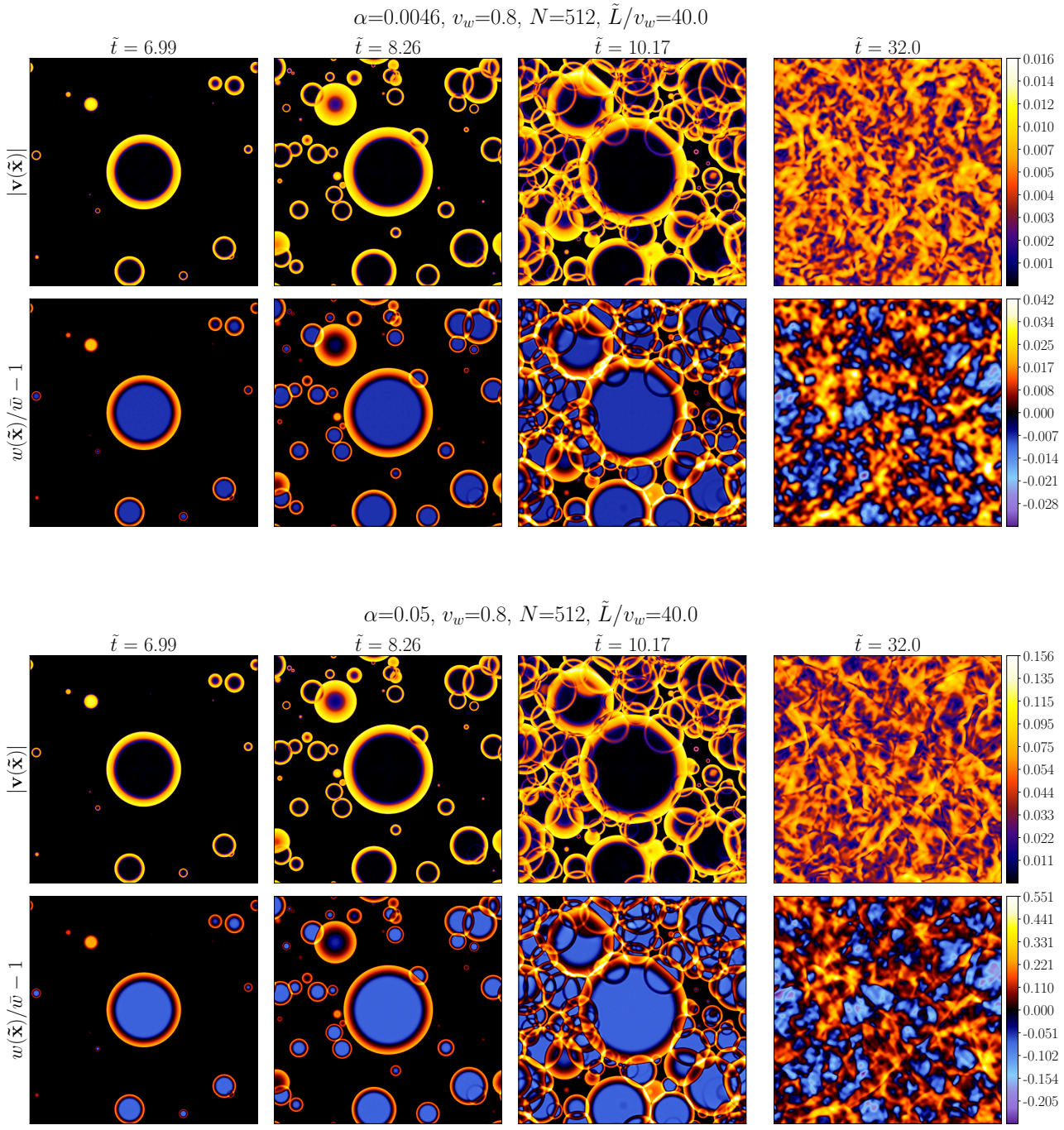

Figure 16: Same as in figure 14 but with $v_w = 0.80$ corresponding to detonations.

results are reliable, we proceed to make use of this information and compute the associated GW production.

5.5.2 GW production

To set the stage for this Section, in Figure 17, I present a few illustrative examples of the GW spectrum growth rate Q' as measured in the simulations according to (286) and which is related to the GW spectrum through (276). In this figure, the black dots represent individual data points, while the colored line segments represent a fit which is introduced and discussed in Section 5.5.2.2.

5.5.2.1 Impact of the simulation box size, time, resolution, on the GW spectrum

Before presenting the results for the GW spectral shape and amplitude, it is essential to first examine how the GW spectrum is affected by our numerical choices. In this Section, I will explore the influence of box size $\tilde{L}$, grid resolution N, and simulation time $\tilde{T}$, to elucidate the numerical factors that could impact the interpretation of the GW spectra, as discussed later in Section 5.5.2.2.

IMPACT OF BOX SIZE AND RESOLUTION Figure 18, in which I illustrate results for box sizes $\tilde{L} = 20v_w$ and $\tilde{L} = 40v_w$ with $N = 512$, as well as one spectrum with $\tilde{L} = 20v_w$ and $N = 256$, presents an illustrative example. To distinguish the latter spectrum, it has been vertically shifted by a factor of 0.85, as the data points would otherwise overlap. The number of bubbles is approximately $N_b \sim 300$ for the smaller box and ~ 2700 for the larger box.

The integration time for the Fourier transformation in 284 is chosen to range from $\tilde{t} = 16$ to $\tilde{t} = 32$ for all simulations. This integration range is selected to minimize contributions from fluid profile collision before percolation (as discussed in Section 5.3.7), while ensuring that the first nucleated bubble does not have sufficient time to collide with its mirror images during this integration window (this is at least true for the larger simulation box size $\tilde{L} = 40v_w$).

The softest modes are characterized by $\tilde{k}_{IR} = \frac{2\pi}{\tilde{L}}$, which translates to $\tilde{k}_{IR} \sim 0.16/v_w$ and $\tilde{k}_{IR} \sim 0.31/v_w$ for simulation box sizes $\tilde{L} = 40v_w$ and $\tilde{L} = 20v_w$, respectively. Consequently, the softest modes are tracked over as little as one and two oscillations (for the most critical v_w) in the Fourier transformation with respect to time. Thus, caution is required when interpreting the GW spectrum at the lowest frequency points. This issue is further discussed in Section 5.5.2.1.

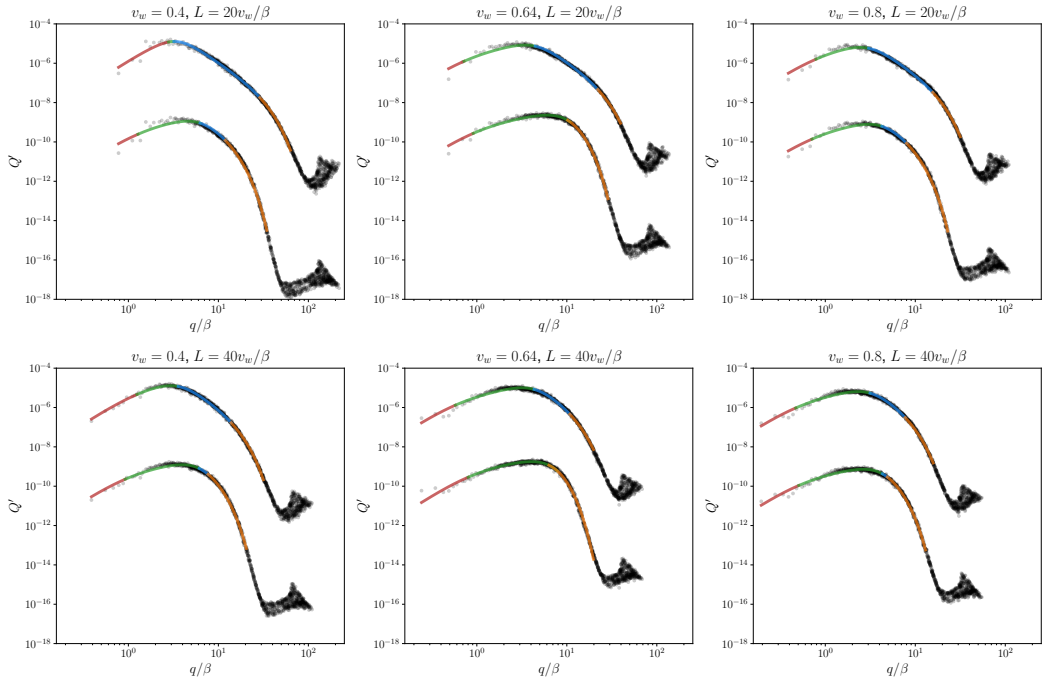

Figure 17: A few example spectra for weak ($\alpha = 0.0046$, lower lines) and intermediate ($\alpha = 0.05$, upper lines) PTs with N $= 512$. The specific parameters for these PTs are detailed in the plot subtitles. The colored lines represent the shape function described in Equation (290), with distinct colors indicating the regions of different power-law indices 3 (red), 1 (green), and -3 (blue), as well as the regime of exponential damping (orange), separated by q_0, q_1, and q_e.

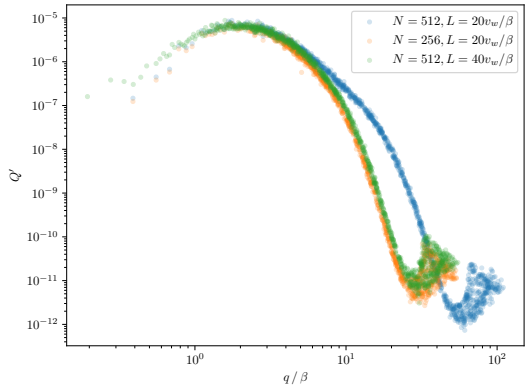

Figure 18: Example of the impact of the box size L and grid size N on the resulting GW spectrum. In this example we use $v_w = 0.8$ and intermediate strength ($\alpha = 0.05$). Note that in order to distinguish orange dots from green and blue, the orange dots have been manually shifted to lower values by a factor of 0.85 as dots would otherwise overlap.

Taking a closer look at the spectra from box size $\tilde{L} = 20 v_w$ in Figure 18 (orange and blue dots), it is evident that the IR part of the GW spectrum obtained from smaller resolution $N = 256$ and larger resolution $N = 512$ agree to a high degree, while the UV parts differ due to the increased dynamical depth of $N = 512$. Doubling the box size to $\tilde{L} = 40 v_w$ (green dots) implies more bubble nucleations and thus better sample statistics as well as halving the magnitude of k_{IR}. Doubling the box size, however, also reduces the dynamical depth since the number of grid points available to resolve the fluid profiles is effectively halved (in the radial direction). Therefore, the spectrum from larger resolution $N = 512$ and box size $\tilde{L} = 40 v_w$ extend the IR part to smaller frequencies and improve statistics while compromising the resolution of the UV part. It is, therefore, expected that $N = 512$ and $\tilde{L} = 40 v_w$ agrees with the UV part of the smaller resolution $N = 256$ and box size $\tilde{L} = 20 v_w$, while some differences are expected in the IR. Figure 18 confirms this expectation.

To conclude, a large box size promotes IR statistics, while a small box size promotes the adequate resolution of UV physics by increasing the dynamical range. Which box size is more optimal thus depends on the measurement which is made. We will elaborate on this point in forthcoming Sections.

IMPACT OF BOX SIZE AND DURATION To study the IR tail of the spectrum in more detail, we run simulations for an even larger box size, $\tilde{L} = 80 v_w$, which implies $\sim$ 20.000 bubbles and thus excellent sample statistics. We run these simulations assuming a PT of intermediate strength and wall velocity $v_w = 0.8$. For the purpose of illuminating the GW spectrum IR part's dependence on some of the complications addressed above, we run these simulations for different simulation durations $\tilde{t}_{fin} \in \{32, 64, 128, 256\}$ with respective time integration windows $[16, 32]$, $[32, 64]$, $[32, 128]$ and $[32, 256]$. The corresponding GW spectrum results are shown in figure 19.

A straightforward interpretation of the IR tail of the spectrum is complicated by several factors. First, to accurately capture the late-time behavior of the system, integration should begin late enough to minimize the contribution from bubble collisions during percolation to the spectrum. Second, correctly capturing the modes in the Fourier transformation with respect to time requires tracking at least $\sim$ 10 oscillations, which argues for longer integration times. However, simulating longer than $\sim L/(2 \max(v_w, c_s)$ results in the first bubble starting to interact with its mirror images, leading to IR artifacts.

The situation is thus challenging and compromises must always be made. Overall, however, a plausibly near-optimal compromise is to run simulations until $T \sim L$ and to neglect the modes in the deep IR. This

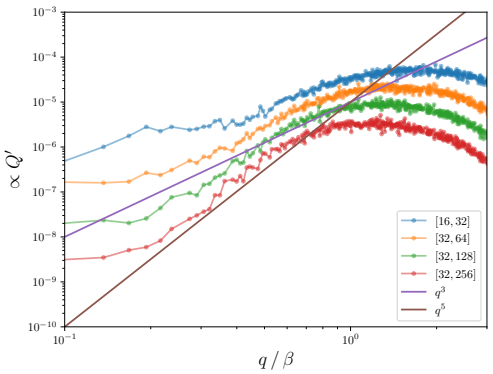

Figure 19: The IR tail of GW spectra obtained from simulations of box size $\tilde{L} = 80v_w$ and resolution $N = 512$ for a PT of intermediate strength, $v_w = 0.8$, and different simulation durations and integration time windows (in units of $1/\beta$) as specified in the plot legends. The lines are shifted by factors of 2 relative to each other to make them better visible. For reference, lines q^3 and q^5 are included.

approach corresponds to the blue and orange spectra, which appear to scale approximately as k^3 in the IR. We will thus employ in the main text this choice of IR scaling.

While we consider the IR part of the spectrum unreliable, it is worth noting that longer integration times result in a slightly steeper decay in the deep IR. Ultimately, shedding light on this observation and the general IR scaling behavior requires even larger simulations and we leave it for future work.

Having addressed how numerical choices affect the resulting GW production and how we can best mitigate such numerical artifacts, let us proceed to discuss the, perhaps more interesting, physical features of the GW spectra and production.

5.5.2.2 The spectral shape and amplitude

We have briefly discussed the presence of two predominant length scales: the sound shell thickness and typical bubble size. As we are about to see, the GW spectra exhibit features at these scales. A spectral shape that accommodates two such scales is a doubly broken power law. For this power law, we identify three regimes: the IR, at frequencies $q < q_0$ (note that $k = q$) identified by a characteristic spectral index n_0, an intermediate regime at $q_0 < q < q_1$ characterized by some spectral index n_1, and a UV regime above some scale $q > q_1$ with spectral index n_2. In our measured spectra, we furthermore observe an exponential damping in the far UV, which must be accounted

for. To this end, we additionally modify the broken power law prescription by introducing an exponential damping factor in the UV beyond some scale q_e. In this description, the resulting GW spectral shape can be parameterized as

$$\Omega'(q) = \Omega'_{\rm int} \times S(q)\,, \tag{287}$$

where

$$S(q) = S_0 \times \frac{(q/q_0)^{n_0}}{1+(q/q_0)^{n_0-n_1}[1+(q/q_1)^{n_1-n_2}]} \times e^{-(q/q_e)^2}\,. \tag{288}$$

The shape function is normalized such that $\int \mathrm{d}\ln q\, S(q) = 1$. The integrated growth rate is defined as

$$\Omega'_{\rm int} = \int \mathrm{d}\ln q\, \Omega'(q)\,. \tag{289}$$

The spectral shape function (288) has six free parameters. As for the scales q_0, q_1, and q_e, we are interested in identifying their dependence on the PT parameters the strength α and the wall velocity v_w. To extract these parameters, we will perform a fit of the shape function to the measured GW spectra. Since these parameters directly control the underlying scales of the problem, we expect q_0 and q_1 to vary as we scan over parameter space.

As for the spectral indices n_0, n_1, and n_2, one could in principle allow them to vary freely when performing the fit. However, with 6 free parameters, one introduces degeneracies that will inevitably produce a better fit at the cost of possibly thwarting precise extraction and interpretation of the remaining parameters. Furthermore, robustly measuring the spectral indices demands substantial resolution of both the UV and IR tails, which is arguably not the case. Since, as we shall see, we find that our data is very well captured assuming fixed values $n_0 = 3$, $n_1 = 1$, and $n_2 = -3$, we refrain from a free spectral index approach and always use these values in the forthcoming fit. First and foremost, we make this decision since this particular choice of indices is in excellent agreement with our data. Furthermore, note that $n_0 = 3$ was justified in Section 5.5.2.1, while the choice $n_1 = 1$ and $n_2 = -3$ is consistent with findings in [25, 67, 69–72, 101], thus placing our decision to fix the spectral indices on solid ground.

With this choice of spectral indices, the spectral shape function becomes

$$S(q) = S_0 \times \frac{(q/q_0)^3}{1+(q/q_0)^2[1+(q/q_1)^4]} \times e^{-(q/q_e)^2}\,. \tag{290}$$

Note that in this form, q_0 constitutes a knee separating the IR from the intermediate regime while q_1 constitutes the peak [1].

1 Strictly speaking, q_1 is not exactly at the peak location. It is, however, always sufficiently close to the spectral maximum that we will simply call it the peak.

We fit Equation (290) to our numerically derived Q′ spectra obtained from simulations with resolution $N = 512$ and box sizes $\tilde{L} = 20v_w$ and $\tilde{L} = 40v_w$ encompassing a parameter scan over $\alpha \in \{0.0046, 0.05\}$ and $v_w \in \{0.32, 0.36, \ldots, 0.8\}$, and thus extract spectral features from our data. Resulting fits are shown in figure 17 for the representative parameter choices $\alpha \in \{0.0046, 0.05\}$ and $v_w \in \{0.4, 0.6, 0.8\}$. The regions separated by q_0, q_1, and q_e are depicted with contrasting colors: the IR is depicted in red, the intermediate regime in green, the UV in blue, and exponential damping in orange.

The parameters in Figure 17 have been selected to highlight various asymptotic behaviors of the spectra. For large simulation boxes, the IR behavior is most discernible, as seen in the bottom panel. Conversely, for smaller box sizes and generic wall velocities, the UV tail is more apparent, as seen in the upper panel. In the case of weak PTs and wall velocities approaching the Jouguet velocities $v_{CJ} = 0.63$ (see Equation (164)), the plateau between the bubble size and the shell thickness is most prominent, as depicted in the middle panels. It is also observed that exponential damping due to numerical viscosity is more pronounced in weaker PTs, as indicated by the lower lines.

In the fitting procedure, we impose the constraint that $q_0 < q_1 < q_e$. For the smaller box size, the first knee q_0 might be measured with some degree of inaccuracy, generally resulting in an overestimated value for q_0. Similarly, when there is an extended plateau with $q_1 \gg q_0$, the exponential decay in the UV region may impede the accurate determination of the peak q_1, as observed for the weak PT in the top middle panel, for which we see that the fit prefers $q_1 = q_e$.

Motivated by these observations, we will utilize simulations with larger box sizes ($\tilde{L} = 40v_w$) to measure the IR quantity q_0, and simulations with smaller box sizes ($\tilde{L} = 20v_w$) to measure q_0 and q_e. For these choices, Figure 20 presents our final results. A comparison between inferred parameters from both small and large box sizes is shown in Figure 21 of the next Section 5.5.2.3.

In the top left panel of Figure 20, inferred values of q_0 over the parameter scan are shown (for box size $\tilde{L} = 40v_w$). We note that for PTs of intermediate strength, a clear downward trend in q_0 is observable. However, for weak PTs, a notable feature appears close to the speed of sound. Our data thus indicate that the IR knee has quite a complex behavior.

The top right panel of figure 20 shows inferred values of q_1 and q_e over the parameter scan (for box size $\tilde{L} = 20v_w$) together with the inverse shell thickness $1/\xi_{\text{shell}}$. The shell thickness is defined from self-similar profiles (see Section 3.1.6):

$$\xi_{\text{shell}} := \xi_{\text{front}} - \xi_{\text{rear}}, \tag{291}$$

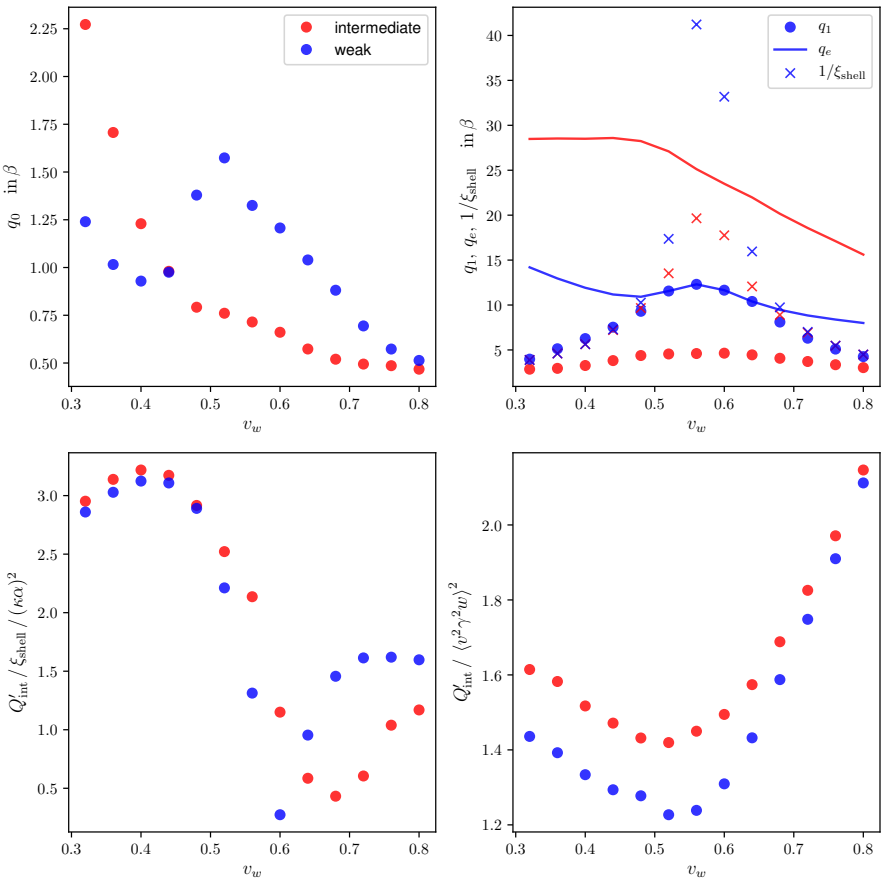

Figure 20: *Upper panel:* The extracted fitting parameters q_0, q_1, and q_e as functions of the wall velocity. Blue (red) points correspond to weak (intermediate) PTs with $\alpha = 0.0046$ ($\alpha = 0.05$). In the upper left figure, we show the IR knee position q_0 for $\tilde{L} = 40 v_w$. In the upper right figure, we show the UV peak q_1 (dots), the shell thickness (crosses) defined in Equation (291), and the exponential damping q_e (solid lines) for $\tilde{L} = 20 v_w$. *Lower panel*: The integral of the GW spectrum growth rate $Q'_{\rm int}$ over momenta, defined in Equation (289), normalized by $\xi_{\rm shell}(\kappa\alpha)^2$ (left) and by the kinetic energy squared $\langle v^2\gamma^2 w\rangle^2$ measured in the lattice (right).

where

$$\xi_{\text{front}} = \begin{cases} \xi_{\text{shock}} & \text{(deflagration, hybrid)} \\ \xi_w & \text{(detonation)} \end{cases}, \tag{292}$$

$$\xi_{\text{rear}} = \begin{cases} \xi_w & \text{(deflagration)} \\ c_s & \text{(detonation, hybrid)} \end{cases}. \tag{293}$$

Note that whenever q_0 approaches q_e, the exponential damping hinders an accurate measurement of the scale q_1. This occurs when the wall velocity is close to the speed of sound for weak PTs ($\alpha = 0.0046$).

For weak PTs, the proposal from [67] that q_1 tracks $1/\xi_{\text{shell}}$ appears to hold well, while for intermediate PTs, q_1 is notably smaller than $1/\xi_{\text{shell}}$. This difference could be attributed to the presence of nonlinear effects, which are more pronounced for stronger PTs, and thus more observable for intermediate PTs.

Additionally, it is interesting to note that q_e is considerably lower for weak PTs compared to stronger ones, despite the box size and resolution being the same. This suggests that the scale q_e cannot be directly, or at least solely, linked to the grid spacing. The variation might be attributed to numerical viscosity, but the potential influence of physical dynamics remains a possibility, especially considering that large fluid velocities associated with stronger PTs form shocks more rapidly.

The bottom left panel of Figure 20 displays the amplitude of the GW spectrum. Specifically, we present the integral Q'_{int} in (289), normalized by the shell-thickness ξ_{shell} times $(\kappa\alpha)^2$, where the vacuum energy transfer efficiency κ is defined in Equation (166) and corresponds to that of self-similar profiles. The numerical values are given in Figure 4. In other words, we plot data for $Q'_{\text{int}}/\xi_{\text{shell}}/(\kappa\alpha)^2$ over the range of wall velocities and weak and intermediate PTs, as proposed in [67]. Our results closely align with the findings in [67].

The amplitudes that we observe vary by approximately a factor of 10 across different PT strengths and wall velocities. It is important to emphasize that, at this point, we can only state this as an observational fact without giving any further justification for the variance. In Chapter 6, however, we will explore how this variance is largely due to insufficient convergence of narrow self-similar profiles for $v_w \lesssim v_{\text{CJ}}$. Despite introducing the additional normalization factor ξ_{shell} to compensate, a considerable spread in values remains.

In the bottom right panel of Figure 20, we plot Q'_{int} normalized to the average kinetic energy measured in the full 3D simulations. This results in less variance and eliminates the need to introduce an additional factor ξ_{shell} to flatten the dependence. Furthermore, this normalization exhibits remarkable independence from the wall velocity or

the strength of the PT, varying only within a factor of approximately 2. However, obtaining the kinetic energy in the fluid is challenging without running the full simulations and is, therefore, less practical.

5.5.2.3 Comparing results for small and large box sizes

The plot in Figure 21 displays the fit parameters for all the simulations we conducted. In the plot, blue and red data points represent weak and intermediate PTs respectively. Dots and solid lines correspond to simulations with a small box size ($\tilde{L} = 20v_w$), while stars and dotted lines correspond to simulations with a large box size ($\tilde{L} = 40v_w$).

In the top left panel of Figure 21, the scale q_0 is shown, but now including results for both box size $\tilde{L} = 20v_w$ and $\tilde{L} = 20v_w$. As we have previously stated, it is notable that simulations with a small box size tend to overestimate q_0 as compared to results from a larger box size, which we deem more trustworthy due to the increased statistics in the IR. As a result, we only reported q_0 from the simulations with a large box size for the main results in Figure 20 in the previous Section.

In the top right panel of Figure 21, we again show inferred values of q_1 and q_e over the parameter scan, including results for both box size $\tilde{L} = 20v_w$ and $\tilde{L} = 40v_w$. We also plot the inverse shell thickness $1/\xi_{\text{shell}}$ for reference. As we saw previously, q_1 is bounded by q_e for weak PTs with $v_w \lesssim v_{\text{CJ}}$. Due to the effectively reduced resolution of $\tilde{L} = 40v_w$, this occurs for a larger set of velocities, making it clear that UV results for box size $\tilde{L} = 40v_w$ are less reliable than $\tilde{L} = 20v_w$ and showing clearly that, for this subset of velocities, higher resolution is necessary to accurately capture the peak. The agreement on q_1 for intermediate PTs when comparing results from both $\tilde{L} = 20v_w$ and $\tilde{L} = 40v_w$ is, however, striking. This indicates that $N = 512$ offers sufficient dynamical depth to capture the peak positions accurately for all v_w for intermediate PTs.

With regards to q_e, we make the interesting observation that for weak PTs, q_e does not double despite halving the box size, contrary to the observation from intermediate PTs. Hence, again, we conclude that q_e does not only depend on the grid spacing.

The bottom panel in Figure 21 shows the integrated GW spectrum growth rate normalized as in Figure 20. The measured values for simulations with small and large box sizes agree relatively well for most wall velocities except the smallest where the smaller box size yields marginally larger values, based on the lower left plot.

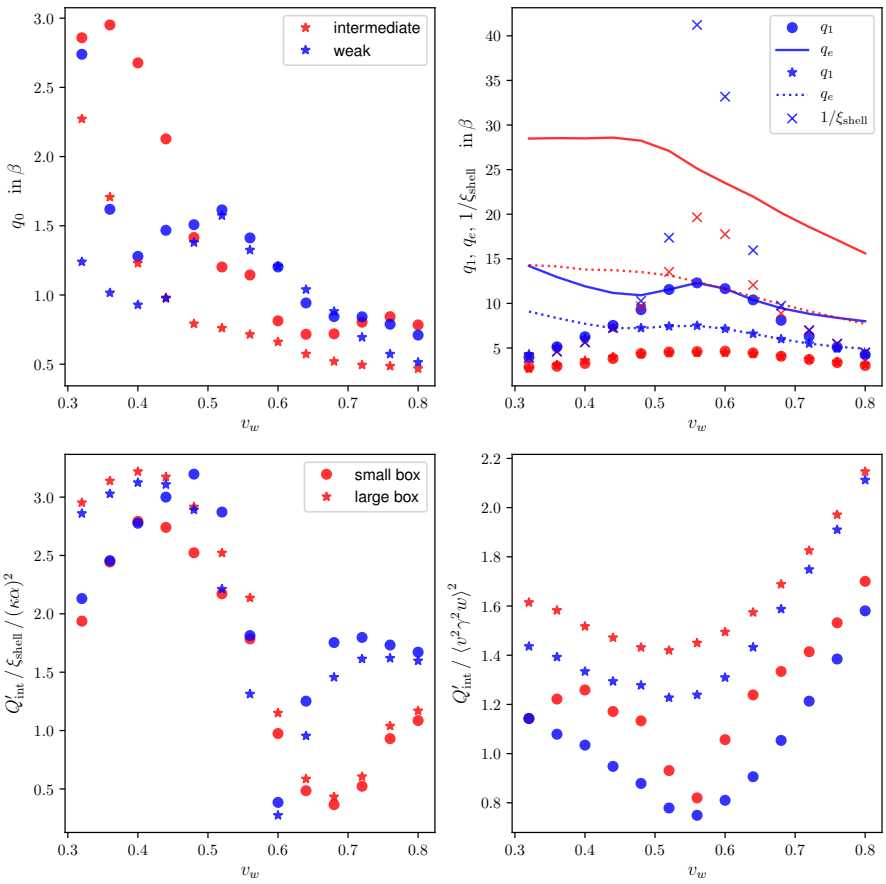

Figure 21: *Upper panel:* The extracted fitting parameters q_0, q_1, and q_e as functions of the wall velocity. Blue (red) data points correspond to weak (intermediate) PTs with $\alpha = 0.0046$ ($\alpha = 0.05$). Dots and solid lines are from simulations with small box size ($\tilde{L} = 20 v_w$) while stars and dotted lines are from simulations with large box size ($\tilde{L} = 40 v_w$). In the upper left figure, we show the IR knee position q_0 for $\tilde{L} = 40 v_w$. In the upper right figure, we show the UV peak q_1 (dots), the shell thickness (crosses) defined in Equation (291), and the exponential damping q_e (solid lines) for $\tilde{L} = 20 v_w$. *Lower panel:* The integral of the GW spectra $Q'_{\rm int}$ over momenta defined in Equation (289) normalized by $\xi_{\rm shell}(\kappa\alpha)^2$ (left) and by the kinetic energy squared $\langle v^2\gamma^2 w\rangle^2$ measured in the lattice (right).

5.6 Discussion

5.6.1 Reconnecting with the literature

In this Section, I compile various findings from the literature, focusing on how our results align with or differ from these studies. Most of these findings have already been presented in Sections 3.2.2.1 and 3.2.3. Here, we emphasize the key results concerning the fluid's contribution to GW production and compare them to our present findings.

Since the realization that the dominant source of GW production may not be the scalar field, but rather the fluid, strides were made to understand this theoretically through both analytical and numerical methods. In Section 3.2.3, I thus highlighted a few state-of-the-art approaches developed to predict the corresponding GW signal, including the sound-shell model, coupled scalar field + fluid lattice simulations, and hybrid simulations. For further details on these approaches, I refer the reader to Section 3.2.3 and the references I provide there.

The main results of these approaches are as follows:

THE SOUND SHELL MODEL Predictions from the sound-shell model [70, 72] demonstrate GW spectra that exhibit two distinct length scales: the average bubble separation and the sound shell width upon collision. The peak of the power spectrum occurs at wavenumbers determined by the sound shell width. In the UV, the power spectrum is found to decrease as k^{-3}. In the IR, recent sound-shell model results with refined assumptions [73, 74] have found a k^3 scaling (to be contrasted with the earlier prediction of k^9 scaling). An intermediate regime between the two scales corresponding to the typical bubble size and sound shell thickness with a linear k^1 scaling is furthermore observed. With the refined assumptions, an intricate spectrum structure emerges where, e.g. the previously found k^9 UV scaling is observed in a narrow band just to the left of the peak. The detailed form of the spectrum depends sensitively on the wall velocity and PT strength.

SCALAR FIELD + FLUID LATTICE SIMULATIONS Diametrically opposite to the sound-shell model, coupled scalar field + fluid lattice simulations [25, 69, 71, 101] enter the stage as a robust attempt at capturing the GW spectrum from the PT dynamics employing a fully numerical approach without many compromising assumptions. Here, quite straightforwardly, the authors solve on the lattice for the dynamical evolution of a scalar field and the fluid coupled through a phenomenological friction term.

In coupled scalar field + fluid lattice simulations [25, 69, 71, 101], it is found a GW spectrum consistent with the UV k^{-3} scaling as predicted in the sound-shell model. This observation is particularly clear for detonations, while for deflagrations it is moderately steeper. I will quote the k^{-3} scaling as their main finding in this regard. It is furthermore found that sound-shell thickness sets the location of the peak of the GW spectrum peak. In these simulations, the IR behavior of the GW spectrum could not be reliably determined.

HYBRID SIMULATIONS Bridging the gap between the sound-shell model and the scalar field + fluid lattice simulations, one finds the hybrid scheme [67]. In this approach, bubbles are modeled as spherically symmetric and expand at a constant wall velocity, similar to the Higgsless simulations. In the hybrid approach, it is found that the IR part of the GW spectrum scales as k^a where $a \in [2, 4]$, the UV part scales as k^b where $b \in [-4, -3]$, and that an intermediate plateau is present between the inverse scales of the average bubble size and shell thickness at collision with a scaling k^c where $c \in [-1, 0]$.

It is with the Hybrid scheme that the Higgsless simulations connect most strongly. While both methods rely on the assumption of spherically expanding bubbles and the effective removal of the Higgs field, the Higgsless simulations allow the self-similar profiles to develop spontaneously on the 3D grid rather than relying on a 3D embedding of radial 1D profiles. Moreover, Higgsless simulations constitute a fully nonlinear solver, enabling the exploration of the intricate dynamics associated with stronger PTs while relying on a more general solver framework.

	IR	Intermediate	UV	References
Sound-shell model	3	1	-3	[70, 72]
Scalar + fluid lattice simulations	-	1	-3	[25, 69, 71, 101]
Hybrid simulations	[2,4]	[-1,0]	[-4,-3]	[67]
Higgsless simulations	3	1	-3	This work

Table 3: GW spectrum slopes obtained from various approaches targeting fluid sound-wave-induced GW production. These models exhibit distinct features at wavenumbers k_0 and k_1, with three corresponding slopes: IR, intermediate, and UV.

In Table 3, I present a summary of the observed scaling behaviors of the GW spectrum as obtained using the various approaches. All approaches are reasonably consistent with the observation in this paper that the spectrum scales as k^3 in the IR, apart from the hybrid simulations, which find a certain spread in the IR slope around 3, depending

on the PT parameters. Additionally, all approaches agree with the k^{-3} scaling observed in the UV, though the hybrid simulations observe a slightly steeper scaling, bounded by k^{-4}.

Furthermore, all approaches identify the presence of an intermediate regime connecting the length scales associated with the inverse average bubble size and shell thickness at collision. In all approaches except the hybrid simulations, the scaling in this regime is found to be linear, k^1. Interestingly, in the hybrid approach, the observed scaling is negative, with an exponent in the range $[-1, 0]$.

Since the Higgsless and hybrid approaches share the assumptions of constant wall velocity, neglect of the Higgs field, and exponential-in-time bubble nucleation histories, while differing in that the Higgsless simulations are fully nonlinear, we can gain interesting insights by comparing their respective predictions.

One intriguing result shared by both approaches is that, for weak PTs, the scale associated with the peak q_0 appears to closely follow the shell thickness $1/\xi_{\text{shell}}$, whereas for stronger PTs, it does not. Agreement on this discrepancy suggests that the difference cannot originate from late-time nonlinear effects, as these are not accounted for in the hybrid approach. The most plausible explanation is that this difference arises from the nonlinear evolution of the radial 1D profile following the instantaneous removal of the forcing Higgs boundary (which is how bubble collisions are modeled in the Hybrid approach), rather than from nonlinear interactions among the bubbles.

Furthermore, the characteristic features observed in the GW spectrum are mostly consistent between both hybrid and Higgsless simulations, which serves as a reassuring validation of the methodologies employed. However, it is important to note that the amplitudes obtained from the hybrid method are systematically larger by a factor of $2-3$ compared to those from the Higgsless simulations, part of which could be explained by simply employing different bubble nucleation histories.

Lastly, a comparison between the current Higgsless results with the coupled scalar-fluid lattice simulations in [25, 69, 71, 101] is warranted. These simulations are recognized as the most precise and advanced predictions of the GW spectrum to date. Notably, there are no significant differences between the two methods across most of the parameter space. Although the IR slope was not directly derived from the GW spectrum in [71], the intermediate and UV slopes defining the GW power spectrum show good consistency, and the amplitude matches closely. Upon comparing individual results, we found that the amplitude between the two methods generally differed by less than a factor of 2. Moreover, our analysis reveals several features in the data that

have not been systematically studied before. For instance, the knee frequency, q_0, exhibits a complex dependence on the wall velocity.

While our results generally demonstrate good agreement, a significant difference we identified between the Higgsless simulations and the scalar-fluid simulations is their reported reduction in GW power for deflagrations, as discussed in [101] and further explored in [125]. This reduction arises because if the fluid heats up in front of the bubble wall, the pressure difference driving the expansion decreases, slowing down the wall. In extreme cases, the bubble wall may completely stop, leading to a period of phase coexistence. Clearly, since in our Higgsless approach, a constant wall velocity is assumed, observing such a slowdown in bubble wall expansion is not possible. This feature of the Higgsless method may be viewed as a deficiency but is better seen as a feature of it being model-independent in the following sense: the friction term in scalar-fluid simulations is phenomenological, represented by an additional term in the Higgs equation of the form $\eta u^\mu \partial_\mu \phi$, with η being a free parameter [25]. The slowdown of the wall in deflagrations critically depends on this parameter. Therefore, the statement on the reduction of the GW amplitude does, too. The Higgsless simulation results are thus model-independent in the sense of neglecting the variability of this friction.

In conclusion, by assuming a constant wall velocity, the Higgsless simulations avoid the model dependence associated with the above discussion.

5.6.2 Obtaining present day GW spectra

With the fitting parameters in figure 20 at our disposal, I wish to outline a sequence of steps through which these parameters can be used to derive the corresponding present-day GW spectrum given a specific model. The presumption is that for a given model, one has obtained the PT strength α, the duration of the PT β/H, the wall velocity v_w, and the PT temperature T (see e.g [52] and [88, 89]). Then, one can proceed as follows:

1. Knowledge of α and v_w implies that the shell thickness ξ_{shell} as in Equation (291) and the efficiency factor κ [86] as in Equation (166) and shown in Figure 4 can be determined. An informative plot of ξ_{shell} as a function of v_w for many choices of α can be found in see [67], while [88, 89] present useful figures and code snippets for the computation of the efficiency κ. With these quantities determined, the amplitude normalization quantity $\xi_{\text{shell}}/(\kappa\alpha)^2$ can be computed.

2. Knowing α and v_w, figure 20 allows to simply read off the spectral features q_0, q_1, q_e. The value of $Q'_{\rm int}$ can similarly be obtained by reading of the value for $Q'_{\rm int}/\xi_{\rm shell}/(\kappa\alpha)^2$ and multiplying with with value of $\xi_{\rm shell}/(\kappa\alpha)^2$ obtained in the previous step.

3. The spectral shape $S(q)$ in Equation (290) and its normalization constant S_0 can now be constructed from the condition that $\int d\ln q\, S(q) = 1$ for the given q_0, q_1, q_e.

4. Having found $S(q)$ and $Q'_{\rm int}$, Q' can be constructed from (287), i.e. one simply computes $Q'(q) = Q'_{\rm int} \times S(q)$.

5. With $Q'(q)$ at hand, the present-day GW spectrum is obtained as in Equation 276, i.e.,

$$\Omega_{\rm GW}(q) = \mathcal{T}_{\rm GW} \frac{4(H_*/\beta)(H_*\, t_{\rm sw})}{3\pi^2} \times Q'(q)\,,$$

   where the transfer coefficient $\mathcal{T}_{\rm GW}$, defined in 67, has the value

$$h^2\mathcal{T}_{\rm GW} = 1.65\times 10^{-5}\left(\frac{100}{g_*^p}\right)^{1/3},$$

   $t_{\rm sw}$ is the GW sourcing duration, and H_* is the Hubble rate at the time of GW production. An estimate of $t_{\rm sw}$ can be attained assuming the time it takes nonlinearities to develop, $t_{\rm sw} \sim R_*/\sqrt{K}$, as we discussed in Section 2.2.5 and with $R_* \equiv (8\pi)^{1/3}\max(v_w, c_s)/\beta$. An estimate of K is $K = K_\xi$ from self-similar profiles in Equation (168).

6. The next and last point concerns the redshifting of wavenumbers at production time k_* to the present-day values k_0, obtained as $k_0 = (a_*/a_0)k_*$. According to Equation–169, the present-day frequency is

$$f_0 = 2.63\cdot 10^{-6}\,{\rm Hz}\times\left(\frac{q_*}{\beta}\right)\left(\frac{\beta}{H_*}\right)\left(\frac{g_*}{100}\right)^{1/6}\left(\frac{T_*}{100{\rm GeV}}\right)$$

   tells us how to do so. The spectral features q_0, q_1, and q_e are thus easily redshifted to their present-day frequencies.

These 6 steps outline how the Higgsless simulation results can be used to readily obtain observational predictions for the GW spectrum.

5.6.3 Future work

This study should be viewed as an initial report on the implementation, evaluation, high resolution, application, and predictive power of

Higgsless simulations. Throughout this Chapter, we have identified several results that warrant further investigation. Below, I outline a number of observations and additional points that I believe merit future exploration, some of which will be addressed in the forthcoming Chapter 6:

- In the present work, we have chosen to study PTs of weak ($\alpha = 0.0046$) and intermediate ($\alpha = 0.05$) strength to align with the literature and facilitate comparison. Having established the Higgsless simulations as a powerful tool in exploring GWs from PTs, producing results consistent with other methods, and confirming the stability of the scheme, future work should focus on investigating strong PTs. This direction will be pursued in the next Chapter 6.

- While we commented on the convergence of the results with increased resolution, we deferred a systematic convergence study. To fully understand the reliability of the Higgsless results, a more systematic treatment is needed. Such a treatment will be persuaded in the next Chapter 6.

- In the present work, we saw signs of nonlinear dynamics. For example, we saw that the GW spectrum peak q_1 tracks $1/\xi_{\text{shell}}$ for weak PTs, while for intermediate PTs, q_1 is notably smaller than $1/\xi_{\text{shell}}$. We thus concluded that this difference could be attributed to the presence of nonlinear effects, which are more pronounced for stronger PTs. We additionally noted the presence of sharper gradients in the simulation slices in Figures 14, 15, and 16, indicating the development of shocks. Further analysis is required to strengthen the nonlinear hypothesis. Attempts at doing this will be made in the next Chapter 6.

- Our data indicates that the IR knee exhibits a complex behavior. We also concluded that achieving adequate resolution of q_0 and the IR spectral index n_0, which was found to be consistent with $n_0 = 3$, may require larger simulations. This warrants further investigation. While I will not run larger simulations, I will comment on this behavior in the next Chapter 6.

- We also saw how the amplitude varies by approximately a factor of 10 across different PT strengths and wall velocities. In Chapter 6, we will explore how this variance is due primarily to insufficient convergence of narrow self-similar profiles for $v_w \lesssim v_{\text{CJ}}$.

These and additional points will be addressed in Chapter 6, which will provide significant improvements to the understanding of the simulation results.

5.7 Summary and conclusion

In this Chapter, which is based on the publication [1], I have extensively reviewed the implementation, evaluation, application, and results from the novel Higgsless simulations designed to model in a fully nonlinear way the relativistic hydrodynamics of a primordial fluid and associated GW production in a first-order cosmological PT, with emphasis on extracting the linear GW spectrum growth rate as expected from sound-wave production of GWs.

5.7.1 Summary

A concise summary of the scientific work and results is presented below.

- *Physical setup:* The physical ingredients relevant for the setup are reviewed in Section 5.2, in which I demonstrated the construction of realistic exponential-in-time bubble nucleation histories, assuming constant wall velocity, a key assumption of the Higgsless approach. The wall interface of these Higgs bubbles is approximated as a step function, enabling us to encode the PT evolution using the bag equation of state. Here, the space-time dependence of the bag constant is determined directly from the bubble nucleation history. By solving for the spatial components of T^{ij} in terms of the conserved quantities K^{μ}, we explain how the fluid is coupled to the state of the vacuum through the time-varying bag constant $\epsilon(t, \mathbf{x})$. As $\epsilon(t, \mathbf{x})$ varies in accordance with a bubble nucleation history, the fluid responds to the vacuum energy injection, eliminating the need to solve for the Higgs field evolution; the equation of state suffices. The perturbed fluid induces bulk motion as sound waves, or more generally compressional modes, and possibly turbulence, leading to anisotropic stress that sources a spectrum of GWs. The growth rate of these GWs is measured in the Higgsless simulations using Weinberg's formula (104).

- *Numerical setup:* In Section 5.3, I review numerical methods and programmatic considerations to highlight some technical choices and their connection with the physics we are attempting to model. The main points concern the usage of the KT+RK3 numerical scheme defined in 207 to numerically solve 216 and 217, subject to the time-varying boundary conditions $\epsilon(t, \mathbf{x})$ which model spherically expanding bubbles. This grants us detailed information about the energy-momentum tensor, which is subse-

quently used to derive the GW production on the lattice as in Equation (286).

- *Simulation evaluation:* I evaluate the simulations in Section 5.4.1, where it is found that the KT+RK3 scheme is remarkably successful at recovering the analytically understood self-similar dynamics of single bubbles, as well as well as conserving energy to machine precision. The 3D Higgsless simulation implementation swiftly produces accurate single-bubble wall profiles and maintains precise shock dynamics over time. Notably, the accurate reproduction of self-similar profiles is less dependent on the parameter α and more on the shell thickness. This suggests that the framework can be extended to model stronger PTs with minimal adjustments, primarily involving the simulation's time step and refining the definition of the local velocity a to preserve stability as outlined in Sec. 4.3. The robustness and precision of the 3D Higgsless simulation framework in resolving self-similar profiles make it a powerful tool for studying PTs with multiple bubbles.

- *Multi-bubble simulations:* Following successful simulation evaluation, I use the Higgsless simulations to model realistic PT scenarios with hundreds to thousands of bubbles nucleating according to a physically motivated exponentially growing nucleation rate. Simulations with resolution $N = 512$ and box sizes $\tilde{L} = 20v_w$ and $\tilde{L} = 40v_w$, encompassing a parameter scan over $\alpha \in \{0.0046, 0.05\}$ and $v_w \in \{0.32, 0.36, \dots, 0.8\}$, were thus performed.

- *GW spectral shape and growth rate:* The observed spectra are characterized by a doubly broken power law, with IR, intermediate, UV, and exponential damping regimes separated at scales q_0, q_1, and q_e. Our data is consistent with q^3, q^1, and $q^{-}3$ scaling in the IR, Intermediate, and UV regimes, respectively. These scales q_0, q_1, and q_e were extracted across different strengths of PTs and wall velocities from fits of the spectral shape function (290) to the data. These parameters, as well as the GW frequency integrated growth rates, are presented in Figure 20. For intermediate-strength PTs, a clear downward trend in q_0 with increasing wall velocities was observed, whereas weak PTs exhibited notable features near the speed of sound. Our findings indicate that the IR knee behavior is quite complex. Additionally, q_1 for weak PTs aligns well with the proposal in [67] that it tracks $1/\xi_{\text{shell}}$, while for intermediate PTs, a departure from this trend is observed possibly due to nonlinear effects. The variation in q_e suggests influences beyond numerical grid spacing, possibly including nu-

merical viscosity effects and physical dynamics such as shock formation in intermediate PTs.

As for the GW spectrum growth rate, specifically the integral Q'_{int} normalized by ξ_{shell} and $(\kappa\alpha)^2$, our results are consistent with [67], showing that the amplitude varies significantly across different PT strengths and wall velocities. This variance appears to be due to insufficient convergence to narrow self-similar profiles, particularly for $v_w \sim c_s$. While normalization by ξ_{shell} mitigates part of this effect, a considerable spread remains. This observation highlights the need for more refined simulations to understand the GW amplitude behavior better.

- *Discussion:* In Section 5.6, I put the present results in context and compare them with the main results in the literature, overall finding that our results align well. In 5.6.2, I outline how the Higgsless results can be used as a template to readily compute the present-day GW spectrum.

5.7.2 Conclusion

To conclude, the Higgsless simulations present a novel and highly efficient approach for modeling the nonlinear dynamics of the primordial fluid, enabling the extraction of GW spectra from cosmological first-order PTs. Notably, this method benefits from the simplification of neglecting Higgs field dynamics.

The KT+RK3 scheme has proven effective for solving relativistic hydrodynamic partial differential equations. Our simulations, conducted with relatively modest computational resources, demonstrate the efficiency of the Higgsless approach at capturing the associated high gradient phenomena and resolution of shocks.

The Higgsless simulations thus bridge the gap between simplistic semi-analytical methods and costly numerical simulations, offering valuable insights into GW production in PTs at a fraction of the computational cost.

5.8 Appendix: Gravitational waves from domain wall catalyzed phase transitions

In this Section, which should be viewed as an appendix to the current Chapter, I will demonstrate the application of Higgsless simulations to a scenario where a domain wall (DW) network catalyzes the PT. This Section draws on the work published in [2], but rather than providing a comprehensive account of all the details, I will focus on demonstrating how the Higgsless simulations can be adapted to a different context by simply altering the bubble nucleation history, highlighting the flexibility of the Higgsless approach, and how the GW spectrum is altered.

5.8.1 Introduction

The role of impurities, or defects, in PTs cannot be overstated. Condensation cores, to give an example, play a crucial role in cloud and ice crystal formation. These cores, tiny particles suspended in the atmosphere, such as dust, pollen, or aerosols, catalyze the PT by which the droplets or ice crystals form by lowering the energy threshold for the PT to occur. It appears, therefore, to be a natural suggestion that defects play a role in catalyzing PTs also in the early universe. If so, catalyzing elements could influence the course of evolution of a PT and thus potentially lead to modified signatures of the PT. In the following, we will denote non-seeded PTs *homogeneous* and PTs seeded by impurities *inhomogeneous*.

As a matter of fact, a plethora of impurities and defects have been considered in the literature [14, 126–153]. In this Section, we explore the scenario where a DW network acts as a local catalyst, or *seed*, for the first-order PT responsible for bubble nucleation and GW generation [154]. In certain particle physics models, the likelihood of nucleation is notably higher on the surfaces of DWs compared to the bulk of the Universe. Consequently, the bubble nucleation history deviates from that of homogeneous PTs, as bubbles tend to nucleate preferentially on the DWs [154].

The presence of a DW network introduces an additional length scale, ξ_{DW}, representing the average separation between DWs. When ξ_{DW} is much larger than the mean bubble separation, R_*, as defined in Equation 137,

$$\xi_{DW} \gg R_*, \tag{294}$$

we expect the network to leave a distinct imprint on the GW spectrum. Specifically, this should manifest as a shift in the peak frequency

towards lower wave numbers, along with an increase in the peak amplitude, analogous to the effects observed in GW spectra from PTs influenced by macroscopic thermal fluctuations, as described in Ref. [68]. This increase in amplitude arises because the correlation scale of fluid perturbations is governed by ξ_{DW}, rather than R_*. Moreover, the spatially inhomogeneous distribution of bubbles induced by the DW network may lead to alterations in the spectral shape. Instead of conventional bubble collisions, in the extreme limit of instantaneous bubble nucleation on the DWs, the network causes the propagation of sheets that move away from the walls, eventually colliding after an average time of ξ_{DW}/v_w.

To examine these expectations and to derive quantitative results, we construct modified bubble nucleation histories based on a DW network model. After obtaining these nucleation histories, we use Higgsless simulations to compute the resulting GW signal.

5.8.2 Modeling of the domain wall network and catalyzed bubble nucleation

As an illustrative example, consider the potential

$$V = \frac{\lambda}{4}(\phi^2 - v^2)^2 + \frac{\lambda_m}{4}s^2\phi^2 + \frac{\lambda_m}{4}s^4 - \frac{1}{2}\mu_S^2 s^2\,, \tag{295}$$

where ϕ represents the Higgs field and s is a gauge singlet with a Z_2 symmetry. In certain regions of the parameter space, this system undergoes a two-step PT. Initially, the system transitions into a phase where s acquires a vacuum expectation value (VEV), which spontaneously breaks the Z_2 symmetry and generates DWs. At lower temperatures, the system reaches its ground state characterized by a non-zero VEV for ϕ while the Z_2 symmetry is restored, $\langle s\rangle = 0$. The DWs then disappear when the system fully transitions into this low-temperature phase.

Compared to conventional PTs, the bubble nucleation history is altered because bubbles preferentially nucleate on the DWs [154], with the potential barrier arising from the gradient of the s-field. In the extreme limit given by Equation (294), bubble nucleations can be considered effectively simultaneous across the DW network relative to the timescale for bubbles to traverse between walls, making β an irrelevant parameter. In this limit, the dynamics of the DWs can be neglected, and since β governs the inter-bubble separation within the DW network, which is much smaller than ξ_{DW}, the features of the GW spectrum become independent of β.

Thus, it suffices to have a snapshot of a DW network with a specified correlation length ξ_{DW} to construct a bubble nucleation history.

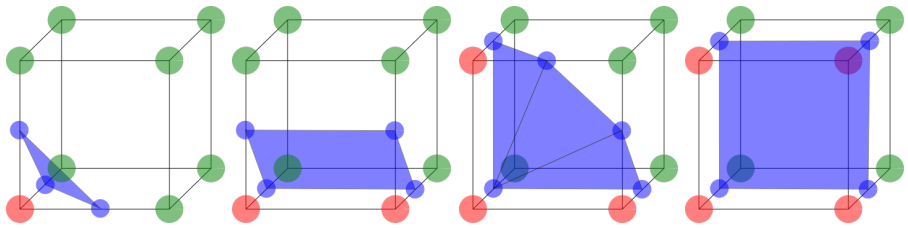

Figure 22: Representative DW configurations for cells with 0 to 4 corners in the opposite phases are shown. The corresponding surface weights of the DW network are $\{0, \sqrt{3}/8, 1/\sqrt{2}, 1/\sqrt{2}+\sqrt{11}/8, 1\}$. The trivial case for the empty cell with all corners in the same phase and zero weight is not shown.

To achieve this, we model the DW network using a Monte Carlo implementation of the Ising model with the Metropolis algorithm [155], iterating until the desired correlation length is reached [2]. This snapshot is then used to determine the phenomenological implications for the GW spectrum. For further details, I refer the reader to [2]. It is noteworthy that the Ising model effectively captures the appearance of DWs as seen in genuine simulations of DW networks. An example realization of a DW network is shown in the left column of Figure 23.

To generate bubble nucleation histories from the Ising model realizations of the DW network, we map the Ising data to a realistic DW network. The procedure we employ essentially involves determining the area of the DW network in each grid cell by means of counting how many corners are in the respective phase. This area is proportional to a cell weight w_{ijk}, so that the probability of nucleating a bubble in cell ijk at time t is proportional to $w_{ijk}\exp(t\beta)$. Bubble nucleation histories are then constructed using this probability distribution, as otherwise detailed in 5.3.5. See Figure 5.8.2 for an example of how these weights are computed. Since weights are zero outside the DW network, bubbles nucleate only within the DWs. We have shown that the final results are robust to variations in this procedure. With our parameter choices, the DW correlation length is typically an order of magnitude larger than the mean bubble size, though this can be controlled as desired.

As previously noted, the DW network is characterized by the mean separation between DWs, ξ_{DW}. To estimate this, we consider the total

2 The Ising model Hamiltonian can be written as, $H = -J\sum_{\langle ij\rangle} S_i S_i$ where S_i, often called the spin, take on values ± 1, $\langle ij\rangle$ implies nearest-neighbor interaction only, and $J > 0$ is the strength of exchange interaction. The Metropolis algorithm consists of the following steps: (1) Prepare an initially random configuration of S_i, (2) flip the spin of a randomly chosen lattice site i (which is really a site in a 3D lattice in our case), (3) calculate the change in energy ΔE associated with the spin-flip and the Hamiltonian H, (4) if $\Delta E < 0$, accept the move, otherwise accept the move with probability $e^{-\Delta E/T}$, and (5) repeat (2)-(4) until desired correlation length is achieved.

surface area of the DW network, S_{DW}. The mean separation is approximately given by

$$\xi_{DW} \sim \frac{V}{S_{DW}} \tag{296}$$

where $V = L^3$ represents the volume of the simulation. For the DW network shown in Fig. 23, we find $\xi_{DW} \sim 0.1 \times L$, with L being the box size. Using the Metropolis algorithm, starting from a random initial state, we perform 4×10^8 phase updates on a 128^3 grid with the parameter $J/T = 2$ to achieve this correlation length (see footnote 2). The total surface area of the DW network was determined using the previously discussed weights.

5.8.3 Simulations and numerical results

Having established the methods for modeling the DW network, characterizing them with the correlation length ξ_{DW}, and generating the corresponding bubble nucleation histories, we proceed to run simulations to solve for the hydrodynamical evolution and obtain the GW spectra. In the presence of DWs, we use relatively large box sizes, $L = 160 v_w/\beta$, to ensure that the mean separation between the DWs is greater than the mean bubble size in the PT without DWs. For the simulations without the DW network, we instead use $L = 80 v_w/\beta$ to gain IR resolution as compared to the simulation in the previous Sections of this Chapter but still resolve the self-similar profiles reasonably well upon PT completion.

In Figure 24, I present the final spectra from our simulations. Consistent with expectations, the GW signal exhibits a shift towards lower frequencies and a corresponding increase in amplitude. Additionally, the spectrum displays a marginally steeper slope in the IR range. To analyze these features, we use a shape function akin to (290), but with a free IR index $n_1 = n$. This adjustment accommodates different IR behaviors from the typical q^3 and utilizes the enhanced IR range more effectively.

$$S_f(q) = S_0 \times \frac{(q/q_0)^n}{1 + (q/q_0)^{(n-1)}[1 + (q/q_1)^4]} \times e^{-(q/q_e)^2} . \tag{297}$$

Table 4 presents our numerical results. The parameter Ω_{int} represents the frequency-integrated GW power, while q_0 and n are fitting parameters defined in (297). Values with a bar indicate results from simulations without a DW network. The peak frequency of the spectrum appears closely related to the correlation length of the DW network, with $q_0 \simeq 3/\xi_{DW}$. As we expected, the presence of DWs shifts the peak to

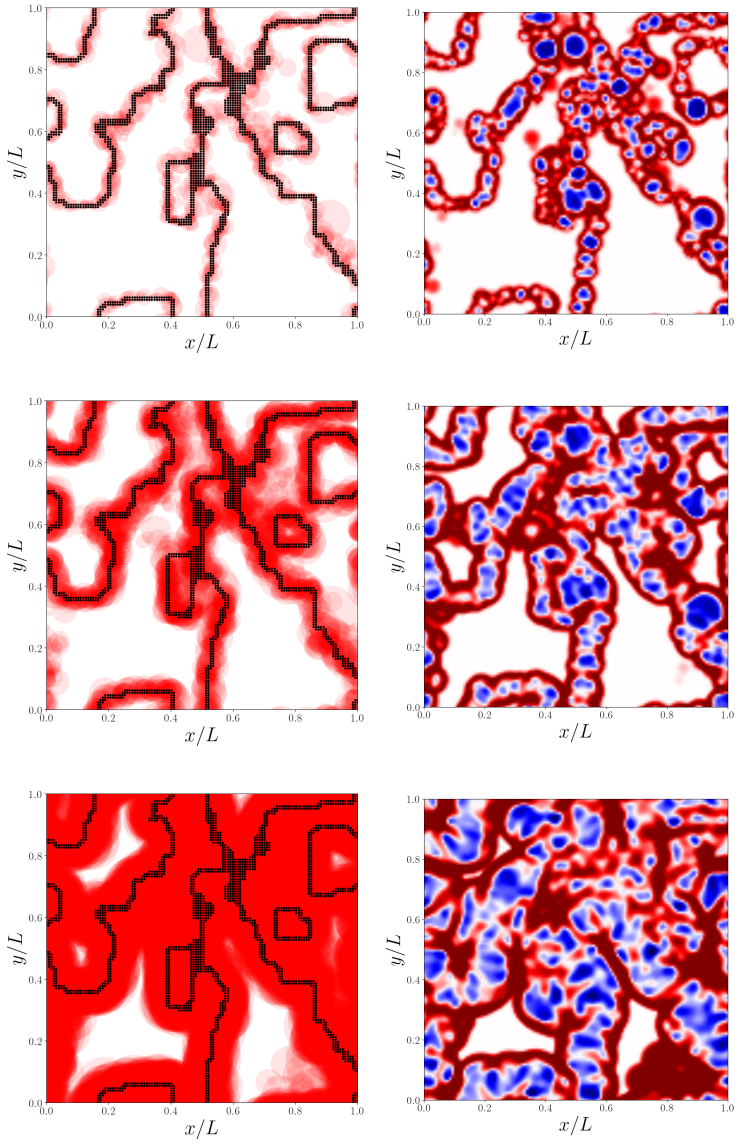

Figure 23: *Left column:* A realization of a DW network as per the method in the main text and footnote 2 is shown as dark lines. The bubble wall interface is shown as expanding red circles at various times in the simulation. *Right column:* The kinetic energy in the fluid is as obtained in the simulation at corresponding time steps. The PT parameters are $\alpha = 0.05$, $v_w = 0.8$, $L = 160 v_w/\beta$, and $\xi_{DW} = 0.1L$.

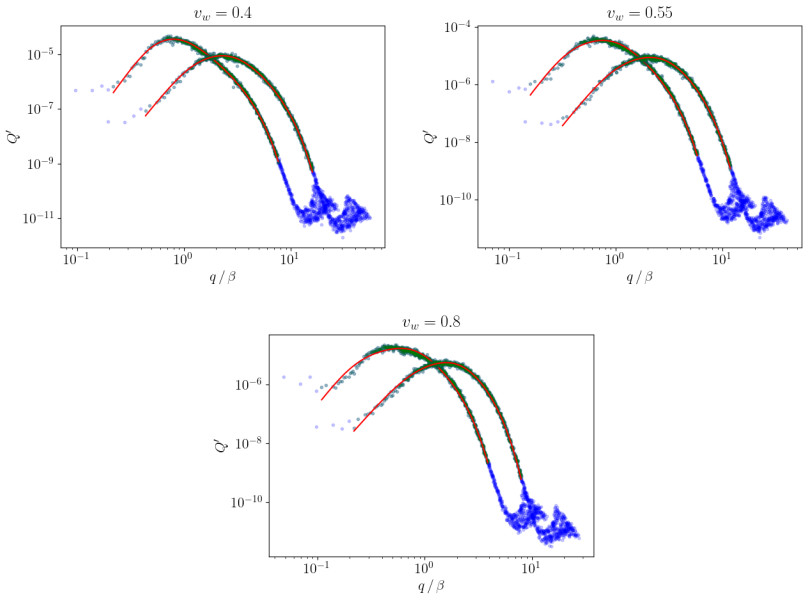

Figure 24: Final spectra of the gravitational waves with (left) and without (right) a DW network. The strength of the PT is $\alpha = 0.05$, and the velocities of the bubble walls are $v_w = 0.4$, 0.55, and 0.8. The green points indicate the part of the spectrum used in the fit (shown in red).

v_w	q_0/β	ξ_{DW}/β^{-1}	$q_0 \cdot \xi_{DW}$	$q_0/\bar{q}_0$	$\Omega_{int}/\bar{\Omega}_{int}$	n	$\bar{n}$
0.4	0.50	6.4	3.19	3.69	2.37	5.51	4.87
0.55	0.35	8.8	3.07	3.95	2.75	5.03	4.63
0.8	0.22	12.8	2.81	3.40	3.44	4.78	4.14

Table 4: Parameters extracted from the spectra shown in Fig. 24 are summarized. Values with a bar denote quantities obtained from simulations without DWs. q_0 is derived by fitting Equation (297) to the simulation data. The domain wall correlation length ξ_{DW} is determined from our model of the DW network using the Ising.

lower frequencies and enhances the amplitude by a similar factor. In the fits, the IR tail appears somewhat steeper, but this result is only tentative as the simulation boxes are generally too small to accurately determine the IR behavior slope n.

5.8.4 Conclusion

In this application of the Higgsless simulations, we examined the gravitational wave spectrum arising from a first-order PT influenced by domain walls. When bubble nucleation occurs preferentially on domain walls, the relevant length scale becomes the correlation length of the domain wall network, provided it is larger than the typical bubble size in a homogeneous first-order PT. Once this correlation length is sufficiently large, the inverse duration β of the PT ceases to dictate the scale of fluid perturbations.

Consequently, the effective correlation length of the sound waves in the fluid increases. This results in a shift of the peak frequency to lower wave numbers and a corresponding enhancement of the peak amplitude. Additionally, while the IR tail of the spectrum in our seeded inhomogeneous simulations shows a steeper slope than that of conventional homogeneous PTs, this observation remains tentative due to substantial statistical uncertainties affecting the IR region.

6

GRAVITATIONAL WAVES FROM DECAYING SOURCES IN STRONG PHASE TRANSITIONS

In this Chapter, I delve into the previously uncharted realm of GWs originating from strong first-order PTs. The Chapter extensively draws upon the scientific research outlined in the publication *Gravitational waves from decaying sources in strong phase transitions* [3], a collaborative effort involving myself, the coauthors of the publication [1] and developers of the Higgsless approach Ryusuke Jinno, Thomas Konstandin, and Henrique Rubira, as well as Chiara Caprini and Albero Roper Pol.

In Section 6.1, I introduce the study and the broader context and outline its scientific objectives. In Section 6.2, I extend the model for gravitational wave production to account for damped sources and cosmic expansion. Section 6.3 discusses updates to the simulation code and the chosen parameters. The main numerical results, including findings from strong PTs and a template for gravitational wave production, are presented in Section 6.4. Finally, Section 6.5 summarizes the key findings and concludes the Chapter.

6.1 Introduction

6.1.1 Background

During a first-order PT, the initial fluid motion manifests as compression waves around the bubbles. Following bubble collisions, the fluid motion nevertheless evolves nonlinearly, allowing for the formation of vorticity and shocks, ultimately leading to the development of turbulence. This nonlinear evolution is an inevitable consequence of the high Reynolds number of the fluid in the early Universe [156]. The transition from the sound-wave regime to the turbulence regime is particularly significant in strong PTs, where nonlinearities can play a crucial role, damping the fluid motion on time scales shorter than Hubble, as we shall soon see. For weak PTs, the fluid motion is effectively characterized as a linear combination of sound waves [1, 25]. However, in stronger PTs, the emergence of rotational modes and turbulence is observed [101], which could significantly influence the gravitational wave signal [22, 94]. In fact, it is evident that LISA is more sensitive to detecting stronger PTs due to their boosted signals [71, 106], where nonlinear effects, such as shocks and turbulence, become significant.

While recent studies have begun to explore the aspects of nonlinear dynamics, including gravitational wave generation from vortical turbulence [20, 75–77, 93–96, 157–163], there is presently, to my knowledge, only one study that explores the dynamics and GW production in simulations of arising in first-order PTs capturing the evolution form initial bubble seeds to developed turbulence [101]. While this study shed some light on the GW amplitude and overall dynamics, there are no results for the GW spectrum.

In this Chapter, we explore the previously uncharted realm of GWs from strong first-order PTs with $\alpha = 0.5$ while also updating results for weak and intermediate PTs. Building upon the foundation laid in Chapter 5 and aiming to address some of the points outlined in Section 5.6.3, I run a comprehensive series of approximately 1000 simulations. These simulations involve a detailed parameter scan over wall velocities $v_w \in [0.32, 0.8]$ in increments of 0.04, covering weak ($\alpha = 0.0046$), intermediate ($\alpha = 0.05$), and strong ($\alpha = 0.5$) PTs. Utilizing the Higgsless approach, this study systematically explores the dependence of various characteristics of the GW spectrum on the underlying physical scales. As we track the long-term evolution of the system, this work sees the emergence of nonlinearities and studies their impact on gravitational wave production. To this end, we decompose the velocity spectra into longitudinal and transverse components to shed additional light on the dynamics at play.

6.1.2 Scientific objectives

The scientific objectives of this study are briefly summarized as follows: In particular, we aim to

- improve the stability of numerical scheme to allow simulating strong PTs,
- obtain, for the first time, GW spectra from strong PTs,
- provide templates for the GW spectrum aligning with the sound-shell model GW spectrum parameterization in Equation (109),

$$\Omega_{\mathrm{GW}}(k) = 3\,\mathcal{T}_{\mathrm{GW}}\,\tilde{\Omega}_{\mathrm{GW}}\,K^2\,(H_* R_*)(H_* t_{\mathrm{sw}})\,S(kR_*)\,,$$

- generalize the GW spectrum parameterization in Equation (110) to accommodate decaying sources with and without expansion,
- shed light on the interpretation and determination of all parameters entering the parameterization (110) and its generalizations, including the GW production efficiency $\tilde{\Omega}_{\mathrm{GW}}$, source lifetime t_{sw},

correlation scale of the fluid R_*, energy budget K^2, and spectral shape $S(kR_*)$,

- perform systematic convergence studies to understand and quantify associated errors,
- further explore the presence and implications of nonlinear dynamics such as shock formation and turbulence,
- and quantify the variance associated with the sample statistics of the used bubble nucleation histories.

In essence, we push the Higgsless simulations to the next level and derive results that have high scientific value.

6.2 GW production

6.2.1 Connecting with the notation in Chapter 5

In the previous Chapter 5 we extracted the dimensionless growth rate Q' as in Equation (277),

$$Q' \equiv \frac{\tilde{q}^3}{\tilde{V}\tilde{t}_{GW}} \int \frac{d\Omega_k}{4\pi} \left[\Lambda_{ij,kl}\tilde{T}_{ij}(\tilde{q},\tilde{\mathbf{k}}\,|\,\tilde{t})\tilde{T}^*_{kl}(\tilde{q},\tilde{\mathbf{k}}\,|\,\tilde{t})\right]_{\tilde{q}=|\tilde{\mathbf{k}}|} . \tag{298}$$

where $\tilde{t}_{GW} = \tilde{t} - \tilde{t}_{init}$ is the duration of GW souring at simulation time $\tilde{t}$, and written in terms of the dimensionless simulation variables $\tilde{q} \equiv q/\beta$, $\tilde{\mathbf{k}} \equiv \mathbf{k}/\beta$, $\tilde{T} = T\beta$, and $\tilde{V} = V\beta^3$. The definition and measurement of Q' was justified by the assumption of a linear growth rate, which, as was discussed in Section 6.2, implies that the average kinetic energy in the system K is constant. This is a good assumption if the dynamics is indeed characterized by sound waves.

In the present Chapter, we have set out to explore strong PTs and anticipate, therefore, that nonlinear damping of the sourcing kinetic energy may become significant. Thus, we should employ a description that honors this fact and thus depart from the Q' prescription.

In Equation (95), we introduced the present-day GW parameterization

$$\Omega_{GW}(k) = \frac{1}{\rho_c}\frac{d\rho_{GW}}{d\ln k} = 3\,\mathcal{T}_{GW}\,\mathcal{I}(k)\,,$$

where $\mathcal{I}(k)$, in Equation (94), is defined in terms of the UETC $E_\Pi(t_1,t_2,k)$ in Equation (87) by

$$\mathcal{I}(\tau_*,\tau_{fin},k) = \frac{k}{2}\int_{\tau_*}^{\tau_{fin}}\frac{d\tau_1}{\tau_1}\int_{\tau_*}^{\tau_{fin}}\frac{d\tau_2}{\tau_2}E_\Pi(\tau_1,\tau_2,k)\cos k(\tau_1-\tau_2) .$$

Neglecting expansion, $\mathcal{I}$ becomes

$$\mathcal{I}(t_*, t_{\rm fin}, k) = \frac{k}{2} H_*^2 \int_{t_*}^{t_{\rm fin}} \int_{t_*}^{t_{\rm fin}} E_\Pi(t_1, t_2, k) \cos k(t_1 - t_2)\, dt_1\, dt_2\,. \quad (299)$$

Then, following the derivation in Section 2.2.4, $\mathcal{I}(t_*, t, k)$ can be expressed in terms of the energy-momentum tensor $\tilde{T}_{ij}(\tilde{q}, \tilde{\mathbf{k}})$ as in Equation (102) through the formidable expression

$$\begin{aligned}
\mathcal{I}(t_*, t_{\rm fin}, q) &= \frac{q^3}{3 \cdot 4\pi^2 V m_{\rm Pl}^2 \bar{\rho}_*} \int_{\Omega_k} \frac{d\Omega_k}{4\pi} \left[\Lambda_{ij,kl} T_{ij}\left(q, \mathbf{k} \,|\, t_{\rm fin}\right) T^*_{kl}\left(q, \mathbf{k} \,|\, t_{\rm fin}\right)\right]_{q=k} \\
&= \frac{\tilde{q}^3}{4\pi^2 \tilde{V} \tilde{\rho}_*^2} \left(\frac{H_*}{\beta}\right)^2 \int \frac{d\Omega_k}{4\pi} \left[\Lambda_{ij,kl} \tilde{T}_{ij}(\tilde{q}, \tilde{\mathbf{k}} | \, \tilde{t}_{\rm fin}) \tilde{T}^*_{kl}(\tilde{q}, \tilde{\mathbf{k}} | \, \tilde{t}_{\rm fin})\right]_{\tilde{q}=|\tilde{\mathbf{k}}|} \\
&\equiv \left(\frac{H_*}{\beta}\right)^2 \mathcal{I}_{\rm sim}(\tilde{t}_*, \tilde{t}_{\rm fin}, \tilde{q})\,,
\end{aligned} \quad (300)$$

where I defined

$$\begin{aligned}
\mathcal{I}_{\rm sim}(\tilde{t}_*, \tilde{t}_{\rm fin}, \tilde{q}) &\equiv \left(\frac{\beta}{H_*}\right)^2 \mathcal{I}(t_*, t_{\rm fin}, q) \\
&= \frac{\tilde{q}^3}{4\pi^2 \tilde{V} \tilde{\rho}_*^2} \int \frac{d\Omega_k}{4\pi} \left[\Lambda_{ij,kl} \tilde{T}_{ij}(\tilde{q}, \tilde{\mathbf{k}}) \tilde{T}^*_{kl}(\tilde{q}, \tilde{\mathbf{k}})\right]_{\tilde{q}=|\tilde{\mathbf{k}}|}
\end{aligned} \quad (301)$$

Then, referring to Section 5.3.7 for details, we can directly compute $\mathcal{I}_{\rm sim}$ from the lattice as

$$\mathcal{I}_{\rm sim}(\tilde{t}_*, \tilde{t}_{\rm fin}, \tilde{q}) = \frac{4}{9\pi^2(1+\alpha)^2} \frac{\tilde{q}^3 \tilde{V} \Delta \tilde{t}^2}{N^6} \left\langle \left|\tilde{T}_+(\tilde{q}, \tilde{\mathbf{k}} \,|\, \tilde{t}_{\rm fin})\right|^2 + \left|\tilde{T}_\times(\tilde{q}, \tilde{\mathbf{k}} \,|\, \tilde{t}_{\rm fin})\right|^2 \right\rangle \Big|_{\tilde{q}=|\tilde{\mathbf{k}}|} \quad (302)$$

where I used that $\tilde{\rho}_* = \frac{3}{4}(1+\alpha)$ and where the volume $\tilde{V} = \tilde{L}^3$ is now interpreted as the volume of the simulation box. This implies for the relation with Q' that

$$\mathcal{I}_{\rm sim} = \frac{\tilde{t}_{\rm GW}}{4\pi^2 \tilde{\rho}_*} Q'\,. \quad (303)$$

6.2.2 GWs from stationary sound waves

We concluded in Section 2.2.5 that if the UETC is stationary, i.e., it only depends on the difference $t_- = t_2 - t_1$, $E_\Pi(t_1, t_2, k) = 2k^2 K^2 f(t_-, k)$, where $K = \langle \rho_{\rm kin} \rangle / \bar{\rho}$ is the kinetic energy density fraction with $\rho_{\rm kin} = \langle w \gamma^2 v^2 \rangle$, then Equation 299 becomes Equation (107),

$$\mathcal{I}(t_*, t_{\rm fin}, k) = k^3 H_*^2 K^2 \int_{t_*}^{t_{\rm fin}} dt \int_{t_* - t}^{t_{\rm fin} - t} \cos(k t_-)\, f(t_-, k)\, dt_-\,.$$

We then discussed how in the sound-shell model [70, 72], the integral limits in t_- were extended to $\pm\infty$, which allowed to separate the two integrals as in Equation (108). The integral over t then became the GW source duration, $t_{sw} = t - t_*$, and we obtained the usually assumed linear growth rate [52]. As we discussed in more detail in Section 2.2.5 and as is shown in [73], for this result to be valid, the period of the oscillations must be much shorter than t_{sw}, i.e. $kt_{sw} \gg 1$ or equivalently $kR_* \gg \sqrt{K}$, and the duration of the sound waves must be long compared to the characteristic scale R_*, i.e., $t_{sw}/R_* \sim 1/\sqrt{K} \gg 1$. For sufficiently small values of K, the linear growth rate should hold at relevant wavenumber $kR_* \gg \sqrt{K}$ in the simulations. We also discussed in Section 2.2.5, that under the same assumptions, the remaining integral over $\tilde{t}_-$ in (107) is proportional to $\beta R_*/c_s$, so that the present-day GW spectrum can be parameterized as in Equation (109), namely

$$\Omega_{GW}(\tilde{k}) = 3\,\mathcal{T}_{GW}\,\tilde{\Omega}_{GW}\,K^2\,(H_*R_*)(H_*\tilde{t}_{sw})\,S(kR_*)\,, \tag{304}$$

or equivalently

$$\mathcal{I}_{sim}(\tilde{t}_*, \tilde{t}_{fin}, \tilde{k}) = \tilde{\Omega}_{GW}\,K^2\,(\beta R_*)\,\tilde{t}_{sw}\,S(kR_*)\,. \tag{305}$$

6.2.3 GWs from a damped source

We have identified the linear growth rate as a characteristic of sound waves that propagate freely without mutual interaction, thereby conserving kinetic energy on average over time. However, as we shall see in Section 6.4.5, intermediate and especially strong PTs exhibit significant damping of the system's kinetic energy. This clearly deviates from the assumption of constant average kinetic energy and suggests the presence of nonlinear interactions within the fluid. Consequently, we need to adapt our description to account for decaying sources.

Therefore, and with this insight, we make the ansatz that the UETC is *locally stationary* so that it can be factorized as

$$E_\Pi\,(t_1, t_2, k) = 2k^2K^2\,(t_+)\,f\,(t_-, k) \tag{306}$$

where $t_+ = \frac{1}{2}\,(t_1 + t_2)$ and $t_- = t_2 - t_1$. See [77] for a discussion on various UETCs in the context of turbulence. In this ansatz, $K^2\,(t_+)$ captures the slowly varying amplitude, while $f\,(t_-, k)$ parameterizes the strength of the correlations at different times separated by t_-, i.e., the support which is assumed stationary.

Then, under the same assumptions $k\tau_{sw} \gg 1$ and $K \ll 1$ from which we obtained the linear growth rate, one can similarly conclude that $K^2\,\tilde{t}_{sw}$ in Equation (305) can be substituted by K^2_{int}, defined by

$$K^2_{int}(\tilde{t}_*, \tilde{t}_{fin}) \equiv \int_{\tilde{t}_*}^{\tilde{t}_{fin}} K^2(\tilde{t})\,d\tilde{t}\,. \tag{307}$$

Therefore, in this framework, the GW spectrum parameterization generalizes to the case of a decaying source as

$$\mathcal{I}_{\mathrm{sim}}(\tilde{t}_*, \tilde{t}_{\mathrm{fin}}, \tilde{k}) = \tilde{\Omega}_{\mathrm{GW}}\, K^2_{\mathrm{int}}(\tilde{t}_*, \tilde{t}_{\mathrm{fin}})\, (\beta R_*)\, S(kR_*)\,. \tag{308}$$

Note that K^2_{int} trivially reduces to $K^2\,(\tilde{t}_{\mathrm{fin}} - \tilde{t}_*) = K^2\,\tilde{t}_{\mathrm{sw}}$ when K^2 is constant so that Equation (305) in the stationary assumption is recovered.

It is not clear a priori that the assumption of a locally stationary UETC is, in fact, a good description. Ultimately, we seek a description that allows to describe the GW spectrum in the simplest possible way for which relevant measurements can be made using the Higgsless simulations. One such measurement concerns the GW efficient $\tilde{\Omega}_{\mathrm{GW}}$. We will see in Section 6.4.6 that in this description utilizing a locally-stationary UETC, $\tilde{\Omega}_{\mathrm{GW}}(\tilde{t})$ is largely time-independent, allowing to robustly measure $\tilde{\Omega}_{\mathrm{GW}}$ as it enters (308). We take this as an indication of the approach's adequateness. Thus, we conclude that generalizing (305) to (308) allows us to measure the GW efficiency $\tilde{\Omega}_{\mathrm{GW}}$ even when the kinetic energy is decaying with time.

As for the decay, I will demonstrate in Section 6.4.5 that the kinetic energy evolution that we observe in the simulations is well described by a power law,

$$K(\tilde{t}) = K_0 \left(\frac{\tilde{t}}{\tilde{t}_0}\right)^{-b}\,. \tag{309}$$

where t_0 will come to represent the time of PT completion. I will proceed to fit Equation (309) to the data for the free parameters K_0 and b.

In view of this equation, note that when neglecting expansion, the physics is time translation invariant, and we can arbitrarily define the origin of time, which we can freely choose to be $\tilde{t}_{\mathrm{ref}} = 0$ and which in our case will always be very close to the beginning of the PT. Then, the proposed fit should be understood as $K(t) = K_0[(\tilde{t} - \tilde{t}_{\mathrm{ref}})/(\tilde{t}_0 - \tilde{t}_{\mathrm{ref}})]^{-b}$ with respect to t_{ref}. From this power law decay prescription and for $2b \neq 1$, K^2_{int} is analytically evaluated as

$$K^2_{\mathrm{int}} = K_0^2\,\tilde{t}_*\,(\tilde{t}_0/\tilde{t}_*)^{2b}\,\frac{(1+\tilde{t}_{\mathrm{sw}}/\tilde{t}_*)^{1-2b} - 1}{1-2b} \simeq K_0^2\,\tilde{t}_*\,\frac{(1+\tilde{t}_{\mathrm{sw}}/\tilde{t}_*)^{1-2b} - 1}{1-2b}\,, \tag{310}$$

at time $\tilde{t} = \tilde{t}_* + \tilde{t}_{\mathrm{sw}}$, where the approximation holds when $\tilde{t}_0 \simeq \tilde{t}_*$.

In the limit that the source duration $\tilde{t}_{sw} \ll \tilde{t}_*$, evidently, $K_{int} \to K_0^2\,\tilde{t}_{sw}$ for any value of b. In the converse limit, $\tilde{t}_{sw} \gg \tilde{t}_*$, one instead finds the following asymptotic behaviors:

$$\lim_{\tilde{t}_{sw}\gg\tilde{t}_*} K_{int}^2 = \frac{K_0^2\,\tilde{t}_0}{1-2b}\left(\frac{\tilde{t}_{sw}}{\tilde{t}_0}\right)^{1-2b}, \qquad \text{when } \; b < \tfrac{1}{2}\,,$$
$$\lim_{\tilde{t}_{sw}\gg\tilde{t}_*} K_{int}^2 = \frac{K_0^2\,\tilde{t}_0}{2b-1}\left(\frac{\tilde{t}_0}{\tilde{t}_*}\right)^{2b-1}, \qquad \text{when } \; b > \tfrac{1}{2}\,. \tag{311}$$

Hence, we see that when decay is weak, i.e., when $2b \leqslant 1$, then K_{int}^2 diverges proportionally to $\tilde{t}_{sw}^{1-2b}$. Conversely, when the decay is strong, i.e., $2b \geqslant 1$, then K_{int} converges in the limit of long source duration $\tilde{t}_{sw}/\tilde{t}_* \gg 1$.

Equation (308) thus presents to us the possibility to generalize the sound-wave results to that of a decaying source, which, as we shall see, is crucially important for the present study involving strong PTs. Under the particular assumption of a power-law decay, (308) becomes

$$\mathcal{I}_{sim}(\tilde{t}_*, \tilde{t}_{sw}, \tilde{k}) = \tilde{\Omega}_{GW}\,K_0^2\,(\beta R_*)\,\tilde{t}_*\,(\tilde{t}_0/\tilde{t}_*)^{2b}\,\frac{(1+\tilde{t}_{sw}/\tilde{t}_*)^{1-2b}-1}{1-2b}S(kR_*). \tag{312}$$

6.2.4 Recovering cosmic expansion

So far, and in particular all of Chapter 5, we have always neglected expansion except when introducing Equation (110),

$$\Omega_{GW}(k) = 3\,\mathcal{T}_{GW}\,\tilde{\Omega}_{GW}\,K^2\,(H_*R_*)\Upsilon(H_*,\tau_{sw})\,S(kR_*)\,.$$

Let us take a moment to appreciate the introduction of the factor $\Upsilon = H_*\tau_{sw}/(1+H_*\tau_{sw})$, where now τ_{sw} is an interval in conformal time, accounting for Hubble damping of fluid kinetic energy in the case of a conformally stationary UETC. We choose $a_* = 1$, such that the conformal Hubble rate is $\mathcal{H}_* = H_*a_* = H_*$. Furthermore, assuming that the PT is short and occurs during radiation domination, we can set the initial and final conformal times of GW production to be $H_*\tau_* = 1$ and $H_*\tau_{fin} = 1 + H_*\tau_{sw}$. To this end, recall that when cosmic expansion is not neglected, then $\mathcal{I}$ of Equation (94) is

$$\mathcal{I}(\tau_*,\tau_{fin},k) = \frac{k}{2}\int_{\tau_*}^{\tau_{fin}}\frac{d\tau_1}{\tau_1}\int_{\tau_*}^{\tau_{fin}}\frac{d\tau_2}{\tau_2}E_\Pi\,(\tau_1,\tau_2,k)\cos k\,(\tau_1-\tau_2)\,.$$

Following [73], we make the change of variables $\{\tau_{1,2}\} \to \{\tau_\pm\}$ where $\tau_+ \equiv (\tau_1+\tau_2)/2$ and $\tau_- \equiv \tau_2 - \tau_1$, or equivalently $\tau_1 = \tau_+ - \frac{\tau_-}{2}$, $\tau_2 = \tau_+ + \frac{\tau_-}{2}$. Then, $d\tau_1\,d\tau_2 = d\tau_+\,d\tau_-$, and the integral becomes

$$\mathcal{I}\,(\tau_*,\tau_{fin}\,,k) = k^3\int_{\tau_*}^{\tau_{fin}}d\tau_+\int_{-\infty}^{\infty}\frac{d\tau_-}{\tau_+^2-\frac{\tau_-^2}{4}}K^2 f\,(\tau_-,k)\cos\,(k\tau_-) \tag{313}$$

where I assumed a stationary UETC as in Equation (106),

$$E_{\Pi}(t_1, t_2, k) = 2k^2 K^2 f(t_-, k) ,$$

and expanded the limits of the second integral to $\pm\infty$ as we did in Section 2.2.5. Following [78] and neglecting τ_- in $1/(\tau_+^2 - \tau_-^2/4)$, which is fully justified when, e.g., the support of f is small, we see that in the stationary case, when commuting the integrals, the integral over time is, in reality, proportional to an integral of a factor $1/\tau^2$ over conformal time τ. If the support is not sufficiently small, then the extension of the integral limits to $\pm\infty$ is only justified when the period of the oscillations is much shorter than τ_{sw}, $k\tau_{sw} \gg 1$, i.e., $kR_* \gg \sqrt{K}$, and when the duration of the sound waves is long compared to the characteristic scale, $\tau_{sw}/R_* \sim 1/\sqrt{K} \gg 1$, as shown in [73].

Therefore, and under these assumptions, whenever the source duration is comparable to or longer than the bubble time, one can account for Hubble damping by multiplying with the suppression factor

$$\frac{\beta}{H_*}\int_{\tilde{\tau}_*}^{\tilde{\tau}_{fin}} \frac{d\tilde{\tau}}{\tilde{\tau}^2} = \frac{H_*}{\beta}\int_0^{\tilde{\tau}_{sw}} \frac{d\tilde{\tau}}{(1+\tilde{\tau}/\tilde{\tau}_*)^2} = \frac{\tilde{\tau}_{sw}(H_*/\beta)}{1+\tilde{\tau}_{sw}(H_*/\beta)} \equiv \Upsilon , \quad (314)$$

which is just the factor Υ in Equation (110) first introduced in [78]. It should be emphasized, nevertheless, that it is not free from assumptions, and to exactly capture the influence of expansion, one should, in principle, solve the GW equations of motion explicitly in an expanding space-time. We will simply regard Υ as a convenient way to attain a plausibly good estimate of the suppression due to cosmic expansion.

A natural generalization suggests itself: To account for Hubble damping also when the source is decaying and its UETC is only locally stationary, one should proceed to define

$$K^2_{int,exp} \equiv (\beta/H_*)^2 \int_{\tilde{\tau}_*}^{\tilde{\tau}_{fin}} \frac{K^2(\tilde{\tau})\, d\tilde{\tau}}{\tilde{\tau}^2} = \int_0^{\tilde{\tau}_{sw}} \frac{K^2(\tilde{\tau}+\tilde{\tau}_*)}{(1+\tilde{\tau}/\tilde{\tau}_*)^2}\, d\tilde{\tau} , \quad (315)$$

so that, now accounting for cosmic expansion,

$$\mathcal{I}_{sim}(\tilde{\tau}_*, \tilde{\tau}_{fin}, \tilde{k}) = \tilde{\Omega}_{GW}\, K^2_{int,exp}(\tilde{\tau}_*, \tilde{\tau}_{fin})\, (\beta R_*)\, S(kR_*) . \quad (316)$$

To provide a closed form of Equation (316) akin to Equation (359), one must solve the integral in Equation (315) assuming the power-law form of the decay (309). Here, the reader may rightfully object, for this law, explicitly derived in cosmic time, neglects expansion while we are now working in conformal time. Therefore, the reader could argue, the Equation (309) is no longer applicable. As of a small miracle[1], however, it happens to be the case that precisely for a radiation-dominated fluid,

1 Actually not. It follows from the presence of only one scale, H.

the conservation law (210) of Section 5.2.2 is conformally invariant in the sense that it takes exactly the same form in comoving space, provided the hydrodynamical variables are interpreted as comoving quantities [164, 165]. After the PT, the fluid obeys the radiation-equation-of-state, rendering conformal invariance of the conservation law manifest. Thus, the observed decay is, in fact, rightfully interpreted as that of comoving space and of comoving quantities, so as to perfectly justify the use of the power-law decay, initially described in cosmological time, also in conformal time. This, comes, however, with one caveat: Earlier, we were free to arbitrarily set the origin of time since in non-expanding space, all laws are time-translation invariant, and times carry only relative significance. Now, with cosmic expansion breaking time-translation invariance, times are instead absolute. Therefore, in conformal and now absolute time $\tilde{\tau}$,

$$K(\tilde{\tau}) \equiv K_0 \left(\frac{\Delta\tilde{\tau}}{\Delta\tilde{\tau}_0}\right)^{-b} \equiv K_0 \left(\frac{\tilde{\tau} - \tilde{\tau}_* + \Delta\tilde{\tau}_*}{\tilde{\tau}_0 - \tilde{\tau}_* + \Delta\tilde{\tau}_*}\right)^{-b} \tag{317}$$

where $\Delta\tilde{\tau}_0 \equiv \tilde{t}_0$ as in the parameter entering (309) and $\Delta\tilde{\tau}_* = \Delta\tilde{\tau}_0 + \tilde{\tau}_* - \tilde{\tau}_0$. Then, the integral 315 takes the form

$$K^2_{\text{int,exp}} = K_0^2 \, \Delta\tilde{\tau}_0^{2b} \int_0^{\tilde{\tau}_{\text{sw}}} \frac{(\tilde{\tau} + \Delta\tilde{\tau}_*)^{-2b}}{\left[1 + \tilde{\tau}\,(H_*/\beta)\right]^2} \, d\tilde{\tau} \equiv K_0^2 \, \Upsilon_b(\tilde{\tau}_{\text{sw}}) \, (\beta/H_*) \,, \tag{318}$$

where I defined the generalized Hubble damping suppression factor

$$\Upsilon_b(\tilde{\tau}_{\text{sw}}) = \Delta\mathcal{F}_b \, (H_*/\beta)(1-2b)^{-1} \tag{319}$$

where $\Delta\mathcal{F}_b \equiv \mathcal{F}_b(\tilde{\tau}_{\text{sw}}) - \mathcal{F}_b(0)$ and the function $\mathcal{F}_b$ defined by

$$\mathcal{F}_b(\tilde{\tau}) = \frac{(\Delta\tilde{\tau}_* + \tilde{\tau})^{1-2b} \Delta\tilde{\tau}_0^{2b}}{(1 - \Delta\tau_* H_*)^2} \, {}_2F_1\left[2, 1-2b, 2-2b, -\frac{H_*\Delta\tau_* + \tilde{\tau}H_*/\beta}{1 - H_*\Delta\tau_*}\right], \tag{320}$$

${}_2F_1$ being the hypergeometric function. Note that that $\Upsilon_b(\tilde{\tau}_{\text{sw}})$ reduces to $\Upsilon(\tilde{\tau}_{\text{sw}})$ of a stationary stationary sources when $b = 0$.

While Equation (319) is convenient in that it provides a format that can be directly evaluated without explicitly computing the integral, we don't see that the emergence of the hypergeometric function carries any deep physical meaning, as Equation (320) simply arises from introducing the power-law form (309) of the decay of $K(\tau)$ in Equation (315). Instead, the modification Υ_b with respect to Υ is ultimately what is of physical interest.

Thus, the GW spectrum incorporating effects of both source decay and expansion is given by

$$\mathcal{I}_{\text{sim}}(\tilde{t}_*, \tilde{t}_{\text{fin}}, \tilde{k}) = \tilde{\Omega}_{\text{GW}} \, K_0^2 \, \Upsilon_b(\tilde{\tau}_{\text{sw}}) \left(\frac{\beta}{H_*}\right) (\beta R_*) \, S(kR_*) \,. \tag{321}$$

so that the present-day GW spectrum becomes

$$\Omega_{\mathrm{GW}}(k) = 3\,\mathcal{T}_{\mathrm{GW}}\,\tilde{\Omega}_{\mathrm{GW}}\,K_0^2\,(H_* R_*)\,\Upsilon_b(\tau_{\mathrm{sw}})\,S(kR_*)\,, \tag{322}$$

Let me iterate that the value of $\Delta\tilde{\tau}_0 \equiv \tilde{t}_0$ will be fixed to that of PT completion in the relative times of our simulations while $\Delta\tilde{\tau}_* = \tilde{\tau}_* - \tilde{\tau}_0 + \Delta\tilde{\tau}_0$ allows to initiate sourcing of GWs any time $\tilde{\tau}_*$. Furthermore, it should be emphasized as we did for Υ, that Υ_b should be regarded as a plausibly good way to a posteriori account for expansion, but that one should, in principle, solve the GW equations of motion explicitly in an expanding space-time to validate this estimate.

6.2.5 Summary of intended usage

Having established the main theoretical framework and assumptions within which we operate, let me outline how the results of this Section 6.2 will be put in use.

First, I will define t_0 as the time of PT completion and extract numerical values of K_0 and b for each simulation by fitting Equation (309) to the simulation data in Section 6.4.5. As we shall see, the power-law prescription works flawlessly for the current situation duration up to $\tilde{t} = 32$.

Then, in Section 6.4.6, we compute integrated GW amplitude $\mathcal{I}_{\mathrm{sim}}^{\mathrm{int}} \equiv \int \mathcal{I}_{\mathrm{sim}}\,\mathrm{d}\ln k$, where $\mathcal{I}_{\mathrm{sim}}(\tilde{t}_{\mathrm{init}}, \tilde{t}, k)$ is evaluated at $\tilde{t}_{\mathrm{init}} = 16$ and we allow $\tilde{t}$ to vary from $\tilde{t}_{\mathrm{init}}$ to $\tilde{t}_{\mathrm{end}} = 32$. This allows computing the time evolution of the GW efficiency

$$\tilde{\Omega}_{\mathrm{GW}}(\tilde{t}) = \frac{\mathcal{I}_{\mathrm{sim}}^{\mathrm{int}}(\tilde{t}_{\mathrm{init}}, \tilde{t})}{K_{\mathrm{int}}^2(\tilde{t}_{\mathrm{init}}, \tilde{t})(\beta R_*)}\,, \tag{323}$$

where K_{int}^2 is determined from our numerical simulation data.

We subsequently establish the validity of the adequateness of Equation (308) within the duration of our simulations by observing the approximate time-independence $\tilde{\Omega}_{\mathrm{GW}}(\tilde{t})$ in (338), and take $\tilde{\Omega}_{\mathrm{GW}}(\tilde{t}_{\mathrm{end}})$ as our measurement of the GW efficiency.

Then, having established the time independence of the GW efficiency and obtained a robust measurement, we can use the power-law decay of $K(t)$ in Equation (309) to emulate GW production all the way back to $\tilde{t}_0$ under the assumption that the locally stationary UETC description holds until that time. This allows computing the GW spectrum sourced by a locally stationary source of sound waves from the completion of the PT for a duration of $\tilde{t}_{\mathrm{sw}}$, thus attempting to recover the part of the GW productions which the simulations have neglected.

Finally, having established the conformal invariance of the fluid equations of motion, we can interpret the power-law decay in conformal

and now absolute time in order to model the damping of the fluid kinetic energy due to Hubble expansion as in (315) and the consequent suppression of the GW spectrum amplitude, thus transcending the confines of the initial neglect of cosmic expansion.

6.3 Numerical setup

6.3.1 Updates to the simulation implementation

In this work, I update the simulation implementation in a number of ways, leading to Version-2 of the Higgsless simulation. While the physical setup in Version-2 of the Higgsless simulation code is identical to that of the original version in the previous Chapter 5, which we will call Version 1, in the present study, we take the opportunity to refine the numerical implementation of the Higgsless simulation code. While some changes are generic and benefit all simulations regardless of PT parameters, one was required to enhance the stability numerical stability in simulations of stronger PTs.

In this Section, I highlight three updates that were made to the numerical implementation. These updates aim at improving (1) the time integration scheme, (2) the mapping between the discrete and the continuum momenta, and (3) the criterion for numerical stability in simulations of strong PTs ($\alpha = 0.5$). Since otherwise all details of the simulation implementation are identical to Version 1 of the Higgsless simulation code, as outlined in Section 5.3 of Chapter 5, I refer readers to that Section for general details on the implementation.

6.3.1.1 Improvement of the time integration routine

Commencing with update (1), in practice, the time integral in the Fourier transform of Equation (236) must be computed numerically on the grid of time. In the first iteration of the Higgsless simulation code, the time integral was approximated as in Equation (284) (here including $\delta\tilde{t}$, previously added first in the final normalization),

$$T_{ij}(q, \mathbf{k}\,|\,t) = \sum_{t_n = t_{\text{init}}}^{t} \delta\tilde{t}\, e^{iqt_n} T_{ij}\,(t_n, \mathbf{k})\ , \tag{324}$$

i.e., through its Riemann sum, by stacking past time slices weighed by a complex factor from t_{init} until $t \leqslant t_{\text{end}}$ for each time step over which the GWs are sourced. In our case, we usually take $\tilde{t}_{\text{init}} = 16$ and $t_{\text{end}} = 32$, following the discussion in Section 5.3.7.

In the current Version 2 of the Higgsless simulations, I improve upon this method by treating T_{ij} as a piecewise linear function interpolating

between the support points, using a similar scheme to the one proposed in [157] for solving the GW equation. Following this approach, the discrete Fourier transform-in-time is instead approximated as

$$e^{iqt}\left(T_{ij}\left(t_i,\mathbf{k}\right)+\left.\frac{dT_{ij}}{dt}\right|_{t_i}\left(t-t_i\right)\right), \tag{325}$$

which can be integrated analytically on small intervals $t\in(t_i,t_i+\delta\tilde{t})$ between the simulation time steps. The Fourier transform-in-time is then better approximated as

$$\begin{aligned}
&T_{ij}(q,\mathbf{k}\,|\,t)\\
&=\int_{t_{\text{init}}}^{t}dt'e^{iqt'}T_{ij}\left(t',\mathbf{k}\right)\\
&\approx\sum_{t_n=t_{\text{init}}}^{t}\int_{t_n}^{t_n+\delta\tilde{t}}dt'e^{iqt'}\left(T_{ij}\left(t_n,\mathbf{k}\right)+\left.\frac{dT_{ij}}{dt}\right|_{t_n}\left(t-t_n\right)\right)\\
&=\sum_{t_n=t_{\text{init}}}^{t}\frac{1}{q^2}\left[e^{iq(t_n+\delta\tilde{t})}\left(T_{ij,n}{}'-iq\left(T_{ij,n}+\delta\tilde{t}T_{ij,n}{}'\right)\right)-e^{iqt_n}\left(T_{ij,n}{}'-iqT_{ij,n}\right)\right]
\end{aligned} \tag{326}$$

Since the integrand, which involves an oscillating exponential and the linearized T_{ij}, is now analytically integrated, this modified routine better captures the UV behavior at large k. This approach alleviates the constraints on the time-step $\delta\tilde{t}$ required to obtain accurate spectra in this regime (see discussion in [157]). However, for the dynamical range and choice of $\delta\tilde{t}$ used in the simulations, no significant discrepancies have been observed in the UV range of the GW spectrum due to this change. Overall, it should improve the UV reliability and may become important in future simulation runs.

6.3.1.2 Updated mapping between discrete and continuum momenta

Continuing with update (2), let us revisit Version 1 of the code and note that this initial version utilized a sin-based method to map discrete grid momenta to their continuum counterparts since it is necessary to ensure that Fourier modes with momenta $\tilde{n}_j$ and $\tilde{n}_j+N$ in the j:th direction, etc., are mapped to the same physical wavenumber. Additionally, momenta near $\tilde{n}_j\simeq N$ are equivalent to those near $\tilde{n}_j\simeq 0$ and should be treated as soft modes. This led to the use of two different mappings depending on whether the sign of momentum was important:

$$k_i=\frac{\sin\left(2\pi\tilde{n}_i/N\right)}{\delta\tilde{x}},$$

as in Equation (256), for cases where the sign is relevant, and

$$k_i = 2\frac{\sin(\pi\tilde{n}_i/N)}{\delta\tilde{x}}$$

as in Equation (255), for cases where it is not.

In the current Version 2 of the simulation code, I adopt a *saw* prescription for the mapping of momenta:

$$k_i = \mathrm{saw}(\tilde{n}_i) \equiv \begin{cases} \frac{2\pi\tilde{n}_i}{N\delta\tilde{x}} & \text{for } \tilde{n}_i < \frac{N}{2}\,, \\ 0 & \text{for } \tilde{n}_i = \frac{N}{2}\,, \\ \frac{2\pi(\tilde{n}_i - N)}{N\delta\tilde{x}} & \text{for } \tilde{n}_i > \frac{N}{2}\,. \end{cases} \tag{327}$$

This saw mapping eliminates the need for different treatments in different contexts, thus providing a consistent momentum map up to $\tilde{n}_i \simeq N/2$, to be contrasted with the previous sin-based method which was only accurate within the linear regime of the sin function. Therefore, the saw prescription ensures consistency across the entire range. Note that in Version 1, the hardest mode corresponds to the physical wavenumber $k_{UV} = \sqrt{3}/\delta\tilde{x}$, which is the UV cutoff beyond which no results are obtained. For the saw-prescription, the UV cutoff is instead $k_{UV} = \sqrt{3}\pi/\delta\tilde{x}$

Although no significant differences have been observed between the two methods in our current simulations, we anticipate the saw prescription to enhance accuracy at smaller scales.

6.3.1.3 Improved numerical stability in strong phase transitions

The third point (3) concerns the choice of the maximal local velocity $a_{j+1/2,k,l}$, etc., (on a staggered cell in direction j), appearing in Equation (205). We have seen how this quantity locally regulates the numerical viscosity of the KT scheme, which consequently helps preserve shock structures in the lattice by reducing spurious oscillations. Larger local velocities $a_{j+1/2,k,l}$ thus increase numerical viscosity and thus improve upon the stability of the numerical scheme. In the limit of small fluid velocities, i.e., for weak and intermediate PTs, $a_{j+1/2,k,l} = c_s = \sqrt{1/3}$, etc., is a good choice. In the case of strong PTs, however, fluid velocities often supersede $\sqrt{1/3}$ and approach 1. To improve the numerical stability of the simulation, we therefore choose $a_{j+1/2,k,l} = 1$, etc., for strong PTs. In the weak regime, the numerical changes due to this choice are negligible but for stronger PTs, the stability of the numerical solver is significantly improved.

Furthermore, in rare isolated cases and close to shocks, the simulation encounters that on staggered grid points in the computation of the pressure, the quantity

$$\lambda = \frac{3}{4}\left(\frac{\bar{K}^0}{K}\right)^2 ,$$

defined in Equation (233), locally supersedes 1. Upon taking $\sqrt{1-\lambda}$, as required to compute the enthalpy and the pressure, this causes problems. This problem is solved by locally enforcing that $\lambda < 1$ on staggered grid points and re-scale K accordingly before computing the pressure. While this procedure is necessary to stabilize the numerical solver and to allow running simulations of strong PTs, it appears to have no noticeable effect on either the results or energy conservation.

In all other regards, the current Version 2 of the Higgsless implementation is identical to the first Version 1 in the previous Chapter.

6.3.2 Simulations and parameter choices

Building upon the work in Chapter 5 and [1], I extend the parameter space by including strong PTs with $\alpha = 0.5$. I thus conduct *ref-*

	reference	**seeds**	**single-bubble**
PT strength α	{0.0046, 0.05, 0.5}	{0.0046, 0.05, 0.5}	{0.0046, 0.05, 0.5}
wall velocity v_w	$\in [0.32, 0.8]$	{0.32/0.36, 0.6, 0.8}	$\in [0.32, 0.8]$
box size $\tilde{L}/v_w \equiv L\beta/v_w$	{20, 40}	{20, 40}	{20, 40}
sim. time $\tilde{t}_{end} \equiv t_{end}\beta$	32	32	$\tilde{L}/2/\max(v_w, c_s)$
grid size N	{64, 128, 256, 512}	{64, 128, 256, 512}	512
$\delta\tilde{t}/\delta\tilde{x}$	$< 1/4$	$< 1/4$	$< 1/4$
count.	304	72×9 seeds $= 648$	76

Table 5: Summary of simulation runs with physical and numerical parameter choices. *Reference* indicates simulations constructed from a single reference bubble nucleation history (one for each box size), thereby minimizing statistical differences among the sample of reference simulations. *Seeds* refers to simulations constructed from a set of 9 additional bubble nucleation histories, allowing to infer statistical sample variance for 3 selected wall velocities $v_w = 0.32$ (0.36), 0.6, and 0.8, which correspond to deflagrations, hybrids, and detonations for weak and intermediate PTs, while $v_w = 0.8$ is a hybrid for strong PTs. *Single-bubble* refers to simulations with a single isolated centrally nucleated bubble, allowing us to study the convergence of self-similar profiles. We take a range of $v_w \in [0.32, 0.8]$ in increments of 0.04 besides for strong PTs ($\alpha = 0.5$) for which we take $v_w \in [0.36, 0.8]$. A total of 1028 simulations have been performed.

erence simulations for $\alpha \in \{0.0046, 0.05, 0.5\}$ and wall velocities $v_w \in \{0.32, 0.36, \ldots, 0.76, 0.8\}$, excluding $v_w = 0.32$ for strong PTs due to the absence of deflagrations for $\alpha \gtrsim \frac{1}{3}(1 - v_w)^{-13/10}$ [86]. This results in a total of $3 \times 13 - 1 = 38$ PT parameter points. To obtain our primary results, I perform *reference* simulations for each box size, utilizing a unique bubble nucleation history across all wall velocities, PT strengths, and grid resolutions, thereby ensuring that the sample variance remains constant across different values of v_w, α, and N. I summarize the parameters used in this study in Table 5.

The procedure for constructing bubble nucleation histories, as detailed in Section 5.3.5, leads to simulations featuring approximately $N_b \simeq \tilde{L}^3/(8\pi v_w^3)$ bubbles (Equation (127)), where $\tilde{L} \equiv L\beta$. These bubbles are nucleated according to a statistical distribution that is exponential in time and uniform in space. In our simulations, $\tilde{L}/v_w$ takes on values of 20 and 40, corresponding to approximately 300 and 2500 bubbles, respectively. For a fixed numerical resolution N, simulations with $\tilde{L}/v_w = 40$ achieve a reduction in statistical variance by increasing the number of bubbles, thereby improving the resolution of quantities measured in the IR regime. In contrast, simulations with $\tilde{L}/v_w = 20$ provide a wider dynamical range in the UV. For additional details and comments, refer to Section 5.3.5.

For each of the 76 parameter points $\{v_w, \alpha, \tilde{L}/v_w\}$, I conduct simulations with varying grid resolutions N^3, where $N \in \{64, 128, 256, 512\}$, resulting in a total of $76 \times 4 = 304$ reference simulations. By running simulations at different grid sizes, we assess the convergence of our numerical results and estimate physical quantities in the continuum limit through a well-motivated extrapolation scheme in Section 6.4.3.

To ensure stability, we set the number of time steps $N_t = \tilde{t}_{end}/\delta\tilde{t}$ to satisfy the Courant-Friedrichs-Lewy (CFL) condition, $\delta\tilde{t}/\delta\tilde{x} < 1/4$, where $\delta\tilde{x} = \tilde{L}/N$. We have verified that for strong PTs, increasing N_t beyond this threshold does not alter the numerical results, allowing us to use the smallest permissible value without repercussions.

Additionally, for each parameter set $\{v_w, \alpha, \tilde{L}/v_w\}$, I perform simulations of single centrally nucleated bubbles to monitor the convergence of self-similar fluid profiles, leading to 76 *single-bubble* simulations. Findings associated with these simulations are detailed in Section 6.4.4, where the single-bubble simulations are used to better understand the global state of convergence of the reference multiple-bubble simulations and to refine the extrapolated predictions from Section 6.4.3. We note that single-bubble simulations are run only until $\tilde{t}_{end} = \tilde{L}v_w/(2\max(c_s, v_w))$, approximately when the fluid sound shell reaches the boundary of the simulation domain.

In addition to the reference and single-bubble simulations, I also run multiple-bubble simulations based on 9 additional distinct bub-

ble nucleation histories per box size for all strengths, resolutions, and box sizes, for $v_w \in \{0.32/0.36, 0.6, 0.8\}$, where the lower $v_w = 0.32$ is used for weak and intermediate PTs and $v_w = 0.36$ for strong ones. These velocities correspond to deflagrations, hybrids, and detonations, respectively, except for strong PTs for which also $v_w = 0.8$ corresponds to a hybrid. This implies a total of $3 \times 3 \times 2 \times 4 \times 9 = 648$ *seed* simulations from which the statistical variance of the results can be estimated. We will use these simulations to provide error bars in our measured quantities corresponding to the standard deviation from the 10 different bubble nucleation histories in Section 6.4.

All reference and seed simulations are conducted within the time range $0 < \tilde{t} \equiv t\beta < 32$, with the GW spectrum extracted from the interval $\tilde{t}_{\text{init}} = 16$ to $\tilde{t}_{\text{end}} = 32$. The time origin $\tilde{t} = 0$ is set such that the first bubble nucleates at $\tilde{t} = 0.5$ (consistent with the time translation invariance of our equations when the expansion of the Universe is negligible).

Similarly to Chapter 5 and according to the discussion in Section 5.3.7, we exclude early times up to $\tilde{t}_{\text{init}} = 16$ to focus on fluid perturbations post-bubble collisions, thereby minimizing realization-dependent effects on GW production. This approach also suppresses contributions to the GW spectrum from the initial collisions. For $\tilde{t} > 16$, we compute $\mathcal{I}_{\text{sim}}(\tilde{t}_{\text{init}}, \tilde{t}_{\text{fin}}, \tilde{k})$ to robustly test the scaling of Eq. (308) and calculate the GW efficiency $\tilde{\Omega}_{\text{GW}}$ and the spectral shape $S(kR_*)$. The time $\tilde{t}_{\text{init}} = 16$ occurs after PT completion when the broken phase has filled the entire simulation volume, which for the reference nucleation history with $\tilde{L}/v_w = 20$ happens at $\tilde{t}_0 \simeq 10$. Additionally, we consider times $\tilde{t} > \tilde{t}_0$ to fit the time evolution of the kinetic energy fraction $K(\tilde{t}) = K_0 \, (\tilde{t}/\tilde{t}_0)^{-b}$ in Section 6.4.5.

In total, in this study, I have performed 1028 simulations, summarized in Table 5, with an estimated computational time of approximately 10^6 CPU hours. Each high-resolution simulation with $N = 512$ requires around 10^3 CPU hours.

6.4 Numerical results

6.4.1 Overview

This work has produced a large and complex set of data, results, and conclusions, which may be difficult to discern due to the sheer volume and rather technical complexity of the presentation. Therefore, before delving into the details of our numerical results, I would like to offer some context. In summary, our findings can be outlined as follows:

- *Simulations of strong first-order PTs with* $\alpha = 0.5$: In this work, I update the results from Chapter 5, particularly focusing on strong PTs across a wide range of wall velocities. I conduct systematic convergence studies and, for the first time, provide the full GW spectra for strong PTs. In Section 6.5, I present a template for the expected GW spectrum from compressional fluid perturbations, extended to decaying sources as discussed in Sections 6.2.2 and 6.2.3, incorporating insights from our simulations. This template is the relevant result for the reader interested in using our results in phenomenological studies. Figures 25 and 26 illustrate central 2D slices of the fluid velocity $|\mathbf{v}(\tilde{\mathbf{x}})|$ and enthalpy $w(\mathbf{x})$ at four different simulation times for weak and intermediate PTs with a box size of $\tilde{L} = 40 v_w$.

- *Template parameterizations*: Ideally, the numerical findings should be expressed in terms of as few physical quantities as possible, thus facilitating their use in further studies and indicating the correct underlying physical relations have been identified. In our simulations, all simulation variables and quantities are dimensionless, meaning that β/H_* does not enter the numerical setup and results but only appears when recovering physical quantities. This and the assumed linear GW spectrum growth rate motivated the use of the dimensionless GW spectrum growth rate Q' in Equation (286) in the previous Chapter 5 and to interpret results in the system variable normalization with β. While this offered convenience, it may not align optimally with physical expectations. In this work, motivated by the parameterization (109), we instead measure quantities based on R_* and K^2_{int}, as in Equation (308), which allows presenting the essential results in a straightforward physically motivated manner, with an *almost* time-invariant GW efficiency $\tilde{\Omega}_{\text{GW}}$. This approach accommodates deviations from the linear growth of the GW amplitude with the source duration, as expected for stationary sources and discussed in Section 6.2.2 and 6.2.3. Additionally, we provide a definition for $K^2_{\text{int,exp}}$ to incorporate the effect of cosmic expansion, which can be accommodated a posteriori in Equation (318) following the realization that the fluid equations of motion are conformally invariant.

- *Development of nonlinearities*: For strong and some intermediate PTs, we observe several phenomena likely arising from the nonlinear dynamics of the fluid. First, we notice that the growth of the GW amplitude with the source duration begins to deviate from the expected linear trend, approaching saturation toward the end of the simulations, possibly as a result of fluid damp-

ing. This observed decay in the fluid's kinetic energy, which is found to be accurately modeled as a power-law within the simulation duration following PT completion, could suggest that nonlinearities are causing a cascade from larger to smaller scales in the fluid perturbations, leading to energy dissipation at smaller scales. This effect might impact the UV portion of the GW spectrum, potentially leading to a shift from the expected k^{-3} behavior found for sound waves [1, 25, 67, 69–71, 73, 74] towards a shallower turbulent spectrum of $k^{-8/3}$ [75, 77, 92–96], which, in fact, is supported by our measured UV slopes. We demonstrate the numerical robustness of our results throughout this Section and discuss future studies needed to verify some of our findings. In particular, in Section 6.4.9, I present a preliminary investigation of the development of vorticity in our simulations.

Overall, this work aimed to systematically investigate the accuracy of the simulation results. I thus demonstrate the convergence of the findings with respect to the grid spacing $\delta\tilde{x}$ through this Chapter, with a particular focus on the convergence of energies measured in the simulation in Section 6.4.3. In Section 6.4.5, the time dependence of the fluid kinetic energy ratio K is analyzed, with the decaying power-law model presented in Section 6.2.3 fitted to the numerical results.

Section 6.4.6 examines the expected scaling of the GW spectrum with K_{int}^2 and R_*, considering the evolution of the integrated GW amplitude with source duration, and computing the GW efficiency $\tilde{\Omega}_{\text{GW}}$ in accordance with Equation (308). Additionally, this Section provides an estimate of the expected GW amplitude in flat Minkowski spacetime based on the numerical results from Sections 6.4.3, 6.4.4 and 6.4.6, as well as in an expanding background using the model from Section 6.2.4.

Finally, in Section 6.4.7, the spectral shape of the GW spectrum is studied, with a particular focus on the UV regime, where deviations from the expected slope in the sound-wave regime are observed.

6.4.2 Simulation slices

Again, but now, for strong PTs, I wish to present a few 2D time slices of the simulations to illustrate the rich dynamics and geometry of the colliding sound shells. I thus show in Figures 25, and 26 central 2D simulation slices of the fluid velocity $|\mathbf{v}(\tilde{\mathbf{x}})|$ and the enthalpy $w(\tilde{\mathbf{x}})$, at four different simulation times and box size $\tilde{L} = 40v_w$, but this time for strong PTs. For a comparison with weak and intermediate PTs, see Figures 14, 15 and 16 in the previous Chapter 5. The first three slices are chosen at equidistant times to show the bubble evolution before

PT completion, while the fourth slice is at the end of the simulation at $\tilde{t} = 32$ to highlight the long-term evolution. These parameter choices correspond to one deflagration and two hybrids. In Chapter 5, we observed the tendency of intermediate PTs to exhibit sharper features at the end of the simulation compared to weak PTs. With strong PTs, we observe even sharper features, thus strengthening the hypothesis of shock formation being the driver of this behavior. While not clearly visible in the velocity and enthalpy fields, we observe the presence of macroscopic and sizeable vorticity, which is produced mainly during the collision phase. This can be seen in the 2D simulations slices of Figure 41 in Section 6.4.9, where I discuss preliminary findings on vorticity.

6.4.3 Convergence analysis of the kinetic energy and GW amplitude

In this Section, we focus on the convergence and extrapolation of energies in multi-bubble simulations. To study the convergence of the simulations, I conducted simulations for each parameter point $\{\alpha, v_w\}$ at four resolutions $N \in \{64, 128, 256, 512\}$ and two box sizes $\tilde{L}/v_w \in \{20, 40\}$. Given that our Higgsless simulations employ relatively sparse grids compared to those with scalar fields [25, 69, 71, 101], the resolution can pose challenges in accurately reproducing the self-similar profiles induced by uncollided bubbles during the initial simulation stages. This issue is particularly pronounced for parameter points with $v_w \lesssim v_{CJ}$, where v_{CJ} denotes the Chapman-Jouguet speed, which separates hybrids from detonations.

As v_w approaches v_{CJ}, the fluid profiles become increasingly thin hybrids. For our parameters, the Chapman-Jouguet speeds are $v_{CJ} = \{0.63, 0.73, 0.89\}$ for $\alpha = \{0.0046, 0.05, 0.5\}$, respectively. Consequently, as can be seen in Figure 3, very thin profiles are observed when $v_w = 0.6$ for weak PTs, when $v_w = 0.72$ for intermediate PT, and when $v_w = 0.8$ for strong PTs. In these cases, the resolution in $\xi \equiv r/(t - t_n)$, where r is the radial distance from the nucleation location, and t_n is the nucleation time, may be insufficient to resolve the self-similar profiles accurately at the moment of a bubble collision. This is due to the initially low resolution in ξ for a fixed N, which improves as time progresses.

In addition to the resolution requirements for accurately capturing thin self-similar profiles prior to collisions, we anticipate that high numerical resolutions will be necessary to fully capture the dynamics of fluid perturbations as they transition to nonlinear behavior during and after collisions. This increased resolution is essential to resolve the

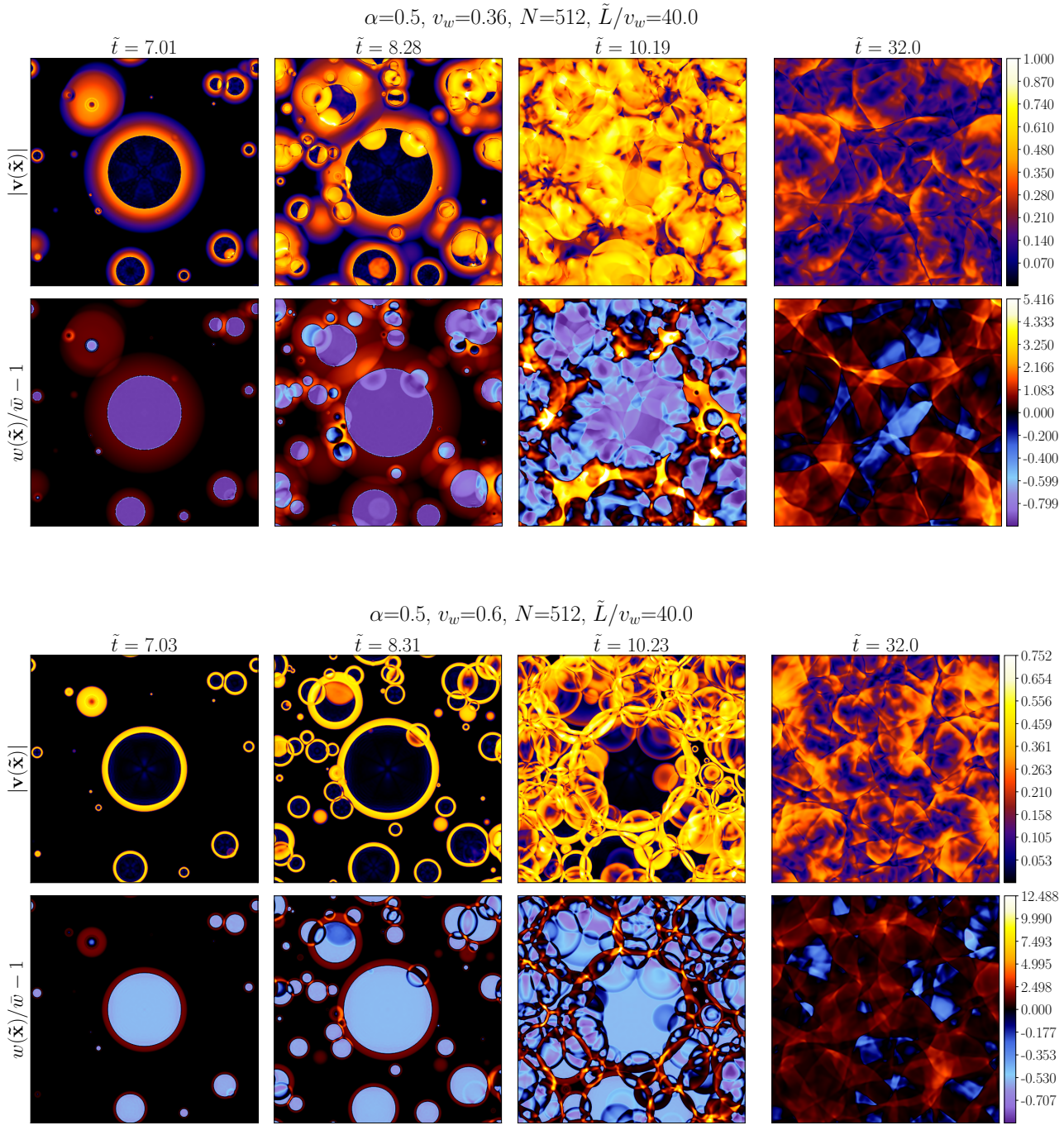

Figure 25: Central 2D simulation slices of the fluid velocity amplitude $|\mathbf{v}(\tilde{\mathbf{x}})|$ and enthalpy $w(\tilde{\mathbf{x}})$ for a strong PT with $\alpha = 0.5$ The resolution is $N = 512$, and the box size $\tilde{L} = 40v_w$. The first three slices are chosen at equidistant times to show the bubble evolution before PT completion, while the fourth slice is at the end of the simulation to display the long-term behavior. The upper (lower) panels corresponds to a deflagration with $v_w = 0.5$ (hybrid with $v_w = 0.6$).

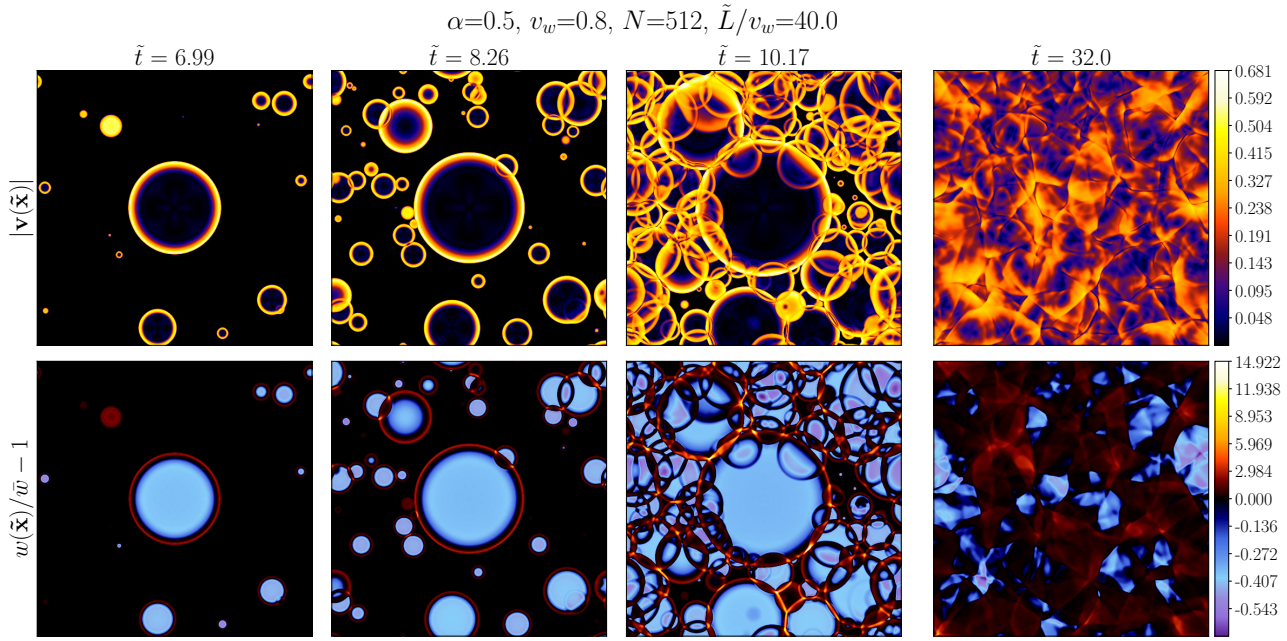

Figure 26: Same as the Figure 25, but for $v_w = 0.8$, corresponding to a hybrid. Note that for weak and intermediate PTs, this wall velocity gives rise to detonation solutions.

complex interactions and evolving features of the fluid as the dynamics become more intricate.

To assess the convergence of energies in the simulations, we analyze the numerical results as a function of N and aim to enhance our measurements by extrapolating the results to the limit $N \to \infty$, assuming the validity of our extrapolation scheme.

On general grounds, one can define a specific number of grid points N_* such that for $N \gg N_*$, the simulation results appear to converge as N increases beyond this threshold. Thus, when $N \gg N_*$, we can assume that the measured quantities are close to their continuum values in the limit of infinite resolution.

Empirically, we observe that with insufficient resolution, the kinetic energy fraction K is generally *underestimated*. This underestimation occurs because the velocity profiles appear smeared around their self-similar counterparts, resulting in correspondingly lower velocities. These realizations motivated us to employ the following function to model the convergence of the kinetic energy fraction:

$$K = \frac{K_\infty}{1 + (N_*/N)^a}\,, \tag{328}$$

where α, N_*, and K_∞ are found by fitting the numerical results as a function of N. The values of K_∞ will be called *extrapolated* or *continuum* values. We furthermore define the relative error

$$\varepsilon_K \equiv \frac{|K_\infty - K_{512}|}{K_\infty} = (\delta\tilde{x}/\delta\tilde{x}_*)^\alpha + \mathcal{O}(\delta\tilde{x}^{2\alpha})\,, \tag{329}$$

where $\delta\tilde{x}_* = \tilde{L}/N_*$ and K_{512} is the measure value of K at highest resolution $N = 512$. Note that the value of α in Equation (328) indicates the degree of numerical convergence. This effect degree of convergence, however, is a result of the geometry of the dynamics itself and is not fundamentally related to the degree of the employed KT+RK3 scheme defined in (207), which is second order in spatial discretization.

A few words of caution are warranted: Equation (328) is guided by the empirical observation that kinetic energies of single bubbles are, in almost all cases, underestimated [2]. Therefore, as we increase resolution, the profiles sharpen and we expect to measure kinetic energies closer to K_∞. However, this also implies more prominent nonlinear dynamics. In fact, in certain cases, as we reach a critical resolution, numerical viscosity and under-resolution of self-similar profiles appear to be dominated by the emergence of nonlinear dissipation of energy. In these cases, we will see a *decrease* in the kinetic energy with increased resolution and the breakdown of the convergence prescription (328). Thus, when we observe that the energy for $N = 512$ is smaller than for $N = 256$, i.e., $K_{512} < K_{256}$, we deem (328) inappropriate and resort to measured values for the highest resolution, so as to report $K_\infty = K_{512}$ with corresponding relative error 329 instead defined as $\varepsilon_K \equiv |K_{512} - K_{256}|/K_{512}$.

Furthermore, while Equation (328) was justified from considerations of the kinetic energy alone, we will use it more generally. In particular, we will use the convergence prescription (328) to study the convergence of the energy fraction K_0 entering the power-law decay formula (309) as obtained from the fitting procedure in Section 6.4.5. We will use it for the RMS kinetic energy fraction, computed from K_{int} in Equation 307 as $\tilde{T}_{\text{GW}}\, K_{\text{rms}}^2 \equiv K_{\text{int}}^2$, where $\tilde{T}_{\text{GW}} \equiv \tilde{t}_{\text{end}} - \tilde{t}_{\text{init}} = 16$ corresponds to the time interval over which the GW spectrum is computed. And we will use if for the GW amplitude $\mathcal{I}_{\text{sim}}^{\text{int}} \equiv \int \mathcal{I}_{\text{sim}}\, \mathrm{d}\ln k$, where $\mathcal{I}_{\text{sim}}(\tilde{t}_{\text{init}}, \tilde{t}_{\text{end}}, \tilde{k})$ is defined in (302) for initial and final times $\tilde{t}_{\text{init}} = 16$ and $\tilde{t}_{\text{end}} = 32$. Thus, we will make the replacement in (328) $K \to K_0$, K_{rms} and $\mathcal{I}_{\text{sim}}^{\text{int}}$.

In Figure 27, I show the results of fitting Equation (328) to the reference simulation energies for the various resolutions. Since smaller

2 The only exception being strong deflagrations for $v_w = 0.36$ and $v_w = 0.4$, for which the kinetic energy is in fact marginally overestimated (see the top-right plot in Figure 28.)

box size $\tilde{L}/v_w = 20$ yields better conference, I only show data points and fits for these simulations. In table 6, I indicate the resulting values of the fit parameters of Equation (328) for the RMS kinetic energy fraction $K_\infty^{\rm rms}$, normalized by the single-bubble kinetic energy fractions K_ξ as in Equation (168), a_K, and the relative errors ε_K as defined in Equation (329), for the set of PTs shown in Figure 27. I also indicate numerical values of the extrapolated $\mathcal{I}_\infty^{\rm int}$, the fit parameter $a_\mathcal{I}$, and the relative error $\varepsilon_\mathcal{I}$. While K_0 and its extrapolated values will ultimately not be used in the final GW template, it is a robust measurement of the kinetic energy in the system and serves to demonstrate the usefulness of the extrapolation scheme (328). Thus, we neglect giving numerical values for it in the table. We will instead attempt to improve upon the estimate of K_0^∞ by considering the results of single-bubble simulations in Section 6.4.4, leading to a new estimate, $\mathcal{K}_0$, in Equation (334), which eventually is the value we use in the final templates in Section 6.5.1.

α	v_w	$K_\infty^{\rm rms}/K_\xi$	a_K	ε_K	$\mathcal{I}_\infty^{\rm int}$	$a_\mathcal{I}$	$\varepsilon_\mathcal{I}$
0.0046	0.36	1.04	1.34	6.41×10^{-2}	9.97×10^{-10}	1.88	2.04×10^{-2}
	0.44	1.03	1.29	1.47×10^{-1}	2.11×10^{-9}	1.64	8.26×10^{-2}
	0.52	1.07	1.11	4.33×10^{-1}	5.35×10^{-9}	1.34	3.35×10^{-1}
	0.60	0.35	1.06	5.44×10^{-1}	5.36×10^{-9}	1.36	3.83×10^{-1}
	0.68	0.78	1.16	3.08×10^{-1}	2.35×10^{-9}	1.51	1.87×10^{-1}
	0.76	0.76	1.26	1.69×10^{-1}	1.19×10^{-9}	1.69	8.38×10^{-2}
0.05	0.36	0.96	1.35	4.80×10^{-2}	8.65×10^{-6}	2.16	6.70×10^{-3}
	0.44	0.82	1.40	6.72×10^{-2}	1.24×10^{-5}	2.04	1.26×10^{-2}
	0.52	0.55	1.46	7.21×10^{-2}	1.33×10^{-5}	2.14	1.20×10^{-2}
	0.60	0.31	1.54	6.52×10^{-2}	1.04×10^{-5}	2.43	2.13×10^{-2}
	0.68	0.25	1.61	5.52×10^{-2}	8.10×10^{-6}	–	3.49×10^{-2}
	0.76	0.48	1.44	7.37×10^{-2}	6.98×10^{-6}	2.21	2.28×10^{-2}
0.5	0.36	0.35	1.25	2.06×10^{-2}	1.82×10^{-3}	25.03	7.14×10^{-4}
	0.44	0.32	1.27	2.05×10^{-2}	2.18×10^{-3}	–	9.55×10^{-3}
	0.52	0.29	1.44	1.26×10^{-2}	2.79×10^{-3}	–	1.74×10^{-2}
	0.60	0.25	1.85	3.97×10^{-3}	2.56×10^{-3}	–	3.68×10^{-2}
	0.68	0.21	–	3.97×10^{-3}	2.26×10^{-3}	–	8.88×10^{-2}
	0.76	0.18	–	3.91×10^{-2}	1.80×10^{-3}	–	1.80×10^{-1}

Table 6: Numerical values of the fit parameters a, $K_\infty^{\rm rms}$, and $\mathcal{I}_\infty^{\rm int}$ of Equation (328) for the RMS kinetic energy fraction $K_{\rm rms}/K_\xi$ and the integrated GW amplitude $\mathcal{I}_{\rm sim}^{\rm int}$, as shown in the middle and lower panels of Figure 27. Relative errors ε are computed by comparing the extrapolated values to those obtained in the largest resolution simulations $N = 512$ when the fit is appropriate. When the fit is inappropriate (indicated with '–' in the values of a) we instead compare values among the two largest resolutions $N = 256$ and $N = 512$.

Empirical observations show that the parameter a generally falls between one and two. This suggests that the system's dynamics reduce

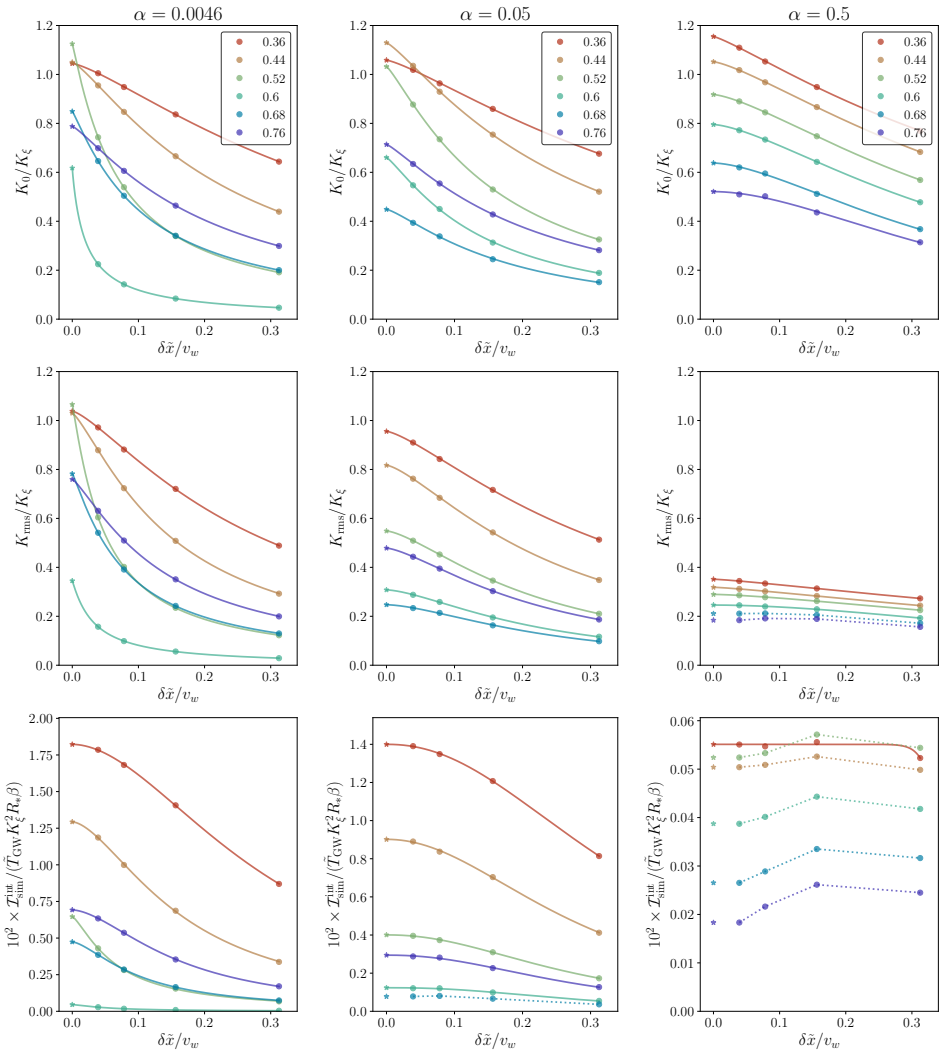

Figure 27: Plots showing the kinetic energy fraction K and the integrated GW spectrum $\mathcal{I}^{\rm int}_{\rm sim}$ as a function of grid spacing $\delta\tilde{x}/v_w = (\tilde{L}/v_w)/N$ for simulations with $\tilde{L}/v_w = 20$. *Upper panel:* Fit of Equation (328) to least-squares fitted values of the parameter K_0 in Equation (309) for simulations of resolutions $N \in \{64, 128, 256, 512\}$, normalized to K_ξ (defined from self-similar bubbles in Equation (168)). Solid lines indicate the fits, dots the data, and stars the extrapolated values. The left, middle, and right panels indicate weak, intermediate, and strong PTs, respectively. *Middle panel:* Same as upper panel, but for $K_{\rm rms} \equiv K_{\rm int}/\tilde{T}_{\rm GW}^{1/2}$ normalized to K_ξ. Note that for strong PTs, the fit is inappropriate as per the definition in the main text for $v_w = 0.68$ and $v_w = 0.76$, in which case we instead connect the data points with dotted lines and indicate extrapolated values with the value at $N = 512$. *Lower panel:* Same as upper panel, but for $\mathcal{I}^{\rm int}_{\rm sim}$ normalized by a the product of $\tilde{\Omega}_{\rm GW} \sim 10^{-2}$ [25, 69, 71] and $\tilde{T}_{\rm GW} K_\xi^2 R_* \beta$, based on the expected scaling of Equation (308). Both $K_{\rm rms}$ and $\mathcal{I}^{\rm int}_{\rm sim}$ are computed for $\tilde{t}_{\rm init} = 16$ and $\tilde{t}_{\rm end} = 32$, with $\tilde{T}_{\rm GW} = 16$.

the effective convergence rate compared to the expected second-order accuracy of the numerical KT scheme, as discussed in Chapter 5.8. Nevertheless, for most PTs, except those with highly confined profiles where $v_w \lesssim v_{CJ}$ for weak, the relative errors fall below 10%, as shown in Table 6. For confined profiles, the relative errors are significant, indicating a higher degree of uncertainty in the extrapolated result K_∞. In such cases, the lack of convergence propagates artifacts to the GW spectrum, leading, e.g., to an inaccurate resolution of the peak position due to the limited dynamical range for weak PTs. Additionally, this lack of convergence is possibly responsible for masking the expected UV behavior $S(k) \sim k^{-3}$ with an exponential decay. The spectral shape is analyzed in Section 6.4.7.

As for the appropriateness of the extrapolation scheme, we note that for a few parameter points marked by "—" in Table 6, the measured energy of $N = 512$ is lower than that of $N = 256$, in which case we discarded the usage of the scheme. For GW amplitude, the breakdown of the scheme is particularly evident for strong PTs for most of the wall velocities. However, the extrapolation scheme remains appropriate for weak and intermediate PTs. Even when assessing relative errors based on simulations with $N = 512$ and $N = 256$, these errors remain very small.

6.4.4 Corrections to the kinetic energy for multiple bubbles

As is evident from Equation (308), the GW amplitude is directly governed by the squared kinetic energy in the system. In this generalized form accounting for decaying sources, the kinetic energy is characterized by the time integral of the kinetic energy fraction, K_{int}. In Section 6.5.1, I ultimately provide templates for the present-day GW spectrum, which are derived from K_{int} and $K_{int,exp}$ in (310) and (318) assuming the power-law decay (309), which consequently requires knowledge of the continuum limit of K_0. To enhance the accuracy of our simulation measurements, we previously explored in the previous Section an extrapolation scheme aimed at both understanding the convergence behavior of our simulations and deriving continuum values. This gave as us an estimate K_0^∞ of the continuum value of K_0 using the extrapolation scheme (328). However, in the case of weak PTs, relatively large extrapolations were required, potentially introducing significant uncertainties in these estimates.

In this Section, I will outline an alternative method to obtain a potentially more robust estimate $\mathcal{K}_0$ for the continuum limit of K_0. This method consists of comparing the convergence of multi-bubble simulations to that of simulations with a single centrally nucleated bubble,

for which we a priori know the self-similar asymptotic solutions. For visual depictions of the self-similar velocity and enthalpy profiles, consult Figure 3. We previously defined the kinetic energy fraction K such that $\bar{\rho}\, K(\tilde{t}) \equiv \langle \rho_{\rm kin}(\mathbf{x}, \tilde{t}) \rangle$, where $\langle \rho_{\rm kin} \rangle$ represents the kinetic energy density averaged over the simulation volume V. However, we note that K_ξ for single bubbles, defined in (168), is taken as the average of the kinetic energy density fraction induced by a single bubble over the broken-phase volume. Then, defining the ratio of the volume in the broken phase (bp) to the total volume,

$$\mathcal{V}(\tilde{t}) = \frac{V_{\rm bp}}{V}\,, \tag{330}$$

we can define the analog of K_ξ for multiple bubbles as the ratio $K(\tilde{t})/\mathcal{V}(\tilde{t})$. Before fluid sound shells collide, and in the limit of infinite resolution, this ratio should be identical to K_ξ after a very short transient period during which the fluid profiles develop. Deviations from K_ξ before collisions thus correspond to an artifact due to numerical inaccuracy. I plot the ratio $K(\tilde{t})/[\mathcal{V}(\tilde{t})K_\xi]$ as solid lines in Figure 28 for all four resolutions $N \in \{64, 128, 256, 512\}$ with increasing opacity.

In the multi-bubble simulations, we can similarly define the kinetic energy fraction for each individual bubble i before its first collision as $\bar{\rho}\, K_i(\tilde{t}) = \langle \rho_{{\rm kin},i}(\mathbf{x}, \tilde{t}) \rangle$. Additionally, we define the ratio $K_i(\tilde{t})/\mathcal{V}_i(\tilde{t})$ in analogy with K_ξ, where $\mathcal{V}_i$ now represents the fractional volume of the broken phase occupied by each bubble i.

To monitor the time-dependence of K_i, we simulate single bubbles nucleated at the center of the simulation box (see '*single-bubble* simulations in Table 5). As the convergence of the single-bubble profiles depends on the resolution in $\xi \equiv r/(t - t_i)$, where t_i is the nucleation time of the bubble i and r the radial distance to the nucleation center, we empirically find that doubling the resolution from N to $2N$ is equivalent to evaluating the profile at time $2(\tilde{t} - \tilde{t}_i)$, an observation which already noted in Chapter 5. Hence, the kinetic energy of single-bubble simulations (with $t_i = 0$) obeys $K_i^{2N}(\tilde{t})/\mathcal{V}_i(\tilde{t}) = K_i^{N}(2\tilde{t})/\mathcal{V}_i(\tilde{t})$ to an excellent degree and it suffices to run single-bubble simulations for the largest resolution $N = 512$. These simulations are run approximately until the front of the fluid profile collides with its own mirror image at the edge of the simulation box, which occurs around $\tilde{t}^{\rm sb}_{\rm end} = \tilde{L} v_w / 2 / \max(c_s, v_w)$.[3]

3 Note that this $\tilde{t}^{\rm sb}_{\rm end}$ (where sb stands for "single-bubble" simulations) is always smaller than $\tilde{t}_{\rm end} = 32$, the final time of the multiple-bubble simulations. Thus, in producing Figure 28, we extend the fit of the observed convergence for times greater than $\tilde{t}_{\rm end}$, enforcing that in the limit of infinite time, it converges to the value of K_ξ. This extrapolation always represents $K_i(\tilde{t})$ accurately from the measured values (below 1% error). In any case, since we never use values of $K_i(\tilde{t})$ at times larger than the initial colli-

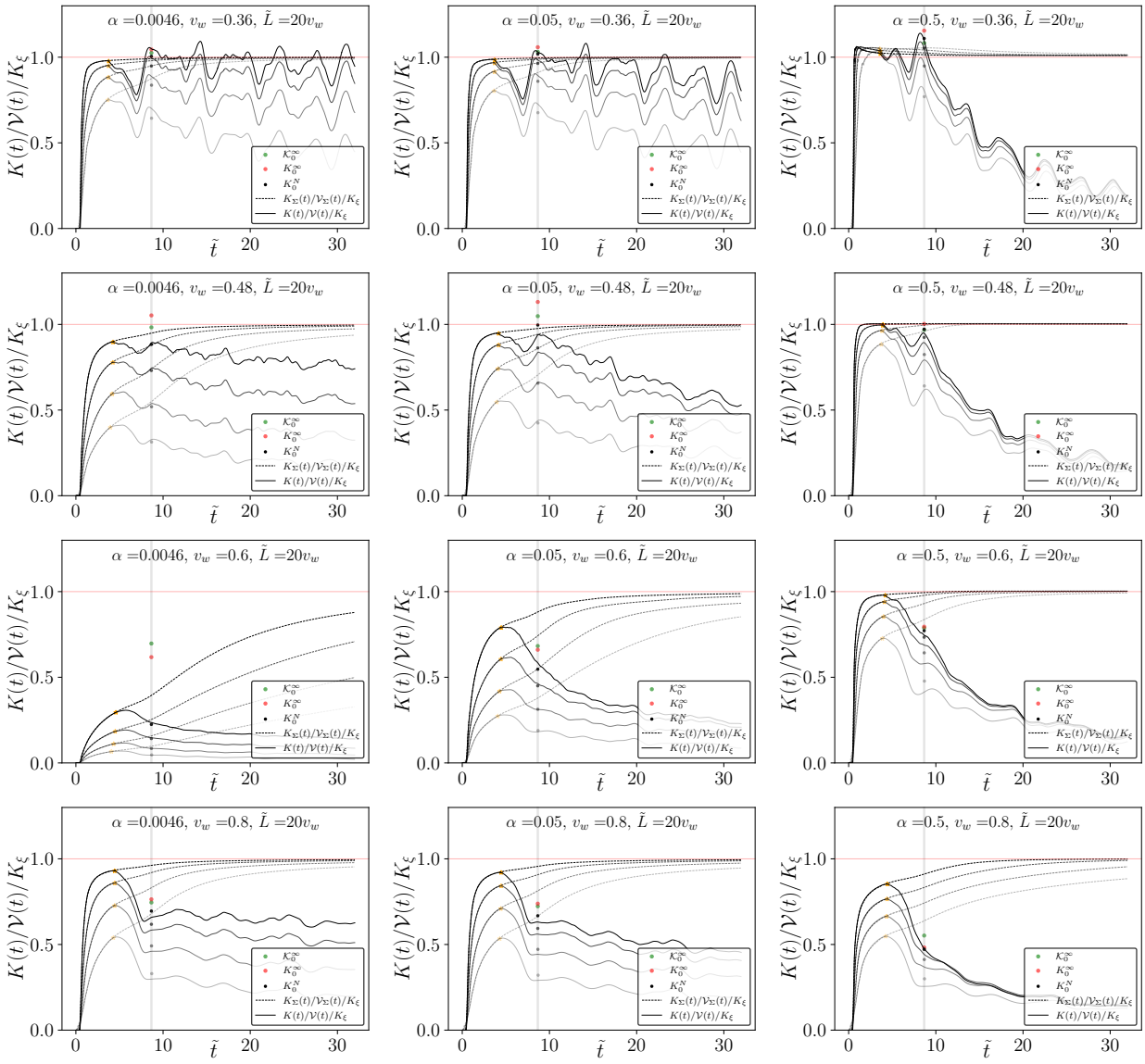

Figure 28: Time evolution of the kinetic energy fraction in the broken-phase volume $K(\tilde{t})/\mathcal{V}(\tilde{t})$ for multiple-bubble simulations (solid lines), normalized by the single-bubble K_ξ, for different resolutions $N = \{64, 128, 256, 512\}$ in increased opacity and box size $\tilde{L}/v_w = 20$. Results are shown for weak (left panels), intermediate (middle panels), and strong (right panels) PTs, and for a range of wall velocities $v_w = \{0.36, 0.48, 0.6, 0.8\}$. Dashed lines correspond to the ratio $K_\Sigma(\tilde{t})/\mathcal{V}_\Sigma(\tilde{t})$ computed from the single-bubble simulations, such that the departures between the solid and dashed lines indicate the time when fluid-shell collisions take place in the multiple-bubble simulations. Black dots are the values of K_0 obtained from the fit $K(\tilde{t}) = K_0(\tilde{t}/\tilde{t}_0)^{-b}$ studied in Section 6.4.5 for different N. Red and green dots correspond to the estimated values $\mathcal{K}_0$ (see Equation (333)) and K_0^∞ (obtained from the convergence analysis of Section 6.4.3). Orange stars correspond to the factor $\mathcal{S}$ (see Equation (333)) at the collision $\tilde{t}_{\text{coll}}$, used to correct $\mathcal{K}_0$.

Then, in the full simulations and before fluid sound shells collide, the state of the simulation is exactly the superposition of single bubbles nucleated at times $\tilde{t}_i < \tilde{t}$ in the bubble nucleation history. We thus construct the sum

$$K_\Sigma(\tilde{t}) \equiv \sum_{i:\{\tilde{t}_i<\tilde{t}\}} K_i(\tilde{t}-\tilde{t}_i)\,, \tag{331}$$

which corresponds to the expected kinetic energy fraction for multiple-bubbles simulations in the hypothetical case that no single bubble would collide, following the bubble nucleation history up to time $\tilde{t}$. Then, before the first fluid-shell collision occurs, we have that $K_\Sigma(\tilde{t}) = K(\tilde{t})$, while $K_\Sigma(\tilde{t})$ starts to deviate from $K(\tilde{t})$ after the first collision at $\tilde{t}_{\rm coll}$.

Similarly, we can construct the fractional broken-phase volume occupied by the superposition of single bubbles as

$$\mathcal{V}_\Sigma(\tilde{t}) \equiv \sum_{i:\{\tilde{t}_i<\tilde{t}\}} \mathcal{V}_i(\tilde{t}-\tilde{t}_i)\,, \tag{332}$$

which can become larger than one, as it ignores interactions between bubbles. However, the ratio $K_\Sigma/\mathcal{V}_\Sigma$ is bounded by K_ξ.[4] I plot the time evolution of the ratio $K_\Sigma/\mathcal{V}_\Sigma$ as dotted lines in Figure 28 using the nucleation history of the reference multiple-bubble simulations with $\tilde{L}/v_w = 20$.

The ratio $K_\Sigma/\mathcal{V}_\Sigma$ indicates the global degree of convergence of the full multiple-bubble simulations in the hypothetical case that all bubbles keep evolving without interacting with other bubbles. Therefore, the ratio $K/\mathcal{V}$ computed in the multiple-bubble simulations is initially identical to $K_\Sigma/\mathcal{V}_\Sigma$ at times $\tilde{t} < \tilde{t}_{\rm coll}$. However, as collisions take place, we clearly see in Figure 28 that both fractions deviate from each other, as a consequence of mainly four phenomena: (1) the simulation shell profiles stop converging towards self-similarity upon colliding, and since the kinetic energy of the un-collided bubbles is in general underestimated, also the maximum value of $K(\tilde{t})/\mathcal{V}(\tilde{t})$, which is realized quickly after the first collision, will be underestimated; (2) oscillatory conversion between thermal and kinetic energy; (3) upon collisions, the fluid self- and inter-shell interactions may be nonlinear and dissipate kinetic energy, leading to the decay studied in Section 6.4.5; and (4)

sion time, it does not affect the analysis and it is only used to indicate the expected convergence of the self-similar profiles in Figure 28.

4 This bound holds for all considered PT parameter points, except for strong PTs with $v_w = 0.36$ and $v_w = 0.4$, where values of $K_\Sigma/\mathcal{V}_\Sigma \gtrsim K_\xi$ are observed prior to collisions, likely due to numerical oscillations at the shock front, as can be seen in the upper-right panel of Figure 28. However, as time progresses, the ratio asymptotically approaches K_ξ.

numerical viscosity dampen the kinetic energy. The first and last phenomena are purely numerical, while the remaining two are physical effects.

In Figure 28, we mark with orange stars the time of first collision $\tilde{t}_{\rm coll}$, which is always very close to the time of maximum degree of convergence, as collisions affect the development of the fluid-shell profiles at later times. Thus, we can attempt to compensate for the underestimation of the kinetic energy fraction due to insufficient resolution at $\tilde{t} > \tilde{t}_{\rm coll}$ multiplying $K(\tilde{t})$ by the factor $\mathcal{S} = \mathcal{V}(\tilde{t}_{\rm coll})\, K_\xi / K(\tilde{t}_{\rm coll})$, effectively correcting to the expected value of K_ξ at the time of the first collision when at which time we are close to peak convergence. In particular, the kinetic energy fraction K_0 entering as the fitted parameter in Equation (309) can be corrected to the value

$$\mathcal{K}_0 = \mathcal{S}\, K_0 = \frac{\mathcal{V}(\tilde{t}_{\rm coll})\, K_\xi}{K(\tilde{t}_{\rm coll})}\, K_0 \,. \tag{333}$$

In Figure 29, I plot $\mathcal{K}_0$ obtained for numerical resolutions $N \in \{64, 128, 256, 512\}$ as well as the corresponding vacuum energy transfer efficiency efficiency κ_0, defined by

$$\mathcal{K}_0 \equiv \frac{\kappa_0\, \alpha}{1+\alpha}\,, \tag{334}$$

in analogy with that of self-similar profiles in (166). We observe a general trend where $\mathcal{K}_0/K_\xi \gtrsim 1$ for $v_w < c_s$, and $\mathcal{K}_0/K_\xi \lesssim 1$ for $v_w > c_s$. Averaging $\mathcal{K}_0$ over the PT parameters v_w and α yields the $\text{mean}^{\rm max}_{\rm min}$ values

$$\mathcal{K}_0 = 0.84^{+0.24}_{-0.29}\, K_\xi \,, \tag{335}$$

implying that the conventional use of K_ξ for estimating kinetic energy could overestimate the GW production by as much as a factor of $(K_\xi/\mathcal{K}_0)^2 \sim 0.55^{-2} \sim 3$. For different PT parameters (α and v_w), the values in Figure 29 can be used to predict the corresponding correction to the kinetic energy entering the GW amplitude.

In comparison to the extrapolated value of K_0 shown in Figure 27, we observe a more rapid convergence of $\mathcal{K}_0$ when comparing the results from the two highest resolutions, $N = 256$ and $N = 512$. By accounting for the known convergence behavior of the self-similar profiles in the calculation of $\mathcal{K}_0$, we propose that it constitutes a more robust estimate of the true value at $\tilde{t}_0$ than K_0^∞. Additionally, the resulting values are closer to K_ξ, thus offering a more conservative estimate and minimizing potential deviations from K_ξ, which might otherwise be attributed to numerical artifacts. Nevertheless, it is important to recognize that under-resolution during the collision phase could significantly impact the subsequent evolution of the kinetic energy, particularly when nonlinear effects dominate the dynamics.

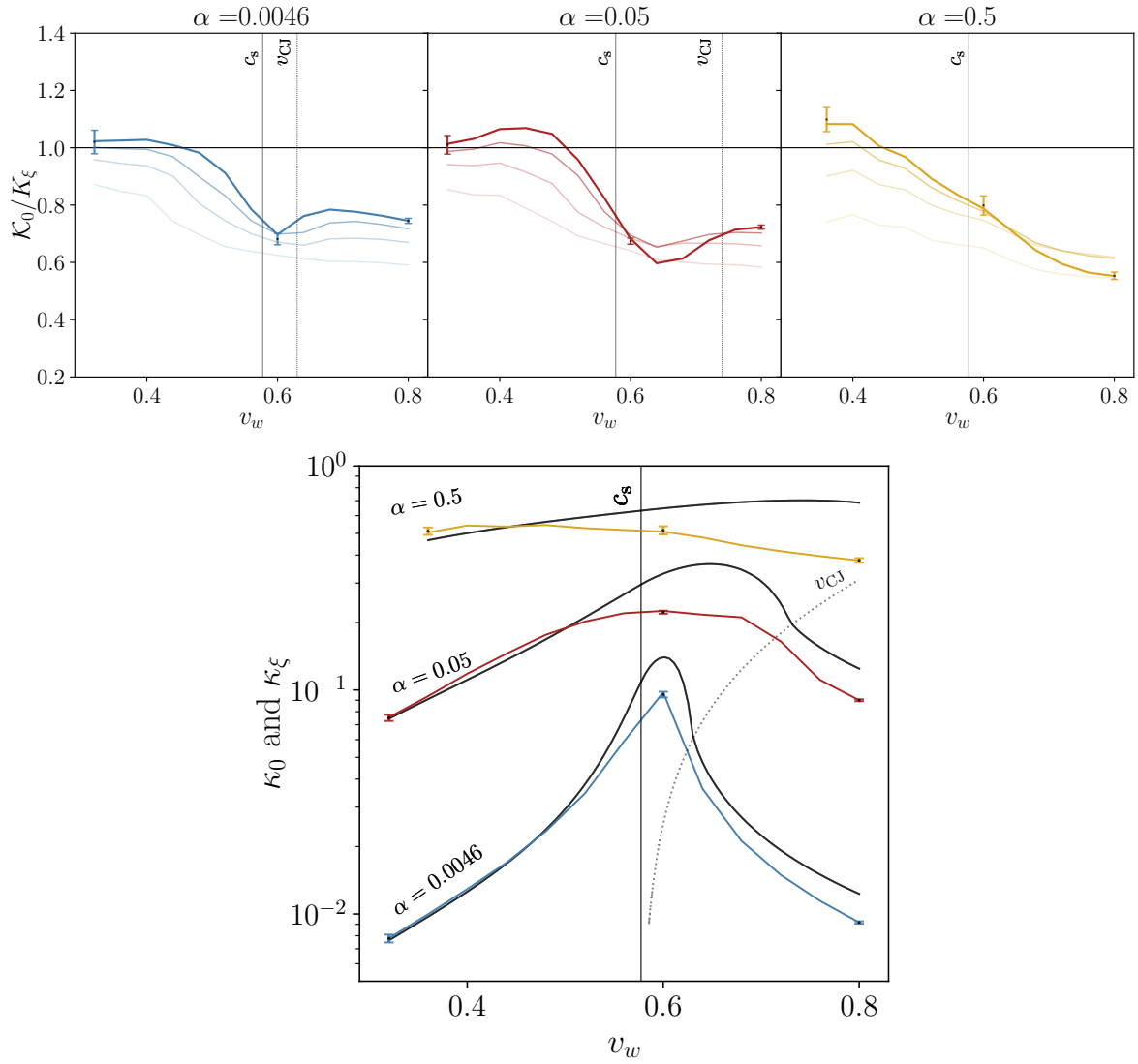

Figure 29: *Upper panel:* Values of the convergence-corrected continuum limit estimate $\mathcal{K}_0$ of K_0 as defined in (333) for resolution $N = 512$, normalized to K_ξ for self-similar profiles defined in Equation (168), for weak (left panel), intermediate (middle panel), and strong (right panel) PTs, as a function of v_w. Lines in increasing opacity correspond to increasing numerical resolution $N \in \{64, 128, 256, 512\}$. The vertical solid gray line indicates the sound speed, c_s, while the dashed lines indicate the Chapman-Jouguet velocity, v_{CJ}. Error bars show the standard deviation from 10 different bubble nucleation histories. *Lower panel:* Kinetic energy efficiency $\kappa_0 \equiv \mathcal{K}_0(1+\alpha)/\alpha$ defined from $\mathcal{K}_0$ as defined in (333) for resolution $N = 512$, for weak (blue), intermediate (red), and strong (orange) PTs. I also plot κ_ξ (black) for self-similar solutions as defined in Equation (166). The vertical line corresponds to c_s, and v_{CJ} is indicated by the dotted gray line.

6.4.5 Kinetic energy evolution

In this Section, I will demonstrate the time-evolution and decay of the kinetic energy fraction K in the simulations. In particular, I will present fits of the power-law decay prescription (309).

To begin this discussion, consider first the upper panel of Figure 30, where I plot $K(t)$ for the largest resolution simulations $N = 512$ as well as the fit (328) to demonstrate the overall evolution. This figure makes apparent what we have already discussed in the previous Section: the kinetic energy is underestimated due to incomplete convergence (which is evident since I normalize to K_ξ). At later times when $\tilde{t} \gtrsim \tilde{t}_0 \approx 10$), we generally observe a decay in kinetic energy, which is more or less pronounced depending on the PT strength and velocity profiles.

In addition to the time decay of K, we observe fluctuations in time. These fluctuations are associated with oscillatory conversion between kinetic and thermal energy, originating in the superposition of compressional modes. This conversion is indeed confirmed since I showed in Section 5.4.2 that the simulations conserve T^{00} to machine precision.

To characterize and quantify the decay, we use the power-law decay prescription (328), an equation which we fit to the numerical data of $K(\tilde{t})$ at times $\tilde{t} > \tilde{t}_0$ after PT completion, i.e., we fit

$$K(\tilde{t} > \tilde{t}_0) = K_0 \left(\frac{\tilde{t}}{\tilde{t}_0} \right)^{-b} , \tag{336}$$

where b indicates the power-law decay rate of K. This power-law decay prescription accurately fits the numerical data, and we have checked that it remains accurate up to $\tilde{t}_{\text{end}} = 64$ for a strong PT with $\alpha = 0.5$ and $v_w = 0.8$. Based on this power-law decay, we define the half-life of the kinetic energy as the time when $K(\tilde{t}_0 + \tilde{t}_{1/2}) = \frac{1}{2} K_0$, i.e.,

$$\tilde{t}_{1/2} = \left(2^{\frac{1}{b}} - 1 \right) \tilde{t}_0 \, . \tag{337}$$

In the lower panel of Figure 30 I highlight the power-law description by plotting in log-log both the kinetic energy $K(t)$ as well as the fit (336), but for the different resolutions $N = \{64, 128, 256, 512\}$. To clarify the dependence of the decay on resolution, I normalize all plots to K_0, making evident how the slopes compare.

Since the kinetic energy is typically damped by numerical viscosity,[5] it is generally expected that reducing the grid spacing mitigates this decay, as evidenced for weak and most intermediate PTs. This expected behavior is indeed observed for all weak PTs and some intermediate,

5 In the Kurganov-Tadmor scheme used in our simulations [1], the numerical viscosity is expected to scale with $(\delta\tilde{x})^3$ [112] .

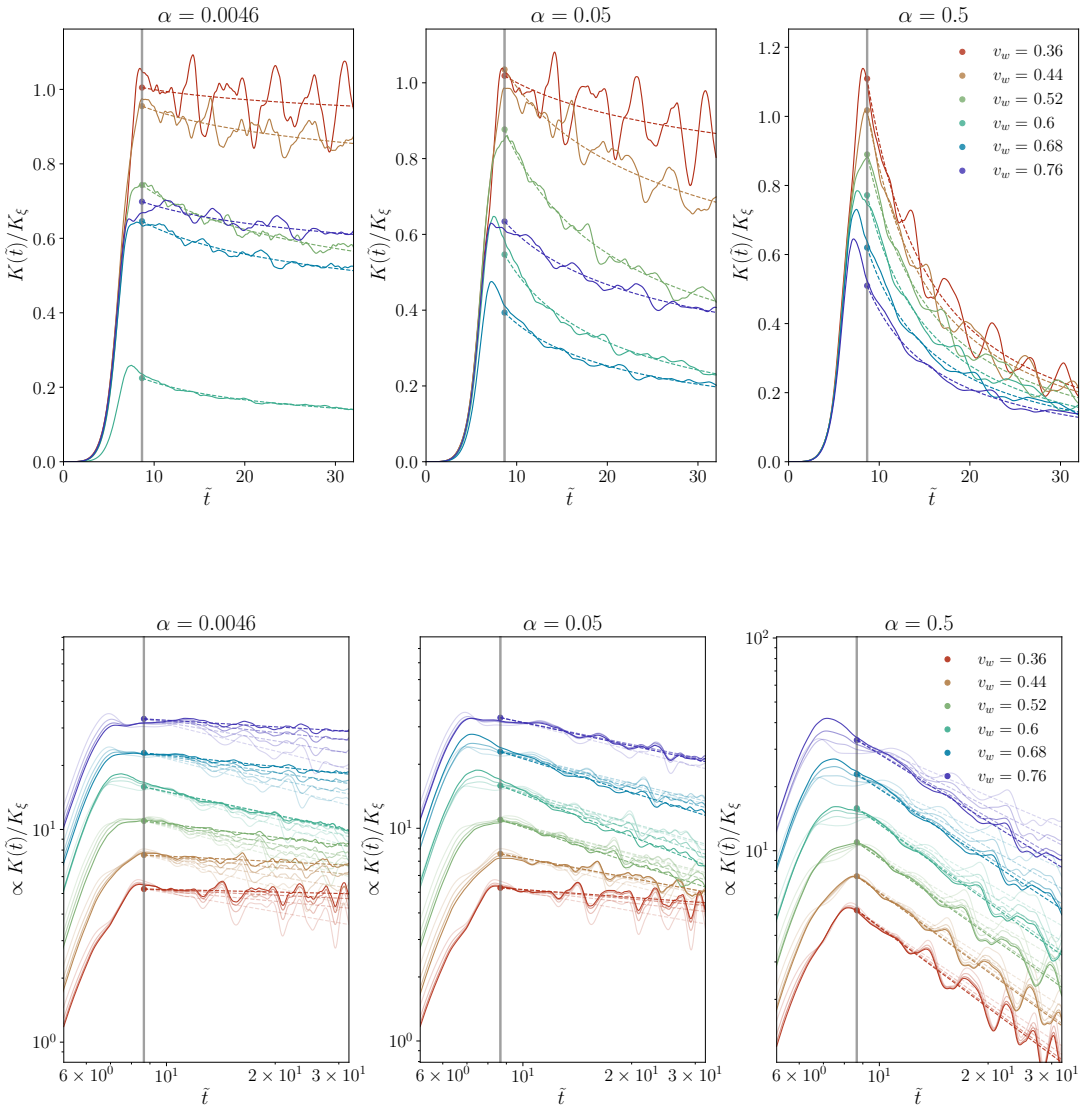

Figure 30: Evolution of the measured kinetic energy fraction $K(\tilde{t})$ normalized to the single-bubble values K_ξ (see Equation (168)) for weak (left panels), intermediate (middle panels), and strong (right panels) PTs, for $N = 512$ (solid lines) and $\tilde{L}/v_w = 20$, and the same wall velocities as those in Figure 27. Dashed lines indicate the fits to the power-law decay of Equation (336) at times $\tilde{t} > \tilde{t}_0$. Values corresponding to K_0/K_ξ are marked with circles. In the lower panels, the kinetic energy fraction is shown for different numerical discretizations $N = \{64, 128, 256, 512\}$ (solid lines with increasing opacity), normalized to the corresponding values of the fit K_0 at each resolution N. The results for each v_w are shifted by a constant to distinguish between wall velocities. The presentation in the lower panels is chosen to emphasize the dependence of the time decay on resolution.

evident though the clearly decreasing steepness of slopes in the lower panel of Figure 30 and the increasing values of the lines of b in the left column of Figure 31, as we increase the resolution.

For strong PTs and certain intermediate PTs with thin hybrid profiles ($v_w \lesssim v_{CJ}$), the trend of reduced decay with increased resolution reverses. In these scenarios, the decay of kinetic energy actually becomes steeper as resolution increases. This enhanced decay with higher resolution suggests that the fluid sound shells, which carry greater kinetic energy at the time of collision, experience amplified nonlinearities that may eventually dominate over decay due to numerical viscosity.

Figure 31 displays the fit of the decay index b (left column) and the half-life $\tilde{t}_{1/2}$ (right column) as functions of v_w for weak, intermediate, and strong PTs.[6] In the right panel of Figure 31, we also plot the eddy turnover time $\tilde{t}_{eddy} = (\beta R_*)/\sqrt{K_\xi}$, based on the kinetic energy ratio expected for un-collided bubbles, which corresponds to the time scale of fluctuations in the fluid and is expected to determine the decay time into turbulent motion. We compare $\tilde{t}_{1/2}$ to $\tilde{t}_{eddy}$ in Figure 31. The eddy turnover time is $\tilde{t}_{eddy} \simeq 5$ for strong PTs, $\tilde{t}_{eddy} \simeq 10$–$30$ for intermediate PTs, and $\tilde{t}_{eddy} \sim \mathcal{O}(100)$ for weak PTs. Therefore, as seen in Figure 31, for strong PTs, nonlinearities are expected to have developed within the simulation duration. For some intermediate and weak PTs, the eddy turnover time occurs towards the end of our simulations, suggesting that nonlinear evolution may have started, while for the remaining cases, it is likely not as developed. To evaluate the onset of vortical motion and turbulence in the simulations, I demonstrate the development of vorticity and present quantitative results in Section 6.4.9.

For weak PTs, the rate of kinetic energy damping is greatly reduced as we increase the resolution, which we interpret as a reduction of the numerical viscosity (see footnote 5). This observation, therefore, means that for weak PTs, decay is always dominated by numerical viscosity. Only for the hybrid solution with $v_w = 0.6 \lesssim v_{CJ}$, when larger velocities can be achieved (see self-similar profiles in Figure 3), does b (and hence $\tilde{t}_{1/2}$) appear to stagnate with increasing resolution, pointing towards the onset of resolving the physics responsible for the damping.

The results are more interesting in the case of intermediate PTs. For both small and large v_w, corresponding to subsonic deflagrations and detonations, respectively, b decreases with increasing resolution. However, for a large range of intermediate velocities $v_w \in \{0.52, 0.6, 0.68\} \lesssim v_{CJ}$, the trend is reversed for the highest resolutions. We interpret this

6 In this case, we do not extrapolate to infinite resolution due to the complex behavior of the index. Instead, we use the values obtained from the highest-resolution simulations with $N = 512$ and the best UV resolution, $\tilde{L}/v_w = 20$.

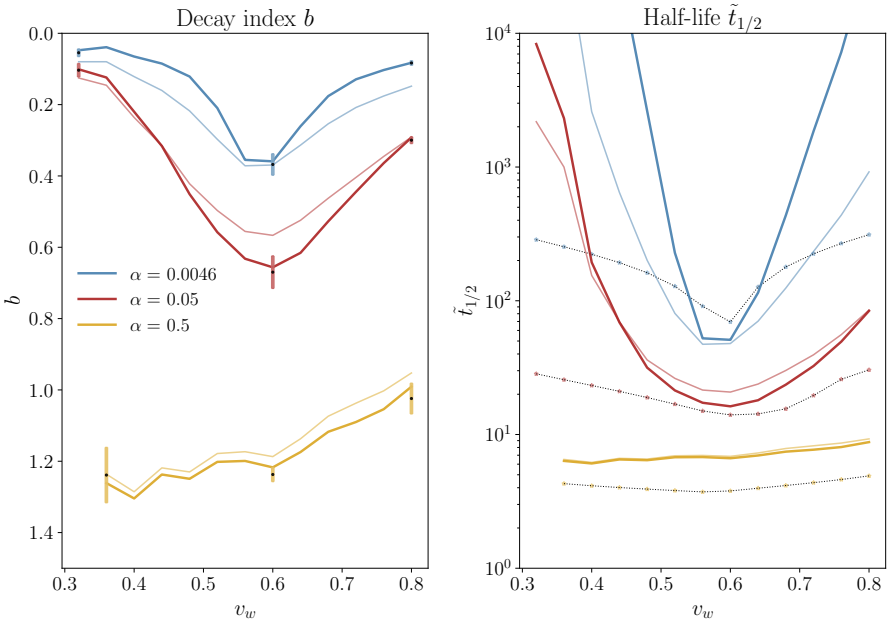

Figure 31: Decay index b (left panel) and half-life $\tilde{t}_{1/2}$ (right panel) as a function of v_w for $N = \{256, 512\}$ in increasing opacity for weak (blue lines), intermediate (red lines), and strong (orange lines) PTs. Dashed black lines with colored stars in the right panel correspond to the eddy turnover time $\tilde{t}_{\text{eddy}} = (\beta R_*)/\sqrt{K_\xi}$ that we compare with $\tilde{t}_{1/2}$ as we expect both time scales to be inversely proportional to K_ξ. Error bars in the left panel show the standard deviation from 10 different bubble nucleation histories for $N = 512$.

point of reversal as a transition from a decay of the kinetic energy dominated by numerical viscosity to a decay determined by the development of nonlinearities.

For strong PTs, we consistently observe that increasing the numerical resolution N leads to a more pronounced decay of kinetic energy, suggesting that physical nonlinear energy dissipation is dominant over the effects of numerical viscosity. As previously discussed, this is anticipated since the eddy turnover time, $\tilde{t}_{\text{eddy}} \simeq 5$, which marks the onset of nonlinearities, falls within the timeframe of our simulations.

Finally, let me comment on the fact that a similar decay of the kinetic energy has already been found in coupled scalar-fluid simulations of intermediate PTs in [71, 101]. Since their resolution is substantially larger, this points towards the physicality of the decay.

6.4.6 Time evolution of the integrated GW spectrum and GW efficiency

In Figure 32 (upper panels), I present the time evolution of the integrated GW amplitude $\mathcal{I}_{\rm sim}^{\rm int} \equiv \int \mathcal{I}_{\rm sim}\, \mathrm{d}\ln k$, where $\mathcal{I}_{\rm sim}(\tilde{t}_{\rm init}, \tilde{t}, k)$ is evaluated at $\tilde{t}_{\rm init} = 16$, and $\tilde{t}$ varies from $\tilde{t}_{\rm init}$ to $\tilde{t}_{\rm end} = 32$. For weak and intermediate PTs, the evolution with the source duration $\tilde{t} - \tilde{t}_{\rm init}$ is nearly linear in most cases (except when $v_w \lesssim v_{\rm CJ}$), aligning with the expected stationary behavior in the sound-wave regime as we discussed in Section 6.2.2. In these scenarios, the kinetic energy K remains relatively constant during the simulations (see Figure 30). However, significant decay in K results in deviations from linear growth, consistent with expectations from the generalized locally stationary UETC, which I discussed in Section 6.2.3.

To verify the validity of Equation (308), derived under this assumption, I plot the upper panel of Figure 32 the following ratio:

$$\tilde{\Omega}_{\rm GW}(\tilde{t}) = \frac{\mathcal{I}_{\rm sim}^{\rm int}(\tilde{t}_{\rm init}, \tilde{t})}{K_{\rm int}^2(\tilde{t}_{\rm init}, \tilde{t})(\beta R_*)}\,. \tag{338}$$

The validity of Equation (308) under the assumption of a locally stationary UETC is then inherited from the observed time-independence of this ratio, since then, we can meaningfully measure the GW efficiency $\tilde{\Omega}_{\rm GW}$ also in the case of decaying $K(t)$. It is important to note that when K does not decay significantly over time, we recover the expected linear growth, $K_{\rm int}^2 \to K^2\, \tilde{T}_{\rm GW}$.

For weak PTs with $\alpha = 0.0046$ and $v_w = 0.6$, corresponding to a confined hybrid PT (see Figure 3), K exhibits a steeper decay compared to other wall velocities, as is evident from Figure 30. This decay, while not very strong, nevertheless implies that the growth of the GW amplitude deviates from linear and weakens over time. A similar behavior is observed for confined hybrids in intermediate PTs with $\alpha = 0.05$ and wall velocities $v_w \in \{0.6, 0.68\} \lesssim v_{\rm CJ}$. For these parameters, as can be seen in Figure 32, the GW amplitude grows slower than linearly with the source duration. For strong PTs, the kinetic energy exhibits significant decay across all wall velocities during the simulation time frame, leading to a appreciable deviation from linear growth in the GW amplitude.

However, as illustrated in Figure 32, despite the significant decay in K, the GW amplitude grows in a manner that keeps the ratio $\tilde{\Omega}_{\rm GW}(\tilde{t})$ nearly constant. This constancy supports the generalization from linear growth to a growth proportional to $K_{\rm int}^2(\tilde{t})$, as proposed in Equation (308), and allows for a robust measurement of the GW efficiency.

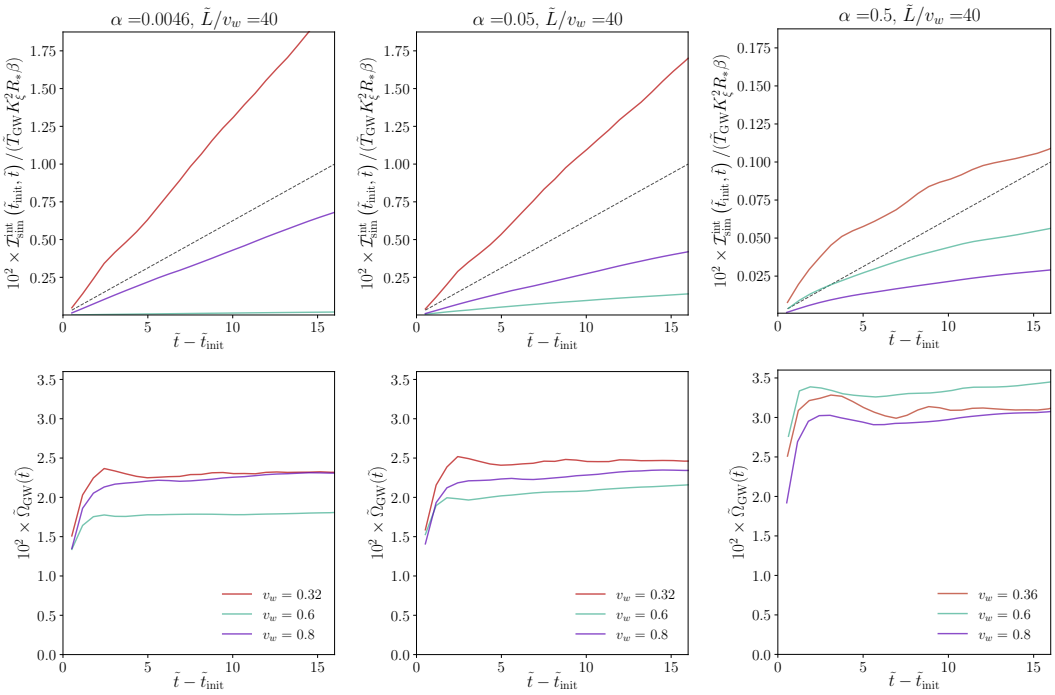

Figure 32: *Upper panel:* Dependence of the numerical integrated GW amplitude found in the simulations with $\tilde{L}/v_w = 40$ and $N = 512$ as a function of the source duration $\tilde{t} - \tilde{t}_{\rm init}$ for weak (left column), intermediate (middle column), and strong (right column) PTs. The integrated GW amplitude is normalized as in the lower panels of Figure 27 for consistency. Dashed lines exemplify the linear growth expected under the stationary UETC assumption. *Lower panel:* Time evolution of $\tilde{\Omega}_{\rm GW}$ computed as in Equation (338).

As long as the fit $K(\tilde{t}') = K_0 \, (\tilde{t}'/\tilde{t}_0)^{-b}$ accurately describes the numerical results for $\tilde{t}' \in [\tilde{t}_{\rm init}, \tilde{t}]$, which is indeed the case as is evident from Figure 30, the GW amplitude follows:

$$\mathcal{I}^{\rm int}_{\rm sim}(\tilde{t}_{\rm init}, \tilde{t}) = \tilde{\Omega}_{\rm GW} \, K_0^2 \, (\beta R_*) \, \tilde{t}_{\rm init} \, (\tilde{t}_0/\tilde{t}_{\rm init})^{2b} \, \frac{[1 + (\tilde{t} - \tilde{t}_{\rm init})/\tilde{t}_{\rm init}]^{1-2b} - 1}{1 - 2b} \,, \tag{339}$$

as defined in (359) but now with $\tilde{t}_0 = \tilde{t}_{\rm init}$.

Given that $\tilde{\Omega}_{\rm GW}(\tilde{t})$ remains approximately constant over time after incorporating $K^2_{\rm int}$ into the scaling of the GW amplitude, when quoting measurements of $\tilde{\Omega}_{\rm GW}(\tilde{t})$, we always indicate its value at $\tilde{t}_{\rm end}$, the end of the simulations, unless the complete time evolution is provided. The resulting GW efficiency, $\tilde{\Omega}_{\rm GW}$, is shown in Figure 33 for various numerical resolutions N and for both box sizes, $\tilde{L}/v_w = 20$ and 40. The extrapolated values of $\tilde{\Omega}^\infty_{\rm GW}$ are calculated from (338) using the extrapolated values $\mathcal{I}^{\rm int,\infty}_{\rm sim}$ and $K^\infty_{\rm int}$ as per the description in Section 6.4.3. We

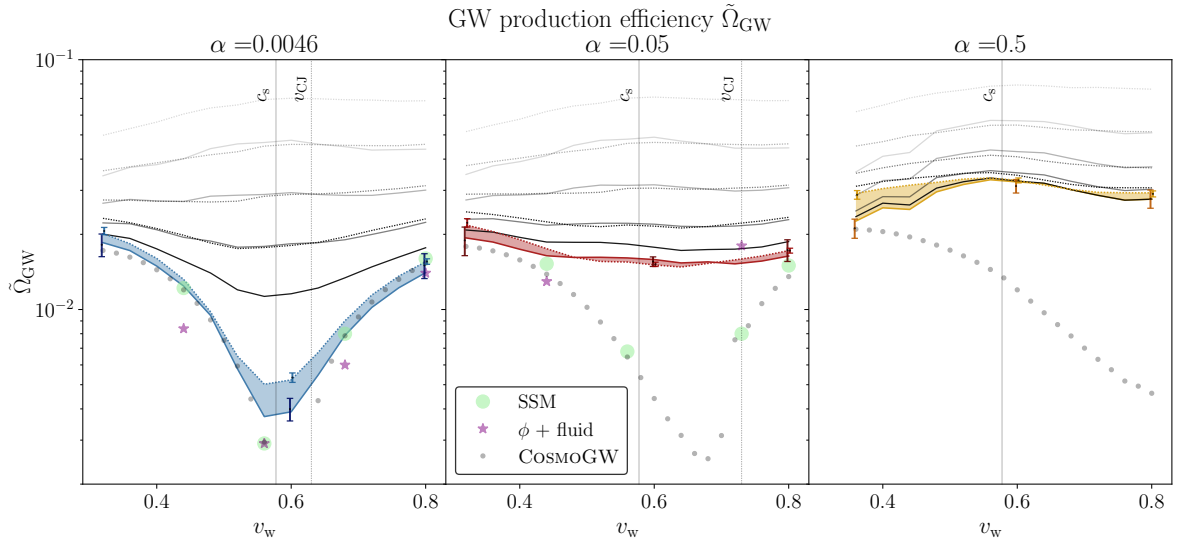

Figure 33: Gravitational wave production efficiency $\tilde{\Omega}_{\rm GW}$ for weak (left), intermediate (middle), and strong (right) first-order PTs. Solid (dotted) lines correspond to $\tilde{L}/v_w = 20$ (40). Black lines with increasing opacity correspond to increasing resolutions $N \in \{64, 128, 256, 512\}$, while colored lines indicate $\tilde{\Omega}^{\infty}_{\rm GW}$ as computed from the extrapolated values of $\mathcal{I}^{\rm int,\infty}_{\rm sim}$ and $K^{\infty}_{\rm int}$ as per the description in Section 6.4.3. Dots and stars mark $\tilde{\Omega}_{\rm GW}$ as presented in Tables 2 and 3 of [72] corresponding to predictions from the sound-shell model (SSM) for exponential nucleation of bubbles [72] and scalar field-hydrodynamical simulations for simultaneous nucleation [71], respectively. Gray dots correspond to SSM values found using the assumption described in 6.2.2 (following Appendix B of Ref. [73]), and computed using CosmoGW [166]. Error bars indicate the standard deviation from 10 different bubble nucleation histories for $\tilde{L}/v_w = 20$ (darker) and 40 (lighter).

compare these estimates of continuum-limit efficiencies with those predicted by the sound-shell model [70, 72, 73] and those obtained from coupled scalar field-hydrodynamical simulations [69, 71]. However, it is important to note that the latter scalar field-hydrodynamical simulations are based on bubble nucleation histories with simultaneous bubble nucleation. Simultaneous bubble nucleation, rather than exponential as in our case, generally leads to smaller values of $\tilde{\Omega}_{\rm GW}$ (see Tables 2 and 3 in [72]). Note that we have modified the values of $\tilde{\Omega}_{\rm GW}$ from [69, 71, 72] to account for that they consider $\beta R_* = (8\pi)^{1/3} v_w$ instead of the corrected $\beta R_* = (8\pi)^{1/3} \max(v_w, c_s)$ that we use in Equation (308).

For weak PTs ($\alpha = 0.0046$), the extrapolated values obtained from the Higgsless simulations accurately reproduce both the numerical values and the trend of $\tilde{\Omega}_{\rm GW}$ with v_w observed in both the sound-shell

model and the coupled scalar field-hydrodynamical simulations. This is important for two reasons: *(1)* the agreement between three independent approaches lends support to the conclusion that the general trend may be physical; *(2)* since weak PTs are expected to be described by linear dynamics, the limit in which the sound-shell model applies, we would *a priori* expect the Higgsless simulations to accurately reproduce the sound-shell model results. Astounding agreement between the two approaches for the wider fluid profiles far from v_{CJ} is thus a remarkable result, validating both the assumption of linear evolution of the sound-shell model and the accuracy of Higgsless simulations.

For wall velocities $v_w \lesssim v_{CJ}$, however, the two methods deviate. This may be a consequence of incorrectly extrapolating to the continuum values since convergence is particularly bad for these thinner profiles. It can also indicate the transition into the nonlinear regime, as these particular solutions are associated with larger fluid velocities.

As α becomes larger, nonlinearities become more relevant and full 3D simulations are necessary to push beyond the reach of the sound-shell model. Only a few points of reference data for $\tilde{\Omega}_{GW}$ exist for intermediate PTs ($\alpha = 0.05$) and so far none[7] for strong PTs ($\alpha = 0.5$). We note that reference data points $\tilde{\Omega}_{GW}$ in Refs. [71, 72] are computed assuming a linear growth with the source duration as in Equation (305). Hence, incorporating K_{int} as in Equation (308) can modify the value of $\tilde{\Omega}_{GW}$ when the source decays. The extrapolation method described in Sec. 6.4.3 and presented in Figure 33 as solid lines seem to behave very well, delivering agreement between the numerical results from both simulation domains $\tilde{L}/v_w = 20$ and 40.

For intermediate PTs, we begin to see deviations from the sound-shell model, in particular for $v_w = 0.68 \lesssim v_{CJ}$. We observe that the v_w-dependence seen for weak PTs has flattened and that the overall efficiency $\tilde{\Omega}_{GW}$ is larger. Our findings are consistent with the two available data points for scalar field-hydrodynamical simulations from [71], indicating a departure from linearity dynamical evolution and, hence, from the sound-shell model. We observe that discrepancies with the numerical results from [71] might arise due to the different nucleation histories employed - simultaneous in [71] versus exponential in our simulations). Nevertheless, the extrapolation generally appears reliable, as the extrapolated values show good agreement for simulations with both $\tilde{L}/v_w = 20$ and 40.

For strong PTs, we observe significantly higher GW efficiencies overall. The deviation from the sound shell model is substantial, and the

7 Reference [101] presents results of $\Omega_{GW}/\Omega_{GW,exp} = \mathcal{I}^{int}_{sim}/\mathcal{I}^{int}_{exp}$, where $\mathcal{I}^{int}_{exp}$ would correspond to the value found using Equation (305) with $K = K_\xi$ and $\tilde{\Omega}_{GW} = 10^{-2}$. The ratio that ref. [101] presents therefore corresponds to a combined estimate of $\tilde{\Omega}_{GW} K^2_{rms}/K^2_\xi$ and extraction of $\tilde{\Omega}_{GW}$ for comparison is not straightforward.

effects of nonlinear evolution appear to diminish the dependence of $\tilde{\Omega}_{\rm GW}$ on the wall velocity.

Averaging the values of $\tilde{\Omega}^{\infty}_{\rm GW}$, the estimation of the continuum limit, over v_w for each strength α, we obtain

$$10^2\,\tilde{\Omega}^{\infty}_{\rm GW} = \begin{cases} 1.04^{+0.81}_{-0.67}\,, & \text{for} \quad \alpha = 0.0046\,; \\ 1.64^{+0.29}_{-0.13}\,, & \text{for} \quad \alpha = 0.05\,; \\ 3.11^{+0.25}_{-0.19}\,, & \text{for} \quad \alpha = 0.5\,, \end{cases} \tag{340}$$

where the super and subscripts indicate maximum and minimum values.

Now, let us attempt to transcend the confines of the simulations. Given the sometimes strong decay of the kinetic energy, we evidently underestimate the GW amplitude as we source GWs only from $\tilde{t}_{\rm init} = 16$. Furthermore, the source is still active by the end of the simulation at $\tilde{t}_{\rm end} = 32$, so the measured integrated amplitude has not yet reached saturation within the simulation. However, if we assume that the time invariance of $\tilde{\Omega}_{\rm GW}$ is sustained from the time of PT completion, $\tilde{t}_0 \sim 32$, at which time we can approximate the GW sourcing begins, up until some time $\tilde{t}_{\rm fin} > 32$, we can model the GW amplitude beyond the measurements in the simulation by replacing in Equation (339) $\tilde{t}_{\rm init} \to \tilde{t}_0$ and $\tilde{t} \to \tilde{t}_{\rm fin}$, and explicitly defining the growth model in terms of the continuum values $\mathcal{K}_0$ reported in Figure 29 and $\Omega^{\infty}_{\rm GW}$ as reported in Figure 33, so that

$$\mathcal{I}^{\rm int}_{\infty}(\tilde{t}_0, t_{\rm fin}) \equiv \tilde{\Omega}^{\infty}_{\rm GW}\,\mathcal{K}_0^2\,(\beta R_*)\,\tilde{t}_0\,\frac{[1+(\tilde{t}_{\rm fin}-\tilde{t}_0)/\tilde{t}_0]^{1-2b}-1}{1-2b}\,, \tag{341}$$

In fact, now in conformal time, we may potentially do even better by accounting for cosmic expansion and instead use Equation (321), by similarly defining

$$\mathcal{I}^{\rm int}_{\beta/H}(\tilde{t}_0, \tilde{t}_{\rm fin}) = \tilde{\Omega}^{\infty}_{\rm GW}\,\mathcal{K}_0^2\,\Upsilon_b(\tilde{t}_{\rm fin}-\tilde{t}_0)\,\left(\frac{\beta}{H_*}\right)\,(\beta R_*)\,. \tag{342}$$

Note that the two models are equivalent in the limit of $\beta/H_* \to \infty$. I thus illustrate in Figure 34 GW amplitude growth with the source duration $\tilde{\tau}_{\rm sw} \equiv \tilde{t} - \tilde{t}_{\rm init}$ as modeled in Equation (341) (corresponding to $\beta/H_* = \infty$) and Equation (342), for the two values of $\beta/H_* = 1000$ and 100. I furthermore indicate the numerical growth of the GW spectrum as found in the simulations but re-scaled by a factor $(\mathcal{K}_0/K_0)^2$ and vertically translated by $\mathcal{I}^{\rm int}_{\infty}(\tilde{t}_0, t_{\rm init})$.

This plot constitutes one of the main results of this work, and indeed my PhD, as it incorporates the full machinery of the Higgsless simulations, careful analysis of the results, incorporating systematic

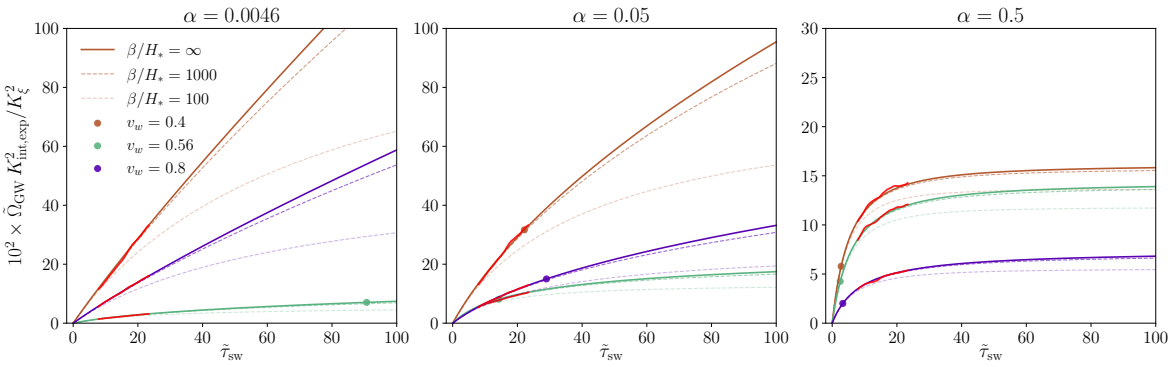

Figure 34: Plots of the GW amplitude growth with the source duration $\tilde{\tau}_{sw} \equiv \tilde{t} - \tilde{t}_{init}$ as modeled in Equation (341) corresponding to $\beta/H_* = \infty$ (solid lines) and Equation (342) (dashed lines), for the two values of $\beta/H_* = 1000$ (normal opacity) and 100 (lower opacity). I furthermore indicate the numerical growth of the GW spectrum as found in the simulations but re-scaled by a factor K_0/K_0 and vertically translated by $\mathcal{I}^{int}_\infty(\tilde{t}_0, t_{init})$ (red line segments). Dots indicate the eddy turnover time $\tilde{t}_{eddy} = \beta R_*/\sqrt{K_\xi}$, which determines the expected scale for nonlinearities to develop (they do not appear in the plot for weak PTs with $v_w = 0.4$ and 0.8).

extrapolation and understanding of uncertainties, the assumption of a locally-stationary UETC, generalization of the GW parameterization template to decaying sources as in (308), the realization that the fluid equations of motion are conformally invariant, and that thus, the effect of cosmic expansion may be estimated a posteriori as in Equation (321).

From this plot, we can make a number of interesting conclusions. Naturally, we expect that the UETC deviates from the locally stationary description as vortical motion and turbulence begin to dominate the kinetic energy in the simulation [76, 77, 79, 96]. This can effectively be modeled by an appropriate choice of the source duration $\tilde{\tau}_{sw}$ at which to stop the GW sourcing. A natural choice of the source duration would therefore be $\tilde{\tau}_{sw} = \tilde{t}_{eddy} = \beta R_*/\sqrt{K_\xi}$, as this captures the time-scale of the formation of turbulence. However, marking with dots in Figure 34 $\tilde{t}_{eddy}$, it is evident that for strong PTs, $\tilde{t}_{eddy}$ occurs well within the simulation. Yet, it is clear from Figure 32 that the GW efficiency is constant in this regime under the assumption of a locally stationary UETC. It appears, therefore, that substantial GW production modeled by (308) still occurs at times many times larger than $\tilde{t}_{eddy}$, and thus, that naively taking $\tau_{sw} = \tilde{t}_{eddy}$ may severely underestimate the GW amplitude.

For strong PTs, source damping is sufficiently strong that the half-life $\tilde{t}_{1/2}$ is always around 5, as seen in Figure 31. Therefore, for a

plausible $\beta/H_* \sim 100$, the final amplitude of GWs from strong PTs is always dominated by damping due to nonlinear dynamics rather than Hubble damping. This is clear from Figure 34, as varying β/H_* has only a marginal effect on the saturated GW amplitude. In fact, we see that already within the simulations duration is the GW amplitude reasonably close to saturation of the GW amplitude. In these cases, therefore, the saturated amplitude of the GW spectrum is less sensitive to the final sourcing time τ_{sw} which we know must be larger than $\tilde{t}_{end} - \tilde{t}_0 > \text{few} \times \tilde{t}_{eddy}$.

For weak PTs, the situation is reversed, with nonlinear damping subdominant to Hubble damping away from $v_w \sim c_s$ if $\beta/H_* \sim 100$, referring to the half-life $\tilde{t}_{1/2}$ in Figure 31. If we similarly assume that $\tilde{\tau}_{sw} > \text{few} \times \tilde{t}_{eddy}$, the final GW amplitude is dictated by Hubble expansion, and we are again relatively insensitive to the actual choice of $\tilde{\tau}_{sw}$, and expect that, for as long as (321) reasonably well captures the effect of expansion, the model (342) constitute a good estimate of the final GW amplitude.

For weak PTs with $v_w \sim c_s$ and most intermediate PTs, the situation is more subtle, and the final GW amplitude may depend more sensitively on the assumptions on $\tilde{\tau}_{sw}$ as the hierarchy between Hubble damping and nonlinear damping is not as prominent, and few $\times \tilde{t}_{eddy}$ and β/H_* are of similar order.

I wish to point out, however, that these conclusions do require further investigation. For example: (1) One must verify the validity of taking $t_{init} \to t_0$ in the models (341) and (342) and validate the constancy of $\tilde{\Omega}_{GW}$ in this limit. (2) The power-law decay, which has been observed to remain accurate for all reference simulations and one strong simulation up to $\tilde{t}_{end} = 64$ for $\alpha = 0.5$ and $v_w = 0.8$, may ultimately break down, thus requiring refined modeling. (3) Even if a power-law decay remains a good description, it is not clear when the locally stationary UETC description breaks down and what is the exact relation with $\tilde{t}_{eddy}$. At this point, we have nevertheless shown that our models work well within the simulation duration and at least up until $\tilde{t}_{sw} \sim \text{few} \times \tilde{t}_{eddy}$ for strong PTs.

Ultimately, while the above paragraphs may deliver some insight, we avoid making a strong statement on the final value $\tilde{t}_{sw}$ and instead regard it as a free parameter.

6.4.7 The shape of gravitational wave spectrum

In this Section, I analyze GW spectra to present findings on the spectral shape for weak, intermediate, and strong PTs. Specifically, I provide fits to the data and extract key spectral features. Note that the

previous results of Chapter 5 for weak and intermediate PTs were obtained using Version 1 of the Higgsless simulation code. Utilizing the enhanced Version 2, I obtain new results for weak and intermediate PTs as well as derive new results for strong PTs, utilizing an updated fitting function to better capture the peak positions and smoothness of the spectral knee and peak.Example spectra, including fits, are shown in Figure 35. The main findings including extracted spectral features are presented in Figure 37.

6.4.7.1 Shape function

The results presented in Chapter 5 demonstrate that the GW spectrum $\Omega_{GW}(k)$ is characterized by a doubly broken power law. At small wavenumbers k, a scaling of $\Omega_{GW}(k) \propto k^3$ is observed, which aligns with expectations from causality. For large k, the spectrum was found to decay following $\Omega_{GW}(k) \propto k^{-3}$. At intermediate scales, a linear scaling regime of $\Omega_{GW}(k) \propto k$ was identified. Beyond a damping scale k_e, the spectrum exhibits an exponential decay, likely due to viscosity effects and limited resolution. At scales approaching the Nyquist wavenumber $k_{Nyq} = \beta N/\tilde{L}$, $\Omega_{GW}(k)$ begins a moderate and artificial growth, forming a far UV tail. This erratic portion is consistently excluded from analysis and in plots, but is relatively similar to the UV tail observed in the GW spectra of the previous Chapter 5 in Figure 17.

To capture the spectral shape $S(\tilde{k}) \equiv \mathcal{I}_{sim}(\tilde{k})/\mathcal{I}^{int}_{sim}$, we use doubly-broken power law with exponential damping, consistent with the previous Chapter 5. The spectral shape can then be parameterized as

$$S(k, k_1, k_2, k_e) = S_0 \times \left(\frac{k}{k_1}\right)^{n_1} \left[1 + \left(\frac{k}{k_1}\right)^{a_1}\right]^{\frac{-n_1+n_2}{a_1}} \left[1 + \left(\frac{k}{k_2}\right)^{a_2}\right]^{\frac{-n_2+n_3}{a_2}} \times e^{-(k/k_e)^2}. \tag{343}$$

This shape function is modified with respect to that introduced in [82] to incorporate an exponential damping factor effective above a certain damping scale $k > k_e$. The normalization constant, S_0, is defined such that $\int S, d\ln k = 1$. The parameters a_1 and a_2 allow for control over the sharpness or smoothness of the knee and peak at k_1 and k_2.

It is noteworthy that the choice of parameters $a_1 = 2$, $a_2 = 4$, $n_1 = -3$, $n_2 = 1$, and $n_3 = -3$ renders Equation (343) equivalent to the shape function

$$S_f(k, k_1, k_2, k_e) = S_0 \times \frac{(k/k_1)^3}{1 + (k/k_1)^2 \left[1 + (k/k_2)^4\right]} \times e^{-(k/k_e)^2}, \tag{344}$$

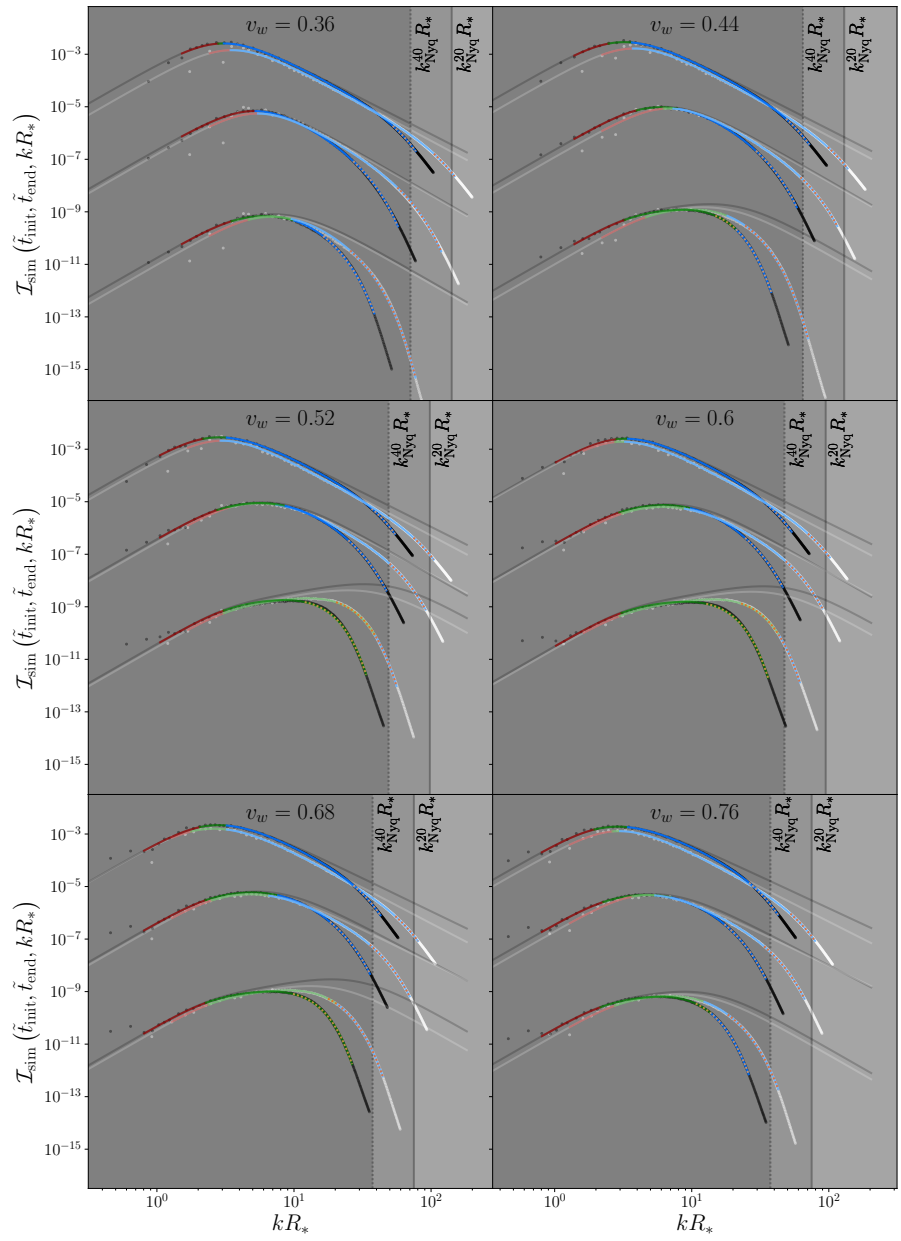

Figure 35: Fits of Equation (343) to the numerical results from weak, intermediate, and strong PTs (in each panel, amplitudes increase with larger α) with $N = 512$ for a range of v_w, and for $\tilde{L}/v_w = 20$ in brighter colors (white dots for the numerical data), and $\tilde{L}/v_w = 40$ in darker colors (black dots for the numerical data). Red lines indicate wave numbers below the knee k_1, green indicates intermediate wave numbers $k_1 < k < k_2$, and blue corresponds to wave numbers above the peak k_2. The dotted orange lines indicate wave numbers $k > k_e$, where exponential damping dominates. The light and dark gray lines indicate the resulting fitted double-broken power laws excluding the exponential damping. Vertical lines indicate the Nyquist wave numbers $k_{\mathrm{Nyq}} R_* = \beta R_* N/\tilde{L}$.

used in the analysis of Chapter 5. Note that, to align with the notation in [82], we have renamed the spectral features $q_0 \to k_1$ and $q_1 \to k_2$. Equation (343), however, provides a more robust method for recovering the peak position of the GW spectrum. This robustness is achieved by enabling control over the sharpness or smoothness of the knees and peaks, which allows for a more accurate representation of the spectral features.

6.4.7.2 The fitting procedure

I fit Equation (343) to our numerically derived $\mathcal{I}_{\rm sim}(\tilde{t}_{\rm init}, \tilde{t}_{\rm end}, \tilde{k})$ spectra, thereby extracting spectral features from the data. The resulting fits are illustrated in Figure 35 for different wall velocities v_w. During the fitting process, I enforce the constraint that $k_1 < k_2$. However, I do not require that $k_2 < k_e$. Instead, k_e is allowed to assume any value independently, which is different from the strategy of Chapter 5. In cases where $k_2 > k_e$, the peak of the spectrum is not accurately resolved and is pushed to smaller wavenumbers by predominantly numerical viscosity. Note that in these cases, k_2 does not indicate the peak location of numerical spectra.

In order to make effective use of the scarce data in the deep IR, I refrain from binning the first 5 data points, performing average only over identical discrete momenta. For the remaining data points, we distribute them into ~ 1000 equispaced bins, with corresponding wave numbers defined at the bin center.

Furthermore, in honor of the discussion in Section 5.5.2.1 of the previous Chapter 5, we neglect the first one or two frequency bins for box size $\tilde{L}/v_w = 20$ and box size $\tilde{L}/v_w = 40$ respectively, (corresponding to the first data point(s) as seen in Figure 35). To highlight the exact fitting region, the red IR tail in Figure 35 is plotted only until the lowest frequency for which we use the numerical data.

As mentioned previously, I also discard the spurious growth seen in the far UV tail of the spectrum (see Figure 17 in Chatper 5). In practice, this means that I discard parts of the spectra beyond which the exponential damping description breaks down, indicated in Figure 35 as the wavenumber at which the dashed orange lines stop.

To accurately reflect the asymptotic behavior that we observed in the previous Chapter 5, we prescribe that set $n_1 = 3$ and $n_2 = 1$. However, as we are looking for indicators of nonlinear dynamics, we explore the possibility o n_3. As is clear in Figure 35, the simulations of strong PTs demonstrate adequate dynamical range to thoroughly sample the UV slope of the GW spectrum across more than an order of magnitude in wavenumber. This is particularly significant because, for strong PTs, we anticipate deviations from $n_3 = -3$ — the value predicted by the

linear sound-shell model [70, 72] — if turbulence and nonlinear dynamics induce a cascade of energy to smaller sales, thereby making the UV slope shallower with respect to the otherwise expected $n_3 = -3$. If the dynamics is described by Kolmogorov turbulence, we expect that the GW spectrum UV slope scales as $n_3 = -8/3$ [75, 77, 92–96]. We deem that the UV slope is sufficiently well sampled for both intermediate and strong PTs that we can let $n_3 \geqslant -3$ when fitting spectra for strong and intermediate PTs. Conversely, we constrain n_3 to be -3 for weak PTs, as weak spectra generally lack the dynamical range necessary to measure n_3 due to thinner shells and $k_2 \gtrsim k_e$.

With these choices, the spectral shape function that we fit to our numerically derived spectra takes the form

$$\begin{aligned} &S(k, k_1, k_2, k_e) \\ &= S_0 \times \left(\frac{k}{k_1}\right)^3 \left[1 + \left(\frac{k}{k_1}\right)^{a_1}\right]^{\frac{-3+1}{a_1}} \left[1 + \left(\frac{k}{k_2}\right)^{a_2}\right]^{\frac{-1+(-3)}{a_2}} \times e^{-(k/k_e)^2}, \end{aligned} \tag{345}$$

where $n_3 > -3$.

I show in figure 35 fits of this function to the spectra for every other v_w. In figure 37, I plot the extracted spectral features k_1, k_2, k_e, and k_{peak} as functions of v_w for $\alpha \in \{0.0046, 0.05, 0.5\}$, normalized to β (upper panel) and R_* (lower panel). In Figure 36, I plot the fitted UV index n_3.

Determining the scale of exponential damping, k_e, is essential for assessing the reliability of the measurement of k_2. If $k_2 > k_e$, we are in a regime where damping already influences scales larger than the spectral peak. In such cases, even though for weak PTs k_2 aligns well with $1/\xi_{shell}$ above k_e (suggesting a trend consistent with physical expectations), caution is warranted when interpreting k_2 and k_{peak} as true physical parameters. We will simply consider spectra where $k_2 > k_e$ as under-resolved.

Assuming that the exponential damping is purely a numerical artifact, it may nonetheless be insightful to consider the spectra without exponential damping. Therefore, in Figure 37, I also present the shape function without exponential damping. Differences in peak positions with and without damping are significant only for weak PTs, box size $\tilde{L}/v_w = 40$, and wall velocities approaching the speed of sound.

Let us proceed to discuss the findings concerning each fitting parameter one by one.

6.4.7.3 UV spectral index n_3

Figure 36 displays the optimal values of n_3 obtained through the fitting procedure. I only display results for box size $\tilde{L}/v_w = 20$ due to its

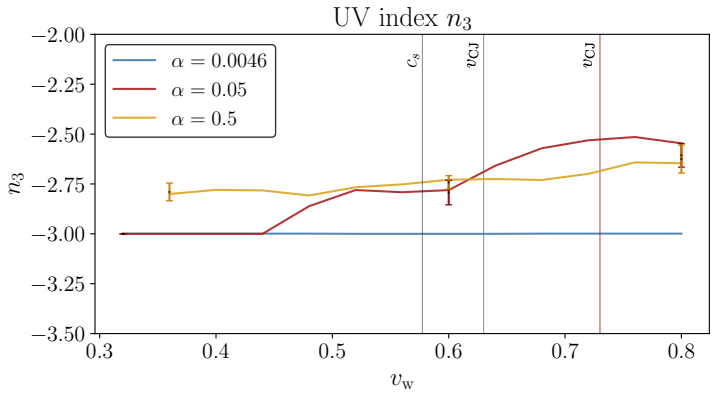

Figure 36: Fitted UV index $n_3 \geqslant -3$. Note that for weak PTs, we fix $n_3 \equiv -3$ (shown for reference). The sample standard deviation, as determined from the *seed* simulations, is depicted as 1σ error bars at selected representative velocities.

larger dynamical range. For weak PTs (shown in blue, for reference), n_3 is constrained to -3. For intermediate PTs, a slight increase in n_3 toward approximately -2.5 is observed as the wall velocity increases. Strong PTs display a similar trend but with the optimal n_3 always larger than -3 and generally around or above -2.75 even for low v_w values.

6.4.7.4 Smoothing vs. sharpening of the knee and the peak

Introducing the new free parameters a_1 and a_2 allows for more accurate fits compared to those obtained with the simpler shape function in Equation (344) from Chapter 5. However, while promoting a_1 and a_2 to free parameters enhances the fit, it also introduces significant degeneracies among the fitting parameters. This, in turn, complicates the reliable extraction and dependence on v_w and α of the spectral features. Therefore, we opt for a different approach.

Given the peak of the GW spectrum's significant phenomenological relevance, I adjust the parameters a_1 and a_2 to constants that consistently recover the peak position across all wall velocities and PT strengths. Empirically, we find that slightly sharpening the knee and smoothing the peak typically enhances peak position recovery and results in a well-fitted spectrum overall. Determining a_1 benefits from simulations with more data points in the IR; therefore, we exclusively use box size $\tilde{L}/v_w = 40$ for this estimation, resulting in $a_1 = 3.6$ (an increase from $a_1 = 2$ used in Chapter 5). Conversely, determining a_2 benefits from resolving the UV, leading us to exclusively use box size $\tilde{L}/v_w = 20$ and find that $a_2 = 2.4$ (a reduction from $a_2 = 4$ used in

Chapter 5) is suitable. We utilize these values for a_1 and a_2 throughout the study.

6.4.7.5 Spectral feature k_1

The spectral feature k_1 marks the transition from cubic to linear scaling of $\Omega_{GW}(k)$. We discovered that moderately sharpening this knee with $a_1 = 3.6$ universally improves the fits. In the left column of Figure 37, I display the scaling behavior of k_1 with v_w for $\alpha \in \{0.0046, 0.05, 0.5\}$, normalized to β (upper panel) and R_* as defined in Equation (135) (lower panel). I plot values for both box size $\tilde{L}/v_w = 20$ and box size $\tilde{L}/v_w = 40$, along with the colored regions in between. Note that error bars for box size $\tilde{L}/v_w = 20$ are significantly larger due to data scarcity and larger sample variance associated with the fewer number of bubbles. Furthermore, as evident from Figure 35, box size $\tilde{L}/v_w = 20$ has sparse data in the IR, making it questionable whether k_1 can be reliably extracted in the first place. Therefore, results for k_1 presented below pertain exclusively to data derived from simulations box size $\tilde{L}/v_w = 40$.

Grouping all reference simulations together, we find that

$$\frac{k_1 R_*}{2\pi} \simeq 0.39 \pm 0.11 \,. \tag{346}$$

where the uncertainty describes the corresponding standard deviation. Thus, in this normalization, the resulting variability in $k_1 R_*$ among the wall velocities is only about 27%.

A comparison with results on k_1 from Chapter 5 is warranted. The intricate structure observed for weak PTs featuring a bump around velocities $v_w \sim 0.56$ is no longer observed, probably because of the more robust fitting function now accommodating a sharpening of the knee. Overall, the scatter with wall velocity has reduced significantly compared to the previous results where k_1 varied by a factor of ~ 6 across the range of wall velocities. We furthermore recognize the decreasing trend with k_1/β normalization, as seen in the upper left plot in Figure 37, as a result of normalizing to the wrong underlying scale, $1/\beta$, rather than the typical scale of fluid perturbations R_*. With the more justified R_* normalization, the residual variability with wall velocity is small, and the complex behavior that was observed in Chapter 5 is eliminated. With the introduction of strong PTs, we furthermore observe that k_1 is largely independent of strength.

I finally want to note that we explored an additional normalization. As an alternative to R_*, an effective bubble size can be defined based

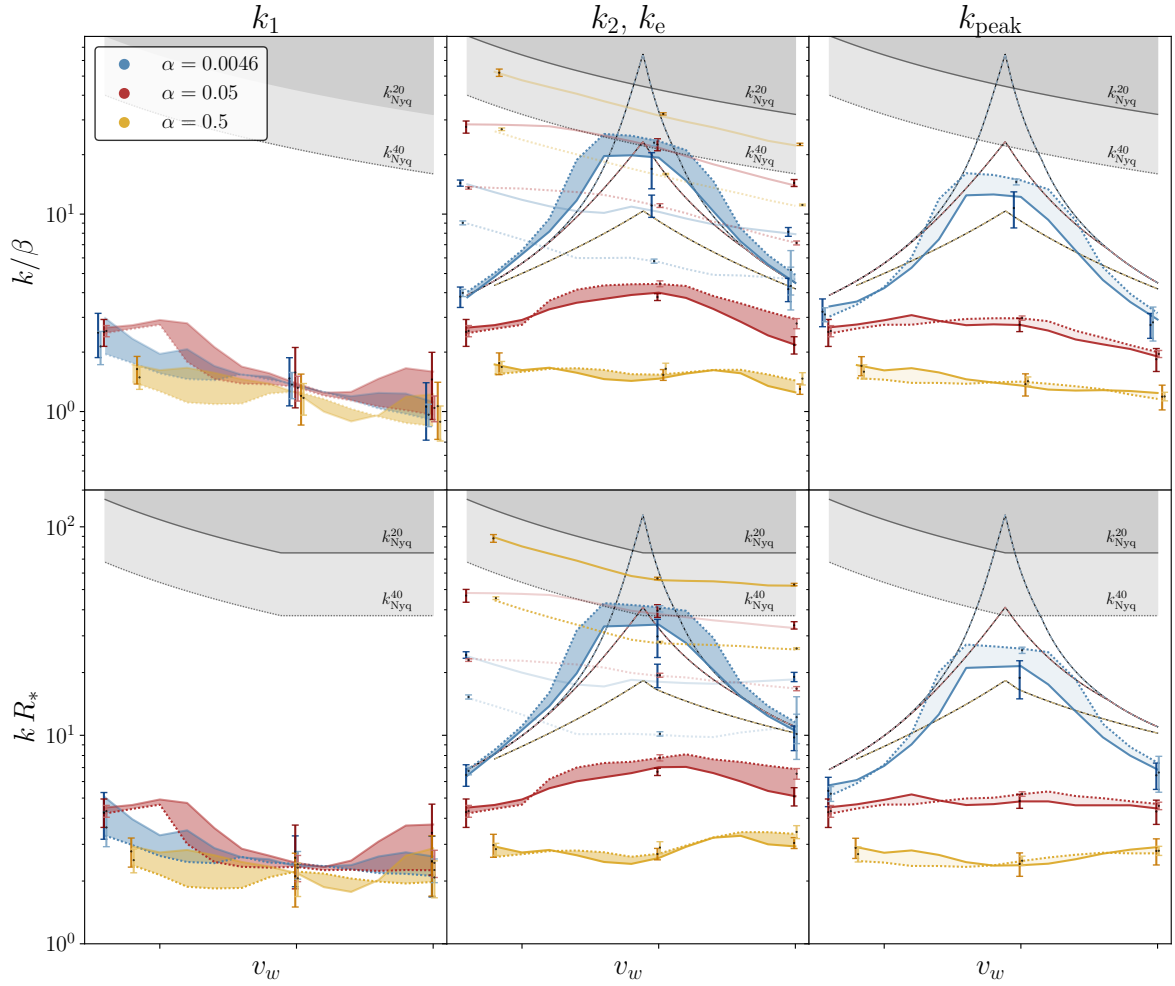

Figure 37: Fitted characteristic wave numbers k_1 (left column), k_2 and k_e (middle column), and k_{peak} (right column) for weak (blue), intermediate (red), and strong (orange) PTs, using simulations with $N = 512$ and $\tilde{L}/v_w = 20$ (40) in solid (dotted) lines. Gray regions indicate the Nyquist frequency $\tilde{k}_{Nyq} = N/\tilde{L}$. In the upper panel, wave numbers are normalized as k/β, as presented in [67] and Chapter 5, while in the lower panel, they are normalized as $k\,R_*$. Thick colored lines of low opacity in middle panels indicate k_e for $\tilde{L}/v_w = 20$ (40) in solid (dotted) lines. In the upper panel (middle and right), thin black-and-color dashed lines indicate $1/\xi_{shell}$, while in the lower panel, they indicate the fitted value $2\pi * 0.49/\Delta_w$ (see Equation (349)). In the right column, the lower opacity regions indicate the peak as obtained using the double broken power law fit of Equation (343), neglecting the exponential numerical damping.

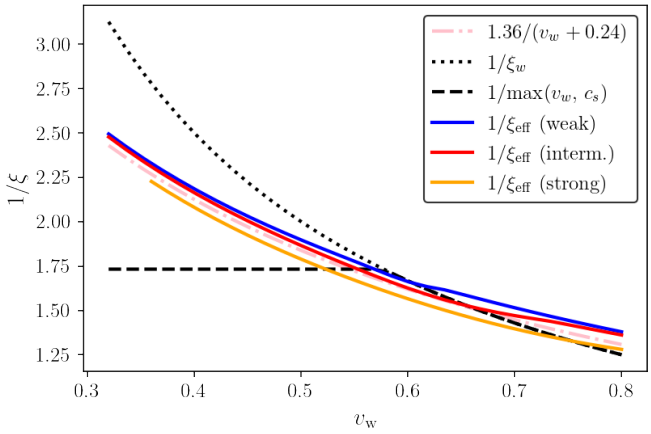

Figure 38: Comparison between the re-scalings associated with R_* and $R_{\rm eff}$. The pink dashed-doted line corresponds to a fit $1.36/(v_w + 0.24)$ to facilitate using $R_{\rm eff}$ without knowledge of the profiles.

on the kinetic energy profile. Define the radius of the center of kinetic energy $\xi_{\rm eff}$ in self-similar coordinates $\xi = r/t$,

$$\xi_{\rm eff} = \frac{\int_{\xi\in\xi_{\rm shell}} T(\xi)\xi^3 \, d\xi}{\int_{\xi\in\xi_{\rm shell}} T(\xi)\xi^2 \, d\xi'} \tag{347}$$

where $T(\xi) = w(\xi)\gamma(\xi)^2 v(\xi)^2$ represents the kinetic energy, and the ξ^2 factor arises from integrating over spherical symmetry. Then, we can define the effective radius $R_{\rm eff}$

$$R_{\rm eff} = (8\pi)^{1/3}\frac{\xi_{\rm eff}}{\beta}. \tag{348}$$

We hypothesize that, perhaps, this radius further flattens the trend of k_1 with wall velocity and reduces the small scatter with PT strength. In Figure 38, I show a comparison between $1/\xi_{\rm eff}$ and $1/\max(v_w, c_s)$. Since the normalization of $R_{\rm eff}$ does not become flat below c_s, it compensates for the small rise in k_1 at small wall velocities. Furthermore, we note that for strong PTs, the lower values of $1/\xi_{\rm eff}$ would indeed bring up the strong line of k_1 relative to those of weak and intermediate PTs. Overall, we conclude that normalizing to $R_{\rm eff}$ rather than R_* mitigates the small but residual trend with of k_1 with v_w and reduces the scatter from 27% to only 19%. Nevertheless, the gain is small for the added complexity, and we defer from pushing the agenda of normalizing to $R_{\rm eff}$ rather than R_* in this work.

6.4.7.6 Spectral features k_2 and k_e

The spectral feature k_2 marks the transition from linear $n_2 = 1$ to $n_3 \sim -3$ scaling of $\Omega_{GW}(k)$, occurring essentially at the peak (when $k_2 < k_e$). The scale k_e indicates the wavenumber at which exponential damping becomes important. We found that a moderate smoothing of the knee at k_2 with $a_2 = 2.4$ leads to better fits. In the middle column of figure 37, I plot the scaling behaviour of k_2 and k_e with v_w for $\alpha \in \{0.0046, 0.05, 0.5\}$ normalized to $1/\beta$ in the upper panel, R_* in the lower panel. For reference, I plot $1/\xi$shell in thin dashed black-colored lines.

WEAK PHASE TRANSITIONS For weak PTs, the plot indicates an association of k_2 with the inverse shell thickness $1/\xi_{shell}$, as was previously observed in Chapter 5. However, the presence of damping on scales $k_e < k_2$ renders the measurements of k_2 questionable for all but the smallest $v_w \in \{0.32, 0.36, 0.40\}$ for box size $\tilde{L}/v_w = 40$, and $v_w \in \{0.32, 0.36, 0.40, 0.44, 0.72, 0.76, 0.8\}$ for box size $\tilde{L}/v_w = 20$. It is nevertheless interesting to note that the trend of scaling with $1/\xi_{shell}$ is also found when $k_2 > 1/k_e$ except in the vicinity of $v_w \sim c_s$. In conclusion, damping at $k_e < k_2$ thwarts reliable extraction of k_2, but findings suggest an intimate association with $1/\xi_{shell}$. Larger resolution simulations are needed to find at which scale this association breaks down and nonlinear physical damping becomes significant.

INTERMEDIATE AND STRONG PHASE TRANSITIONS Shifting our attention to intermediate and strong PTs, we observe notably different behavior. As previously discussed in Chapter 5, intermediate PTs exhibit a significant deviation from the trend $k_2 \propto \xi_{shell}$. This departure is observed to be even more pronounced for strong PTs, where k_2 remains approximately constant with wall velocity. Thus, it appears that for stronger PTs, the shell thickness ξ_{shell} may no longer be the most relevant scale, with k_2 potentially being determined directly by the larger characteristic length scale of the fluid R_*, as in the limit of very strong PTs. This shift could be attributed to the emergence of nonlinearities. However, this hypothesis requires further investigation through additional large-scale and higher-resolution numerical simulations to be substantiated.

Using our numerical results from the reference simulations pertaining exclusively to data from simulations with box size $\tilde{L}/v_w = 20$ for their improved dynamical depth and averaging over v_w, we find the following values for k_2,

$$\frac{k_2\, R_*}{2\pi} \simeq \begin{cases} 0.49 \pm 0.024/\Delta_w\,, & \alpha = 0.0046\,, \\ 0.93 \pm 0.13\,, & \alpha = 0.05\,, \\ 0.45 \pm 0.042\,, & \alpha = 0.5\,, \end{cases} \tag{349}$$

where $\Delta_w = \xi_{\rm shell}/\max(v_w, c_s)$ is the normalized sound-shell thickness and the $\pm$ range corresponds to the standard deviation in the measurement associated with the reference simulations. Sample variance is generally quite small and of the order of scatter with wall velocity.

6.4.7.7 GW spectrum peak $k_{\rm peak}$

While our spectrum is parameterized by the scale k_2, the peak wavenumber $k_{\rm peak}$ is phenomenological important, and I thus plot it in the right column of Figure 37. Note that when presenting the peak, I choose to neglect the exponential damping factor of shape function (345) since this damping is ultimately expected to go away in the limit of infinite resolution. Clearly, reporting $k_{\rm peak}$ neglecting expansion constitutes a leap of faith, and reported peak positions must be taken not too seriously whenever $k_2 > k_e$ (as determined from the middle column of the same Figure). Generally, k_2 typically nearly coincides with $k_{\rm peak}$. For intermediate PTs, it is interesting to note the almost complete flattening of the dependence of $k_{\rm peak}$ on v_w using $k_{\rm peak} R_*$ normalization.

To conclude, we observe that all three scales, $k_1 R_*$ (for weak, intermediate, and strong PTs), $k_2 R_*$ and $k_{\rm peak} R_*$ (for intermediate and strong PTs), exhibit quite small variation with v_w. For weak PTs, we find that $k_2\, R_*\, \Delta_w$ is also nearly independent of v_w, consistent with the predictions from the sound-shell model.

Time evolution of the spectral shape in the simulations

In Figure 39, I present the GW spectrum $\mathcal{I}_{\rm sim}(\tilde{t}_{\rm init}, \tilde{t}, \tilde{k})$ at various times $\tilde{t}$ throughout the simulation. Generally, the causal tail, which scales as k^3 at small k, is observed from the early stages. As time progresses, we notice indications of more intricate structures emerging below the peak, shifting the transition of the causal k^3 tail to lower wave numbers, consistent with predictions from [73, 74].

Initially, the growth rate of the GW amplitude for IR modes appears faster than linear, closer to the quadratic growth described in [73], where the transition from quadratic to linear growth occurs later for smaller values of k.

As for our final measurements of the spectral shape $S(k R_*)$, which will be utilized in models (308) and (321), we use the spectral shape at the end of the simulation, $\tilde{t}_{end} = 32$. At this point, the wavenumbers around the peak grow proportionally to K_{int}^2 as described in (308). The spectra at $\tilde{t}_{end} = 32$ are displayed in Figure 35.

As discussed in Section 6.2.3, the growth rate model used for the GW spectrum is valid only at wave numbers $k \gg 1/(t - t_{init})$. Therefore, when using the GW spectrum shapes measured at $\tilde{t}_{end}$ to inform our GW spectrum growth models (308) and (321), we implicitly assume that all wave numbers evolve uniformly with the source duration until a final time $\tilde{t}_{fin} > \tilde{t}_{end}$ is reached.

However, if different time evolutions occur for wave numbers that do not significantly contribute to the integrated amplitude or after the end of the simulation, the resulting spectral shape of the GWs could be affected. This possibility arises within the sound-shell model, particularly in the IR regime, as shown in [73], where a transition from linear to quadratic growth is expected at small k in the stationary case. Additionally, deviations from the sound-shell model, or its generalization in Section 6.2.3 to decaying sources, may occur due to the potential development of nonlinear fluid perturbations and vortical motion.

In such cases, the resulting GW spectrum is expected to exhibit a different time evolution compared to that of compressional motion [75, 93–96, 161], with GW modes likely reaching their saturation amplitudes within this regime.

6.4.8 Sample variance of the GW spectrum

Figure 40 illustrates the mean, standard deviation, and min-max range of GW spectra obtained from the *seed* simulations and the corresponding *reference* simulation. The primary impact of varying nucleation histories is a shift in the overall amplitude of the spectra, while the spectral shape remains largely unchanged. The left and right panels show simulations with box sizes $\tilde{L}/v_w = 20$ and $\tilde{L}/v_w = 40$, respectively. It is noteworthy that artifacts appear in the IR region of the spectra for the smaller box size $\tilde{L}/v_w = 20$ at low wall velocities. These artifacts likely arise from the shock wave ahead of the bubble colliding with its mirrored images due to periodic boundary conditions before the PT is complete.

6.4.9 Initial findings and discussion on vorticity

We have observed various indications of turbulence and nonlinear dynamics, such as shallower UV tails of the GW spectrum in strong PTs

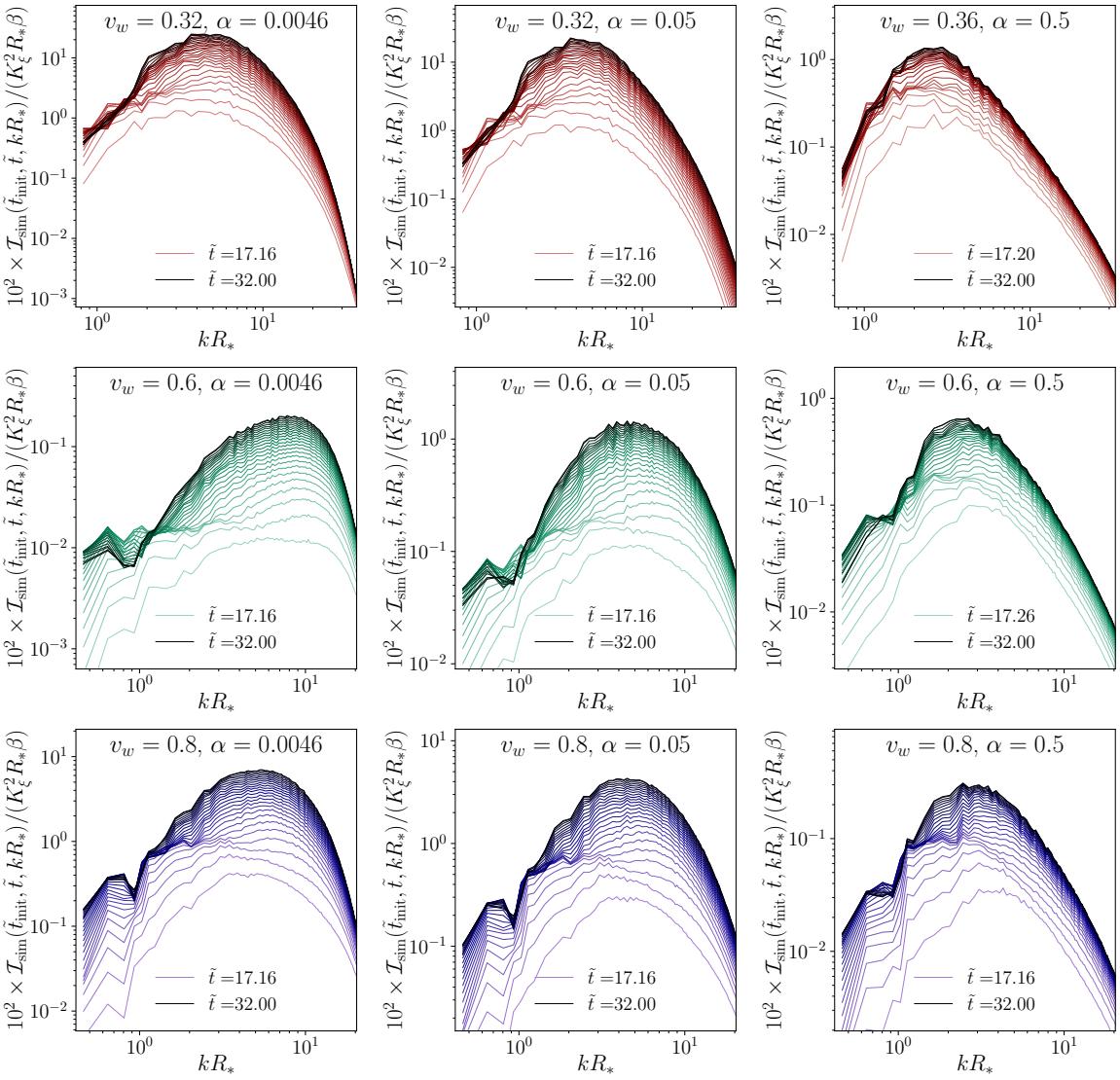

Figure 39: Time evolution of the GW spectrum $\mathcal{I}(\tilde{t}_{\rm init}, \tilde{t}, \tilde{k})$, evaluated at times $\tilde{t} \in [17, 32]$ with $\tilde{t}_{\rm init} = 16$, for weak (left column), intermediate (middle column), and strong (right column) PTs. The wall velocities are $v_w = 0.32$ (0.36 for strong PTs) in the upper panels, 0.6 in the middle panels, and 0.8 in the lower panels. The numerical resolution is $N = 512$, and the box size is $\tilde{L}/v_w = 40$. The GW spectra are normalized by the reference value $\tilde{\Omega}_{\rm GW} \simeq 10^{-2}$ and the expected scaling $K_\xi^2 R_* \beta$.

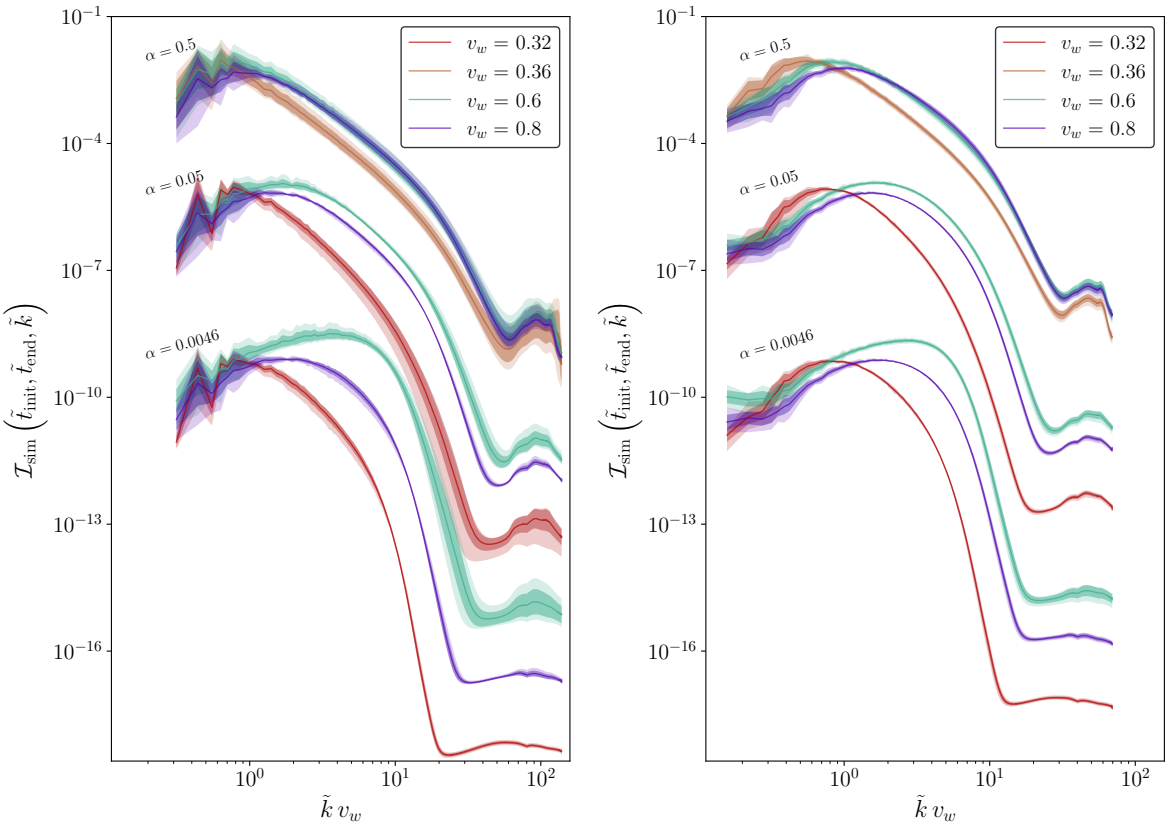

Figure 40: Various GW spectral growth rates obtained as averages over 10 different bubble nucleation histories. Each spectrum shows the mean, the variance, and the min-max over the ten nucleation histories. The left (right) plots show spectra from simulations with box size $\tilde{L}/v_w = 20$ (box size $\tilde{L}/v_w = 40$).

and strong damping, which appears unrelated to numerical viscosity. To firmly establish the presence of nonlinear dynamics, in this Section, I will demonstrate the production of vorticity in the simulation by looking at 2D snapshots of the vorticity field and the growing presence of a transverse velocity component in velocity power spectra. I will move beyond the scope of the publication [3] by presenting slices for a simulation of resolution $N = 1024$, delivering a significantly improved resolution of the UV physics and thus dynamical depth, allowing to unambiguously establish the production of macroscopic vorticity.

6.4.9.1 Vorticity on the lattice

The vorticity is computed as

$$\nabla \times \mathbf{v} = \left(\frac{\partial v_z}{\partial y} - \frac{\partial v_y}{\partial z}\right)\hat{\mathbf{x}} + \left(\frac{\partial v_x}{\partial z} - \frac{\partial v_z}{\partial x}\right)\hat{\mathbf{y}} + \left(\frac{\partial v_y}{\partial x} - \frac{\partial v_x}{\partial y}\right)\hat{\mathbf{z}}\,. \quad (350)$$

On the lattice, we must approximate the derivative through some difference-method, and choose for this task the central difference prescription

$$\frac{\partial v_i}{\partial \tilde{x}_j}(\tilde{\mathbf{x}}) \simeq \frac{v_i\left[\tilde{\mathbf{x}} + \delta\tilde{x}\,\hat{x}_j\right] - v_i\left[\tilde{\mathbf{x}} - \delta\tilde{x}\,\hat{x}_j\right]}{2\,\delta\tilde{x}}\,, \tag{351}$$

where $\delta\tilde{x} = \delta\tilde{x}_j\beta$ is the uniform grid spacing.

With this choice of derivative operator, the magnitude of the curl $|\tilde{\nabla} \times \mathbf{v}|$ is computed at every grid point. 2D simulation slices at different times are shown in Figure 41. Note that the definition of the numerical derivative operator (351) inevitably introduces potentially large vorticity at points where the velocity field varies considerably from lattice site to lattice site. This occurs, e.g., around the bubble shock fronts where discontinuities are present. Ideally, the velocity gradients are aligned with the radial direction, in which case no vortical component is present. However, on the lattice, artifacts may arise from the discretization, causing rather strong vorticity to appear at and just around the wall. This is clearly seen in the lower left frame in Figure 41. The numerical nature of this vorticity is nevertheless clear from the observation that the vortical structure, as we traverse around the bubble wall, is seen to inherit the symmetry of the lattice. Furthermore, mostly small but spurious oscillations of the fluid velocity occur at the bubble wall interface, as discussed in Section 5.3.6 of the previous Chapter 5. These oscillations additionally give rise to extremely local but steep velocity gradients, potentially showing up as a large-amplitude spurious vorticity component confined to the wall.

In Figure 41, and in particular when presented with the opportunity to study the full time-evolution of the system frame by frame, it is observed that production of vorticity occurs at the interface of a sound-shell from one bubble crossing over the bubble wall of another. The velocity field in the upper panel is included to make vorticity production easy to correlate with the velocity field. In this sense, the resulting vorticity pattern initially appears to track the *sweeping* of this sound-shell-bubble-wall-crossing interface over time. However, during this process, frame-by-frame inspections reveal that convective and turbulent motions are induced in the fluid. These are observed as slowly evolving structures compared to the sound waves. Sound waves evolve on time scales proportional to the speed of sound, whereas convective structures evolve on time scales proportional to the average convection speeds, which are typically much smaller. It therefore appears that, in addition to a pure longitudinal velocity component, a fluid velocity field characterized by convective motions develops as a result of fluid interactions during, and possibly after, the collision phase. This convective component is marginally evident in the top-right plot in Figure 41,

where additional small-scale structures are hinted in the velocity field but are absent in the enthalpy field. This additional small-scale structure appears to originate from convective motion.

6.4.9.2 Velocity power spectra

We have observed the presence of spurious vorticity components associated with the choice of the derivative operator and the lattice structure, as well as spurious oscillations around the bubble wall interface. These are very localized effects and do not contribute meaningfully to large-scale vorticity correlated over macroscopic scales. Therefore, vorticity components that emerge from numerically induced oscillations and limited grid resolution will contribute mostly to the UV part of related velocity spectra. Furthermore, the presence of convective motion implies the presence of transverse velocity components. The development of such a component should thus be visible in spectra of the velocity fields decomposed into longitudinal and transverse contributions, and in particular, physical macroscopic contributions should distinguish themselves from numerical contributions through a separation of scales. I will dedicate this Section to a discussion of these matters.

Under the assumptions of statistical spatial homogeneity and isotropy, the two-point correlation function of the velocity field is characterized in terms of the full velocity spectrum $P_v(k)$, the longitudinal component $P_v^{\parallel}(k)$, and transverse component $P_v^{\perp}(k)$, which are defined by

$$\langle v_i(\mathbf{k})\, v_i^*(\mathbf{k}')\rangle = (2\pi)^3\, \delta^3(\mathbf{k}-\mathbf{k}')\, P_v(k)\,, \tag{352}$$

$$\langle \hat{k}_i\, v_i(\mathbf{k})\, \hat{k}_j\, v_j^*(\mathbf{k}')\rangle = (2\pi)^3\, \delta^3(\mathbf{k}-\mathbf{k}')\, P_v^{\parallel}(k)\,, \tag{353}$$

and

$$\left\langle \left[\hat{\mathbf{k}}\times\boldsymbol{v}(\mathbf{k})\right]_i \left[\hat{\mathbf{k}}'\times\boldsymbol{v}^*(\mathbf{k}')\right]_i \right\rangle = (2\pi)^3\delta^3(\mathbf{k}-\mathbf{k}')\, P_v^{\perp}(k)\,, \tag{354}$$

respectively, such that $P_v(k) = P_v^{\parallel}(k) + P_v^{\perp}(k)$.

Therefore, it suffices to compute any two of the three velocity spectra, in the sense that, e.g.,

$$P_v^{\perp}(k) = P_v(k) - P_v^{\parallel}(k)\,. \tag{355}$$

Since $\mathbf{v}$ and $\hat{\mathbf{k}}\cdot\mathbf{v}$ are more readily obtainable than $\hat{\mathbf{k}}\times\mathbf{v}$, we proceed to compute

$$P_v(k) = \frac{1}{V}\left\langle |\mathbf{v}(\mathbf{k})|^2\right\rangle \quad \text{and} \quad P_v^{\parallel}(k) = \frac{1}{V}\left\langle |\hat{\mathbf{k}}\cdot\mathbf{v}(\mathbf{k})|^2\right\rangle \tag{356}$$

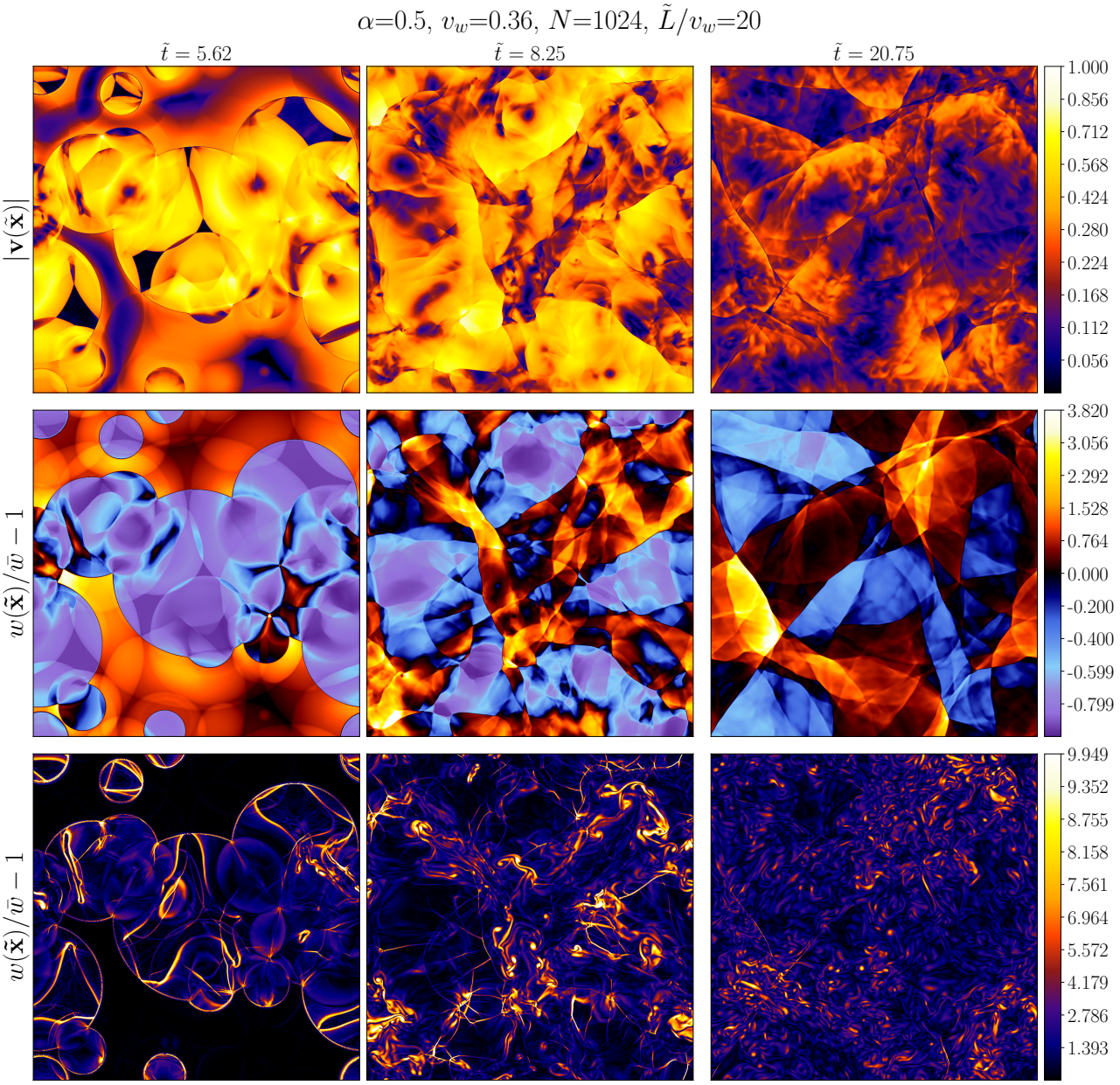

Figure 41: 2D simulation slices of the velocity amplitude $|\mathbf{v}(\tilde{\mathbf{x}})|$, enthalpy $w(\tilde{\mathbf{x}})$, and the vorticity $|\tilde{\nabla} \times \mathbf{v}(\tilde{\mathbf{x}})|$ field for a strong PT with $\alpha = 0.5$ and $v_w = 0.36$. The resolution is N = 1024, twice that of the simulations of the highest resolution in previous parts of this Chapter, and the box size $\tilde{L}/v_w = 20$. The wall velocity is chosen to be $v_w = 0.36$ since the production of vorticity is observed to be maximal at low wall velocity. Around the expanding bubble, spurious small-scale vorticity is seen, which is caused in part by small fluid transients around the shock and in part by the definition of the central numerical derivative, which picks up artifacts from the lattice symmetry. Sizeable macroscopic production is, however, observed in the interactions of overlapping fluid sound shells, indicating the physical presence and build-up of vorticity.

on the lattice. Following Section 5.3.3 in the previous Chapter 5, we take the volume V to mean the volume of the simulation box and approximate the ensemble average as the average over momenta of equal length $|\mathbf{k}| = k$ on the sphere. As for the mapping of momenta on the lattice to their physical counterpart, we follow the updated saw-prescription (327) outlined in Section 6.3.1.2, so that the unit vector $\hat{k}$ in the direction of wave propagation reads

$$\hat{\mathbf{k}} = \mathrm{saw}(\mathbf{k})/|\mathrm{saw}(\mathbf{k})|\,. \tag{357}$$

The Discrete Fourier Transform $\mathbf{v}(\mathbf{k})$ is computed using the same Fast-Fourier-Transform routine [121] as in the rest of the simulation code. Following these specifications, we compute the longitudinal and transverse velocity spectra $P_v^{\parallel}$ and $P_v^{\perp}$, for which time series are illustrated in Figure 42.

6.4.9.3 Interpretation of $P_v^{\parallel}$ and $P_v^{\perp}$

Sound waves involve compressions and rarefactions along the direction of wave propagation $\mathbf{k}$. Under the assumption of linearity, the system can be represented as a superposition of non-interacting plane waves. In this context, the pressure gradients are always orthogonal to the wavefronts and parallel to the direction of propagation, which consequently ensures that fluid acceleration and the resulting velocities always align with the direction of propagation $\mathbf{k}$. Therefore, a pure sound field is characterized by exclusively longitudinal motion, which renders the transverse power spectrum $P_v^{\perp}$ identically equal to zero.

In our situation of interest, the system is characterized, at least before bubble collisions, by expanding sound shells that constitute either rarefaction waves, compression waves, or a combination of both. After collisions, if we assume linearity, this statement still holds true. We can thus appreciate the importance of having at our disposal time series of the velocity spectra $P_v^{\parallel}$ and $P_v^{\perp}$, for we understand that upon departure from linearity, we no longer expect that $P_v^{\perp}$ be identically zero. Observation of a non-zero $P_v^{\perp}$ is hence a powerful indication of physics beyond linear evolution, which, after all, is from where simulations and the present study gain motivation.

The transverse velocity power spectrum $P_v^{\perp}(k)$ captures the energy in the rotational, i.e., vortical, components of the velocity field, which are hallmarks of turbulent flows characterized by chaotic, vortical structures and energy cascades across scales. Both longitudinal and transverse components of the velocity field are important, but the transverse components are particularly indicative of the vortical structures. Therefore, the growth of the transverse power spectrum $P_v^{\perp}(k)$ indicates the production of turbulence in the flow field. At the very least,

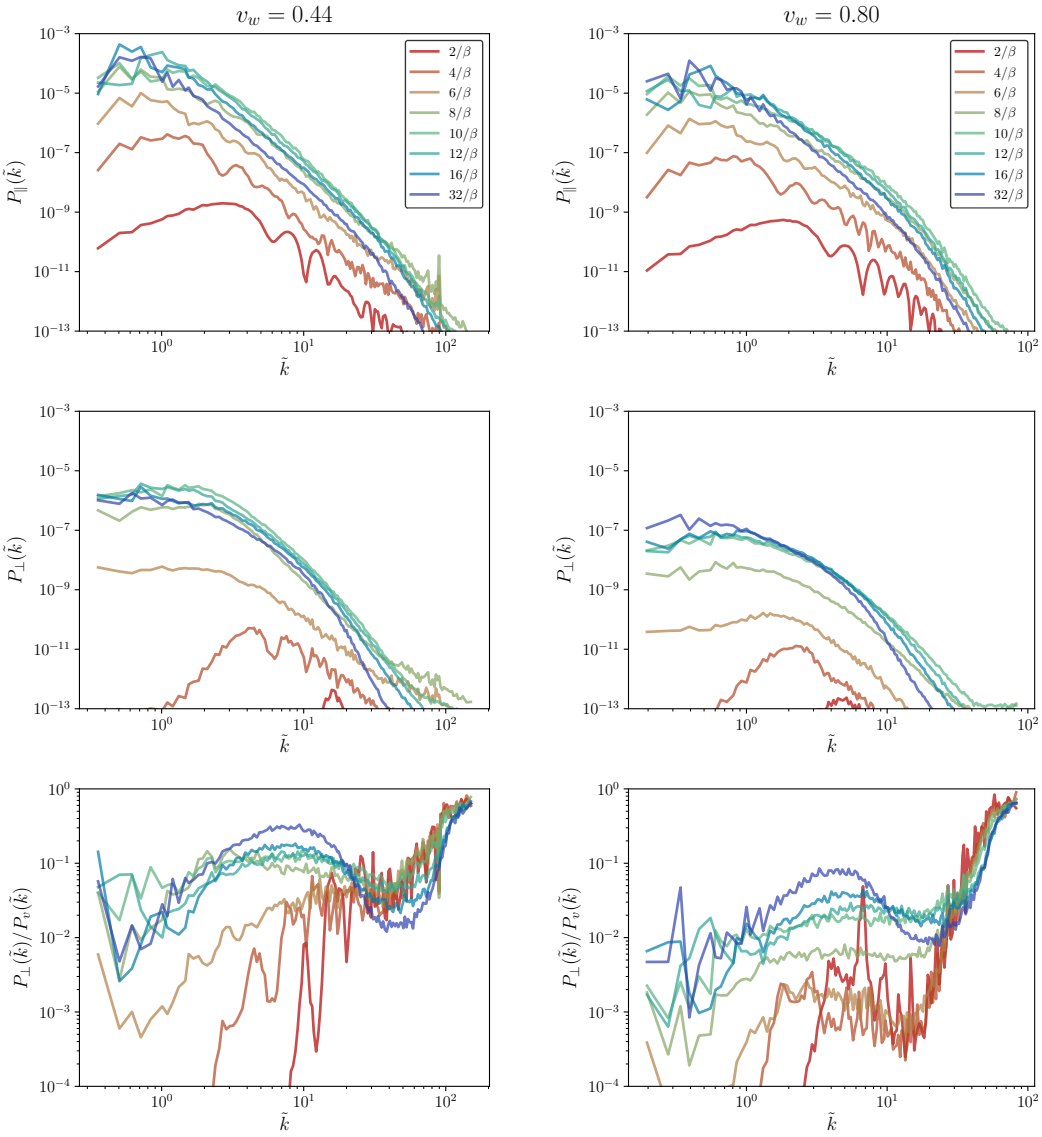

Figure 42: Longitudinal and transverse velocity power spectra of the fluid for two strong PTs with $\alpha = 0.5$ and wall velocities $v_w = 0.44$ (left column) and $v_w = 0.8$ (right column). The top panel illustrates the power in the longitudinal modes, the middle panel the power in the vortical modes, and the bottom panel the fraction of power in the vortical modes. Different lines correspond to different times in the simulation. For reference, bubble nucleation begins around $\tilde{t} \simeq 0$, first collisions occur around $\tilde{t} \simeq 5$, and PT completion takes place around $\tilde{t} \simeq 10$.

since we start from a purely longitudinal velocity field, the growth of $P_v^{\perp}(k)$ proves the presence of mode coupling in the fluid. In the context of sound waves, this means that longitudinal sound waves (which involve compression and rarefaction) can transfer energy to transverse wave modes (which involve shear or rotational motion), which occur as a purely nonlinear effect. In our scenario, mode coupling might occur near bubble wall interfaces, in line with what we observed in the previous Section 6.4.9.1.

Having established the importance and certain interpretations of the velocity spectra $P_v^{\parallel}$ and $P_v^{\perp}$, let me highlight some trends seen in Figure 42. In this Figure, we present time-series of the velocity spectra $P_v^{\parallel}$ and $P_v^{\perp}$ for two choices of wall velocities $v_w = 0.44$ and $v_w = 0.8$ for strong PTs. We additionally plot the fraction $P_v^{\perp}/P_v^{\parallel}$, to highlight their relative contributions.

In the upper panel, we can follow the growth of energy in longitudinal modes. In the middle panel, we can similarly follow the growth of energy in transverse modes. At early times, the fluid field is dominated by a longitudinal component, with only negligible vortical contributions, as is clear from the bottom panel. Only in the UV are transverse contributions comparable to the longitudinal. The contributions in the UV correspond to scales much smaller than any of the two predominant scales in the system: the typical bubble size and wall thickness. Therefore, and as we discussed in Section 6.4.9.1, we interpret this contribution as largely stemming from numerical artifacts such as spurious oscillations and the finite resolution of the lattice. However, at around $\tilde{t} = 6$, a transverse velocity component contributes to a flat part of the transverse velocity power spectrum $P_v^{\perp}(k)$ with support all the way down to the smallest wavenumber which keeps growing with time. At late times following bubble collision, we observe that while the absolute power in vortical modes saturates, the ratio $P_{\perp}/P_v$ still grows at wavenumber just below $\tilde{k} \lesssim 10$, reaching values around $P_{\perp}/P_v \simeq 0.3$ and $P_{\perp}/P_v \simeq 0.1$ for the deflagration, $v_w = 0.44$, and strong hybrid, $v_w = 0.8$, respectively by of the simulation. In both cases, a sizable fraction of vorticity is thus observed. The growing fraction of power in vortical modes may eventually lead to the fluid system being completely dominated by convective turbulent motion.

Additionally, velocity power spectra for weak and intermediate PTs were obtained, revealing that $P_{\perp}/P_v < 10^{-3}$ in these cases. This suggests that turbulence becomes increasingly significant as the PT strength increases. For strong PTs ($\alpha = 0.5$), turbulence already exerts an important influence on the hydrodynamical evolution following the PT completion. These findings underscore the importance of perform-

ing fully nonlinear 3D simulations to accurately capture the complex dynamics involved.

All in all, the observed growth of vortical motion and flatter vorticity spectra supports the hypothesis of an energy cascade towards the UV, where the energy dissipates. This conclusion nevertheless requires further investigation in larger-scale simulations.

6.5 Summary and conclusions

6.5.1 GW spectrum template

Ultimately, the utility value of this work lies in the delivery of specific predictions of the GW spectrum and its dependence on the parameters α, v_w, τ_{sw}, and β/H_*. Before proceeding to give an executive summary of this work, I will therefore take the opportunity to compile the main results into a template for the GW spectrum.

To briefly recapitulate, let me reiterate that in the initial part of this Chapter, in Section 6.2.2, we discussed the sound wave-parameterization of the present-day GW spectrum, derived assuming a stationary UETC, in Equation (304),

$$\Omega_{GW}(\tilde{k}) = 3\,\mathcal{T}_{GW}\,\tilde{\Omega}_{GW}\,K^2\,(H_* R_*)(H_*\tilde{t}_{sw})\,S(kR_*)\,,$$

or equivalently as in Equation (305),

$$\mathcal{I}_{sim}(\tilde{t}_*, \tilde{t}_{fin}, \tilde{k}) = \tilde{\Omega}_{GW}\,K^2\,(\beta R_*)\,\tilde{t}_{sw}\,S(kR_*)\,,$$

where $\tilde{t}_{sw} = \tilde{t}_{fin} - \tilde{t}_*$, so that the present-day GW spectrum is expressed in terms of $\mathcal{I}_{sim}$ defined in Equation (301)

$$\Omega_{GW}(k) = 3\,\mathcal{T}_{GW}\left(\frac{H_*}{\beta}\right)^2 \mathcal{I}_{sim}(k)\,. \tag{358}$$

Following the realization that the source kinetic energy in our simulations decays, we generalized the description to that of locally-stationary UETC in Section 6.2.3, thus obtaining the generalized GW spectrum parameterization in Equation (308),

$$\mathcal{I}_{sim}(\tilde{t}_*, \tilde{t}_{fin}, \tilde{k}) = \tilde{\Omega}_{GW}\,K^2_{int}(\tilde{t}_*, \tilde{t}_{fin})\,(\beta R_*)\,S(kR_*)$$

where K^2_{int} is defined in Equation (307), thus replacing the conventional linear scaling $K^2\tilde{t}_{sw}$ with the integrated kinetic energy K^2_{int}. We demonstrated in Section 6.4.6 that this description render the GW efficiency $\tilde{\Omega}_{GW}$ essentially time independent, allowing to robustly measure $\tilde{\Omega}_{GW}$ within the simulations and validate the adequacy of the locally-stationary UETC approach.

In Section 6.4.5, we saw that with high accuracy, the time dependence of kinetic energy can be modeled as power-law decay, Equation (309), so that K^2_{int} can be estimated analytically as in Equation (310) allowing to directly model the measured $\mathcal{I}_{\text{sim}}$ as in Equation (359),

$$\mathcal{I}_{\text{sim}}(\tilde{t}_*, \tilde{t}_{\text{sw}}, \tilde{k}) = \tilde{\Omega}_{\text{GW}}\, K_0^2\, (\beta R_*)\, \tilde{t}_*\, (\tilde{t}_0/\tilde{t}_*)^{2b}\, \frac{(1+\tilde{t}_{\text{sw}}/\tilde{t}_*)^{1-2b}-1}{1-2b} S(kR_*). \tag{359}$$

Then, in Section 6.2.4, we used that the fluid equations of motion are conformally invariant under cosmic expansion to derive a corrected GW amplitude in an attempt to model the effect of cosmic expansion, as in Equation (316),

$$\mathcal{I}_{\text{sim}}(\tilde{\tau}_*, \tilde{\tau}_{\text{fin}}, \tilde{k}) = \tilde{\Omega}_{\text{GW}}\, K^2_{\text{int,exp}}(\tilde{\tau}_*, \tilde{\tau}_{\text{fin}})\, (\beta R_*)\, S(kR_*)$$

where $K^2_{\text{int,exp}}$ is defined in Equation (315). Assuming the power-law decay prescription (309), Equation (316) can be computed explicitly, whereby we obtain expression (321),

$$\mathcal{I}_{\text{sim}}(\tilde{t}_*, \tilde{t}_{\text{fin}}, \tilde{k}) = \tilde{\Omega}_{\text{GW}}\, K_0^2\, \Upsilon_b(\tilde{\tau}_{\text{sw}}) \left(\frac{\beta}{H_*}\right) (\beta R_*)\, S(kR_*)\,,$$

where $\Upsilon_b(\tilde{\tau}_{\text{sw}})$ is defined in Equation (319), and $\tilde{\tau}_{\text{sw}} = \tilde{\tau}_{\text{fin}} - \tilde{\tau}_*$. This expression incorporated all the physics that we aim to model.

As for the numerical values of the parameters α, v_w, τ_{sw}, and β/H_*, we performed a careful analysis of the simulation results including a systematic extrapolation study of the results in Section 6.4.5 incorporating information about the global state of convergence in 6.4.4, aimed at estimating continuum values of the GW production efficiency $\tilde{\Omega}^{\infty}_{\text{GW}}$ as well as the available kinetic energy fraction K_0^{∞}, for which we obtain the plausible estimate $\mathcal{K}_0$ as defined in Equation (333).

We present our numerical finding on the GW efficiency $\tilde{\Omega}_{\text{GW}}$ in Figure 33, which can be summarized as in Equation (340),

$$10^2\, \tilde{\Omega}^{\infty}_{\text{GW}} = \begin{cases} 1.04^{+0.81}_{-0.67}\,, & \text{for} \quad \alpha = 0.0046\,; \\ 1.64^{+0.29}_{-0.13}\,, & \text{for} \quad \alpha = 0.05\,; \\ 3.11^{+0.25}_{-0.19}\,, & \text{for} \quad \alpha = 0.5\,. \end{cases}$$

Our findings on $\mathcal{K}_0$ are presented in Figure 29, which can be summarized as in Equation (335),

$$\mathcal{K}_0 = 0.84^{+0.24}_{-0.29}\, K_\xi\,.$$

As for the source duration $\tilde{\tau}_{\text{sw}}$, we find in Section 6.4.6 that the UETC description works well at least until the end of all simulation runs in

the sense that $\tilde{\Omega}_{\rm GW}$ remains approximately constant, which interestingly implies for strong PTs, $\alpha = 0.5$, that the source duration $\tilde{\tau}_{\rm sw}$ is a factor of at least a few time larger than the otherwise natural cutoff of the source duration $\tilde{t}_{\rm eddy} = \beta R_*/\sqrt{K_\xi}$. We nevertheless leave $\tilde{\tau}_{\rm sw}$ as a free parameter. The remaining parameter β/H_* remains, of course, free for the individual to decide.

With all theoretical and numerical advances outlined, we transcend the realms of the simulations by assuming that the GW efficiency remains constant back until the time of PT completion, $\tilde{t}_0$, and initiate GW production at that point. Then, assuming an arbitrary source duration $\tau_{\rm sw}$, we arrived at one of the main results - a model for the integrated GW spectrum amplitude growth based on our simulation results - in Equation (342),

$$\mathcal{I}^{\rm int}_{\beta/H}(\tilde{t}_0, \tilde{t}_{\rm fin}) = \tilde{\Omega}^{\infty}_{\rm GW}\, \mathcal{K}_0^2\, \Upsilon_b(\tilde{\tau}_{\rm sw}) \left(\frac{\beta}{H_*}\right) (\beta R_*)\,.$$

where now $\tilde{\tau}_{\rm sw} = \tilde{\tau}_{\rm fin} - \tilde{\tau}_0$. Translating this result into a template for the present day GW spectrum, we have that

$$\Omega_{\rm GW}(\tilde{k}) = 3\,\mathcal{I}_{\rm GW}\,\tilde{\Omega}^{\infty}_{\rm GW}\,\mathcal{K}_0^2\,\Upsilon_b(\tilde{\tau}_{\rm sw}) \left(\frac{\beta}{H_*}\right)^{-1} (\beta R_*)\, S(kR_*)\,, \quad (360)$$

where $\beta R_* = (8\pi)^{1/3} \max(v_w, c_s)$ and $S(k\,R_*)$ is the spectral shape.

The spectral shape was studied in detail in Section 6.4.7. In particular, it was discussed in Section 6.4.7.1 that the spectral shape function is a doubly-broken power law with an exponential damping factor in the UV, as described by Equation (343). This exponential damping, however, seems to be related to numerical viscosity. Therefore, the final spectral shape which we propose for modeling the GW spectrum neglects the exponential damping and reads

$$\begin{aligned} &S(k,\, k_1,\, k_2) \\ &= S_0 \times \left(\frac{k}{k_1}\right)^{n_1} \left[1 + \left(\frac{k}{k_1}\right)^{a_1}\right]^{\frac{-n_1+n_2}{a_1}} \left[1 + \left(\frac{k}{k_2}\right)^{a_2}\right]^{\frac{-n_2+n_3}{a_2}}\,, \end{aligned} \quad (361)$$

with $n_1 \simeq 3$, $n_2 \simeq 3$, $a_1 \simeq 3.6$ and $a_2 \simeq 2.4$. The slope of the UV tail is $n_3 \simeq -3$ for weak and intermediate PTs with small wall velocity v_w and somewhat larger for intermediate PTs with larger wall velocity v_w and strong PTs, as reported in Figure 36. Numerical results for the parameters k_1, k_2 are given in Figure 37, which can be summarized as in Equation (346),

$$\frac{k_1\, R_*}{2\pi} \simeq 0.39 \pm 0.11\,,$$

applicable to all PT strengths, and Equation (349),

$$\frac{k_2 R_*}{2\pi} \simeq \begin{cases} 0.49 \pm 0.024/\Delta_w\,, & \alpha = 0.0046\,, \\ 0.93 \pm 0.13\,, & \alpha = 0.05\,, \\ 0.45 \pm 0.042\,, & \alpha = 0.5\,. \end{cases}$$

Finally, the production time wave-numbers $\tilde{k}$ in can be redshifted to the present day frequency as in Equation (169),

$$f_0 = 2.63 \cdot 10^{-6}\,\mathrm{Hz} \times \tilde{k} \left(\frac{\beta}{H_*}\right) \left(\frac{g_*}{100}\right)^{1/6} \left(\frac{T_*}{100\mathrm{GeV}}\right)$$

This compilation thus demonstrates how the results of this Chapter can be used to obtain predictions for the present-day GW spectrum. These predictions are expected to soon be implemented in CosmoGW [166], to promote and facilitate access by the broader community.

6.5.2 Summary

In this Chapter, I have presented a scientific investigation aimed at pushing our understanding of GW production from first-order PTs. The main new results are predictions from strong PTs and a template of the present-day GW spectrum, presented in the previous Section 6.5.1, where I compile the numerical results. Overall, the achievement of this study can be summarized as follows:

1. *Improved simulation setup:* The time integration scheme was improved to reduce artifacts at high wavenumber as compared to the simulation setup in Chapter 5 (Section 6.3.1.1). The mapping of momenta on the lattice to their physical counterpart was updated to a saw-prescription (Section 6.3.1.2), increasing the linear regime as compared to the sin-prescription as well as eliminating the need to consider whether the sign of the wavenumber is important. The numerical stability was improved to accommodate simulations of strong PTs (Section 6.3.1.3) by increasing the maximal local speeds entering the numerical scheme from c_s to 1 and manually reducing energies at isolated grid points to avoid unphysical velocities.

2. *Simulation runs:* I conducted simulations for $\alpha \in \{0.0046, 0.05, 0.5\}$ and wall velocities $v_w \in \{0.32, 0.36, ..., 0.76, 0.8\}$, thus updating results from the previous Chapter 5, while adding strong PTs to the scan. I additionally run simulations utilizing 9 distinct bubble nucleation histories to infer statistical sample

variance for 3 selected v_w, and simulations with only a single centrally nucleated bubble to study the convergence of self-similar profiles. Table 5 summarizes the physical and numerical parameters of the simulations. A total of 1044 simulations were performed. Notably, simulating strong PTs poses significant challenges in terms of numerical stability and the accurate resolution of nonlinearities, but our simulations have demonstrated excellent ability to handle the violent dynamics, demonstrating the remarkable success of the KR+RK3 scheme (207) lying at the core of the Higgsless simulation approach. 2D simulation frames of three examples of strong PT are shown in Figures 25 and 26.

3. *GW production in strong PTs:* For the first time, we present results on the GW amplitude and spectral shape generated by fluid perturbations from strong PTs with $\alpha = 0.5$. Our findings provide strong numerical evidence for the decay of the kinetic energy fraction K over time in intermediate PTs with highly confined profiles and in strong PTs. This decay leads to a significant deviation from the linear growth of the GW amplitude with source duration observed in previous numerical simulations and analytical studies and typically assumed in GW templates in the literature. We attribute this deviation to the decay of K and extend the stationary UETC model to a locally stationary UETC, incorporating the numerically observed decay rate of K over time. Additionally, we have shown that GW production may not cease abruptly when nonlinearities develop; instead, it may continue to increase for an uncertain duration. Consequently, we present our results as a function of the GW source duration.

4. *Convergence Analysis:* We have performed systematic checks to understand the numerical convergence of our results. This has brought detailed understanding of the underestimation of energies associated with insufficient resolution and allowed to extrapolate simulations results closer to their continuum values, thus helping to benefit maximally from the efficiency of our simulations despite rather modest simulation sizes (Section 6.4.3).

5. *Spectral Shape Analysis:* We investigated the spectral shape of the GW power spectrum (Section 6.4.7). We thus introduced the fitting function (343) corresponding to a doubly broken power law. We fitted this function to the data to extract spectral features. The IR knee is strongly related to the maximal correlation length in the system R_* corresponding to the average bubble size at collision. The peak seems related to the thickness of the sound shells, but this connection gradually breaks down as the strength is in-

creased. The IR part of the spectrum is consistent with a k^3 scaling, the intermediate regime as k^1, while the UV tail scales as k^{-n} where $n = 3$ for weak PTs, $n \in [3, 2.5]$ for intermediate and $n \sim 2.6$ for strong. We furthermore observed exponential decay in the far UV, likely caused in part by numerical viscosity.

6. *Sample variance:* We have estimated sample variance in our measurements by running 10 simulations with different bubble nucleation histories for three selected wall velocities for weak, intermediate, and strong PTs, thus allowing us to give alongside results from reference simulations the standard deviation from these 10 nucleation histories. The variance in the measurements is generally quite small, indicating the insensitivity of our results to the sample statistics associated with the construction of bubble nucleation histories assuming an exponentially increasing nucleation probability.

7. *Development of turbulence and nonlinearities:* We have observed various indications of turbulence and nonlinear dynamics, such as shallower UV tails of the GW spectrum in strong PTs and strong damping, which appears unrelated to numerical viscosity. Nonlinear dynamics is firmly established in Section 6.4.9 through the observation of sizable vorticity (Figure 41) and the growing presence of a transverse velocity component in velocity power spectra (Figure 42).

8. *GW spectrum templates:* Finally, in Section 6.5.1, I consolidate the numerical results and provide a template for the present-day GW spectrum. This template is intended for use in future studies and will soon be made accessible via CosmoGW [166], thereby promoting and facilitating access for the broader scientific community.

6.5.3 Conclusion

In this Chapter, we have extended the application of the Higgsless simulations into previously unexplored regimes of strong PTs. The KT+RK3 scheme (207) has once again proven to be highly effective in modeling the nonlinear dynamics, including the presence of shocks and phenomena characterized by large gradients.

Furthermore, we have addressed all the points outlined in Section 5.6.3 of Chapter 5. This study has significantly expanded our understanding of the violent hydrodynamics associated with PTs, providing valuable insights that will guide future research and reinforcing the state-of-the-art predictions concerning GW production.

With the completion of this study, I am confident that the Higgsless simulations are now positioned to become a pivotal tool in advancing our understanding of GW production in PTs, laying the groundwork for future breakthroughs in the field.

7

POSTLUDIUM

At the opening of this thesis, I emphasized that gravitational wave (GW) astronomy is at the forefront of a new scientific frontier, with the potential to revolutionize cosmology and fundamental physics with the detection of a stochastic GW background. As detectors like LIGO, Virgo, PTAs, and the upcoming LISA mission rapidly increase their sensitivity to GWs, the demand for precise and accurate predictions becomes ever more critical. For cosmological sources, this implies detailed predictions of GW spectra, and in this thesis, we focus especially on spectra from first-order phase transitions (PTs). The ability to detect and interpret such signals hinges on the accuracy of our theoretical models, underscoring the importance of the work presented here.

In this thesis, I have made significant contributions toward ensuring that theoretical developments keep pace with experimental advancements. The generation of GWs from first-order PTs has been a central focus, with substantial progress achieved in understanding the hydrodynamical evolution associated with the expanding bubbles and associated GW production. These contributions were made possible through the development and implementation of the novel *Higgsless simulations*, which were employed to provide the physics community with accurate predictions of GW spectra, parameterized by just a few fundamental quantities, allowing to scan large parameter space.

I have accounted for work that has pushed the boundaries of our understanding of first-order PTs and their role in GW production. By extending the Higgsless simulations into previously unexplored regimes of strong PTs, new insights have been gained into the violent hydrodynamics characterizing these events. This is particularly significant because strong PTs produce more intense GW signals, which are more likely to be detected, yet their predictions are challenging due to the strong nonlinear evolution of the fluid. It is precisely in this challenging regime that the Higgsless approach has proven indispensable. It efficiently models the nonlinear dynamics, including shock waves and the development of vorticity, which are crucial for producing realistic GW predictions. This advancement has significantly enhanced the accessibility of GW predictions and established a robust instrument for future research.

In conclusion, the Higgsless simulations developed and applied in this thesis represent a powerful tool for advancing our understanding of GW production in PTs. As these simulations continue to be refined

and applied, they position us to make significant contributions to the field. This thesis, therefore, marks not an end but a beginning, opening new horizons for research that will further illuminate the complex dynamics playing on the strings of space and time.

As we look ahead, there are several important research directions to explore. In this thesis, although I developed the Higgsless simulations to model fluid dynamics, once the simulations were established and the hydrodynamical evolutions obtained, our primary focus shifted to GW production rather than characterizing and analyzing the underlying dynamics. Yet, it is the latter that ultimately governs GW generation. Therefore, it is crucial to take a step back and solidify our understanding of the hydrodynamical evolution. This includes investigating the forward cascade of energy, the development of turbulence, the conditions under which our locally-stationary assumption of the UETC breaks down, and the long-term decay and lifetime of the source. Addressing these fundamental questions could significantly enhance our understanding of the spectral shape evolution, GW amplitude saturation, and the emergence of complex and characteristic features in the GW spectrum.

Additionally, we have observed substantial kinetic energy decay in strong PTs, implying that GW production during the initial collision phase may become increasingly important. In such cases, it is essential to explore the GW evolution until eventual saturation, providing a complete final spectrum that incorporates contributions from sound-shell collisions, long-term evolution of compressional modes, and turbulence.

Ongoing work to integrate the Higgsless approach into the widely-used Pencil Code [167] will enhance its accessibility and applicability. This integration will allow for a more thorough examination of our results and facilitate the exploration of the aforementioned points.

While the Higgsless simulations were specifically designed with PTs in mind, the high-resolution numerical framework employed is capable of solving for the time evolution of any relativistic hydrodynamical system as it has demonstrated exceptional stability even in the presence of shocks, with minimal numerical viscosity. Coupled with its built-in GW solver, this simulation code can be applied to a diverse range of physical scenarios, potentially uncovering new sources of GWs from the early universe.

To ultimately conclude, the space of opportunity that we identified, namely the need for a method to produce accurate and cost-efficient GW predictions while solving for the full nonlinear evolution, has indeed been claimed by the Higgsless simulations. These simulations are now poised to provide the community with increasingly refined predictions, ready in time for the much-anticipated detection of the

cosmological GW background and the transformative impact it will have on modern cosmology.

Part III

APPENDIX

In Appendix A, I comment on the hydrodynamics and gravitational wave production in inverse phase transitions as a response to recent advances in the field.

A

HYDRODYNAMICS AND GRAVITATIONAL WAVES FROM INVERSE PHASE TRANSITIONS

A.1 Introduction

This appendix offers a concise response to the recent publication by Barni *et al.* [168], which investigates the hydrodynamics of inverse PTs. In their study, the authors examine the unique dynamics of inverse PTs, where a system transitions from a deeper minimum of the zero-temperature potential to a higher one, driven solely by thermal corrections. Unlike ordinary PTs, where bubble expansion is facilitated by the release of vacuum energy, inverse PTs involve the bubble expanding against the vacuum energy. The authors identify several expansion modes for these inverse bubbles, noting a mirror symmetry with the modes known for ordinary PTs.

In this appendix, I will engage with their findings using the Higgsless simulations, providing confirmation of their results on self-similar profiles (Section 3.1.6) and, for the first time, obtaining a prediction for the GW production resulting from inverse PTs (Section A.3). For a detailed account of their work, I refer the reader to [168].

A.2 Self-similar profiles of inverse phase transitions

In [168], and in complete analogy to [86], the authors derive self-similar profiles in inverse PTs under the assumptions of the Bag equation of state. For ordinary PTs, the bag constant ϵ is defined as positive in the false vacuum, resulting in a positive strength parameter α. However, for inverse PTs, the situation is reversed, rendering the strength parameter effectively negative. As the Higgsless simulations take α as an input parameter, running simulations of inverse PTs should, in principle, be as simple as choosing $\alpha < 0$, with no further modifications required.

The authors of [168] find the rather curious result that the shape of the self-similar profiles resembles those of ordinary PTs, but in reverse, and with flipped signs on the velocity. Specifically, small wall velocities produce self-similar profiles that resemble inverted detonations, wall velocities larger than the speed of sound but smaller than the Jouguet velocity result in inverted hybrids, and large wall velocities give rise

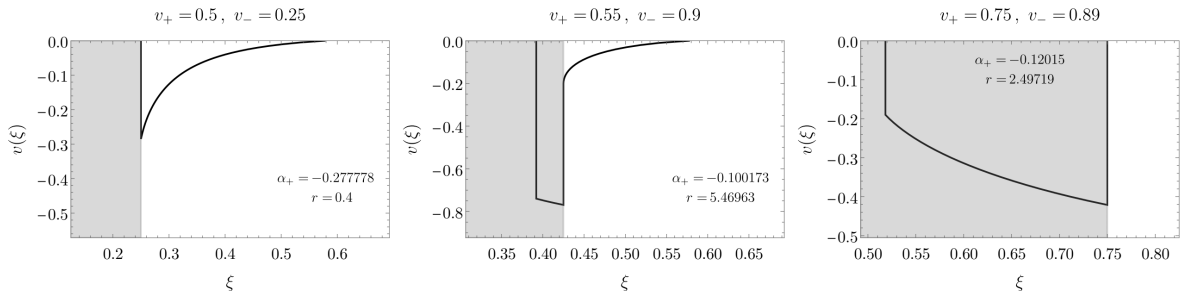

Figure 43: Examples of self-similar velocity profiles for inverse detonations (left), inverse hybrids (middle), and inverse deflagrations (right). This Figure is adopted from [168], to which I refer the reader for details.

to self-similar profiles in the form of inverted deflagrations. For three examples, see Figure 43, which I adopt from [168].

To test the results in [168], I run a single bubble simulation for the parameter point $\alpha = -0.1202$ and $v_w = 0.750$. The convergence towards the theoretical self-similar profile is shown in Figure 44. We see that, indeed, the Higgsless simulations correctly reproduce their result in the limit of convergence. However, there is a brief transitory period before convergence is reached that displays additional features in the solution. Overall, the simulation swiftly converges to their theoretical results, serving as a validation while demonstrating the applicability of the Higgsless simulations in modeling the hydrodynamics also of inverse PTs. I thus proceed to compute the GW spectrum also from inverse PTs.

A.3 Gravitational wave production

For the same parameter point $\alpha = -0.1202$ and $v_w = 0.750$, I run a simulation with multiple bubbles, as in the simulations of Chapter 6, of box size $L/\beta/v_w \equiv \tilde{L}/v_w = 20$ to asses the GW production. In Figure 45, I show an off-center simulation slice of the velocity magnitude and enthalpy field, and in Figure 46, I demonstrate the GW spectrum and its fit. For the fit, and the other reported measurements, I follow the formalism and methodology of Chapter 6, to which I refer the reader for details. For the GW spectrum, I measure a somewhat shallower UV slope of $n_3 = -2.67$ compared to -3. For the extrapolated GW efficiency, I measure $\tilde{\Omega}_{GW}^{\infty} = 0.0217$, with a relative error of 8% compared to the highest resolution simulation $N = 512$, based on a series of simulations with $N \in \{64, 128, 256, 512\}$. Overall, there appears to be no characteristic smoking gun feature in the GW production of inverse PTs based on this one parameter point alone, as is, perhaps ex-

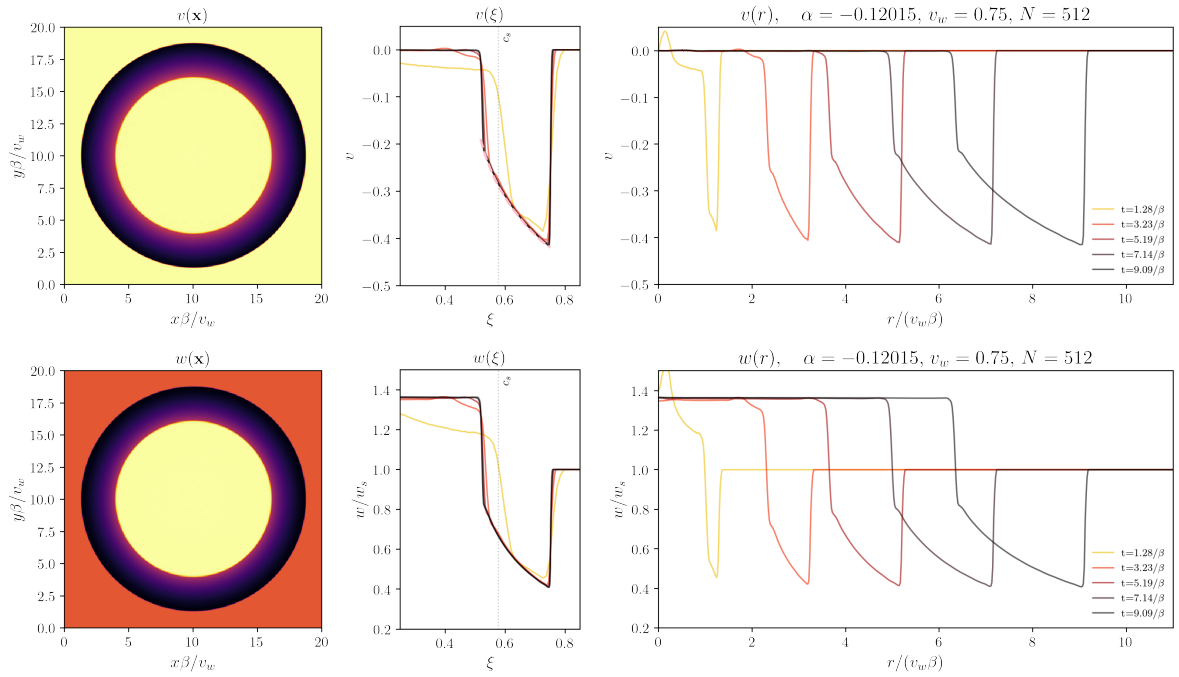

Figure 44: Convergence towards the self-similar fluid profile for an inverse deflagration for $v_w = 0.75$ and $\alpha = -0.1202$. The pink dashed line for the self-similar velocity profiles is taken from [168] for the same parameters.

pected by virtue of its similar sound-wave nature. Future studies are needed to verify this statement.

This final endeavor concludes the new scientific material of the thesis.

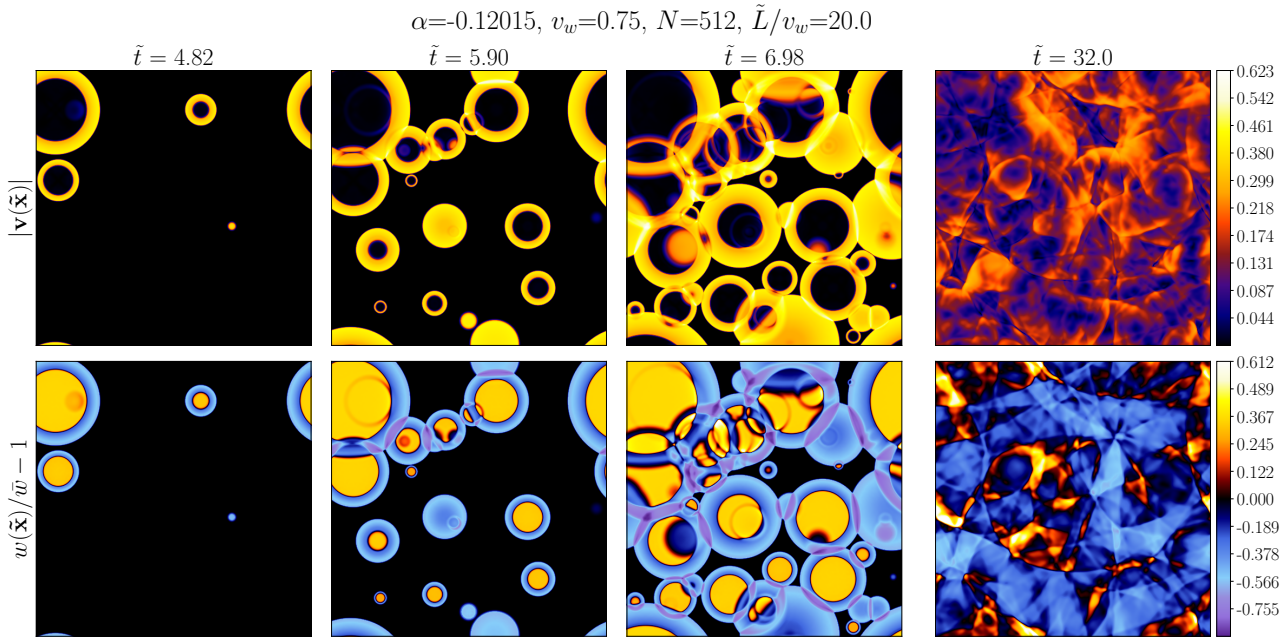

Figure 45: Off-central 2D simulation slices for an inverse-deflagration of the fluid velocity amplitude $|\mathbf{v}(\tilde{\mathbf{x}})|$ (upper panel), and enthalpy $w(\tilde{\mathbf{x}})$ (lower panel). The wall velocity is $v_w = 0.75$ and the strength $\alpha = -0.1202$ ($\tilde{x} \equiv x/\beta$). The resolution is $N = 512$, and the box size $\tilde{L}/v_w = 20$. The first three slices are chosen at equidistant times to show the bubble evolution before PT completion, while the fourth slice is at the end of the simulation to display the long-term behavior.

BIBLIOGRAPHY

[1] Ryusuke Jinno, Thomas Konstandin, Henrique Rubira, and Isak Stomberg. "Higgsless simulations of cosmological phase transitions and gravitational waves." In: *JCAP* 02 (2023), p. 011. DOI: 10.1088/1475-7516/2023/02/011. arXiv: 2209.04369 [astro-ph.CO].

[2] Simone Blasi, Ryusuke Jinno, Thomas Konstandin, Henrique Rubira, and Isak Stomberg. "Gravitational waves from defect-driven phase transitions: domain walls." In: *JCAP* 10 (2023), p. 051. DOI: 10.1088/1475-7516/2023/10/051. arXiv: 2302.06952 [astro-ph.CO].

[3] Chiara Caprini, Ryusuke Jinno, Thomas Konstandin, Alberto Roper Pol, Henrique Rubira, and Isak Stomberg. *Gravitational waves from decaying sources in strong phase transitions*. 2024. arXiv:

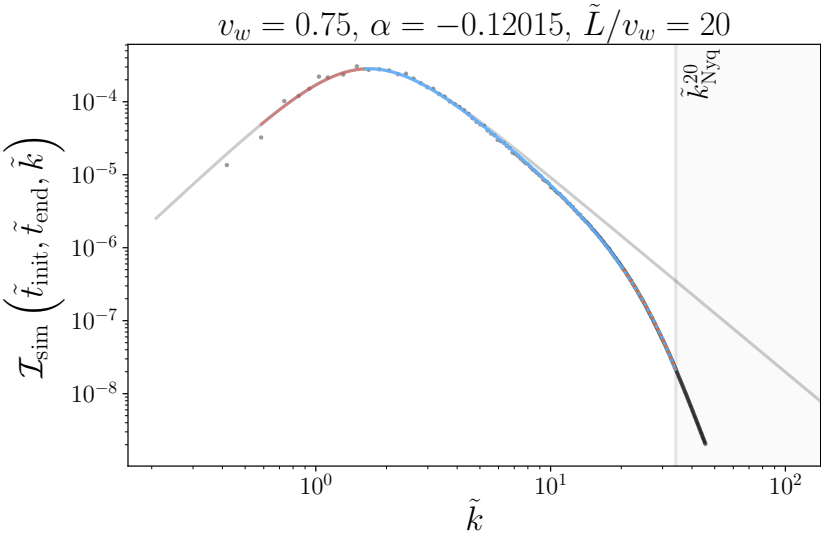

Figure 46: Fit of equation (345) to GW spectrum data for the inverse deflagration with $v_w = 0.75$ and strength $\alpha = -0.1202$. The color transition between red-blue marks the peak k_2, which in this example is equal to k_1, i.e., $k_1 = k_2$, as the sound shell thickness is rather thick and with, correspondingly, no separation of scales leading to an intermediate regime of linear scaling. The start location of dashed orange lines marks the scale k_e where exponential damping begins to dominate. Colored regions demarcate the range of wavenumber used for the fit, whereas transparent gray indicates the fitted function excluding exponential damping.

2409.03651 [gr-qc]. URL: https://arxiv.org/abs/2409.03651.

[4] Dario Grasso and Hector R. Rubinstein. "Magnetic fields in the early universe." In: *Phys. Rept.* 348 (2001), pp. 163–266. DOI: 10.1016/S0370-1573(00)00110-1. arXiv: astro-ph/0009061.

[5] T. Vachaspati. "Magnetic fields from cosmological phase transitions." In: *Phys. Lett. B* 265 (1991), pp. 258–261. DOI: 10.1016/0370-2693(91)90051-Q.

[6] V. A. Kuzmin, V. A. Rubakov, and M. E. Shaposhnikov. "On the Anomalous Electroweak Baryon Number Nonconservation in the Early Universe." In: *Phys. Lett. B* 155 (1985), p. 36. DOI: 10.1016/0370-2693(85)91028-7.

[7] Andrew G. Cohen, D. B. Kaplan, and A. E. Nelson. "Progress in electroweak baryogenesis." In: *Ann. Rev. Nucl. Part. Sci.* 43 (1993), pp. 27–70. DOI: 10.1146/annurev.ns.43.120193.000331. arXiv: hep-ph/9302210.

[8] V. A. Rubakov and M. E. Shaposhnikov. "Electroweak baryon number nonconservation in the early universe and in high-energy collisions." In: *Usp. Fiz. Nauk* 166 (1996), pp. 493–537. DOI: 10.1070/PU1996v039n05ABEH000145. arXiv: hep-ph/9603208.

[9] Antonio Riotto and Mark Trodden. "Recent progress in baryogenesis." In: *Ann. Rev. Nucl. Part. Sci.* 49 (1999), pp. 35–75. DOI: 10.1146/annurev.nucl.49.1.35. arXiv: hep-ph/9901362.

[10] David E. Morrissey and Michael J. Ramsey-Musolf. "Electroweak baryogenesis." In: *New J. Phys.* 14 (2012), p. 125003. DOI: 10.1088/1367-2630/14/12/125003. arXiv: 1206.2942 [hep-ph].

[11] Michael J. Baker, Moritz Breitbach, Joachim Kopp, and Lukas Mittnacht. "Primordial Black Holes from First-Order Cosmological Phase Transitions." In: (May 2021). arXiv: 2105.07481 [astro-ph.CO].

[12] Karsten Jedamzik. "Primordial black hole formation during cosmic phase transitions." In: (June 2024). arXiv: 2406.11417 [astro-ph.CO].

[13] Rong-Gen Cai, Yu-Shi Hao, and Shao-Jiang Wang. "Primordial black holes and curvature perturbations from false vacuum islands." In: *Sci. China Phys. Mech. Astron.* 67.9 (2024), p. 290411. DOI: 10.1007/s11433-024-2416-3. arXiv: 2404.06506 [astro-ph.CO].

[14] Edward Witten. "Cosmic Separation of Phases." In: *Phys. Rev. D* 30 (1984), pp. 272–285. DOI: 10.1103/PhysRevD.30.272.

[15] C. J. Hogan. "Gravitational radiation from cosmological phase transitions." In: *Mon. Not. Roy. Astron. Soc.* 218 (1986), pp. 629–636.

[16] Sidney R. Coleman. "The Fate of the False Vacuum. 1. Semiclassical Theory." In: *Phys. Rev. D* 15 (1977). [Erratum: Phys.Rev.D 16, 1248 (1977)], pp. 2929–2936. DOI: 10.1103/PhysRevD.16.1248.

[17] Andrei D. Linde. "Fate of the False Vacuum at Finite Temperature: Theory and Applications." In: *Phys. Lett. B* 100 (1981), pp. 37–40. DOI: 10.1016/0370-2693(81)90281-1.

[18] Paul Joseph Steinhardt. "Relativistic Detonation Waves and Bubble Growth in False Vacuum Decay." In: *Phys. Rev. D* 25 (1982), p. 2074. DOI: 10.1103/PhysRevD.25.2074.

[19] Arthur Kosowsky, Michael S. Turner, and Richard Watkins. "Gravitational radiation from colliding vacuum bubbles." In: *Phys. Rev.* D45 (1992), pp. 4514–4535. DOI: 10.1103/PhysRevD.45.4514.

[20] Arthur Kosowsky, Michael S. Turner, and Richard Watkins. "Gravitational waves from first order cosmological phase transitions." In: *Phys. Rev. Lett.* 69 (1992), pp. 2026–2029. DOI: 10.1103/PhysRevLett.69.2026.

[21] Arthur Kosowsky and Michael S. Turner. "Gravitational radiation from colliding vacuum bubbles: envelope approximation to many bubble collisions." In: *Phys. Rev.* D47 (1993), pp. 4372–4391. DOI: 10.1103/PhysRevD.47.4372. arXiv: astro-ph/9211004 [astro-ph].

[22] Marc Kamionkowski, Arthur Kosowsky, and Michael S. Turner. "Gravitational radiation from first order phase transitions." In: *Phys. Rev. D* 49 (1994), pp. 2837–2851. DOI: 10.1103/PhysRevD.49.2837. arXiv: astro-ph/9310044.

[23] Stephan J. Huber and Thomas Konstandin. "Gravitational Wave Production by Collisions: More Bubbles." In: *JCAP* 0809 (2008), p. 022. DOI: 10.1088/1475-7516/2008/09/022. arXiv: 0806.1828 [hep-ph].

[24] Thomas Konstandin. "Gravitational radiation from a bulk flow model." In: *JCAP* 1803.03 (2018), p. 047. DOI: 10.1088/1475-7516/2018/03/047. arXiv: 1712.06869 [astro-ph.CO].

[25] Mark Hindmarsh, Stephan J. Huber, Kari Rummukainen, and David J. Weir. "Gravitational waves from the sound of a first order phase transition." In: *Phys. Rev. Lett.* 112 (2014), p. 041301. DOI: 10.1103/PhysRevLett.112.041301. arXiv: 1304.2433 [hep-ph].

[26] Michela D'Onofrio and Kari Rummukainen. "Standard model cross-over on the lattice." In: *Phys. Rev. D* 93.2 (2016), p. 025003. DOI: 10.1103/PhysRevD.93.025003. arXiv: 1508.07161 [hep-ph].

[27] K. Kajantie, M. Laine, K. Rummukainen, and Mikhail E. Shaposhnikov. "Is there a hot electroweak phase transition at $m_H \gtrsim m_W$?" In: *Phys. Rev. Lett.* 77 (1996), pp. 2887–2890. DOI: 10.1103/PhysRevLett.77.2887. arXiv: hep-ph/9605288.

[28] M. Gurtler, Ernst-Michael Ilgenfritz, and A. Schiller. "Where the electroweak phase transition ends." In: *Phys. Rev. D* 56 (1997), pp. 3888–3895. DOI: 10.1103/PhysRevD.56.3888. arXiv: hep-lat/9704013.

[29] F. Csikor, Z. Fodor, and J. Heitger. "Endpoint of the hot electroweak phase transition." In: *Phys. Rev. Lett.* 82 (1999), pp. 21–24. DOI: 10.1103/PhysRevLett.82.21. arXiv: hep-ph/9809291.

[30] James M. Cline, Kimmo Kainulainen, and Michael Trott. "Electroweak Baryogenesis in Two Higgs Doublet Models and B meson anomalies." In: *JHEP* 11 (2011), p. 089. DOI: 10.1007/JHEP11(2011)089. arXiv: 1107.3559 [hep-ph].

[31] Amine Ahriche. "What is the criterion for a strong first order electroweak phase transition in singlet models?" In: *Phys. Rev. D* 75 (2007), p. 083522. DOI: 10.1103/PhysRevD.75.083522. arXiv: hep-ph/0701192.

[32] Y. Aoki, G. Endrodi, Z. Fodor, S. D. Katz, and K. K. Szabo. "The Order of the quantum chromodynamics transition predicted by the standard model of particle physics." In: *Nature* 443 (2006), pp. 675–678. DOI: 10.1038/nature05120. arXiv: hep-lat/0611014.

[33] Tillmann Boeckel, Simon Schettler, and Jürgen Schaffner-Bielich. "The cosmological QCD phase transition revisited." In: *Progress in Particle and Nuclear Physics* 66.2 (Apr. 2011), 266–270. ISSN: 0146-6410. DOI: 10.1016/j.ppnp.2011.01.017. URL: http://dx.doi.org/10.1016/j.ppnp.2011.01.017.

[34] Gaoqing Cao. "First-order QCD transition in a primordial magnetic field." In: *Phys. Rev. D* 107.1 (2023), p. 014021. DOI: 10.1103/PhysRevD.107.014021. arXiv: 2210.09794 [nucl-th].

[35] Pedro Schwaller. "Gravitational Waves from a Dark Phase Transition." In: *Phys. Rev. Lett.* 115.18 (2015), p. 181101. DOI: 10.1103/PhysRevLett.115.181101. arXiv: 1504.07263 [hep-ph].

[36] Chiara Caprini and Daniel G. Figueroa. "Cosmological Backgrounds of Gravitational Waves." In: *Class. Quant. Grav.* 35.16 (2018), p. 163001. DOI: 10.1088/1361-6382/aac608. arXiv: 1801.04268 [astro-ph.CO].

[37] B.P. Abbott et al. "Observation of Gravitational Waves from a Binary Black Hole Merger." In: *Physical Review Letters* 116.6 (2016), p. 061102.

[38] B. P. Abbott et al. "GW151226: Observation of Gravitational Waves from a 22-Solar-Mass Binary Black Hole Coalescence." In: *Phys. Rev. Lett.* 116.24 (2016), p. 241103. DOI: 10.1103/PhysRevLett.116.241103. arXiv: 1606.04855 [gr-qc].

[39] B. P. Abbott et al. "GW170817: Observation of Gravitational Waves from a Binary Neutron Star Inspiral." In: *Phys. Rev. Lett.* 119.16 (2017), p. 161101. DOI: 10.1103/PhysRevLett.119.161101. arXiv: 1710.05832 [gr-qc].

[40] R. Abbott et al. "GWTC-3: Compact Binary Coalescences Observed by LIGO and Virgo during the Second Part of the Third Observing Run." In: *Phys. Rev. X* 13.4 (2023), p. 041039. DOI: 10.1103/PhysRevX.13.041039. arXiv: 2111.03606 [gr-qc].

[41] J. Antoniadis et al. "The second data release from the European Pulsar Timing Array - III. Search for gravitational wave signals." In: *Astron. Astrophys.* 678 (2023), A50. DOI: 10.1051/0004-6361/202346844. arXiv: 2306.16214 [astro-ph.HE].

[42] Gabriella Agazie et al. "The NANOGrav 15 yr Data Set: Evidence for a Gravitational-wave Background." In: *Astrophys. J. Lett.* 951.1 (2023), p. L8. DOI: 10.3847/2041-8213/acdac6. arXiv: 2306.16213 [astro-ph.HE].

[43] Daniel J. Reardon et al. "Search for an Isotropic Gravitational-wave Background with the Parkes Pulsar Timing Array." In: *Astrophys. J. Lett.* 951.1 (2023), p. L6. DOI: 10.3847/2041-8213/acdd02. arXiv: 2306.16215 [astro-ph.HE].

[44] Heng Xu et al. "Searching for the Nano-Hertz Stochastic Gravitational Wave Background with the Chinese Pulsar Timing Array Data Release I." In: *Res. Astron. Astrophys.* 23.7 (2023), p. 075024. DOI: 10.1088/1674-4527/acdfa5. arXiv: 2306.16216 [astro-ph.HE].

[45] J. Antoniadis et al. "The second data release from the European Pulsar Timing Array: IV. Implications for massive black holes, dark matter and the early Universe." In: (June 2023). arXiv: 2306.16227 [astro-ph.CO].

[46] Adeela Afzal et al. "The NANOGrav 15 yr Data Set: Search for Signals from New Physics." In: *Astrophys. J. Lett.* 951.1 (2023), p. L11. DOI: 10.3847/2041-8213/acdc91. arXiv: 2306.16219 [astro-ph.HE].

[47] Pau Amaro-Seoane et al. "Laser Interferometer Space Antenna." In: (Feb. 2017). arXiv: 1702.00786 [astro-ph.IM].

[48] Pau Amaro Seoane et al. "The Gravitational Universe." In: (May 2013). arXiv: 1305.5720 [astro-ph.CO].

[49] Pierre Auclair et al. "Cosmology with the Laser Interferometer Space Antenna." In: (Apr. 2022). arXiv: 2204.05434 [astro-ph.CO].

[50] Guillaume Boileau, Nelson Christensen, Chloe Gowling, Mark Hindmarsh, and Renate Meyer. "Prospects for LISA to detect a gravitational-wave background from first order phase transitions." In: *JCAP* 02 (2023), p. 056. DOI: 10.1088/1475-7516/2023/02/056. arXiv: 2209.13277 [gr-qc].

[51] Kai Schmitz. "New Sensitivity Curves for Gravitational-Wave Signals from Cosmological Phase Transitions." In: *JHEP* 01 (2021), p. 097. DOI: 10.1007/JHEP01(2021)097. arXiv: 2002.04615 [hep-ph].

[52] Chiara Caprini et al. "Detecting gravitational waves from cosmological phase transitions with LISA: an update." In: *JCAP* 03 (2020), p. 024. DOI: 10.1088/1475-7516/2020/03/024. arXiv: 1910.13125 [astro-ph.CO].

[53] B. P. Abbott et al. "GWTC-1: A Gravitational-Wave Transient Catalog of Compact Binary Mergers Observed by LIGO and Virgo during the First and Second Observing Runs." In: *Phys. Rev. X* 9.3 (2019), p. 031040. DOI: 10.1103/PhysRevX.9.031040. arXiv: 1811.12907 [astro-ph.HE].

[54] R. Abbott et al. "GW190521: A Binary Black Hole Merger with a Total Mass of $150M_{\odot}$." In: *Phys. Rev. Lett.* 125.10 (2020), p. 101102. DOI: 10.1103/PhysRevLett.125.101102. arXiv: 2009.01075 [gr-qc].

[55] B. P. Abbott et al. "Gravitational Waves and Gamma-Rays from a Binary Neutron Star Merger: GW170817 and GRB 170817A." In: *The Astrophysical Journal Letters* 848.2 (Oct. 2017), p. L13. ISSN: 2041-8213. DOI: 10.3847/2041-8213/aa920c. URL: http://dx.doi.org/10.3847/2041-8213/aa920c.

[56] B. P. Abbott et al. "A gravitational-wave standard siren measurement of the Hubble constant." In: *Nature* 551.7678 (2017), pp. 85–88. DOI: 10.1038/nature24471. arXiv: 1710.05835 [astro-ph.CO].

[57] Edward W. Kolb. *The Early Universe*. Vol. 69. Taylor and Francis, May 2019. ISBN: 978-0-429-49286-0, 978-0-201-62674-2. DOI: 10.1201/9780429492860.

[58] Michele Maggiore. "Gravitational wave experiments and early universe cosmology." In: *Phys. Rept.* 331 (2000), pp. 283–367. DOI: 10.1016/S0370-1573(99)00102-7. arXiv: gr-qc/9909001.

[59] Chiara Caprini and Daniel G. Figueroa. "Cosmological Backgrounds of Gravitational Waves." In: *Class. Quant. Grav.* 35.16 (2018), p. 163001. DOI: 10.1088/1361-6382/aac608. arXiv: 1801.04268 [astro-ph.CO].

[60] Michele Maggiore. *Gravitational Waves. Vol. 1: Theory and Experiments*. Oxford University Press, 2007. ISBN: 978-0-19-171766-6, 978-0-19-852074-0. DOI: 10.1093/acprof:oso/9780198570745.001.0001.

[61] Michele Maggiore. *Gravitational Waves. Vol. 2: Astrophysics and Cosmology*. Oxford University Press, Mar. 2018. ISBN: 978-0-19-857089-9.

[62] Steven Weinberg. *Gravitation and Cosmology: Principles and Applications of the General Theory of Relativity*. New York: John Wiley and Sons, 1972. ISBN: 978-0-471-92567-5, 978-0-471-92567-5.

[63] Ruth Durrer. *The Cosmic Microwave Background*. Cambridge: Cambridge University Press, 2008. ISBN: 978-0-511-81720-5. DOI: 10.1017/CBO9780511817205.

[64] C. Patrignani et al. "Review of Particle Physics." In: *Chin. Phys. C* 40.10 (2016), p. 100001. DOI: 10.1088/1674-1137/40/10/100001.

[65] Edward W. Kolb and Michael S. Turner. *The Early Universe*. Vol. 69. 1990. ISBN: 978-0-201-62674-2. DOI: 10.1201/9780429492860.

[66] *2. ASTROPHYSICAL CONSTANTS AND PARAMETERS*. 2013.

[67] Ryusuke Jinno, Thomas Konstandin, and Henrique Rubira. "A hybrid simulation of gravitational wave production in first-order phase transitions." In: *JCAP* 04 (2021), p. 014. DOI: 10.1088/1475-7516/2021/04/014. arXiv: 2010.00971 [astro-ph.CO].

[68] Ryusuke Jinno, Thomas Konstandin, Henrique Rubira, and Jorinde van de Vis. "Effect of density fluctuations on gravitational wave production in first-order phase transitions." In: *JCAP* 12.12 (2021), p. 019. DOI: 10.1088/1475-7516/2021/12/019. arXiv: 2108.11947 [astro-ph.CO].

[69] Mark Hindmarsh, Stephan J. Huber, Kari Rummukainen, and David J. Weir. "Numerical simulations of acoustically generated gravitational waves at a first order phase transition." In: *Phys. Rev.* D92.12 (2015), p. 123009. DOI: 10.1103/PhysRevD.92.123009. arXiv: 1504.03291 [astro-ph.CO].

[70] Mark Hindmarsh. "Sound shell model for acoustic gravitational wave production at a first-order phase transition in the early Universe." In: *Phys. Rev. Lett.* 120.7 (2018), p. 071301. DOI: 10.1103/PhysRevLett.120.071301. arXiv: 1608.04735 [astro-ph.CO].

[71] Mark Hindmarsh, Stephan J. Huber, Kari Rummukainen, and David J. Weir. "Shape of the acoustic gravitational wave power spectrum from a first order phase transition." In: (2017). arXiv: 1704.05871 [astro-ph.CO].

[72] Mark Hindmarsh and Mulham Hijazi. "Gravitational waves from first order cosmological phase transitions in the Sound Shell Model." In: *JCAP* 1912 (2019), p. 062. DOI: 10.1088/1475-7516/2019/12/062. arXiv: 1909.10040 [astro-ph.CO].

[73] Alberto Roper Pol, Simona Procacci, and Chiara Caprini. "Characterization of the gravitational wave spectrum from sound waves within the sound shell model." In: *Phys. Rev. D* 109.6 (2024), p. 063531. DOI: 10.1103/PhysRevD.109.063531. arXiv: 2308.12943 [gr-qc].

[74] Ramkishor Sharma, Jani Dahl, Axel Brandenburg, and Mark Hindmarsh. "Shallow relic gravitational wave spectrum with acoustic peak." In: *JCAP* 12 (2023), p. 042. DOI: 10.1088/1475-7516/2023/12/042. arXiv: 2308.12916 [gr-qc].

[75] Arthur Kosowsky, Andrew Mack, and Tinatin Kahniashvili. "Gravitational radiation from cosmological turbulence." In: *Phys. Rev. D* 66 (2002), p. 024030. DOI: 10.1103/PhysRevD.66.024030. arXiv: astro-ph/0111483.

[76] Chiara Caprini, Ruth Durrer, Thomas Konstandin, and Geraldine Servant. "General Properties of the Gravitational Wave Spectrum from Phase Transitions." In: *Phys. Rev. D* 79 (2009), p. 083519. DOI: 10.1103/PhysRevD.79.083519. arXiv: 0901.1661 [astro-ph.CO].

[77] Peter Niksa, Martin Schlederer, and Günter Sigl. "Gravitational Waves produced by Compressible MHD Turbulence from Cosmological Phase Transitions." In: *Class. Quant. Grav.* 35.14 (2018), p. 144001. DOI: 10.1088/1361-6382/aac89c. arXiv: 1803.02271 [astro-ph.CO].

[78] Huai-Ke Guo, Kuver Sinha, Daniel Vagie, and Graham White. "Phase Transitions in an Expanding Universe: Stochastic Gravitational Waves in Standard and Non-Standard Histories." In: *JCAP* 01 (2021), p. 001. DOI: 10.1088/1475-7516/2021/01/001. arXiv: 2007.08537 [hep-ph].

[79] Chiara Caprini, Oriol Pujolàs, Hippolyte Quelquejay-Leclere, Fabrizio Rompineve, and Danièle A. Steer. "Primordial gravitational wave backgrounds from phase transitions with next generation ground based detectors." In: (June 2024). arXiv: 2406.02359 [astro-ph.CO].

[80] L. D. Landau and E. M. Lifshitz. *Fluid Mechanics*. Second. Vol. 6. Course of Theoretical Physics. Pergamon, 1987. URL: http://www.worldcat.org/isbn/9781483161044.

[81] A. Roper Pol, A. Neronov, C. Caprini, T. Boyer, and D. Semikoz. "LISA and γ-ray telescopes as multi-messenger probes of a first-order cosmological phase transition." In: (July 2023). arXiv: 2307.10744 [astro-ph.CO].

[82] Chiara Caprini, Ryusuke Jinno, Marek Lewicki, Eric Madge, Marco Merchand, Germano Nardini, Mauro Pieroni, Alberto Roper Pol, and Ville Vaskonen. "Gravitational waves from first-order phase transitions in LISA: reconstruction pipeline and physics interpretation." In: (Mar. 2024). arXiv: 2403.03723 [astro-ph.CO].

[83] Sidney R. Coleman and Erick J. Weinberg. "Radiative Corrections as the Origin of Spontaneous Symmetry Breaking." In: *Phys. Rev. D* 7 (1973), pp. 1888–1910. DOI: 10.1103/PhysRevD.7.1888.

[84] Cedric Delaunay, Christophe Grojean, and James D. Wells. "Dynamics of Non-renormalizable Electroweak Symmetry Breaking." In: *JHEP* 04 (2008), p. 029. DOI: 10.1088/1126-6708/2008/04/029. arXiv: 0711.2511 [hep-ph].

[85] Alan H. Guth and Erick J. Weinberg. "Cosmological Consequences of a First Order Phase Transition in the SU(5) Grand Unified Model." In: *Phys. Rev. D* 23 (1981), p. 876. DOI: 10.1103/PhysRevD.23.876.

[86] Jose R. Espinosa, Thomas Konstandin, Jose M. No, and Geraldine Servant. "Energy Budget of Cosmological First-order Phase Transitions." In: *JCAP* 06 (2010), p. 028. DOI: 10.1088/1475-7516/2010/06/028. arXiv: 1004.4187 [hep-ph].

[87] A. Chodos, R. L. Jaffe, K. Johnson, Charles B. Thorn, and V. F. Weisskopf. "A New Extended Model of Hadrons." In: *Phys. Rev. D* 9 (1974), pp. 3471–3495. DOI: 10.1103/PhysRevD.9.3471.

[88] Felix Giese, Thomas Konstandin, and Jorinde van de Vis. "Model-independent energy budget of cosmological first-order phase transitions: A sound argument to go beyond the bag model." In: *JCAP* 07.07 (2020), p. 057. DOI: 10.1088/1475-7516/2020/07/057. arXiv: 2004.06995 [astro-ph.CO].

[89] Felix Giese, Thomas Konstandin, Kai Schmitz, and Jorinde Van De Vis. "Model-independent energy budget for LISA." In: (2020). arXiv: 2010.09744 [astro-ph.CO].

[90] Guy D. Moore and Tomislav Prokopec. "How fast can the wall move? A Study of the electroweak phase transition dynamics." In: *Phys. Rev. D* 52 (1995), pp. 7182–7204. DOI: 10.1103/PhysRevD.52.7182. arXiv: hep-ph/9506475.

[91] Guy D. Moore and Tomislav Prokopec. "Bubble wall velocity in a first order electroweak phase transition." In: *Phys. Rev. Lett.* 75 (1995), pp. 777–780. DOI: 10.1103/PhysRevLett.75.777. arXiv: hep-ph/9503296.

[92] Chiara Caprini and Ruth Durrer. "Gravitational waves from stochastic relativistic sources: Primordial turbulence and magnetic fields." In: *Phys. Rev. D* 74 (2006), p. 063521. DOI: 10.1103/PhysRevD.74.063521. arXiv: astro-ph/0603476.

[93] Grigol Gogoberidze, Tina Kahniashvili, and Arthur Kosowsky. "The Spectrum of Gravitational Radiation from Primordial Turbulence." In: *Phys. Rev. D* 76 (2007), p. 083002. DOI: 10.1103/PhysRevD.76.083002. arXiv: 0705.1733 [astro-ph].

[94] Chiara Caprini, Ruth Durrer, and Geraldine Servant. "The stochastic gravitational wave background from turbulence and magnetic fields generated by a first-order phase transition." In: *JCAP* 12 (2009), p. 024. DOI: 10.1088/1475-7516/2009/12/024. arXiv: 0909.0622 [astro-ph.CO].

[95] Alberto Roper Pol, Sayan Mandal, Axel Brandenburg, Tina Kahniashvili, and Arthur Kosowsky. "Numerical simulations of gravitational waves from early-universe turbulence." In: *Phys. Rev. D* 102.8 (2020), p. 083512. DOI: 10.1103/PhysRevD.102.083512. arXiv: 1903.08585 [astro-ph.CO].

[96] Alberto Roper Pol, Chiara Caprini, Andrii Neronov, and Dmitri Semikoz. "Gravitational wave signal from primordial magnetic fields in the Pulsar Timing Array frequency band." In: *Phys. Rev. D* 105.12 (2022), p. 123502. DOI: 10.1103/PhysRevD.105.123502. arXiv: 2201.05630 [astro-ph.CO].

[97] Chiara Caprini et al. "Science with the space-based interferometer eLISA. II: Gravitational waves from cosmological phase transitions." In: *JCAP* 04 (2016), p. 001. DOI: 10.1088/1475-7516/2016/04/001. arXiv: 1512.06239 [astro-ph.CO].

[98] Ryusuke Jinno and Masahiro Takimoto. "Gravitational waves from bubble collisions: An analytic derivation." In: *Phys. Rev.* D95.2 (2017), p. 024009. DOI: 10.1103/PhysRevD.95.024009. arXiv: 1605.01403 [astro-ph.CO].

[99] Ryusuke Jinno and Masahiro Takimoto. "Gravitational waves from bubble dynamics: Beyond the Envelope." In: *JCAP* 1901 (2019), p. 060. DOI: 10.1088/1475-7516/2019/01/060. arXiv: 1707.03111 [hep-ph].

[100] Daniel Cutting, Mark Hindmarsh, and David J. Weir. "Gravitational waves from vacuum first-order phase transitions: from the envelope to the lattice." In: *Phys. Rev. D* 97.12 (2018), p. 123513. DOI: 10.1103/PhysRevD.97.123513. arXiv: 1802.05712 [astro-ph.CO].

[101] Daniel Cutting, Mark Hindmarsh, and David J. Weir. "Vorticity, kinetic energy, and suppressed gravitational wave production in strong first order phase transitions." In: *Phys. Rev. Lett.* 125.2 (2020), p. 021302. DOI: 10.1103/PhysRevLett.125.021302. arXiv: 1906.00480 [hep-ph].

[102] Yu-Mei Wu, Zu-Cheng Chen, and Qing-Guo Huang. "Cosmological interpretation for the stochastic signal in pulsar timing arrays." In: *Sci. China Phys. Mech. Astron.* 67.4 (2024), p. 240412. DOI: 10.1007/s11433-023-2298-7. arXiv: 2307.03141 [astro-ph.CO].

[103] Katherine Freese and Martin Wolfgang Winkler. "Have pulsar timing arrays detected the hot big bang: Gravitational waves from strong first order phase transitions in the early Universe." In: *Phys. Rev. D* 106.10 (2022), p. 103523. DOI: 10.1103/PhysRevD.106.103523. arXiv: 2208.03330 [astro-ph.CO].

[104] Gemma Janssen et al. "Gravitational wave astronomy with the SKA." In: *PoS* AASKA14 (2015). Ed. by Tyler L. Bourke et al., p. 037. DOI: 10.22323/1.215.0037. arXiv: 1501.00127 [astro-ph.IM].

[105] Felix Giese, Thomas Konstandin, and Jorinde van de Vis. "Finding sound shells in LISA mock data using likelihood sampling." In: *JCAP* 11 (2021), p. 002. DOI: 10.1088/1475-7516/2021/11/002. arXiv: 2107.06275 [astro-ph.CO].

[106] Chloe Gowling and Mark Hindmarsh. "Observational prospects for phase transitions at LISA: Fisher matrix analysis." In: *JCAP* 10 (2021), p. 039. DOI: 10.1088/1475-7516/2021/10/039. arXiv: 2106.05984 [astro-ph.CO].

[107] Stefanie Kroker and Ronny Nawrodt. "The Einstein telescope." In: *IEEE Instrum. Measur. Mag.* 18.3 (2015), pp. 4–8. DOI: 10.1109/MIM.2015.7108211.

[108] G. M. Harry, P. Fritschel, D. A. Shaddock, W. Folkner, and E. S. Phinney. "Laser interferometry for the big bang observer." In: *Class. Quant. Grav.* 23 (2006). [Erratum: Class.Quant.Grav. 23, 7361 (2006)], pp. 4887–4894. DOI: 10.1088/0264-9381/23/15/008.

[109] Shuo Cao, Tonghua Liu, Marek Biesiada, Yuting Liu, Wuzheng Guo, and Zong-Hong Zhu. "DECi-hertz Interferometer Gravitational-wave Observatory: Forecast Constraints on the Cosmic Curvature with LSST Strong Lenses." In: *Astrophys. J.* 926.2 (2022), p. 214. DOI: 10.3847/1538-4357/ac4256. arXiv: 2112.00237 [astro-ph.CO].

[110] Peter D. Lax. "Weak solutions of nonlinear hyperbolic equations and their numerical computation." In: *Communications on Pure and Applied Mathematics* 7.1 (1954), pp. 159–193. DOI: https://doi.org/10.1002/cpa.3160070112. eprint: https://onlinelibrary.wiley.com/doi/pdf/10.1002/cpa.3160070112. URL: https://onlinelibrary.wiley.com/doi/abs/10.1002/cpa.3160070112.

[111] K. O. Friedrichs. "Symmetric hyperbolic linear differential equations." In: *Commun. Pure Appl. Math.* 7 (1954), pp. 345–392.

[112] Alexander Kurganov and Eitan Tadmor. "New High-Resolution Central Schemes for Nonlinear Conservation Laws and Convection–Diffusion Equations." In: *Journal of Computational Physics* 160.1 (2000), pp. 241 –282. ISSN: 0021-9991. DOI: https://doi.org/10.1006/jcph.2000.6459. URL: http://www.sciencedirect.com/science/article/pii/S0021999100964593.

[113] Pablo Montes and Oscar Reula. *New Numerical Interface Scheme for the Kurganov-Tadmor second-order Method*. 2021. arXiv: 2105.03452 [math.NA]. URL: https://arxiv.org/abs/2105.03452.

[114] David Gottlieb and Chi-Wang Shu. "On the Gibbs Phenomenon and Its Resolution." In: *SIAM Review* 39.4 (1997), pp. 644–668. DOI: 10.1137/S0036144596301390. eprint: https://doi.org/10.1137/S0036144596301390. URL: https://doi.org/10.1137/S0036144596301390.

[115] E. Abreu, F. Pereira, and S. Ribeiro. *Central Schemes for Porous Media Flows*. 2009. arXiv: math/0610454 [math.NA]. URL: https://arxiv.org/abs/math/0610454.

[116] Jonathan Panuelos, J. Wadsley, and N. Kevlahan. "Low shear diffusion central schemes for particle methods." In: *J. Comput. Phys.* 414 (2020), p. 109454. DOI: 10.1016/j.jcp.2020.109454.

[117] Björn Schenke, Sangyong Jeon, and Charles Gale. "(3+1)D hydrodynamic simulation of relativistic heavy-ion collisions." In: *Phys. Rev. C* 82 (1 2010), p. 014903. DOI: 10.1103/PhysRevC.82.014903. URL: https://link.aps.org/doi/10.1103/PhysRevC.82.014903.

[118] H. Yousefi, Alireza Taghavi Kani, and I. M. Kani. "Response of a spherical cavity in a fully-coupled thermo-poro-elastodynamic medium by cell-adaptive second-order central high resolution schemes." In: *Underground Space* (2018). DOI: 10.1016/J.UNDSP.2018.04.003.

[119] A. Lucas-Serrano, J. A. Font, J. M. Ibáñez, and J. M. Martí. "Assessment of a high-resolution central scheme for the solution of the relativistic hydrodynamics equations." In: *Astronomy amp; Astrophysics* 428.2 (Nov. 2004), 703–715. ISSN: 1432-0746. DOI: 10.1051/0004-6361:20035731. URL: http://dx.doi.org/10.1051/0004-6361:20035731.

[120] Y. Mirbagheri, H. Nahvi, J. Parvizian, and A. Düster. "Reducing spurious oscillations in discontinuous wave propagation simulation using high-order finite elements." In: *Computers Mathematics with Applications* 70.7 (2015). High-Order Finite Element and Isogeometric Methods, pp. 1640–1658. ISSN: 0898-1221. DOI: https://doi.org/10.1016/j.camwa.2015.06.022. URL: https://www.sciencedirect.com/science/article/pii/S0898122115003089.

[121] M. Frigo and S. G. Johnson. "The Design and Implementation of FFTW3." In: *IEEE Proc.* 93.2 (2005), pp. 216–231. DOI: 10.1109/JPROC.2004.840301.

[122] Daniel G. Figueroa, Adrien Florio, Francisco Torrenti, and Wessel Valkenburg. "CosmoLattice: A modern code for lattice simulations of scalar and gauge field dynamics in an expanding universe." In: *Comput. Phys. Commun.* 283 (2023), p. 108586. DOI: 10.1016/j.cpc.2022.108586. arXiv: 2102.01031 [astro-ph.CO].

[123] Ryusuke Jinno, Thomas Konstandin, Henrique Rubira, and Isak Stomberg. "Higgsless simulations of cosmological phase transitions and gravitational waves." In: *JCAP* 02 (2023), p. 011. DOI: 10.1088/1475-7516/2023/02/011. arXiv: 2209.04369 [astro-ph.CO].

[124] OpenMP Architecture Review Board. *OpenMP Application Programming Interface*. Available at https://www.openmp.org/. 2023.

[125] Daniel Cutting, Essi Vilhonen, and David J. Weir. "Droplet collapse during strongly supercooled transitions." In: (Apr. 2022). arXiv: 2204.03396 [astro-ph.CO].

[126] Paul Joseph Steinhardt. "Monopole and Vortex Dissociation and Decay of the False Vacuum." In: *Nucl. Phys. B* 190 (1981), pp. 583–616. DOI: 10.1016/0550-3213(81)90449-1.

[127] Paul Joseph Steinhardt. "Monopole Dissociation in the Early Universe." In: *Phys. Rev. D* 24 (1981), p. 842. DOI: 10.1103/PhysRevD.24.842.

[128] Lars Gerhard Jensen and Paul Joseph Steinhardt. "DISSOCIATION OF ABRIKOSOV-NIELSEN-OLESEN VORTICES." In: *Phys. Rev. B* 27 (1983), p. 5549. DOI: 10.1103/PhysRevB.27.5549.

[129] Yutaka Hosotani. "Impurities in the Early Universe." In: *Phys. Rev. D* 27 (1983), p. 789. DOI: 10.1103/PhysRevD.27.789.

[130] W. A. Hiscock. "CAN BLACK HOLES NUCLEATE VACUUM PHASE TRANSITIONS?" In: *Phys. Rev. D* 35 (1987), pp. 1161–1170. DOI: 10.1103/PhysRevD.35.1161.

[131] Daniel R. Green, Eva Silverstein, and David Starr. "Attractor explosions and catalyzed vacuum decay." In: *Phys. Rev. D* 74 (2006), p. 024004. DOI: 10.1103/PhysRevD.74.024004. arXiv: hep-th/0605047.

[132] Ruth Gregory, Ian G. Moss, and Benjamin Withers. "Black holes as bubble nucleation sites." In: *JHEP* 03 (2014), p. 081. DOI: 10.1007/JHEP03(2014)081. arXiv: 1401.0017 [hep-th].

[133] Philipp Burda, Ruth Gregory, and Ian Moss. "Vacuum metastability with black holes." In: *JHEP* 08 (2015), p. 114. DOI: 10.1007/JHEP08(2015)114. arXiv: 1503.07331 [hep-th].

[134] Kyohei Mukaida and Masaki Yamada. "False Vacuum Decay Catalyzed by Black Holes." In: *Phys. Rev. D* 96.10 (2017), p. 103514. DOI: 10.1103/PhysRevD.96.103514. arXiv: 1706.04523 [hep-th].

[135] D. Canko, I. Gialamas, G. Jelic-Cizmek, A. Riotto, and N. Tetradis. "On the Catalysis of the Electroweak Vacuum Decay by Black Holes at High Temperature." In: *Eur. Phys. J. C* 78.4 (2018), p. 328. DOI: 10.1140/epjc/s10052-018-5808-y. arXiv: 1706.01364 [hep-th].

[136] De-Chang Dai, Ruth Gregory, and Dejan Stojkovic. "Connecting the Higgs Potential and Primordial Black Holes." In: *Phys. Rev. D* 101.12 (2020), p. 125012. DOI: 10.1103/PhysRevD.101.125012. arXiv: 1909.00773 [hep-ph].

[137] Basem Kamal El-Menoufi, Stephan J. Huber, and Jonathan P. Manuel. "Black holes seeding cosmological phase transitions." In: (June 2020). arXiv: 2006.16275 [hep-th].

[138] Naritaka Oshita, Masaki Yamada, and Masahide Yamaguchi. "Compact objects as the catalysts for vacuum decays." In: *Phys. Lett. B* 791 (2019), pp. 149–155. DOI: 10.1016/j.physletb.2019.02.032. arXiv: 1808.01382 [gr-qc].

[139] Reuven Balkin, Javi Serra, Konstantin Springmann, Stefan Stelzl, and Andreas Weiler. "Density Induced Vacuum Instability." In: (May 2021). arXiv: 2105.13354 [hep-ph].

[140] De-Chang Dai, Djordje Minic, and Dejan Stojkovic. "Interaction of cosmological domain walls with large classical objects, like planets and satellites, and the flyby anomaly." In: *JHEP* 03 (2022), p. 207. DOI: 10.1007/JHEP03(2022)207. arXiv: 2105.01894 [gr-qc].

[141] John Preskill and Alexander Vilenkin. "Decay of metastable topological defects." In: *Phys. Rev. D* 47 (1993), pp. 2324–2342. DOI: 10.1103/PhysRevD.47.2324. arXiv: hep-ph/9209210.

[142] U. A. Yajnik. "PHASE TRANSITION INDUCED BY COSMIC STRINGS." In: *Phys. Rev. D* 34 (1986), pp. 1237–1240. DOI: 10.1103/PhysRevD.34.1237.

[143] U. A. Yajnik and T. Padmanabhan. "ANALYTICAL APPROACH TO STRING INDUCED PHASE TRANSITION." In: *Phys. Rev. D* 35 (1987), p. 3100. DOI: 10.1103/PhysRevD.35.3100.

[144] Indranil Dasgupta. "Vacuum tunneling by cosmic strings." In: *Nucl. Phys. B* 506 (1997), pp. 421–435. DOI: 10.1016/S0550-3213(97)00546-4. arXiv: hep-th/9702041.

[145] Brijesh Kumar and Urjit A. Yajnik. "On stability of false vacuum in supersymmetric theories with cosmic strings." In: *Phys. Rev. D* 79 (2009), p. 065001. DOI: 10.1103/PhysRevD.79.065001. arXiv: 0807.3254 [hep-th].

[146] Bum-Hoon Lee, Wonwoo Lee, Richard MacKenzie, M. B. Paranjape, U. A. Yajnik, and Dong-han Yeom. "Battle of the bulge: Decay of the thin, false cosmic string." In: *Phys. Rev. D* 88.10 (2013), p. 105008. DOI: 10.1103/PhysRevD.88.105008. arXiv: 1310.3005 [hep-th].

[147] Bum-Hoon Lee, Wonwoo Lee, Richard MacKenzie, M. B. Paranjape, U. A. Yajnik, and Dong-han Yeom. "Tunneling decay of false vortices." In: *Phys. Rev. D* 88 (2013), p. 085031. DOI: 10.1103/PhysRevD.88.085031. arXiv: 1308.3501 [hep-th].

[148] Issei Koga, Sachiko Kuroyanagi, and Yutaka Ookouchi. "Instability of Higgs Vacuum via String Cloud." In: *Phys. Lett. B* 800 (2020), p. 135093. DOI: 10.1016/j.physletb.2019.135093. arXiv: 1910.02435 [hep-th].

[149] Brijesh Kumar and Urjit Yajnik. "Graceful exit via monopoles in a theory with O'Raifeartaigh type supersymmetry breaking." In: *Nucl. Phys. B* 831 (2010), pp. 162–177. DOI: 10.1016/j.nuclphysb.2010.01.011. arXiv: 0908.3949 [hep-th].

[150] Brijesh Kumar, M. B. Paranjape, and U. A. Yajnik. "Fate of the false monopoles: Induced vacuum decay." In: *Phys. Rev. D* 82 (2010), p. 025022. DOI: 10.1103/PhysRevD.82.025022. arXiv: 1006.0693 [hep-th].

[151] Prateek Agrawal and Michael Nee. "The Boring Monopole." In: *SciPost Phys.* 13.3 (2022), p. 049. DOI: 10.21468/SciPostPhys.13.3.049. arXiv: 2202.11102 [hep-ph].

[152] David I. Dunsky, Anish Ghoshal, Hitoshi Murayama, Yuki Sakakihara, and Graham White. "Gravitational Wave Gastronomy." In: (Nov. 2021). arXiv: 2111.08750 [hep-ph].

[153] Alessandro Strumia. "Black holes don't source fast Higgs vacuum decay." In: (Sept. 2022). arXiv: 2209.05504 [hep-ph].

[154] Simone Blasi and Alberto Mariotti. "Domain Walls Seeding the Electroweak Phase Transition." In: *Phys. Rev. Lett.* 129.26 (2022), p. 261303. DOI: 10.1103/PhysRevLett.129.261303. arXiv: 2203.16450 [hep-ph].

[155] M. E. J. Newman and G. T. Barkema. *Monte Carlo Methods in Statistical Physics*. Clarendon Press, 1999. ISBN: 9780198517979.

[156] Peter Brockway Arnold, Guy D. Moore, and Laurence G. Yaffe. "Transport coefficients in high temperature gauge theories. 1. Leading log results." In: *JHEP* 11 (2000), p. 001. DOI: 10.1088/1126-6708/2000/11/001. arXiv: hep-ph/0010177.

[157] Alberto Roper Pol, Axel Brandenburg, Tina Kahniashvili, Arthur Kosowsky, and Sayan Mandal. "The timestep constraint in solving the gravitational wave equations sourced by hydromagnetic turbulence." In: *Geophys. Astrophys. Fluid Dynamics* 114.1-2 (2020), pp. 130–161. DOI: 10.1080/03091929.2019.1653460. arXiv: 1807.05479 [physics.flu-dyn].

[158] Tina Kahniashvili, Axel Brandenburg, Grigol Gogoberidze, Sayan Mandal, and Alberto Roper Pol. "Circular polarization of gravitational waves from early-Universe helical turbulence." In: *Phys. Rev. Res.* 3.1 (2021), p. 013193. DOI: 10.1103/PhysRevResearch.3.013193. arXiv: 2011.05556 [astro-ph.CO].

[159] Axel Brandenburg, Emma Clarke, Yutong He, and Tina Kahniashvili. "Can we observe the QCD phase transition-generated gravitational waves through pulsar timing arrays?" In: *Phys. Rev. D* 104.4 (2021), p. 043513. DOI: 10.1103/PhysRevD.104.043513. arXiv: 2102.12428 [astro-ph.CO].

[160] Axel Brandenburg, Grigol Gogoberidze, Tina Kahniashvili, Sayan Mandal, Alberto Roper Pol, and Nakul Shenoy. "The scalar, vector, and tensor modes in gravitational wave turbulence simulations." In: *Class. Quant. Grav.* 38.14 (2021), p. 145002. DOI: 10.1088/1361-6382/ac011c. arXiv: 2103.01140 [gr-qc].

[161] Alberto Roper Pol, Sayan Mandal, Axel Brandenburg, and Tina Kahniashvili. "Polarization of gravitational waves from helical MHD turbulent sources." In: *JCAP* 04.04 (2022), p. 019. DOI: 10.1088/1475-7516/2022/04/019. arXiv: 2107.05356 [gr-qc].

[162] Pierre Auclair, Chiara Caprini, Daniel Cutting, Mark Hindmarsh, Kari Rummukainen, Danièle A. Steer, and David J. Weir. "Generation of gravitational waves from freely decaying turbulence." In: (May 2022). arXiv: 2205.02588 [astro-ph.CO].

[163] Ramkishor Sharma and Axel Brandenburg. "Low frequency tail of gravitational wave spectra from hydromagnetic turbulence." In: *Phys. Rev. D* 106.10 (2022), p. 103536. DOI: 10.1103/PhysRevD.106.103536. arXiv: 2206.00055 [astro-ph.CO].

[164] Axel Brandenburg, Kari Enqvist, and Poul Olesen. "Large scale magnetic fields from hydromagnetic turbulence in the very early universe." In: *Phys. Rev. D* 54 (1996), pp. 1291–1300. DOI: 10.1103/PhysRevD.54.1291. arXiv: astro-ph/9602031.

[165] Kandaswamy Subramanian and John D. Barrow. "Magnetohydrodynamics in the early universe and the damping of nonlinear Alfven waves." In: *Phys. Rev. D* 58 (1998), p. 083502. DOI: 10.1103/PhysRevD.58.083502. arXiv: astro-ph/9712083.

[166] Alberto Roper Pol. "GitHub project cosmoGW." In: (). DOI: 10.5281/zenodo.6045844.

[167] A. Brandenburg et al. "The Pencil Code, a modular MPI code for partial differential equations and particles: multipurpose and multiuser-maintained." In: *J. Open Source Softw.* 6.58 (2021), p. 2807. DOI: 10.21105/joss.02807. arXiv: 2009.08231 [astro-ph.IM].

[168] Giulio Barni, Simone Blasi, and Miguel Vanvlasselaer. "The hydrodynamics of inverse phase transitions." In: (June 2024). arXiv: 2406.01596 [hep-ph].